Contributions à la modélisation du comportement de matériaux énergétiques pressés sous sollicitations quasi-statiques

Michael Caliez

HABILITATION À DIRIGER DES RECHERCHES

Discipline : Mécanique

Année universitaire : 2023 / 2024

présentée et soutenue publiquement par :

Michaël CALIEZ

22 Novembre 2023

Contributions à la modélisation du comportement de matériaux énergétiques pressés sous sollicitations quasi-statiques

JURY :

M. Nourredine AÏT HOCINE	Professeur des Universités	INSA CVL
Mme Sabine CANTOURNET	Directrice de Recherche	Mines Paris PSL
M. Nicolas CARRERE	Professeur	ENSTA Bretagne
M. Stéphane MEO	Professeur des Universités	Université Tours
Mme Carole NADOT-MARTIN	Professeure des Universités	ISAE-ENSMA
M. Didier PICART	Ingénieur de recherche, HDR	CEA Le Ripault

PRÉAMBULE

Le premier contact que j'ai eu avec le monde de la recherche a eu lieu alors que je débutais ma Maîtrise de Sciences et Techniques. Je débutais alors une formation universitaire mais plutôt professionnalisante, dans la ligne directe du DUT GMP que je venais d'obtenir. J'ai tout de suite été séduit par ce monde dans lequel la certitude était très souvent remise en cause et où la norme était de se poser des questions. J'ai alors choisi de faire un DEA plutôt qu'un DESS, et d'enchaîner par une thèse de doctorat. J'ai eu la chance de l'effectuer à l'ONERA, auprès de Jean-Louis Chaboche, dans une équipe où se côtoyaient de jeunes doctorants et des chercheurs de très haute renommée. Cette différence ne s'est cependant jamais fait ressentir et je retiens l'humilité de ces chercheurs confirmés, notamment face aux questions ouvertes posées durant les discussions passionnantes (et parfois enflammées) autours d'un café.

J'ai ensuite obtenu en 2003 un poste de Maître de Conférences à l'EIVL (composante de l'Université de Tours) qui deviendra ENIVL puis INSA CVL, et rattaché au Laboratoire de Mécanique et Rhéologie, qui deviendra le LaMé. Tout était à mettre en place dans cette école et ce laboratoire très jeunes. Les différentes restructurations, induisant une succession de modifications de maquettes pédagogiques, associées au manque de moyens humains et matériel a été très chronophage.

La collaboration menée avec le CEA a débuté à cette époque sous l'impulsion de Didier Picart, au travers d'encadrements de doctorants, post-doctorants et parfois stagiaires de fin d'études. Il faut souligner que ces encadrements se sont quasiment toujours faits en équipe avec mes collègues Arnaud Frachon et Michel Gratton. Cette collaboration a été une des bases de la création du Laboratoire de Recherche Correspondant Comportement des Structures et des Matériaux (LRC CoSMa) entre le LaMé et le CEA. Le chapitre 2 de ce document retrace cette « histoire » quasiment dans l'ordre chronologique car les différentes études ont été très cumulatives, partant systématiquement des conclusions des travaux précédents en terme de verrous scientifiques à lever, aussi bien du point de vue expérimental que modélisation. J'ai choisi de m'appuyer sur des publications sélectionnées, ce qui a l'avantage de donner des éléments bibliographiques et de bien synthétiser les différents points abordés.

D'autres thématiques de recherche ont été abordées durant ma carrière, au travers d'opportunités comme les travaux sur le comportement de la peau, où de collaborations plus ancrées concernant notamment le comportement d'aciers inoxydables avec la société CAILLAU. Ces activités sont décrites dans le 1er chapitre du document, qui constitue une synthèse de ma carrière.

REMERCIEMENTS

Je souhaite remercier toutes les personnes que j'ai côtoyées, dans le cadre de mes activités recherche, pédagogique et administrative.

J'adresse quelques remerciements spéciaux aux stagiaires, doctorants et post-doctorants que j'ai encadrés ou en-encadrés.

Je salue et remercie particulièrement mes collègues de bureau : Arnaud Frachon et Michel Gratton, avec lesquels nous faisons équipe pour travailler sur la thématique des matériaux agrégataires.

Je remercie enfin Didier Picart qui nous a fait confiance.

Table des matières

TABLE DES ILLUSTRATIONS

1 NOTICE INDIVIDUELLE

1.1 ÉTAT CIVIL

Nom :	CALIEZ
Prénom :	Michaël
Date de naissance :	13 avril 1975
Lieu de naissance :	Paris (75017)
Nationalité :	Française
Adresse personnelle :	34 rue André Malraux, 41000 Blois
Téléphone personnel :	+33 7 88 87 24 13
Adresse professionnelle :	INSA Centre Val de Loire
	3 rue de la Chocolaterie, CS 23410, 41034 BLOIS Cedex
Téléphone professionnel :	+33 2 54 55 84 51

1.2 SITUATION ACTUELLE

Grade :	Maître de Conférences Hors Classe
Section CNU :	60 – mécanique, génie mécanique, génie civil
Etablissement d'affectation :	Institut National des Sciences Appliquées Centre Val de Loire
	https://www.insa-centrevaldeloire.fr/
Unité de Recherche :	Laboratoire de Mécanique Gabriel Lamé (LaMé) – EA7494
	https://www.mechlabgabriellame.fr/

1.3 PARCOURS ACADÉMIQUE

J'ai effectué ma thèse à l'ONERA, avec une inscription à l'ENS des Mines de Paris, de septembre 1998 à septembre 2001. Cette thèse a été soutenue en décembre 2001.
J'ai été nommé sur un poste d'ATER à plein temps en septembre 2001 à l'Ecole d'Ingénieurs du Val de Loire à Blois, école qui était alors une composante de l'Université François Rabelais de Tours. Ce poste d'ATER a été renouvelé en septembre 2002, là encore à temps plein. J'ai ensuite été nommé Maître de Conférences en septembre 2003 à l'EIVL.
En 2006, l'EIVL est devenue une école autonome en rejoignant le réseau des ENI, pour devenir l'ENI Val de Loire. En 2014, l'ENIVL et ENSI de Bourges fusionnent afin de créer l'INSA Centre Val de Loire, établissement dans lequel j'exerce depuis sa création.
Depuis septembre 2001 je suis membre du Laboratoire de Mécanique et Rhéologie-EA2640, laboratoire sous la tutelle unique de l'Université F. Rabelais de TOURS jusqu'en 2014, et sous la cotutelle de l'Université F. Rabelais de TOURS et de l'INSA Centre Val de Loire jusque fin 2017. Ce laboratoire a, au 1er janvier 2018, fusionné avec des membres du laboratoire PRISME EA4229 pour créer le Laboratoire de Mécanique Gabriel Lamé EA7494 (LaMé) qui regroupe les mécaniciens de la région Centre. Ce laboratoire est sous la tutelle conjointe de l'Université de Tours, l'Université d'Orléans et l'INSA Centre Val de Loire. Le LaMé est structuré en 3 équipes : 1- Génie Civil, 2- Dynamique, Interactions, Vibrations, Structures, 3- Mécanique des Matériaux et des Procédés. Mes activités s'inscrivent dans cette dernière équipe.
Les principales dates qui ont marquées ma carrière sont résumées ci-dessous :

Depuis 2003 **Maître de Conférences** à l'Ecole d'Ingénieurs du Val de Loire, devenue en 2006 ENI Val de Loire, devenue en 2014 INSA Centre Val de Loire, campus de Blois.

Affecté au Laboratoire de Mécanique et Rhéologie (LMR- EA2640), devenu Laboratoire de Mécanique Gabriel Lamé (LaMé – EA7494) en 2016.

Bénéficiaire de la composante C3 du RIPEC depuis Octobre 2022 au titre de l'ensemble des missions

Accès à la Hors Classe en septembre 2018.

2001-2003 **Attaché Temporaire d'Enseignement et de Recherche** à temps plein, EIVL.

Déc. 2001 **Doctorat en Sciences et Génie des Matériaux** de Ecole Nationale Supérieure des Mines de Paris (ENSM-P), effectué à l'ONERA Châtillon, mention Très Honorable :

Titre : Approche locale pour la simulation de l'écaillage des barrières thermique EBPVD.

Directeur : Jean-Louis CHABOCHE

Jury :	*Président :*	Anne-Marie HUNTZ (LEMHE / Univ Paris Sud
	Rapporteurs :	Esteban BUSSO (DME / Imperial College of Science)
		René BILLARDON (LMT / ENS Cachan)
	Examinateurs :	Bertrand BURGARDT (SNECMA)
		Georges CAILLETAUD (ENSMP)
		Jean-Louis CHABOCHE (ONERA)
		Frédéric FEYEL (ONERA)
		Roland FORTUNIER (Centre SMS / ENSM-SE)
		Luc REMY (ENSMP)

1997-1998 **Diplôme d'Etudes Approfondies** en Mécanique et Energétique, Université de Valenciennes.

1995-1997 **Maîtrise de Sciences et Techniques** en Conception Mécanique Assistée par Ordinateur, Université de Valenciennes.

1993-1995 **Diplôme Universitaire de Technologie** en Génie Mécanique et Productique, Institut Universitaire de Technologie A de Lille.

1993 **Baccalauréat** série E.

1.4 ACTIVITÉS D'ENSEIGNEMENT

Lors de mon arrivée à l'Ecole d'Ingénieurs du Val de Loire (EIVL, Université de Tours) en tant qu'ATER en 2001 et de par mon profil orienté technologie mécanique, j'ai pris en charge des enseignements de construction mécanique 2ème année, CAO 4ème année et méthodes de fabrication 3ème année. Ces enseignements étaient dispensés en groupes de travaux dirigés d'environ 24 élèves. Après ma titularisation en tant que Maître de Conférences en 2003, j'ai mis en place progressivement les enseignements de méthodes (5ème année), Fabrication Assistée par Ordinateur (4ème année) et simulations thermomécaniques (5ème année). Mon service s'est toujours accompagné du suivi d'une dizaine de projets ou de stages étudiants.

En 2006, l'EIVL se détache de l'Université de Tours pour intégrer le groupe des ENI et devenir l'Ecole Nationale d'Ingénieurs du Val de Loire (ENIVL). Même si cette création a été accompagnée de créations de poste d'enseignants chercheurs, la filière génie mécanique a dû absorber de nombreuses heures complémentaires. La création de l'ENIVL a été en effet accompagnée d'une refonte des maquettes pédagogiques avec une forte orientation technologique et une mise en avant d'une plus forte proportion de travaux pratiques.

L'école ne possédait à l'époque pas d'atelier de mécanique. J'ai pris en charge cette création progressive conjointement avec un collègue. J'ai mis en place avec ce même collègue un enseignement de procédés de fabrication avec la création de cours magistraux, travaux dirigés en 1ère et 2ème années (niveau L), accompagnés de la mise en place de travaux pratiques de métrologie et d'usinage sur machines. J'assure toujours la responsabilité de cet enseignement. Cette période a donc été synonyme d'une très forte implication pédagogique pour la création des enseignements mais aussi administrative pour l'achat des machines. Mon service atteignait alors environ 230h équivalents TD avec les enseignements de procédés de fabrication (niveau L) et simulations thermomécaniques et méthodes (niveau M). Ce service d'enseignement en face-à-face élèves est toujours accompagné d'une dizaine d'encadrements de projets, stages et missions industrielles. Les missions industrielles sont des dispositifs particuliers concernant généralement un binôme d'étudiants avec un sujet nécessitant des moyens disponibles à l'école mais pas en entreprise (code de calcul, machine...). Cette mission implique un fort encadrement des enseignants référents (40h équivalent TD au référentiel d'équivalences horaires). J'ai encadré depuis 2008 environ une mission industrielle par an.

La création de l'INSA CVL en 2013 s'est accompagnée d'un accroissement d'effectifs avec le quasi doublement des effectifs de la 1ère année avec un passage d'environ 100 à environ 200 élèves. Les maquettes pédagogiques ont été revues notamment pour le 1er cycle pour lequel 75% des enseignements doivent être communs à tous les INSA. Cette évolution a été accompagnée d'une baisse des volumes horaires globaux. Enfin, le département de spécialité GSI a ouvert une voie par apprentissage en 2018, avec le même diplôme final. Cette création n'a pas engendré d'augmentation importante du volume d'enseignement ni du nombre total de groupes de TD et TP, mais le suivi des apprentis et/ou contrat pro induit un volume horaire d'encadrement important.

Sur les 5 dernières années mon service se situe en moyenne aux alentours de 200h équivalents TD, sans compter les activités relevant du référentiel d'équivalence horaire (suivis de stage, projets, missions industrielles et responsabilités) qui sont d'environ 100h. La répartition des heures de face à face élèves est d'environ 20% de CM, 40% de TD et 40% de TP. Mes enseignements sont répartis à 60% en niveau L et 40% en niveau M. Les enseignements en niveau L concernent la CAO (que j'ai dispensée en anglais pendant 3 ans pour les 2 groupes de la Section Internationale Bilingue) et les procédés de fabrication, intégrant une forte composante de TP. Les enseignements du niveau M sont procédés de fabrication (remédiation 3ème année FISE + FISA) matériaux pour l'ingénieur (4ème année FISE + FISA), projet de calcul éléments finis sur Abaqus (4ème année FISE) et simulations thermomécaniques (5ème année FISE). Je suis responsable de trois de ces enseignements.

Trois tableaux synthétiques représentant les services d'enseignement représentatifs des différentes périodes EIVL, ENIVL et INSA-CVL sont présentés ci-après.

		Heures face-à-face			Commentaires	Nb. de groupe			Total face-à-face
		CM	TD	TP		CM	TD	TP	
Niveau L	**Construction méca. 2A**		96				1		138
	Méthodes 3A		42		créé, resp. de l'enseignement		3		
Niveau M	**Mécanique des structures 4A**		32				1		104
	CAO 4A			48				2	
	FAO 5A		12		créé, resp. de l'enseignement		1		
	Méthodes 5A	12			créé, resp. de l'enseignement	1			

Service équivalent TD (coeff. 2/3 sur TP)	232

Projet Fin d'Etudes 5A : 2 (20h)
Suivi stage 4A ou 5A : 3 (15h)

Tableau 1 : Service d'enseignement - année scolaire 2004-2005 (EIVL)

		Heures face-à-face			Commentaires	Nb. de groupe			Total face-à-face
		CM	TD	TP		CM	TD	TP	
Niveau L	**Procédés de fab. 1A**	4	8	80	co-créé, resp. de l'enseignement	1	4	4	156
	Procédés de fab. 2A	4		60	co-créé, resp. de l'enseignement	1		3	
Niveau M	**Méthodes 3A**	4		28		1		2	80
	Modules au choix 4A			12	co-créé, resp. de l'enseignement			1	
	Méthodes 5A	6	6		créé, resp. de l'enseignement	1	1		
	Simulations thermoméca. 5A		24		créé, resp. de l'enseignement		1		

Service équivalent TD (coeff. sur TP calculé au prorata)	224

Mission industrielle 4A : 1 (24h)
Projet Fin d'Etudes 5A : 1 (10h)
Suivi stage 4A ou 5A : 3 (7h)

Tableau 2 : Service d'enseignement - année scolaire 2010-2011 (ENIVL)

		Heures face-à-face			Commentaires	Effectifs			Total face-à-face
		CM	TD	TP		CM	TD	TP	
Niveau L	**CAO 1A**			30.7				2	116
	Procédés de fab. 2A	5.3	20	60	co-créé, resp. de l'enseignement	1	3	6	
Niveau M	**Proc. de fab. 3A (remédiation FISE+FISA)**	2.7	8		co-créé, resp. de l'enseignement	1	1		81
	Matériaux pour l'ingénieur 4A (FISE+FISA)	6.3	24			2	6		
	Calcul EF sur Abaqus 4A (FISE)		16		créé, resp. de l'enseignement		1		
	Simulations thermomécaniques 5A	12	12		créé, resp. de l'enseignement	1	1		

Service équivalent TD (coeff sur TP calculé au prorata)	205

Projet 1A : 3 (3h)
Mission industrielle 4A : 1 (40h)
Projet Fin d'Etudes 5A : 1 (5h)
Suivi stage 4A ou 5A : 3 (7h)
Suivi étudiant en contrat de professionnalisation : 1 (10h)
Suivi étudiant en apprentissage : 3 (30h)

Tableau 3 : Service d'enseignement - année scolaire 2021-2022 (INSA CVL)

1.5 ACTIVITÉS DE RECHERCHE

1.5.1 Description des différentes activités

Mes activités de recherche sont centrées autour de la thématique de la caractérisation et de la modélisation mécanique des matériaux et des structures. Je fais partie de l'équipe Mécanique des Matériaux et Procédés du laboratoire de mécanique Gabriel LaMé. Ces activités vont de la définition et la mise en place d'essais de caractérisation mécanique, à l'identification de lois de comportement, puis à l'intégration de la loi dans un code de calcul par éléments finis. Les travaux effectués ont pour la plupart été destinés à être directement transférés vers l'applicatif, et sont tournés vers la prévision du comportement sous sollicitations sévères, qu'elles soient mécaniques ou thermiques dans le cadre d'une étude de durabilité.

Cette approche a débuté durant ma thèse de doctorat qui portait sur la prévision de la durée de vie d'un revêtement multicouche de type barrière thermique déposé par voie EB-PVD, protégeant une aube de turbine aéronautique. Une modélisation multi-physique éléments finis, couplant calculs de diffusion et mécanique avec endommagement à l'échelle mésoscopique (échelle de la rugosité du multicouche), a permis de décrire la croissance d'une couche d'oxyde à l'interface entre la barrière thermique et la couche d'accroche apposée sur le superalliage de l'aube. La modélisation du comportement (élasto-visco-plastique et élastique fragile) des différentes couches a été basée sur des données expérimentales de la littérature. Les résultats obtenus, comparés aux observations expérimentales post-écaillage, ont permis de confirmer ou d'avancer certaines hypothèses concernant la cinétique et la localisation de l'endommagement, dépendantes du type de sollicitation (oxydation isotherme ou cyclique). La description de l'écaillage du revêtement via des éléments finis de type zone cohésive noyés dans le maillage de la couche d'oxyde a permis de modéliser le passage d'un endommagement diffus à un réseau de fissures discrètes. Ces résultats ont contribué à l'établissement et l'identification d'un modèle de prévision de durée de vie macroscopique basé sur une approche du type Weibull, incorporant la rugosité des interfaces d'une manière statistique.

Les travaux décrits ci-après ont été réalisés depuis mon recrutement en tant que Maître de Conférences avec le même souci de mener une réflexion concernant les données expérimentales pertinentes pour d'une part identifier et d'autre part valider la modélisation. Je présenterai dans la suite les études réalisées par domaine d'application (ou classe de matériau) par souci de clarté, mais elles ont toutes pour point commun 3 thèmes :

- la description d'un comportement matériau non-linéaire,
- la description de l'évolution de ce comportement (endommagement, anisotropie induite, évolution microstructurale…),
- la description du comportement d'une structure.

L'étude du comportement des matériaux énergétiques sous sollicitation quasi-statique a été le fil rouge depuis le début de ma carrière. Ces travaux ont débuté en 2001 lors de mon arrivée à l'EIVL et j'y ai contribué de façon effective à partir de 2002. Ils ont été réalisés dans le cadre d'une collaboration forte avec le CEA Le Ripault (thèses de V.D. Le, A. Benelfellah, M. Chatti, G. Plassart et E. Hamon, post-doctorat de C. Touzeau + 6 contrats de recherche). A l'échelle du laboratoire, dans lequel d'autres actions sont menées avec le CEA, cette collaboration a été concrétisée par la mise en place en 2018 de la convention de Laboratoire de Recherche Correspondant sur le Comportement des Structures et des Matériaux : LRC CoSMa (CEA Le Ripault / LaMé – Université de Tours – Université d'Orléans – INSA CVL). J'ai donc naturellement choisi de consacrer la deuxième partie de ce manuscrit d'HDR à la synthèse de cette activité.

D’autres travaux ont été menés sur les matériaux métalliques. Cette thématique a été initiée en 2005 par la thèse de A. Zinbi portant sur la modélisation du comportement d’un acier inoxydable austénitique AISI 301, incluant des effets de transformations microstructurales. L’application, proposée par la société CAILLAU (41), concernait la modélisation du process de mise en forme d’un collier de serrage, ainsi qu’une optimisation par calcul de sa géométrie. Sous sollicitations mécaniques, la microstructure du matériau étudié est instable et le chargement peut générer une transformation de phase martensitique qui se caractérise par un durcissement structural perturbant l’opération de mise en forme.

Le premier volet de l’étude a été la caractérisation du comportement thermomécanique du matériau. La mesure de la transformation de phase sous charge a été réalisée à l’aide d’un ferritoscope et par Diffraction des Rayons X. Le phénomène de localisation de déformation dans des bandes de transformation de phase a été étudié expérimentalement. L’originalité de l’approche proposée est de fournir une estimation des valeurs de déformations dans les bandes de transformation à partir de mesures de champs de déformations par corrélation d’images.

La seconde partie de l’étude comprenait la modélisation de l’ensemble du process de fabrication, où l’accent a été mis sur l’influence de la cinétique de transformation de phase. Un modèle phénoménologique élasto-visco-plastique avec écrouissage cinématique a été identifié, sur la base d’essais de traction à 0° et 90° par rapport au sens de laminage et d’essais de cisaillement. L’anisotropie plastique initiale est reproduite via un critère de Hill. Le modèle a été couplé à une loi de transformation de phase avec une approche de type champs moyens. Il a été implanté dans le code de calcul par éléments finis ABAQUS via une VUMAT afin d’optimiser la réalisation des colliers au moyen de maquettes numériques. Un bon accord avec l’expérience a été observé sur l’ensemble des résultats des simulations, ce qui confirme la bonne capacité du modèle élasto-visco-plastique à prédire le comportement des aciers à transformation martensitique, de par la prise en compte des évolutions microstructurales du matériau et des paramètres physiques (Cf. Figure 1).

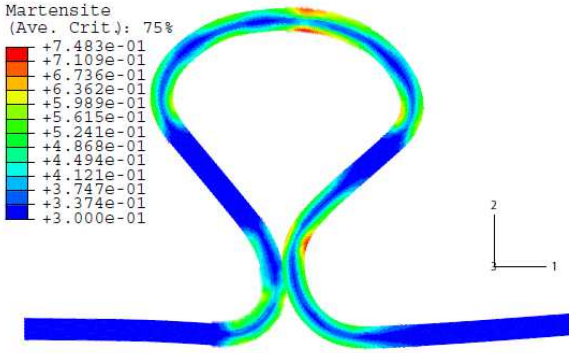

Figure 1 : Taux de martensite simulé après mise en forme de la réserve élastique du collier de serrage [manuscrit A. Zinbi].

A la suite de l’embauche du doctorant dans l’entreprise, une collaboration avec l’ENIVL puis l’INSA CVL a perduré via l’encadrement commun de stagiaires Bac+4 et Bac+5 dans l’entreprise ou de Projets de Fin d’Etudes étudiants (Bac+5) et missions industrielles (Bac+4) au sein de l’INSA CVL. Différents modèles numériques pour la prédiction de l’effort de serrage du collier sous cyclage thermomécanique ont été développés.

Dans le cadre du LabCom LaMé/CAILLAU COFIX (Plateforme de recherche et développement de COlliers de FIXation soumis à sollicitations thermomécaniques et vibratoires) créé en 2019, j’étais co-encadrant d’une thèse démarrée en 2021. Le sujet portait sur l’étude des effets de sollicitations thermomécaniques cyclées et vibratoires sur la tenue en service d’assemblages par colliers métalliques. Un banc d’essai a été conçu et fabriqué mais le doctorant a malheureusement souhaité interrompre son contrat après 1 an et demi. Enfin,

j'ai encadré le stage de Master2 de I. K. Touré concernant le dimensionnement d'une éprouvette représentative d'un collier de serrage. L'objectif était de dimensionner un banc de test simplifié pour l'étude de l'influence de chocs thermiques sur la tenue du collier. Malheureusement, les résultats obtenus ont juste permis de quantifier l'influence du type d'écrouissage (cinématique ou isotrope) sur l'état de contrainte et le retour élastique après mise en forme.

D'autres travaux concernant les matériaux métalliques ont été menés concernant de la compréhension et la modélisation des phénomènes de dégradation subis par un outil d'usinage. La première action entreprise en 2004 a concerné la modélisation du processus d'usinage en coupe orthogonale (stage de DEA de F. Moreau). Un modèle éléments finis associant des zones de maillage purement lagrangien et des zones de maillage ALE a été développé. Les paramètres des lois de comportement et les configurations d'usinage utilisées ont été tirés de la littérature. Cette approche a permis de comparer les résultats des simulations avec les données expérimentales bibliographiques, aussi bien au niveau de la morphologie du copeau que des grandeurs obtenues.

La thèse de D. Joly a poursuivi dans cette voie dans le cadre du Centre d'Etude et de Recherche sur les Outils Coupants (CEROC, situé à Fondettes près de Tours), structure commune entre l'Université de Tours et l'entreprise SANDWICK. Le sujet était plus appliqué et concernait la compréhension des modes d'usure d'outils de fraisage lors de l'usinage de fontes vermiculaires, en vue d'optimiser la conception de ces outils. La loi de comportement de la fonte a été caractérisée par une campagne d'essais de traction. Des calculs éléments finis ont permis une préconception des outils (Cf. Figure 2) et plusieurs configurations (angles d'outil et revêtements) ont été testées dans le cadre d'un plan d'expériences. Les essais ont mis en évidence que l'utilisation de plaquettes avec un revêtement CVD et un angle de coupe positif avait un effet significatif sur l'amélioration de la durée de vie des outils. Ces travaux n'ont malheureusement pas été poursuivis.

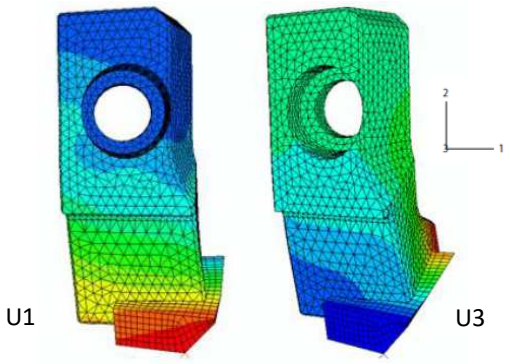

Figure 2 : Estimation des champs de déplacement d'une cartouche de fraise à surfacer [manuscrit D. Joly].

Une autre thématique concerne l'identification et la modélisation du comportement mécanique de la peau. Elle a été initiée dans le cadre de la réponse à un APR d'Intérêt Régional financé par la région Centre en 2013. Le projet PLET (imagerie des Propriétés ultrasonores Locales viscoélastiques de la pEau par Tr-News) a été construit autour d'une collaboration entre l'Unité Imagerie et Cerveau U930 Université de Tours/Inserm (porteur principal), le LMR, la société Orion Concept et l'Institut de Thermomécanique de Prague. J'ai été responsable scientifique de la partie LMR.

L'objectif de ce projet était de proposer une approche couplée mécanique/ultrasons afin de caractériser l'évolution du comportement de la peau vis à vis de son vieillissement. Les retombées concernent l'industrie cosmétique, très implantée en région Centre, qui abrite le pôle de compétitivité Cosmetic Valley. Le projet PLET a été labellisé par ce pôle. J'ai co-encadré dans le cadre de ce projet les post-doctorats de D. Remache et H. Ghorbel ainsi que le stage de Master2 de A. Massod. Les travaux menés ont été principalement expérimentaux.

Des essais de traction simple ont été effectués sur de la peau porcine (qui se rapproche beaucoup de la peau humaine en terme de comportement) afin de connaître les ordres de grandeurs des paramètres à mesurer. Des éprouvettes ont été taillées suivant différentes orientations cutanées. Des essais de traction multicycles et de relaxation nous ont permis de mettre en évidence un comportement hyper-visco-élastique endommageable ainsi qu'une anisotropie très fortement marquée et évolutive dans le temps (Cf. Figure 3). Certains essais ont été accompagnés d'une mesure de champs de déformation par corrélation d'images afin d'observer l'homogénéité des champs de déformation locaux de l'éprouvette, de visualiser la localisation des zones d'endommagement et d'en déduire les directions d'anisotropie, sans contact avec l'échantillon. Une attention particulière a été portée à la synchronisation de la sollicitation mécanique et de la mesure acoustique par le dispositif TR-News.

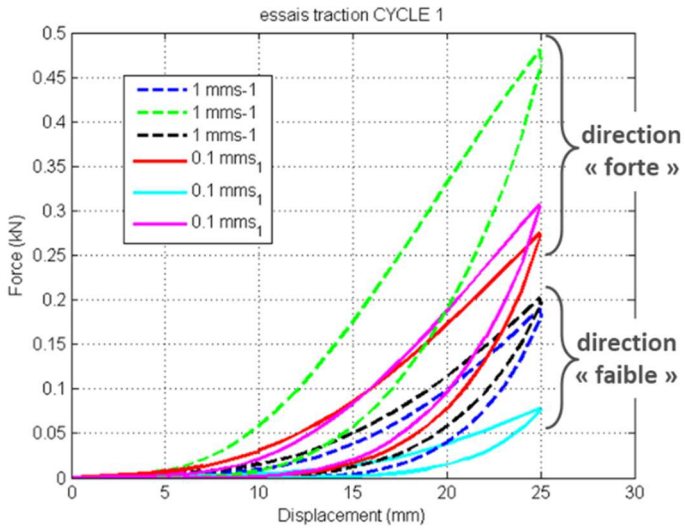

Figure 3 : Essais traction peau porcine ex-vivo 2 vitesses et 2 directions de sollicitation.

Un modèle de type Maxwell généralisé a été utilisé pour modéliser le comportement viscoélastique et les paramètres de deux modèles hyper-élastiques de type d'Ogden-Roxburgh et Yeoh, ont été identifiés. Les résultats des simulations montrent une bonne corrélation avec les essais pour le modèle de Yeoh. Cette thématique est restée pour le moment au stade d'une opportunité qui a été saisie. A la suite du projet PLET, une demande de financement ANR a été déposée en 2015 et une demande de financement région a été déposée en 2018 (APR IR), sans succès.

Enfin, des travaux ont été menés dans le cadre du programme Lavoisier (LAboratoire à VOcation d'Innovation pour la Sécurité et l'Industrialisation des Energies Renouvelables, financement région Centre) concernant la modélisation du comportement du liner PEHD d'un réservoir à Hydrogène de type 4 (post-doctorat de L. Rabemananjara), la modélisation du comportement d'un élastomère amortisseur en vue d'une étude vibratoire de support de batteries (post-doctorat de L. Cortés Mochales), et la modélisation du comportement d'un collier de serrage pour la fixation d'un réservoir hydrogène (stage Master2 de H. Fezaï, collaboration CEA / Caillau / INSA CVL).

1.5.2 Projets ou contrats de recherche

2023-2024 Responsable scientifique pour le LaMé du projet « Standardisation d'essais mécaniques régulés en force ou en déplacement pour caractériser la réponse électrique de nanogénérateurs piézoélectriques dans un contexte de récupération d'énergie mécanique. », collaboration LaMé/GREMAN, financement BQR INSA CVL, durée 2ans (15k€)

2022-2025 Responsable scientifique pour le LaMé du contrat de collaboration avec le CEA Le Ripault « Impact, fragmentation et combustion d'un explosif solide », durée 3 ans (69k€)

2020 Responsable scientifique pour le LaMé de la prestation d'étude pour la société CAILLAU « Conception et dimensionnement de la fixation d'un réservoir composite », durée 6 mois (7k€)

2018-2021 Co-responsable pour le LaMé de la prestation d'étude pour le CEA Le Ripault « Modélisation du comportement thermomécanique du matériau I2 ». Réponse INSA CVL à un appel d'offre CEA, durée 3 ans (120k€)

2013-2016 Responsable scientifique pour le LMR du projet région PLET « imagerie des Propriétés ultrasonores Locales viscoélastiques de la pEau par TR-NEWS » : projet soutenu par la région Centre Val de Loire (APR-IR), labellisé par la Cosmetic Valley. Partenaires : UMR930 Imagerie et Cerveau, LMR, Institut thermomécanique de Prague et société ORION Concept, durée 3 ans. (67k€ pour le LMR)

2013 Responsable pour le LaMé de la prestation d'étude « Modèle viscoélastique viscoplastique endommageable série : stratégie d'intégration et identification en température pour le matériau M1. Modélisation du comportement du matériau M2 » pour le CEA Le Ripault, durée 3 mois (25k€)

2009-2011 Responsable scientifique pour le LMR du contrat de collaboration avec le CEA Le Ripault « Modélisation du comportement d'un matériau agrégataire viscoélastique plastique endommageable des basses aux moyennes vitesses de déformation », durée 3 ans. (90k€)

2004-2007 Co-responsable scientifique pour le LMR du contrat de collaboration avec le CEA Le Ripault « Identification optimisée d'un modèle de comportement élastoviscoplastique », durée 3 ans. (80k€)

2003-2004 Co-responsable scientifique pour le LMR de la prestation d'étude pour le CEA Le Ripault « Intégration d'une loi de comportement viscoélastique à endommagement isotrope dans Abaqus explicit », durée 1 an. (38k€)

1.5.3 Encadrements de thèses

- **Thèses avec %age d'encadrement**

Avril 2017-Déc. 2020 Gaëtane Plassart

Titre : Comportement mécanique anisotrope induit des explosifs comprimés.

Encadrement : D. Picart (Directeur, 40%), M. Caliez (30%), M. Gratton (30%), A. Frachon

Financement : CDD CEA

Situation actuelle : ATER ENSPIMA

Production scientifique associée : ACL 2,4 ; ACTI 2,4 ; ACTN 1 ; PV1

Manuscrit : https://hal.science/tel-03199577/document

Sept. 2008-Sept. 2013 Abdelkibir Benelfellah

Titre : Contribution à la modélisation de l'anisotropie induite par endommagement d'un matériau agrégataire énergétique.

Encadrement : D. Picart (Directeur, 25%), A. Frachon (25%), M. Gratton (25%), M. Caliez (25%)

Financement : contrat collaboration CEA

Situation actuelle : enseignant-chercheur IPSA

Production scientifique associée : ACL 8,10,11,12 ; ACTI 16,17 ; ACTN 4 ; COM2

Manuscrit : https://hal.science/tel-02966078/file/abdelkibir.benelfellah_3801.pdf

Nov. 2006-Nov. 2010 Damien Joly

Titre : Développement d'une méthode de conception et de validation expérimentale d'outils de fraisage : Application au cas de la fonte à graphite vermiculaire.

Encadrement : N. Ranganathan (Directeur, 33%), R. Leroy (34%), M. Caliez (33%)

Financement : bourse CIFRE SANDWICK

Situation actuelle : président société AAMS

Production scientifique associée : ACTI 19 ; ACTN 8

Manuscrit : http://www.applis.univ-tours.fr/theses/2010/damien.joly_3011.pdf

Mai 2005-Juil. 2009 Abdelfettah Zinbi

Titre : Caractérisation et modélisation du comportement mécanique de l'acier inoxydable austénitique AISI 301 à l'état écroui. Simulation d'un process de mise en forme.

Encadrement : C. Gontier (Directeur, 30%), A. Bouchou (40%), M. Caliez (30%)

Financement : contrat prestation CAILLAU

Situation actuelle : responsable service validation numériques et physiques société Caillau

Production scientifique associée : ACTN 5,6,7,9,10 ; AP16

Manuscrit : http://theses.scd.univ-tours.fr/index.php?fichier=priv/2009/abdelfettah.zinbi_2733.pdf

Oct. 2004-Nov. 2007 Viet-Dung Le

Titre : Modélisation et l'identification du comportement plastique visco-élastique endommageable d'un matériau agrégataire.

Encadrement : D. Picart (Directeur, 33%), M. Caliez (33%), M. Gratton (33%), A. Frachon

Financement : contrat collaboration CEA

Situation actuelle : enseignant-chercheur University of civil engineering Hanoï

Production scientifique associée : ACL 13,14 ; ACTI 18,20,21,22 ; AP 17,18,19

Manuscrit : https://insacentre-my.sharepoint.com/:b:/g/personal/michael_caliez_insa-cvl_fr/EZ-kAyaIOcpPoUPADl9g62cBJqVp5XswVxXFAvXX8UdC4A?e=YVcT3R

- **Thèses sans %age d'encadrement**

Oct. 2021-… Emilien Hamon

Titre : Endommagement, fragmentation et combustion d'un matériau explosif comprimé.

Encadrement : D. Picart (Directeur, 33%), P. Bailly (33%), A. Frachon (33%), M. Gratton, M. Caliez

Financement : CDD CEA

Production scientifique associée : ACTI 1

Oct. 2014-Déc. 2018 Marwen Chatti

Titre : Etude expérimentale et modélisation du comportement mécanique d'un matériau agrégataire.

Encadrement : N. Ait Hocine (Directeur, 50%), A. Frachon (50%), M. Gratton, M. Caliez

Financement : cofinancement région CVL/INSA CVL

Situation actuelle : ingénieur développement produits société Henkel

Production scientifique associée : ACL 1,3,6 ; ACTI 7,8,10,11 ; ACTN 3

Manuscrit : https://theses.hal.science/tel-02415344/preview/marwen-chatti.pdf

1.5.4 Encadrements de post-doctorats

Oct. 2018-Oct. 2019 Clément Touzeau

Titre : Modélisation du comportement thermomécanique du matériau I2

Encadrement : M. Caliez, M. Gratton

Financement : contrat de prestation CEA

Production scientifique associée : AP 3,4,5,6,7

Mars 2017-Août 2017 Halima Ghorbel

Titre : Optimisation d'un dispositif de mesures des propriétés mécaniques de la peau et modélisation associée.

Encadrement : M. Caliez, S. Dos Santos

Financement : projet d'Intérêt Régional PLET

Production scientifique associée : ACL 5

Jan. 2016-Déc 2016 Lluis Cortés Mochales

Titre : Characterization and vibration modeling of elastomeric materials.

Encadrement : M. Caliez, J.M. Mencik, S. Méo

Financement : projet SECUBAT (2016), programme LAVOISIER

Production scientifique associée : ACTI 3

Déc. 2015-Mai 2017 Liva Rabemananjara

Titre : Loi de comportement du PEHD constituant le liner d'un réservoir hydrogène de type IV

Encadrement : S. Boucaud-Gauchet, M. Caliez, C. Richard

Financement : projet STOCKH2-Compliner (2016-2017), programme LAVOISIER

Production scientifique associée : ACTN 2 ; COM1

Jan. 2014-Déc. 2014 Djamel Remache

Titre : Imagerie des propriétés ultrasonores locales viscoélastiques de la peau par multi-modalité acousto-mécanique.

Encadrement : M. Caliez, S. Dos Santos, M. Gratton

Financement : projet d'Intérêt Régional PLET

Production scientifique associée : ACL 7 ; ACTI 9,14,15

Déc. 2007-Août 2008 Viet-Dung Le

Titre : Réponse thermo-mécanique d'un matériau visco-élastique plastique : dispersion des fabrications.

Encadrement : M. Caliez, M. Gratton

Financement : contrat de collaboration CEA

Production scientifique associée : AP15

1.5.5 Encadrements de stages recherche de Master2

2022 Imam Katim Touré (Univ. Paris 13)

Titre : Conception et réalisation d'un banc de test et simulation de cyclage thermomécanique sur des éprouvettes en Inox.

Encadrement : M. Caliez

Financement : LabCom COFIX

2021 Houda Fezai (ENSAM Metz)

Titre : Conception et dimensionnement de la fixation d'un réservoir composite.

Encadrement : M. Caliez

Financement : contrat collaboration CAILLAU – projet H2FIX / LAVOISIER

2017 Ali Massod (Univ. Bourgogne)

Titre : Synchronization of TR-NEWS based acousto-mechanical imaging of ex-vivo skin : instrumentation and signal processing.

Encadrement : M. Caliez, S. Dos Santos

Financement : projet d'Intérêt Régional PLET

2004 Franck Moreau (EIVL/Univ. Poitiers)

Titre : Simulation numérique de la coupe des métaux par éléments finis.

Encadrement : A. Bouchou, M. Caliez

Financement : interne

1.5.6 Publications

Articles dans revues internationales à comité de lecture référencées (ACL)

ACL1- M. Chatti, M. Gratton, **M. Caliez**, A. Frachon, D. Picart, N. Ait Hocine, "Experimental investigation of the behavior of a simulant material for plastic-bonded explosives and modelling of the effectivity and damage induced anisotropy.", *Mechanics of Materials*, 2022.
DOI: https://doi.org/10.1016/j.mechmat.2022.104388

ACL2- G. Plassart, D. Picart, M. Gratton, A. Frachon, **M. Caliez**, "Quasistatic anisotropic induced behaviour of a tatb-based plastic-bonded explosive.", *Mechanics of Materials*, 2022.
DOI: https://doi.org/10.1016/j.mechmat.2022.104318

ACL3- M. Chatti, A. Frachon, M. Gratton, **M. Caliez**, F. Lacroix, D. Picart, N. Ait Hocine, "Experimental investigation of multiaxial failure and identification of failure criteria for a PBX simulant material. ", *International Journal of Energetic Materials and Chemical Propulsion*, 20(2), pp. 87-108, 2021.
DOI: https://doi.org/10.1615/IntJEnergeticMaterialsChemProp.2021037739

ACL4- G. Plassart, D. Picart, M. Gratton, A. Frachon, **M. Caliez**, "Quasistatic mechanical behavior of HMX- and TATB-based plastic-bonded explosives.", *Mechanics of Materials*, 2020.
DOI: https://doi.org/10.1016/j.mechmat.2020.103561

ACL5- H. Ghorbel-Feki, A. Masood, **M. Caliez**, M. Gratton, J.-C. Pittet, M. Lints, S. Dos Santos, "Acousto-mechanical behavior of ex-vivo skin: Nonlinear and viscoelastic properties.", *Comptes Rendus Mécanique*, vol. 347(3), pp.218-227, 2019. Disponible en OpenAccess.
DOI: https://doi.org/10.1016/j.crme.2018.12.005

ACL6- M. Chatti, A. Frachon, M. Gratton, **M. Caliez**, D. Picart, N. Aït Hocine, "Modelling of the viscoelastic behaviour with damage induced anisotropy of a plastic-bonded explosive based on the Microplane approach.", *International Journal of Solids and Structures*, pp. 13-25, 2019.
DOI: https://doi.org/10.1016/j.ijsolstr.2018.08.018

ACL7- D. Remache, **M. Caliez**, M. Gratton, S. Dos Santos, "The effects of cyclic tensile and stress-relaxation tests on porcine skin.", *Journal of the Mechanical Behavior of Biomedical Materials*, vol. 77, pp. 242-249, 2018. Disponible en OpenAccess.
DOI: https://doi.org/10.1016/j.jmbbm.2017.09.009

ACL8- A. Benelfellah, M. Gratton, **M. Caliez**, A. Frachon, D. Picart, "VDT microplane model with anisotropic effectiveness and plasticity.", *Mechanics and Industry*, vol. 18(6), 2017.
DOI: https://doi.org/10.1051/meca/2017032

ACL9- S. Dos Santos, · Z. Dvorakova, · **M. Caliez**,·Z. Prevorovsky, "Non linear time reversal signal processing techniques applied to acousto-mechanical imaging of complex materials. ", *Journal of the Acoustical Society of America*, vol. 138(3), pp. 1835, 2015.
DOI: https://dx.doi.org/10.1121/1.4933840

ACL10- D. Picart, A. Benelfellah, J.L. Brigolle, A. Frachon, M. Gratton, **M. Caliez**, "Characterization and modeling of the anisotropic damage of a high-explosive composition." *Engineering Fracture Mechanics*, vol. 131, pp. 525-537, 2014.
DOI: http://dx.doi.org/10.1016/j.engfracmech.2014.09.009

ACL11- A. Benelfellah, A. Frachon, M. Gratton, **M. Caliez**, D. Picart, "Analytical and numerical comparison of discrete damage models with induced anisotropy." *Engineering Fracture Mechanics*, vol. 121-122, pp. 28-39, 2014.
DOI:http://dx.doi.org/10.1016/j.engfracmech.2014.03.022

ACL12- **M. Caliez**, M. Gratton, A. Frachon, A. Benelfellah, D. Picart. "Viscoelastic plastic model and experimental validation for a granular energetic material.", *International Journal of Energetic Materials and Chemical Propulsion*, 13(4), pp. 339-371, 2014. DOI:http://dx.doi.org/10.1615/IntJEnergeticMaterialsChemProp.2014007933.

ACL13- V. D. Le, M. Gratton, **M. Caliez**, A. Frachon, D. Picart, "Experimental Mechanical Characterization of Plastic-Bonded Explosives.", *Journal of Materials Science*, vol. 45, pp. 5802-5813, 2010. DOI:http://dx.doi.org/10.1007/s10853-010-4655-5

ACL14- M. Gratton, V. D. Le, A. Frachon, **M. Caliez**, D. Picart, "Mechanical behaviour of a viscoelastic plastic granular material : experimental procedure and modelling.", *WSEAS transactions on computers*, issue 1, vol.5, pp. 149-156, 2006.

ACL15- U. Schulz, C. Leyens, K. Fritscher, M. Peters, B. Saruhan-Brings, O. Lavigne, J.-M. Dorvaux, M. Poulain, R. Mévrel, **M. Caliez**, "Some recent trends in research and technology of advanced thermal barrier coatings.", *Aerospace Science and Technology*, vol.7, pp. 73-80, 2003. DOI:http://dx.doi.org/10.1016/S1270-9638(02)00003-2

ACL16- **M. Caliez**, J.-L. Chaboche, F. Feyel, S. Kruch, "Numerical simulation of EBPVD thermal barrier coatings spallation.", *Acta Materialia*, vol. 51, n° 4, pp. 1133-1141, 2002. DOI:http://dx.doi.org/10.1016/S1359-6454(02)00518-9

ACL17- **M. Caliez**, F. Feyel, S. Kruch, J.-L. Chaboche, "Oxidation induced stress fields in an EB-PVD Thermal Barrier Coating.", *Surface and Coatings Technology*, vol. 157, n° 2-3, pp. 103-110, 2002. DOI:http://dx.doi.org/10.1016/S0257-8972(02)00167-6

ACL18- **M. Caliez**, F. Feyel, S. Kruch, J.-L. Chaboche, "Simulation numérique de l'initiation de fissures dans une barrière thermique.", *Revue Européenne des Eléments Finis (actuellement European Journal of Computational Mechanics)*, vol. 11, Spécial Giens'01, n° 2-3-4, pp. 527-540, 2002. DOI:http://dx.doi.org/10.3166/reef.11.527-540

Direction d'Ouvrages (DO)

DO1- N. Carrere, **M. Caliez**, (sous la direction de), "Dialogue essai/calcul dans les structures hétérogènes, journée scientifique et technique AMAC." coorganisée par l'Onera et le Laboratoire de Mécanique et Rhéologie, sur le site de l'ENIVL, *Revue des composites et des matériaux avancés*, vol. 15-1, 2005.

Communication avec actes dans un congrès international avec comité de sélection (ACTI)

ACTI1- E. Hamon, D. Picart, P. Bailly, **M. Caliez**, A. Frachon, M. Gratton, "Low velocity impact and damage of a pressed explosive material.", Energetic Materials – Exploring and Understanding. *51st International Annual Conference of the Fraunhofer* ICT, Karlsruhe, Germany, June 2022.

ACTI2- G. Plassart, D. Picart, M. Gratton, A. Frachon, **M. Caliez**, "Mechanical behaviour of a high explosive: multiaxial loading and strain-induced anisotropy." *Europyro – 44th International Pyrotechnics Society Seminar*, Tours, France, June 2019.

ACTI3- J.-M. Mencik, V. Denis, **M. Caliez**, S. Méo, "Application of the wave finite element method to the analysis of locally resonant band gaps in periodic structures with viscoelastic properties.", *28th ISMA conference on Noise and Vibration Engineering*, Leuven, BELGIUM, sept. 2018.

ACTI4- G. Plassart, D. Picart, M. Gratton, A. Frachon, **M. Caliez**, "Damage mechanisms in a TATB-based PBX.", *10th European Solid Mechanics Conference ESMC 2018*, Bologne, Italy, july 2018. (pas d'acte)

ACTI5- S. Dos Santos, A. Masood, M. Lints, A. Salupere, C. Kozena, V. Kus, J.-C. Pittet, **M. Caliez**, M. Gratton, "Multiscale memristive properties of skin induced by memory effects of cyclic stress-relaxation loadings: data fusion from ground truth nonlinear acousto-mechanical testing.", *25th International Congress on Sound and Vibration ICSV25*, Hiroshima, Japan, july 2018.

ACTI6- S. Dos Santos, M. Lints, J.-C. Pittet, **M. Caliez**, M. Gratton, "Acousto-mechanical instrumentation of multiscale hysteretic memristive properties of the skin with nonlinear time reversal imaging.", *Cosmetic Measurements ant Testing congress (COMET) 2017*, Cergy-Pontoise, FRANCE, June 2017. DOI: 10.1109/COMET.2017.8521466

ACTI7- M. Chatti, M. Gratton, A. Frachon, **M. Caliez**, N. AïtHocine, " Experimental failure surfaces and their theoretical predictions for a plastic bonded explosive and its simulant.", *5th International Conference on Computational Modeling of Fracture and Failure of Materials and Structures*, Nantes, FRANCE, June 2017.

ACTI8- M. Chatti, M. Gratton, A. Frachon, **M. Caliez**, N. AïtHocine, "Experimental characterization of the mechanical behaviour of an aggregate material.", *1st International Conference on Advanced Materials, Mechanics and Manufacturing A3M'2016*, Hammamet, TUNISIA, December 2016.

ACTI9- S. Dos Santos, C. Kozena, V. Kus, D. Remache, J.-C. Pittet, M. Gratton, **M. Caliez**, "Memory effects in the biomechanical behavior of ex-vivo skin under acousto-mechanical testings : a multiscale Preisach modeling of aging.", *23rd International Congress on Sound & Vibration ICSV23*, Athens, GREECE, July 2016.

ACTI10- M. Chatti, M. Gratton, A. Frachon, **M. Caliez**, N. AïtHocine, "Failure criteria for energetic materials.", *16th International conference on new trends in fatigue and fracture NT2F16*, Dubrovnik, CROATIA, May 2016.

ACTI11- M. Chatti, M. Gratton, A. Frachon, **M. Caliez**, N. AïtHocine, "Viscoelastic Microplane model for quasi-brittle granular material.", *10th International conference on mechanics of time dependent materials MTDM16*, Paris, FRANCE, May 2016.

ACTI12- S. Dos Santos, · Z. Dvorakova, · **M. Caliez**, ·Z. Prevorovsky, "Non linear time reversal signal processing techniques applied to acousto-mechanical imaging of complex materials.", *170th Meeting of the Acoustical Society of America*, Jacksonville, USA, November 2015.

ACTI13- S. Dos Santos, · M. Lints, · N. Poirot, · Z. Farova,· A. Salupere, · M. Caliez, · Z. Prevorovsky, "Nonlinear Time Reversal for Non Destructive Testing of complex medium : a review based on multi-physics experiments and signal processing strategies.", VIIIth International Workshop NDT in Progress NDTP2015, Prague, CZECH REPUBLIC, October 2015.

ACTI14- S. Dos Santos, D. Remache, M. Gratton, **M. Caliez**, "Skin hysteretic behavior using acousto-mechanical imaging and nonlinear time reversal signal processing.", *22nd International Congress on Sound and Vibration ICSV22*, Florence, ITALY, July 2015.

ACTI15- S. Dos Santos, D. Remache, D. Tokar, M. Gratton, J.C. Pittet, Z. Prevorovsky, **M. Caliez**, "Viscoelastic and/or hysteretic properties of the skin: acousto-mechanical evaluation using nonlinear time reversal imaging in symbiosis with uniaxial loading.", *28th congress of the International Federation of Societies of Cosmetic Chemists IFSCC*, pp. 1561-1570, Paris, FRANCE, October 2014.

ACTI16- A. Benelfellah, A. Frachon, M. Gratton, **M. Caliez**, D. Picart, "Anisotropic damage model with unilateral effect and sliding friction for brittle materials.", *5th International Congress on Design and Modelling of Mechanical Systems*, Djerba, TUNISIA, 2013.

ACTI17- A. Benelfellah, A. Frachon, M. Gratton, **M. Caliez**, D. Picart, "Modelling of the induced anisotropic behavior.", *10th World Congress of Computational Mechanics WCCM10*, Sao Paulo, BRAZIL, 2012.

ACTI18- A. Duchosal, V.-D. Le, M. Gratton, **M. Caliez**, D. Picart, "Non Linear Viscoelasticity in a Plastic Damageable Aggregate Material sensitive to Hydrostatic Pressure.", *8th World Congress of Computational Mechanics WCCM8*, Venice, ITALY, 2008.

ACTI19- N. Ranganathan, D. Joly, R. Leroy, P. Donnadieu, **M. Caliez**, B. Beake, "A study of the nanoimpact resistance of hard coatings at high temperature.", *1st International Congress on Microreliability and Nanoreliability*, Berlin, GERMANY, 2007.

ACTI20- A. Frachon, M. Gratton, **M. Caliez**, V.D. Le, D. Picart, "Mechanical modeling and integration of a viscoelastic plastic material, sensitive to hydrostatic pressure – bend and brazilian tests calculations.", *7th World Congress of Computational Mechanics WCCM7*, Los Angeles, USA, 2006.

ACTI21- M. Gratton, A. Frachon, **M. Caliez**, V.D. Le, D. Picart, "Mechanical characterisation of a viscous-elastic plastic material sensitive to hydrostatic pressure and temperature.", *3rd International Conference on High Performance Structures and Materials*, Ostende, BELGIUM, 2006.

ACTI22- M. Gratton, V.D. Le, A. Frachon, **M. Caliez**, D. Picart, "Mechanical characterization of a viscoelastic plastic granular material sensitive to hydrostatic pressure.", *4th WSEAS/IASME Int. Conf. on System Science and Simulation in Engineering*, Tenerife , SPAIN, 2005.

ACTI23- S. Rja Fi Allah, A. Bouchou, M. Gratton, **M. Caliez**, D. Picart, "Un modèle viscoplastique endommageable appliqué à un matériau agrégataire.", *Colloque International des Problèmes Non-linéaires en Mécanique*, Fès, MAROC, 2004.

ACTI24- **M. Caliez**, F. Feyel, S. Kruch, J.-L. Chaboche, "Initiation and crack growth simulation in a thermal barrier coating.", *4th EUROMECH Solid Mechanics Conference*, Metz, FRANCE, 2000.

Communication avec actes dans un congrès national avec comité de sélection (ACTN)

ACTN1- G. Plassart, D. Picart, M. Gratton, A. Frachon, **M. Caliez**, "Caractérisation de l'anisotropie induite par le chargement d'un matériau agrégataire.", *24ème Congrès Français de Mécanique*, Brest, FRANCE, August 2019.

ACTN2- L. Rabemananjara, S. Boucaud-Gauchet, **M. Caliez**, C. Richard, "Identification des mécanismes d'endommagement du Pemd sollicité en compression.", *DEformation des POlymères Solides 27e édition DEPOS27*, Dourdan, FRANCE, Mars 2017.

ACTN3- M. Chatti, M. Gratton, A. Frachon, **M. Caliez**, N. AitHocine, "Contribution à la modélisation de matériaux agrégataires : proposition d'une loi d'évolution de l'endommagement avec prise en compte de la visco-élasticité.", *22ème Congrès français de Mécanique*, Lyon, FRANCE, Août 2015.

ACTN4- A. Benelfellah, M. Gratton, **M. Caliez**, A. Frachon, D. Picart, "VDT microplane model with anisotropic effectiveness and plasticity.", *22ème Congrès français de Mécanique*, Lyon, FRANCE, Août 2015.

ACTN5- A. Zinbi, A. Bouchou, **M. Caliez**, C. Gontier, "Caractérisation et modélisation de la transformation martensitique dans l'acier austénitique instable AISI 301.", *19ème Congrès français de Mécanique*, Marseille, FRANCE, 2009.

ACTN6- A. Zinbi, A. Bouchou, **M. Caliez**, C. Gontier, N. Rigollet, "Etude du comportement thermomécanique et de la transformation martensitique de AISI 301 écroui.", *9ème congrès de mécanique*, Marrakech, MAROC, 2009.

ACTN7- A. Zinbi, A. Bouchou, **M. Caliez**, C. Gontier, N. Rigollet, "Modélisation du comportement de AISI 301 écroui et la mise en forme par pliage.", *9ème congrès de mécanique*, Marrakech, MAROC, 2009.

ACTN8- D. Joly, R. Leroy, **M. Caliez**, N. Ranganathan, P. Donnadieu, "Usinabilité de la fonte vermiculaire. Quel outil pour assurer l'intégrité de surface usinée ?", *MUGV 2008*, Nantes, FRANCE, 2008.

ACTN9- A. Zinbi, A. Bouchou, **M. Caliez**, C. Gontier, N. Rigollet, "Etude du comportement thermomécanique et de la transformation martensitique de AISI 301 écroui.", *18ème Congrès français de Mécanique*, Grenoble, FRANCE, 2007.

ACTN10-A. Zinbi, A. Bouchou, **M. Caliez**, C. Gontier, "Caractérisation de la transformation martensitique d'un acier austénitique à effet Trip.", *8ème congrès de Mécanique*, El Jadida, MAROC, 2007.

ACTN11-A. Bouchou, M. Gratton, S. Rja Fi Allah, **M. Caliez**, D. Picart, "Modélisation du comportement viscoplastique endommageable d'un matériau sensible à la pression.", *17ème Congrès français de Mécanique*, Nice, FRANCE, 2003.

ACTN12-**M. Caliez**, J.-L. Chaboche, "Approche locale pour la simulation de l'écaillage des barrières thermiques EBPVD.", *Matériaux 2002*, Tours, FRANCE, 2002.

ACTN13-**M. Caliez**, F. Feyel, S. Kruch, J.-L. Chaboche, "Simulation numérique de l'initiation de fissures dans une barrière thermique.", *5ème Colloque national en Calcul des Structures*, Giens, FRANCE, 2001.

Communication sans actes dans un congrès international ou national (COM)

COM1- L. Rabemananjara, S. Boucaud-Gauchet, **M. Caliez**, C. Richard, "Caractérisation expérimentale des mécanismes d'endommagement du polyéthylène moyenne densité (PEMD) sollicité en fatigue par compression.", *36èmes Journées de Printemps de la SF2M (JP 2017) Fatigue des Elastomères*, Polymères et Composites, Paris, FRANCE, Mai 2017.

COM2- M. Gratton, A. Benelfellah, A. Frachon, **M. Caliez**, D. Picart, "Mechanical constitutive law: damage induced anisotropy.", *Journées de la détonique*, Tours, FRANCE, 2015.

COM3- **M. Caliez**, "Modélisation éléments finis de la fissuration aux interfaces et dans un milieu continu.", *3ème Journées Tourangelles de Modélisation & Simulation*, Tours, FRANCE, 2003.

COM4- G. Cardosi, F. Feyel, J.-L. Chaboche, **M. Caliez**, "Simulation of EBPVD thermal barrier coatings spallation.", *Journée Scientifique ONERA, Barrières thermiques : procédés d'élaboration et couches de liaison*, Châtillon, FRANCE, 2002.

COM5- **M. Caliez**, F. Feyel, "Local approach for oxidation induced damage computation in an EB-PVD thermal barrier coating.", *MPSX 2001 Workshop on the Mechanical Behaviour of Superalloys*, Paris, FRANCE, 2001.

COM6- **M. Caliez**, F. Feyel, S. Kruch, J.-L. Chaboche, "Simulation numérique de l'initiation de fissures dans une barrière thermique, prise en compte de l'oxydation." *Invitation du Professeur Anne-Marie Huntz*, LEMHE, Université de Paris XI, mai 2001.

COM7- **M. Caliez**, F. Feyel, S. Kruch, J.-L. Chaboche, "Approche locale pour le calcul de l'endommagement lié à l'oxydation dans les barrières thermiques.", *Journée Scientifique ONERA. Barrières thermiques : aspects thermiques et mécaniques*, Châtillon, FRANCE, 2001.

COM8- **M. Caliez**, "Interactions comportement/oxydation dans une barrière thermique.", *Séminaire Couplages mécanique/diffusion*, ENS Mines de Paris, Paris, FRANCE, 2000.

COM9- **M. Caliez**, F. Feyel, S. Kruch, J.-L. Chaboche, "Interactions comportement/oxydation dans une barrière thermique.", *7ème Journée Jeunes Chercheurs Ile de France*, Paris, FRANCE, 2000.

COM10- **M. Caliez**, S. Kruch, G. Cailletaud, J.-L. Chaboche, "Couplages mécanique/diffusion dans une barrière thermique.", *Conférence Mécamat Couplages Multiphysiques*, Nancy, FRANCE, 1999.

Vulgarisation scientifique (PV)

PV1- Aide à la réalisation d'essais de traction et introduction au concept de comportement matériau à un groupe d'élèves du collège Hubert Fillay de Bracieux (41). Ce groupe a participé au concours national CGénial avec un projet intitulé « Le changement climatique, c'est pas brillant ?! ». Ils ont obtenu le prix Genialissime des partenaires et désigné Coup de cœur de sciences et vie junior.
https://www.insa-centrevaldeloire.fr/fr/actualites/concours-de-sciences-physiques-cgenial
https://www.sciencesalecole.org/c-genial-finale-nationale-palmares/#1685891512888-0c07b6c0-513f
https://www.youtube.com/watch?v=m53VB9zJ4QU

PV2- G. Plassart, D. Picart, M. Gratton, **M. Caliez**, A. Frachon, "Mise en évidence de l'apparition d'anisotropie mécanique dans des explosifs.", *Avancées : Bilan 2020 des publications et de la vie scientifique de la Direction des Applications Militaires*, n°15, pp. 30-31, Octobre 2021.

Rapports de contrat (AP)

AP1- **M. Caliez**, M. Gratton : "Modélisation du comportement thermo-mécanique d'un matériau agrégataire simulant un matériau énergétique", *Contrat CEA n°4600325154, Rapport Sous- Phase 2.2 : Identification des paramètres et implémentation dans ABAQUS/standard*, Juillet 2021

AP2- **M. Caliez**, M. Gratton : "Modélisation du comportement thermo-mécanique d'un matériau agrégataire simulant un matériau énergétique", *Contrat CEA n°4600325154, Rapport Sous- Phase 2.2 : Identification des paramètres et implémentation dans ABAQUS/standard*, Décembre 2020

AP3- C. Touzeau, M. Gratton, **M. Caliez** : "Modélisation du comportement thermo-mécanique d'un matériau agrégataire simulant un matériau énergétique", *Contrat CEA n°4600325154, Rapport Sous- Phase 2.2 : Pré-identification des paramètres du modèle de comportement à 20°C*, Novembre 2019

AP4- C. Touzeau, M. Gratton, **M. Caliez**, G. Trobat : "Modélisation du comportement thermo-mécanique d'un matériau agrégataire simulant un matériau énergétique", *Contrat CEA n°4600325154, Rapport Sous- Phase 2.1 : Caractérisation thermomécanique, essais de compression hydrostatique, essais brésiliens et compression biaxiale*, Septembre 2019

AP5- C. Touzeau, M. Gratton, **M. Caliez**, G. Trobat : "Modélisation du comportement thermo-mécanique d'un matériau agrégataire simulant un matériau énergétique", *Contrat CEA n°4600325154, Rapport Sous- Phase 2.1 : Caractérisation thermomécanique, essais de traction simple*, Aout 2019

AP6- C. Touzeau, M. Gratton, **M. Caliez** : "Modélisation du comportement thermo-mécanique d'un matériau agrégataire simulant un matériau énergétique", *Contrat CEA n°4600325154, Rapport Sous- Phase 2.1 : Caractérisation thermomécanique, essais de compression simple*, Mai 2019

AP7- C. Cardenal, Michel Gratton, **M. Caliez**, C. Touzeau : "Modélisation du comportement thermo-mécanique d'un matériau agrégataire simulant un matériau énergétique", *Contrat CEA n°4600325154, Rapport Phase 1 : Etude prospective*, Novembre 2018

AP8- S. Dos Santos, **M. Caliez**, M. Gratton, J.-C. Pittet, *Rapport d'activité du projet de recherche d'intérêt régional PLET*, 2018.

AP9- **M. Caliez**, M. Gratton, A. Frachon, "Implémentation d'un comportement viscoélastique viscoplastique endommageable. Identification en température.", *Contrat CEA n°4600259100*, 2013.

AP10- **M. Caliez**, M. Gratton, A. Frachon, "Implémentation d'un comportement viscoélastique viscoplastique endommageable. Simulations d'essais longue durée.", *Contrat CEA n°4600245776*, 2012.

AP11- **M. Caliez**, M. Gratton, A. Frachon, “Modélisation viscoélastique viscoplastique endommageable d’un matériau énergétique.”, *Contrat CEA n°4600183072 lot n°3*, 2011.

AP12- **M. Caliez**, M. Gratton, A. Frachon, “Modélisation viscoélastique viscoplastique endommageable d’un matériau énergétique.”, *Contrat CEA n°4600183072 lot n°2*, 2010.

AP13- H. El Amari, D. Picart, **M. Caliez**, M. Gratton, A. Frachon, “ Modélisation du comportement d’un matériau agrégataire viscoélastique plastique endommageable des basses aux moyennes vitesses de déformation - Bibliographie et pistes de résolution.”, *Contrat CEA n°4600183072 lot n°1*, 2009.

AP14- S. Dobol, Y . Bodian, M. Gratton, A. Frachon, **M. Caliez**, D. Picart, “Allumage par impact d’une composition explosive – analyse automatique des résultats de calculs aux éléments finis.”, *contrat CEA n°4600187557*, 2009.

AP15- M. Gratton, V. D. Le, **M. Caliez**, A. Frachon, D. Picart, “Réponse thermo-mécanique d’un matériau visco-élastique plastique : dispersion des fabrications.”, *contrat CEA n°4300166814*, 2008.

AP16- A. Zinbi, A. Bouchou, **M. Caliez**, “Optimisation d’un système de compensation de serrage soumis à des sollicitations thermomécaniques. Simulation de la mise en forme du Clic E.”, *contrat CAILLAU n°V42315*, 2008.

AP17- V.-D. Le, M. Gratton, **M. Caliez**, D. Picart, “Optimisation de l’identification d’un modèle de comportement.“, *contrat CEA n°LR46000109163 lot n°3*, 2007.

AP18- V.-D. Le, M. Gratton, **M. Caliez**, D. Picart, “Optimisation de l’identification d’un modèle de comportement.“, *contrat CEA n°LR46000109163 lot n°2*, 2006.

AP19- V.-D. Le, M. Gratton, **M. Caliez**, D. Picart, “Optimisation de l’identification d’un modèle de comportement.“, *contrat CEA n°LR46000109163 lot n°1*, 2005.

AP20- A. Frachon, M. Gratton, **M. Caliez**, “Etude et identification du comportement mécanique d’un matériau énergétique sous sollicitations quasi-statiques.“, *contrat CEA n°LR46000109505*, 2005.

AP21- A. Frachon, A. Bouchou, **M. Caliez**, “Intégration d’une loi de comportement viscoélastique à endommagement isotrope dans Abaqus explicit.“, *contrat CEA n°LR4600084810 lot n°3*, 2005.

AP22- A. Frachon, A. Bouchou, **M. Caliez**, “Intégration d’une loi de comportement viscoélastique à endommagement isotrope dans Abaqus explicit.“, *contrat CEA n°LR4600084810 lot n°2*, 2004.

AP23- A. Frachon, A. Bouchou, **M. Caliez**, “Intégration d’une loi de comportement viscoélastique à endommagement isotrope dans Abaqus explicit.“, *contrat CEA n°LR4600084810 lot n°1*, 2004.

AP24- A. Frachon, A. Bouchou, **M. Caliez**, “Intégration d’une loi de comportement élastoviscoplastique à endommagement isotrope dans ABAQUS/Explicit, Première approche de l’allumage mécanique.“, *contrat CEA n°LR4600068347*, 2004.

AP25- A. Bouchou, **M. Caliez**, A. Frachon, M. Gratton, S. Rja Fi Allah, H. Tinet, J.L. Brigolle, A.S. Chiarelli, Y. Deburck, D. Picart, H. Trumel, “Modélisation et identification du comportement d'un matériau sensible à la pression hydrostatique.“, *contrat CEA n°4600071291*, 2004.

1.6 RESPONSABILITÉS PÉDAGOGIQUES ET ADMINITRATIVES

Ma carrière a débuté à l'EIVL, école d'ingénieurs appartenant à l'Université de Tours. Cette école étant fortement sous-dotée j'ai dû prendre très tôt des responsabilités administratives, comme la responsabilité de l'emploi du temps du semestre 9 de l'option de 5ème année PMAT (effectif entre 20 et 30 étudiants) en relation avec le service Scolarité.

Lors de la création de l'ENIVL, cette situation ne s'est pas beaucoup améliorée et la direction m'a notamment demandé de prendre en charge la responsabilité de l'emploi du temps des 4 premières années d'étude (environ 400 étudiants). Cette fonction étant prise en charge à cette époque par un personnel enseignant. Cette fonction a été très chronophage durant les années scolaires 2008-2009 et 2009-2010.

Lors de la création de l'ENIVL, les maquettes pédagogiques ont très fortement évolué avec l'introduction de travaux pratiques à fort caractère technologique. Dans ce cadre, un atelier de mécanique a été créé pour lequel j'exerce toujours la responsabilité. En collaboration avec un collègue, des appels d'offre ont été rédigés afin d'acheter les différentes machines (2 fraiseuses, 1 Machine à Mesurer Tridimensionnelle, 1 imprimante 3D). En 2017, il a été décidé de réaménager complètement l'atelier avec la création d'une mezzanine, impliquant des travaux structuraux assez lourds. En tant que responsable pédagogique de l'atelier de mécanique, j'ai donc eu à définir le cahier des charges réunissant toutes les demandes concernant la nouvelle implantation des machines (surfaces, fluides, électricité, gestion du déménagement...).

L'INSA Centre Val de Loire est née de la fusion de l'ENIVL et de l'ENSI de Bourges. Comme tous les autres INSA, l'INSA CVL est structurée en départements. Le département Sciences et Technique Pour l'Ingénieur (STPI) regroupe les deux premières années de formation, viennent ensuite les départements de spécialité. La création de l'INSA CVL s'est accompagnée de changements de maquettes pédagogiques afin de se rapprocher des standards des INSA. A cette époque j'ai pris la responsabilité de la filière mécanique du campus de Blois (15 enseignants et enseignants-chercheurs permanents) et ai coordonné ces évolutions jusqu'en 2016.

De septembre 2016 à septembre 2022 j'ai exercé, pendant 2 mandats consécutifs, la fonction de Directeur du département Sciences et Technologie Pour l'Ingénieur (STPI), département de 1er cycle de l'INSA Centre Val de Loire. Ce département offre la particularité d'être à cheval sur les deux campus historiques de Blois et Bourges, mais aussi depuis 2020 sur le campus de Hué au Vietnam. Le département STPI regroupe environ 450 élèves au total, 250 en 1ère année et 200 en 2ème année. La création du campus de Hué s'inscrit dans le prolongement d'une collaboration initiée par l'ENIVL. Les étudiants sur le campus de Hué suivent durant les 2 années STPI le même programme que nos étudiants avec un renforcement en français. Ils viennent en France à partir de la 3ème année. Les examens sont communs et les résultats des étudiants sont examinés dans le même jury. Il y a donc un travail de suivi, de planification, de mise en relation des enseignants entre eux, de préparation à l'accueil des étudiants en 3ème année à effectuer en collaboration avec le service de Relations Internationales.

En France, la première année est entièrement et uniquement située sur le campus de Blois, alors que la deuxième année est dispensée sur les deux campus. En deuxième année, 80% des enseignements sont communs et 20% sont spécifiques et constituent une pré-orientation vers les départements de spécialité. Selon leur choix de pré-orientation en fin de 1ère année, les étudiants de 2A sont donc dispatchés entre les 2 campus. Cette spécificité entraîne une organisation particulière avec la mise en place d'un jury unique, des dates et horaires d'examens communs et des déplacements sur le campus de Bourges.

De par ma fonction, j'ai présidé les jurys 1A et 2A ainsi que le Conseil de Département STPI, qui prend toute décision concernant la pédagogie dans le département. Un gros travail a notamment été mené en 2021 concernant les nécessaires évolutions des enseignements liés à la réforme du baccalauréat. Des cours de

soutien en Physique/Chimie ont été mis en place ainsi que du tutorat par les étudiants d'années supérieures pour les nouveaux arrivants.
J'ai été nommé en 2018 membre de la CA2I (Commission d'Admission Inter INSA) qui gère les différents aspects des concours d'admission du groupe INSA. J'ai participé avec le responsable concours de l'INSA CVL aux jurys d'admission qui concerne le département STPI.
Je suis membre élu du Comité Technique d'Etablissement (CTE devenu CSAE) et du Comité Hygiène Sécurité et Conditions de Travail (CHSCT devenu FSSSCT) de l'INSA-CVL depuis 2013. J'ai été réélu pour un 3ème mandat fin 2022.
Au niveau du laboratoire, j'ai été membre du Conseil de Laboratoire du LMR pendant 8 ans. Je fais actuellement partie du « bureau » de l'équipe Mécanique des Matériaux et Procédés (MMP) du LaMé depuis 2020, nommé par le responsable de l'équipe. La création de ce bureau repose sur la constatation que l'équipe MMP est présente sur 5 sites (Chartres-Orléans-Blois-Tours-Bourges) et qu'il est donc nécessaire de prendre en compte les contraintes de chacun des sites dans les décisions. De plus, MMP étant une équipe importante en terme de nombre de collègues, la constitution de ce bureau permet de réunir un représentant de chaque site et de fluidifier les remontées d'informations. Ce rôle pourrait donc être qualifié de représentant de site. Le bureau a vocation à gérer le budget alloué à l'équipe, à remonter aussi les propositions de classement de sujets de thèse, de réponses à appels à projet,… au Conseil de Labo qui prend la décision finale.
Enfin, j'ai participé à différents comités de sélection ainsi qu'au jury de recrutement du technicien d'atelier de l'établissement. Les différentes fonctions occupées sont détaillées ci-après.

- **Responsabilités pédagogiques et administratives**

2016-2022	Directeur du département STPI (1er cycle) de l'INSA CVL Président du Conseil de Département STPI Président des jurys de 1A et 2A
2018-2022	Membre de la Commission d'Admission Inter INSA
2016-2018	Correspondant pédagogique pour la restructuration de l'atelier de mécanique
2014-2016	Responsable de la filière génie mécanique du campus de Blois
2012-2016	Responsable des stages de l'option de 5ème année PMAT
2012-2020	Responsable de l'atelier de Mécanique de l'INSA-CVL
2008-2010	Responsable des emplois du temps de l'ENIVL
2002-2008	Responsable de l'emploi du temps de l'option de 5ème année PMAT

- **Fonctions électives**

Depuis 2022 Membre du CSAE de l'INSA CVL

Depuis 2022 Membre de la Formation Spécialisée du CSAE (FSSSCT) de l'INSA CVL

Depuis 2020 Membre du bureau de l'équipe MMP du LaMé

2014-2022 Membre du Comité Hygiène Sécurité et Conditions de Travail de l'INSA CVL

2014-2022 Membre du Comité Technique d'Etablissement de l'INSA CVL

2014-2016 Membre du Conseil du département Génie des Systèmes Industriels de l'INSA CVL

2008-2012 Membre du Conseil d'Administration (CA) de l'ENIVL

2003-2011 Membre du Conseil de Laboratoire du LMR

- **Membre de commissions de recrutement**

2022 Membre de 2 comités de sélection : 2 postes d'agrégés en Sc. Indus. et Lettres

2016 Membre d'un comité de sélection : poste de MCF 60ème section

2009 Membre d'un comité de sélection : poste d'agrégé en Génie Mécanique

2007 Membre d'un jury de concours interne de technicien de fabrication mécanique

1.7 SYNTHESE TEMPORELLE DES PRINCIPALES ACTIVITÉS

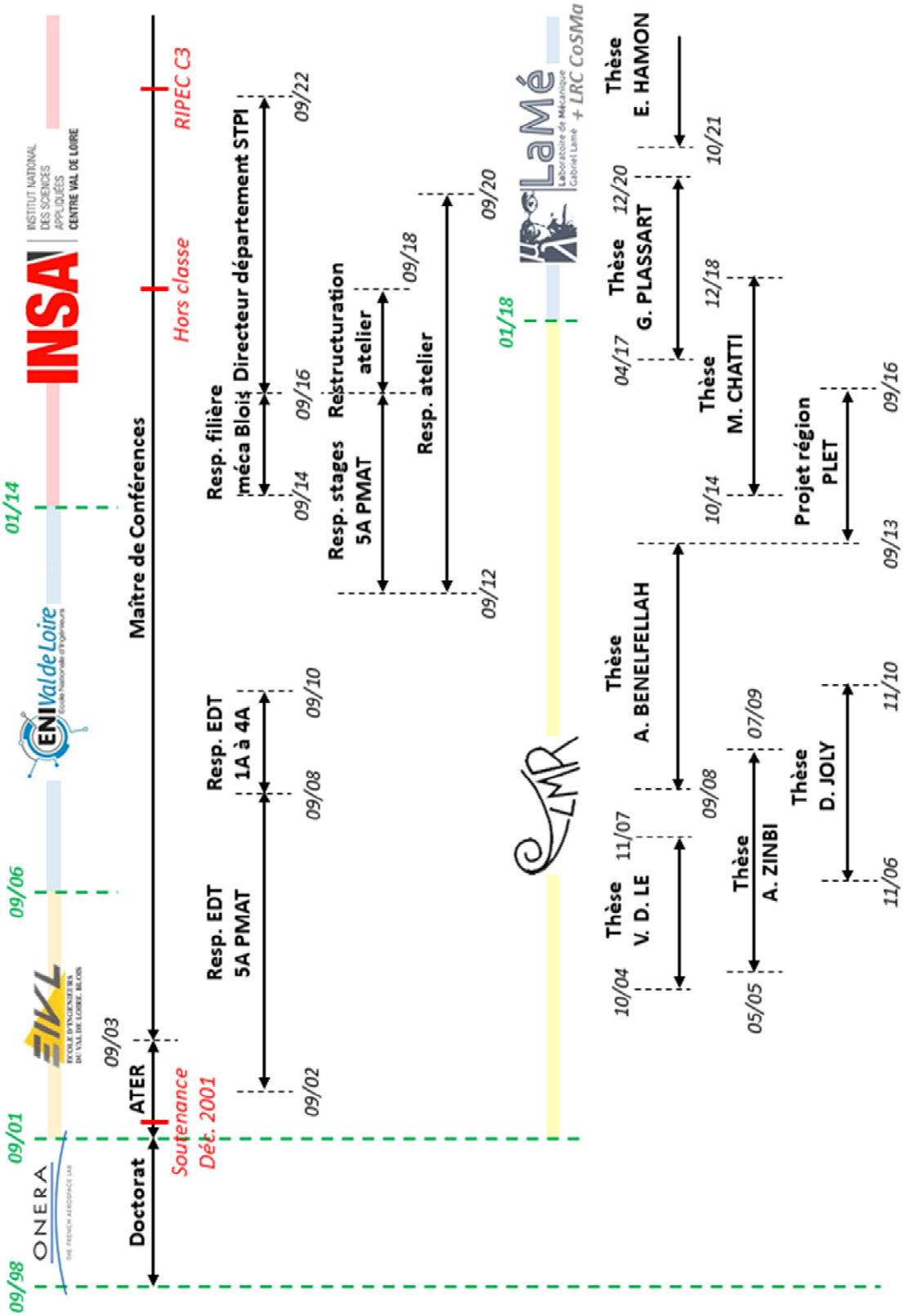

Figure 4 : Synthèse temporelle des principales activités.

2 SYNTHÈSE DES ACTIVITÉS DE RECHERCHE SUR LES MATERIAUX ÉNERGÉTIQUES

La suite du manuscrit synthétise les travaux de recherche menés depuis ma titularisation sur l'étude expérimentale et la modélisation du comportement de matériaux énergétiques comprimés sous sollicitations quasi-statiques. Quelques éléments de contexte sont dans un premier temps évoqués, suivis d'une description de la microstructure des deux matériaux d'études et des principales constatations expérimentales communes. J'ai ensuite choisi une structure de manuscrit qui décrit de manière concise les verrous scientifiques traités et les apports des 4 thèses co-encadrées dans ce domaine. La synthèse des activités retranscrit la temporalité et l'enchaînement des travaux, offrant l'avantage de plus de clarté et de rendre plus visible la démarche menée. Les propos seront illustrés par des publications représentatives permettant au lecteur d'avoir les éléments de bibliographie complets, une description précise des protocoles expérimentaux, des choix de modélisation qui ont été faits et de l'implantation des modèles.

2.1 ÉLÉMENTS DE CONTEXTE

Les activités présentées s'inscrivent dans le cadre d'une collaboration avec le CEA, centre du Ripault (37). Elle a débuté en 2001 pour l'équipe blésoise du laboratoire, et s'inscrit dans le cadre général de la sécurité des édifices pyrotechniques. Actuellement, deux collègues Maîtres de Conférences et moi-même travaillons sur cette thématique. Les matériaux d'études font partie de la classe des explosifs secondaires. Le CEA est chargé de leur conception, de leur fabrication, de leur maintien en conditions opérationnelles et de leur éventuel démantèlement. Ces matériaux peuvent être stockés, ou en tout cas non utilisés, durant plusieurs décennies. Il est donc nécessaire de connaître l'évolution de leurs propriétés mécaniques et de s'assurer qu'un endommagement de la structure ne puisse pas mener à un accident. L'endommagement peut être dû à un simple cycle de température jour/nuit.

Afin de mener des essais de qualification périodiques, une structure est démantelée à l'instant t et des éprouvettes sont prélevées. Le volume matériau disponible est donc contraint et le nombre d'essais et la géométrie des éprouvettes doivent être optimisés. Il est nécessaire d'indiquer ici que la géométrie de la structure ainsi que les conditions limites réelles ne sont pas transmises par le CEA. De plus, du fait de la nature du matériau, les essais mécaniques ne peuvent être effectués qu'au sein du centre du Ripault. Afin de calibrer ou tester les dispositifs expérimentaux, un matériau inerte au comportement équivalent est associé à chaque matériau énergétique. Dans la suite du manuscrit, un matériau nommé M_j sera un matériau énergétique et un matériau nommé I_j sera le matériau inerte associé, pour lequel une étude expérimentale peut être faite au LaMé.

Ne connaissant pas la structure ni les chargements réels, le domaine d'étude est fixé par le CEA : vitesses de déformation comprises entre $\dot{\varepsilon} = 1.0\ 10^{-6}\ s^{-1}$ et $\dot{\varepsilon} = 1.0\ 10^{-3}\ s^{-1}$, pressions de confinement comprises entre P = 0 et P = 10 MPa et températures comprises entre T = -50°C et T = 100°C. La température est considérée comme une variable à évolution lente et on se contentera donc de paramétrer les coefficients matériaux à partir d'essais à température imposée.

Le domaine des sollicitations quasi-statique est assez peu étudié et modélisé sur ce type de matériaux. Au début des années 2000, la bibliographie expérimentale montre le plus souvent des essais monotones pour

lesquels la déformation transversale est rarement mesurée. Il en résulte que les modèles proposés s'appuient sur des connaissances limitées concernant le comportement matériau, avec des paramètres identifiés sur peu d'essais. L'approche la plus publiée à cette époque concerne le modèle Visco-SCRAM développé au Los Alamos National Laboratory (Etats-Unis) concernant le matériau PBX9501, équivalent au matériau M1. Pour une revue exhaustive des données expérimentales et des principaux modèles publiés dans la littérature sur les 2 types de matériaux étudiés, le lecteur pourra se référer à l'article référencé ACL4 disponible en Annexe A. Il est nécessaire de préciser que cet article a été publié en 2020 dans le cadre des travaux de Gaëtane Plassart sur M2. Il situe donc par rapport à la littérature les travaux antérieurs à sa thèse, travaux qui seront présentés dans ce manuscrit dans les chapitres 2.3 à 2.4.

Dans toutes les études effectuées dans le cadre de ce manuscrit, on se restreint à une modélisation phénoménologique en considérant le matériau d'un point de vue macroscopique, mais en s'appuyant le plus possible sur des données expérimentales permettant d'isoler les différents mécanismes du comportement. Cette base de données expérimentales a été construite et enrichie au fur et à mesure des années. Elle est composée d'essais permettant de construire le modèle et d'identifier ses paramètres et d'essais de validation. Enfin, certains essais très spécifiques ont été mis en œuvre afin d'éclairer un trait précis de comportement. Chacune des thèses ou post-doctorat encadrés a donc apporté une amélioration dans la compréhension du comportement matériau et dans sa modélisation, avec à chaque fois un modèle implanté dans une routine utilisateur UMAT dans Abaqus.

Enfin, il m'apparaît nécessaire de préciser que l'environnement de travail à mon arrivée à l'EIVL n'était pas du tout le même que l'actuel, surtout dans le domaine expérimental pour lequel les équipements étaient très peu nombreux et obsolètes. Les différents contrats industriels, les financements Région et établissement (ENIVL puis INSA CVL) nous ont permis de réaliser de nombreux investissements. Cependant, la gestion de ces achats (appel d'offre, installation…) associée à l'absence de collègue technicien depuis quelques années a été chronophage, alors même que des charges administratives et pédagogiques lourdes étaient assurées par l'ensemble de l'équipe.

2.2 MATÉRIAUX D'ÉTUDE ET PRINCIPALES CONSTATATIONS EXPÉRIMENTALES

Les matériaux étudiés sont des explosifs pressés. Ils sont constitués de cristaux d'explosifs mélangés à une très faible quantité de liant polymère thermoplastique qui assure la cohésion du matériau final. La mise en forme de ces matériaux comporte deux étapes :

- une étape d'enrobage des cristaux d'une couche de liant de faible épaisseur
- une étape de mise en forme du matériau par compaction isostatique en température.

L'étape de mise en forme a lieu dans une poche cylindrique en élastomère. Après la mise sous vide, la poche est introduite dans une presse isostatique où elle subit plusieurs cycles de pression de valeur maximale comprise entre 150 et 200 MPa. Après refroidissement, on obtient un matériau compact, macroscopiquement homogène, avec une porosité résiduelle de l'ordre de quelques %. Ce matériau peut alors être usiné par un outil de coupe.

Le matériau M1 est constitué de cristaux d'octogène/HMX (octahydro-1,3,5,7-tetranitro-1,3,5,7-tetrazocine) de tailles très variables, comprises entre 1 et quelques centaines de micromètres. Le liant représente environ 5% en masse. Une micrographie de la microstructure est présentée Figure 5. De la très grande variabilité des tailles de grains résulte une microstructure constituée de grains de taille importante (200µm en moyenne,

exemple en jaune sur la Figure 5) noyés dans une matrice constituée du liant et des grains de faible taille. On distingue très clairement des fissures intra- et inter-granulaires résultant du procédé de fabrication du matériau, ainsi que quelques porosités dont le taux volumique est estimé entre 3 et 5%. Aucune orientation privilégiée des microfissures initiales n'a pu être constatée, confirmée par un comportement macroscopique initialement isotrope.

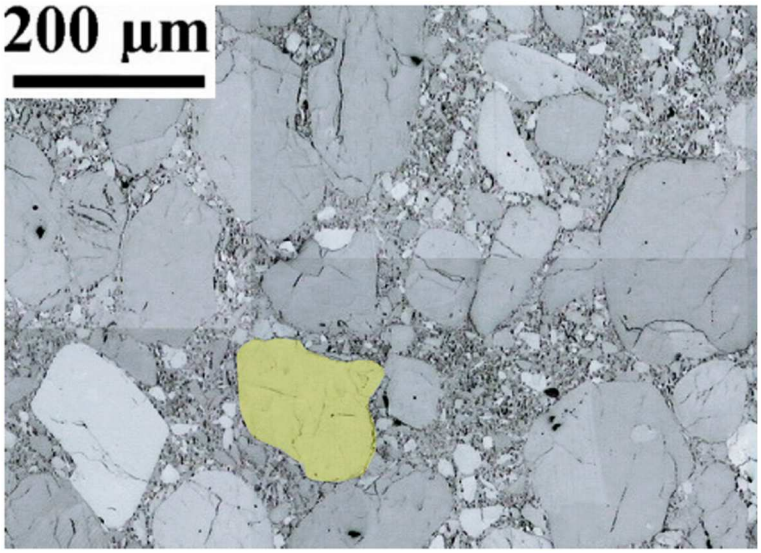

Figure 5 : microstructure du matériau M1 [Mémoire de V.D. Le].

Le matériau M2 est quant à lui composé de cristaux de type TATB (1,3,5-triamino-2,4,6-trinitrobenzene) de taille moyenne de 50µm agglomérés avec un liant polymère thermoplastique, représentant environ 5% en masse. On peut voir sur la micrographie présentée Figure 6 que la distribution des tailles de grains est beaucoup plus réduite que pour M1. On distingue, de plus, beaucoup moins de microfissures intra- et inter-granulaires. La porosité initiale est estimé à environ 5% en volume. Là encore, même si les grains de TATB sont fortement anisotropes, le matériau à l'échelle de l'éprouvette possède un comportement initial isotrope.

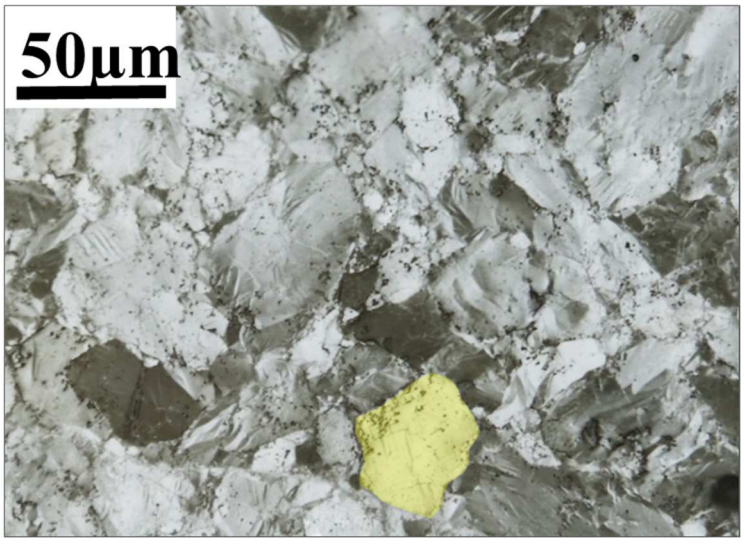

Figure 6 : microstructure du matériau M2 [Mémoire de G. Plassart].

Ces 2 matériaux, de par leur microstructure, possèdent des traits de comportement similaires aux matériaux agrégataires du type béton ou roche. Une description quantitative sera donnée dans la suite du manuscrit au

travers des publications présentées, mais on peut noter plusieurs constatations expérimentales communes pour M1 et M2. Sur la Figure 7, tracée pour M1 à 20°C et $\dot{\varepsilon}$=3.3 $10^{-5}s^{-1}$ on constate :

- une asymétrie de comportement entre traction et compression très fortement marquée,
- une dépendance du comportement à la pression de confinement,
- un endommagement (dégradation du module d'élasticité),
- la présence de déformations irréversibles (plasticité),

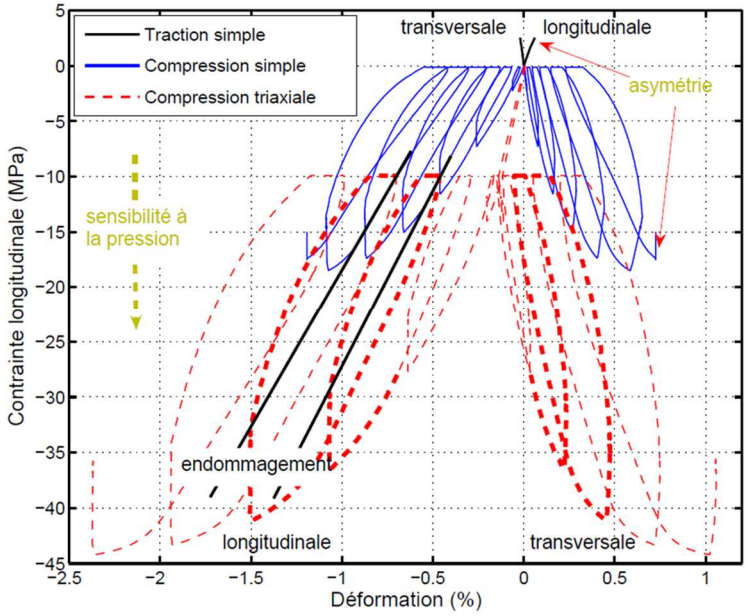

Figure 7 : comportement de M1 à 20°C et $\dot{\varepsilon}$=3.3 $10^{-5}s^{-1}$ en traction, compression et compression sous pression de confinement 10MPa avec cyclage [Mémoire de V.D. Le].

Sur la Figure 8, tracée pour M2 à différentes températures et vitesses de sollicitation :

- une dépendance à la vitesse de sollicitation (viscoélasticité et/ou viscoplasticité), des essais DMA permettent de montrer l'existence d'une composante viscoélastique pour les 2 matériaux,
- une dépendance du comportement à la température.

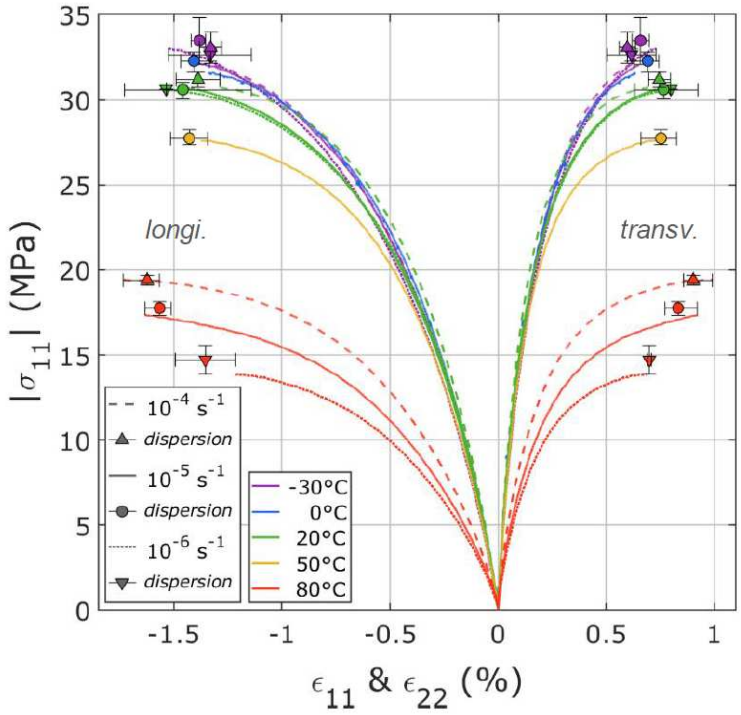

Figure 8 : comportement de M2 en compression simple monotone à 3 vitesses de sollicitation et 5 températures [Mémoire de G. Plassart].

Enfin, on observe que la courbe enveloppe des essais cyclés est la même que celle des essais monotones et ce quelle que soit la condition d'essai (cf. Figure 9 en traction pour M1).

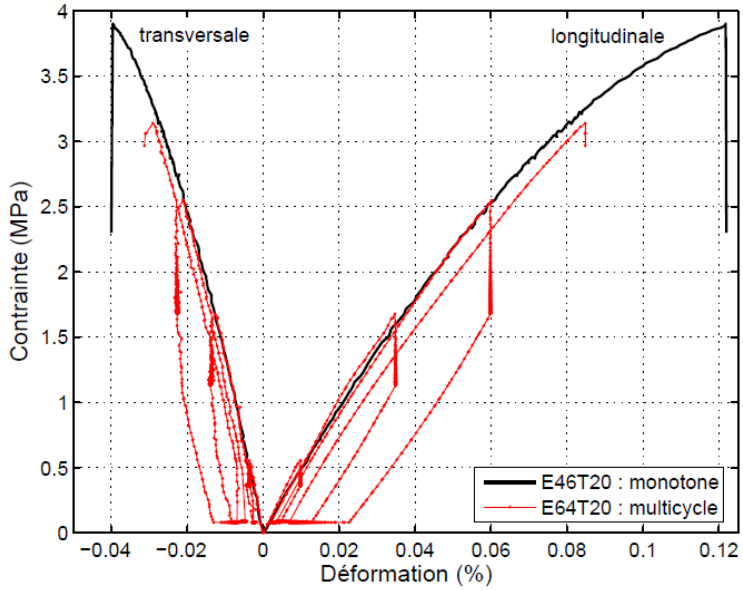

Figure 9 : comparaison entre essais de traction simple monotone et cyclé sur M1 à 20°C et $\dot{\varepsilon}$=3.3 $10^{-5}s^{-1}$ [Mémoire de V.D. Le] .

2.3 1ÈRE BASE EXPÉRIMENTALE ET MODÈLE ISOTROPE (M1)

L'objectif général des premiers travaux encadrés (thèse de V.D. Le) était de développer et d'identifier un modèle phénoménologique dans un contexte isotrope, basé sur des observations expérimentales, identifiable avec un faible nombre d'essais (= volume matière le plus faible possible). Dans ce contexte, une réflexion a été menée concernant la constitution de la base expérimentale. Compte tenu des grands traits de comportement de cette classe de matériau et de l'expérience acquise précédemment, la définition des cycles de charge / relaxation / décharge / recouvrance des essais multicycles a été pensée afin de tirer le maximum d'informations à partir des essais de compression. La compression est la sollicitation de référence du fait de la difficulté à réaliser correctement un essai de traction, du fait de la fragilité du matériau.

Cette base de données expérimentale a été utilisée dans la thèse de V.D. Le afin de construire le modèle présenté dans l'article ACL13 qui suit. Les déformations à rupture les plus importantes mesurées sont de l'ordre de 2 à 3%, ce qui nous permet une écriture dans le cadre de l'hypothèse des petites perturbations. Enfin, on ne cherche pas à modéliser le comportement post-pic du matériau, on considère que la rupture correspond à la contrainte maximale.

Afin de faciliter le dépouillement des essais le choix d'une structure rhéologique de type parallèle, basée sur une additivité des contraintes viscoélastique et élastoplastique a été effectué très tôt. Cette décision permet de profiter pleinement de la base de données expérimentales en permettant d'identifier le maximum de paramètres à partir d'un minimum d'essais. Ce lien entre définition du modèle et des essais est donc très important. Enfin, une structure rhéologique de type parallèle permet de simplifier l'implantation du modèle dans une routine utilisateur UMAT, la donnée d'entrée étant l'incrément de déformation, identique pour toutes les branches dans notre cas.

La méthode de dépouillement des essais exposée dans l'article ci-après permet une identification des paramètres séquentielle et quasiment découplée. L'identification complète est faite dans un premier temps à 20°C, puis certains paramètres sont ensuite identifiés en fonction de la température, qui est pour nous une variable lente.

Le lecteur pourra relever dans l'article présenté un certain nombre d'hypothèses initiales, dont beaucoup feront l'objet d'explorations dans les travaux suivants :

- L'écrouissage est de type isotrope
- L'endommagement affecte la partie élastique de toutes les branches, il est considéré isotrope
- Le module d'élasticité initial correspond à celui identifié en compression simple
- La viscosité du matériau provient uniquement d'un caractère viscoélastique

Le critère de plasticité est de type parabolique (permettant de décrire une asymétrie traction/compression) fonction des 2 premiers invariants de contrainte. La surface initiale est tracée via une estimation des limites d'élasticité (estimation délicate dans notre cas). Une saturation est observée en compression sous confinement, permettant le tracé de la surface à saturation. Afin de s'assurer de la non-intersection des différentes isovaleurs de la surface de charge une fonction de de l'écrouissage est explicitement introduite dans l'expression du critère. Comme sur la plupart des matériaux granulaires, l'écoulement est non-associé. La direction d'écoulement est déterminée via un paramètre de dilatance, couplant les écoulements plastiques volumiques et déviatoriques.

Le modèle a été implanté dans une UMAT dans le code de calcul Abaqus. L'intégration de la partie viscoélastique est analytique et l'intégration de la partie plasticité est basée sur un algorithme de type retour radial.

Les comparaisons essais/calcul montrent une assez bonne corrélation. Plusieurs points sont cependant à noter :

- les boucles d'hystérésis sont mal reproduites,
- les courbes enveloppes des essais cyclés et monotones ne sont pas identiques, surtout pour les vitesses de déformation importantes,
- il a été nécessaire de mettre en œuvre deux critères de rupture distincts, un pour la traction et l'autre en compression.

Une comparaison entre champs de déformations mesurés par corrélation d'images sur un essai brésilien et champs numériques montre une assez bonne cohérence qualitative. Néanmoins, les déformations transverses sont quantitativement mal estimées. Il est à noter que les paramètres en traction ont dû être recalés à partir d'essais de flexion 3 points, illustrant les difficultés expérimentales et de dépouillement concernant cet condition d'essai. Enfin, les observations montrent un comportement avec anisotropie induite, dont la modélisation fera l'objet des études présentées dans le chapitre suivant.

L'article référencé ACL13 est présenté ci-après.

J Mater Sci (2010) 45:5802–5813
DOI 10.1007/s10853-010-4655-5

Experimental mechanical characterization of plastic-bonded explosives

Viet Dung Le · Michel Gratton · Michaël Caliez · Arnaud Frachon · Didier Picart

Received: 26 March 2010 / Accepted: 24 May 2010 / Published online: 8 June 2010

Abstract This article deals with the characterization of the static mechanical behavior of an energetic material. Due to its constituents (crystals and a polymeric binder), the behavior is complicated to model. A specific experimental protocol has been proposed in this article. It involves uniaxial tensile and compressive tests, compression under confinement and dynamic mechanical analysis. A constitutive law has been developed. The behavior is described using a Maxwell's model, in which all the components are influenced by an isotropic damage. The first component takes into account an elasto-plastic behavior. The yield stress evolution is described using a parabolic criterion and an isotropic hardening law. The plastic flow rule is non-associated. A linear visco-elastic behavior is used for the other components. Numerical simulations show that experimental data are quite well reproduced. The last part of the article is devoted to a discussion highlighting the future improvements.

Introduction

Energetic materials are often used under thermal and/or mechanical loading conditions. When modeling the response of these materials, it is necessary to have an in depth knowledge and characterization of the behavior. This article is about a material made of energetic crystals (octahydro-1,3,5,7-tetranitro-1,3,5,7-tetrazocine, HMX) mixed with a few percentage of a binder. An isostatic compaction process eliminates the initial porosity of the powder (Fig. 1), which results in a quasi-brittle concrete-like material, with the largest grains embedded in a "matrix" composed of the binder, the smallest crystals, and the residual porosity. The main difference with concretes is the strain-rate dependence which could be attributed to the small amount of polymeric binder.

Microscopic observations show a lot of micro-cracks inside or between crystals due to the high volume fraction of the solid phase and the pressure applied to compact the material.

During the 1980s, an extended database (several hundred experiments) was necessary to characterize this material [1]. Uniaxial compressive or tensile tests were applied at constant strain rate or stress rate loading conditions, with or without pressure confinement (triaxial experiments) or temperature variation. However, the surveillance of the possible aging of this material implies an accurate determination of the mechanical properties when this material is only available in small amounts after disassembling. Consequently, a reduced number of tests can be performed using small-sized samples. In this study, we have take advantage of the evolution of experimental techniques (machines, measurements) and numerical tools to propose new experiments and a constitutive law.

Many observations were published about PBX 9501, another pressed HMX-based plastic-bonded explosive composition. For tensile or compressive loading conditions, a non-linear increase of the uniaxial stress is obtained [2]. Once the maximum stress is reached, a decrease is registered. The strain at the maximum stress being close to 1% during compressive tests, a quasi-brittle behavior is exhibited. During tensile tests, the strain at the maximum

V. D. Le · M. Gratton · M. Caliez · A. Frachon
ENI Val de Loire, Laboratoire de Mécanique et Rhéologie, Université F. Rabelais-Tours, Rue de la chocolaterie, BP 3410, 41034 Blois Cedex, France

D. Picart (✉)
CEA, DAM, Le Ripault, 37260 Monts, France
e-mail: didier.picart@cea.fr

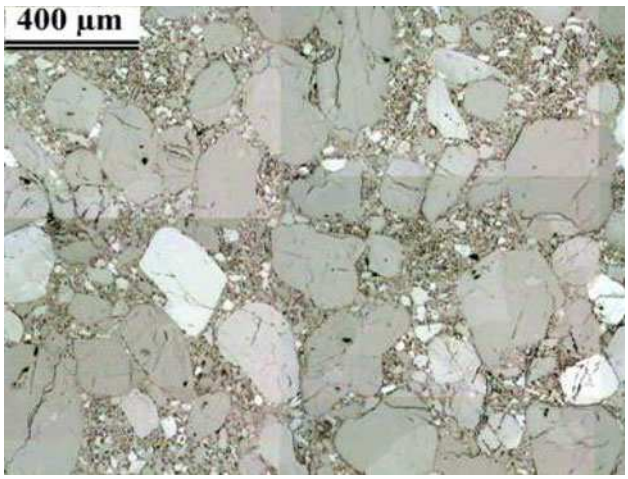

Fig. 1 Microstructure of the explosive composition. Micro-cracks are the consequence of the compaction process

stress was several times less than the one recorded during compressive experiments. The high volume fraction of the granular phase causes, first, the difference between compressive and tensile experiments and, second, the behavior observed at higher hydrostatic pressures [3, 4].

A more ductile behavior appears as the confining pressure increases. The brittle–ductile transition is obtained for a confining pressure above 20 MPa. A dependence of initial Young's modulus on the pressure was also noticed by Wiegand [3]. It is not clear how this dependence is a consequence of the increase of the glass transition temperature of the material, of the decrease of the initial porosity, or of the increase of internal surfaces where friction locks the relative displacements (contacts between crystals, closure of micro-cracks). For compressive and tensile experiments, strain rate and temperature dependences were observed [5–8].

The mode-I fracture process in PBX 9501 was investigated by Liu [9] using symmetric or asymmetric four-points bend tests and Brazilian tests. The process zone ahead of the crack has an extended size and cannot be described by the classical Griffith's theory.

In spite of this extended experimental database, only a little data is available in the literature about tensile behavior. However, this loading path is one of the most dramatic conditions which could lead to explosive part failure, for example, during disambling or cooling. On the other hand, the coupled influence of the strain rate, the temperature and the pressure has not been studied. Experiments were conducted using only a constant variation of the strain and without measurements of the transversal strain. As a consequence, dilatancy mechanism (well-known for soils, concretes, and geomaterials) was not determined and the time-dependent stress could not be separated from the total stress. A new experimental protocol is proposed and detailed in the second part of this article. Experiments were designed to reduce the number of experiments and to conduct more informative tests. Tests were performed at room temperature with loading conditions ranging between 0 and 10 MPa for the mean pressure, and between 10^{-6} and 10^{-3} s^{-1} for the strain rate. The temperature dependence of the behavior is out of the scope of this article. In the third part of this article, the behavior is analyzed. Three main phenomena have been identified: residual strain, time dependence, and damage.

The dynamic and high pressure loading conditions leading to ignition, for example, during an impact, motivated research on the constitutive law of PBX 9501. The well-known Visco-SCRAM model [10] was a combination of the damage theory, denoted SCRAM, proposed by Dienes for brittle materials [11], and a linear visco-elastic Maxwell's model. The initial SCRAM approach was reduced by [10] to a constitutive law incorporating isotropic damage, in which evolution was related to the mean crack radius growth. A discussion on such damage laws can be found in [12]. The model was calibrated from quasi-static to dynamic loading conditions, and predictions were compared to displacement fields obtained using a few impact configurations [13–15]. Later, Hackett and Bennett [16] modified the crack growth to take into account the influence of the pressure, and the difference between tensile and compressive behaviors. An update of SCRAM has been recently proposed by Dienes et al. [17]. The crack distribution anisotropy is taken into account as well as the coalescence and the nucleation of penny-shaped cracks.

Some comments are now proposed about the previous constitutive laws. First, the pressure part of the stress was disconnected from the deviatoric one, except through the damage law. Maxwell's law was only devoted to the deviatoric part of the behavior. Consequently, simulations cannot capture, for example, the evolution of the initial elastic modulus obtained during triaxial tests for various confinement conditions. Second, the degradation mechanism was based on a mode-I failure model when shear localization (mode-II) is suspected to happen for dynamic conditions and/or for high confinement load. Finally, dilatancy or compaction of the material was not allowed. Even if some of the model parameters seemed to be related to the mesoscopic scale (mean crack radius, crack growth rate), an inverse method is necessary to determine these parameters using the macroscopic experimental database.

A constitutive law for our material was proposed [18], assuming a negligible visco-elasticity and describing the time dependence using a visco-plastic flow rule. This model reproduces the loading and the relaxation conditions. However, unloading and hysteretic behavior are poorly reproduced due to the absence of visco-elasticity.

The constitutive law proposed in this article is restricted to quasi-static loading conditions for which a lot of data are now available. A generalized Maxwell's model is adopted with an elasto-plastic and a visco-elastic coupling. Isotropic damage is assumed. It influences the entire model. The main differences between this work and the visco-SCRAM model are (1) the arrangement of the components, which are submitted to the same strain coming from the global equilibrium state and (2) a Maxwell's model applied to the total stress and not only to the deviatoric one.

The fourth and fifth parts of this article are devoted to a description of the constitutive law and comparisons between experimental and computed data. We deduce the limits and assets of this model, and the capability of a modified generalized Maxwell's model to reproduce the quasi-static mechanical behavior of this class of materials.

Experimental procedure

Standard tests made in various material directions shown an initial isotropic behavior. To ensure statistical validity and to check the dispersion level, each test reported in this article was repeated five times. Negative stress or strain values reported refer to compressive conditions on further figures.

Shape ratio of the samples

The specimen size was chosen to keep large dimensions compared to the internal material characteristic lengths (diameter of crystals). Samples were machined in several geometric shapes, which were more than 10 times the length of the material heterogeneity. Different diameters (Ø) and lengths (L) were tested using compressive experiments (cylindrical samples) to analyze the material homogeneity and the shape dependence of data. Figure 2 shows that, for a given geometry of the sample, all the curves are closed to each other. It demonstrates the homogeneity of the material properties.

The analysis proposed in Fig. 3 underlines the shape dependence of the data. One can see the maximum stress (σ_{max}) and the associated strain (ε_{peak}) as a function of the shape ratio (L/Ø). A value of 4/3 increases the stiffness of the longitudinal behavior. However, when the ratio exceeds two, this effect vanishes and an asymptote appears on the maximum stress. Nothing can be said about the strain. Several explanations were proposed such as the influence of friction on the end surfaces of the sample or the intersection of the shear plane with these surfaces [19]. Considering only the maximum stress (σ_{max}), a shape ratio of two is a good compromise for the compressive loading

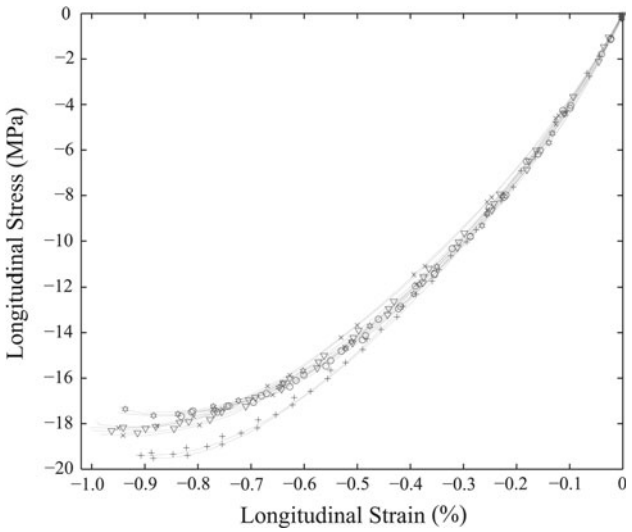

Fig. 2 Stress versus strain for compressive experiments ($\dot{\varepsilon} = 1.7 \times 10^{-4}$ s^{-1}) and different shape ratios (L/Ø): diameter 10 mm and length 20 mm (o), 12.5 and 25 mm (x), 15 and 30 mm (∇), 15 and 20 mm (+), 10 and 30 mm (✡)

paths. The adopted geometry was Ø10L20 mm^2 for uniaxial tests and Ø50L100 mm^2 for triaxial ones.

This study could be reproduced for tensile conditions. The brittle response in tension being highly influenced by initial geometric defaults of the experimental setup, a tied interface is currently being studied. Waiting for these results, dog-bone samples of 150-mm length with a rectangular cross section of 10 × 10 mm^2 were used.

Protocols

Samples were equipped with two opposite pairs of strain gauges. Gauges signals were averaged (after estimation of the strain heterogeneity) to provide the longitudinal and the

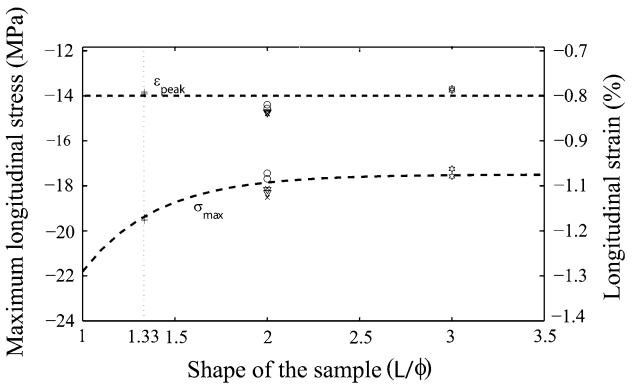

Fig. 3 Evolution of the maximum stress and of the peak strain for compressive tests ($\dot{\varepsilon} = 1.7 \times 10^{-4}$ s^{-1}) and various shape ratios (L/Ø): diameter 10 mm and length 20 mm (o), 12.5 and 25 mm (x), 15 and 30 mm (∇), 15 and 20 mm (+), 10 and 30 mm (✡)

transversal strains during the test. The longitudinal strain rate imposed during experiments was obtained by controlling one of the two longitudinal gauges. Stress was deduced from the force measured by a sensor. The triaxial compression experiments were done using geomaterials characterization tool (hermetic cell, pressure controller, and water). The first stage of the loading program was a hydrostatic loading condition (0, 5, or 10 MPa). Then, an uniaxial load was applied.

One of the main improvements to the usual testing procedure was the use of cyclic loading conditions (five to six cycles) to underline possible evolutions of the elastic properties. After unloading and a delay to recover time-independent data, we measured the residual strains. The viscosity was observed either (1) using uniaxial tests for different loading strain rates (from 3×10^{-6} to 10^{-3} s^{-1}) or (2) using relaxations during cyclic loading conditions. The test was controlled for 30 min (resp. 50 min) during the relaxation condition (resp. the recovery condition) (Fig. 4). Relaxation times were defined to guarantee an almost complete relaxation of the stress. We took into account a maximum test duration of 8 h imposed for safety reasons.

A Dynamic Mechanical Analysis apparatus (denoted DMA in this article) was also used in a tensile-compressive mode with samples of 50-mm long and a cross section of 5×5 mm^2. Samples were glued to the platens.

Global trends of the behavior

Figures 5 and 6 entail arrangements for the mechanical tests and show some of the main features of the material. A non-linear behavior is observed whatever the loading conditions. A quasi-brittle behavior is observed during tensile experiments (Fig. 6). A more ductile one is obtained during tri-axial experiments. The maximum stress is influenced by the hydrostatic pressure. Finally, a hysteretic response is obtained for cyclic loading conditions. These observations show that our material behaves like a concrete due to its quasi-compact granular microstructure. The influence of internal friction can be suspected as well as damage by micro-cracks nucleation and coalescence. Residual strains are registered after unloading and recovery. Optical observations of the microstructure shown that grains are not significantly deforms, irreversibility being associated to local damage. However, a different assumption will be used to model the macroscopic behavior.

The time dependence of the behavior was observed first comparing the maximum stress during constant strain rate tests (Fig. 5). Linear visco-elastic behavior was characterized using DMA experiments. The material was submitted

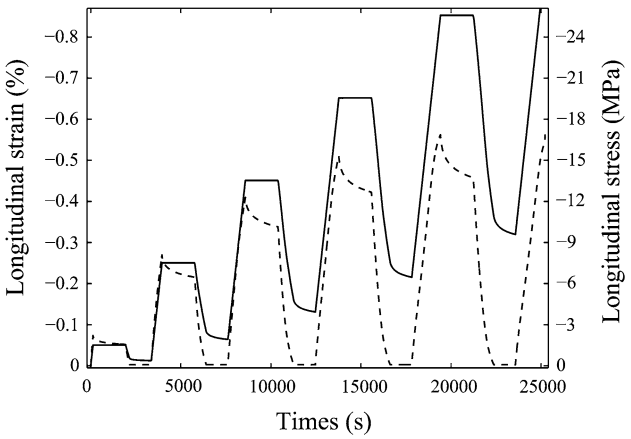

Fig. 4 Longitudinal stress (*dashed line*) and strain (*line*) versus time: an example of relaxation and recovery loading conditions

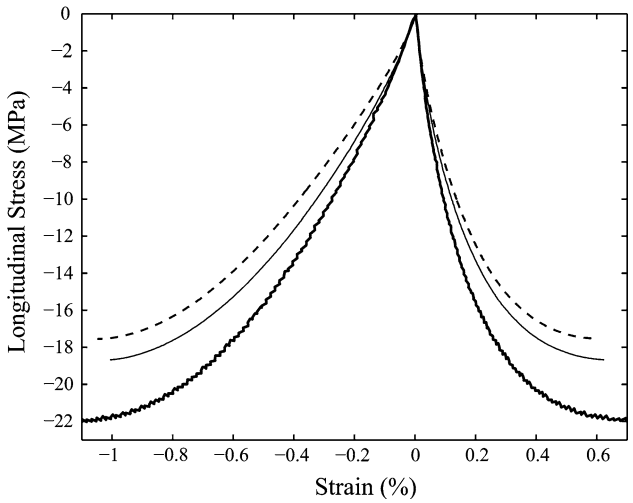

Fig. 5 Influence of the strain rate (compressive tests): 8.3×10^{-4} (*bold line*), 3.3×10^{-5} (*line*), and 3.3×10^{-6} s^{-1} (*dashed line*)

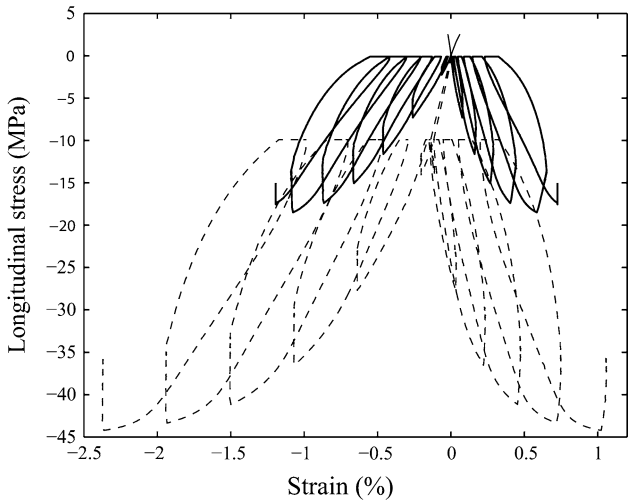

Fig. 6 Influence of the pressure and difference between compressive and tensile loading conditions: tensile (*line*), compressive (*bold line*) and tri-axial experiments (*dashed line*)

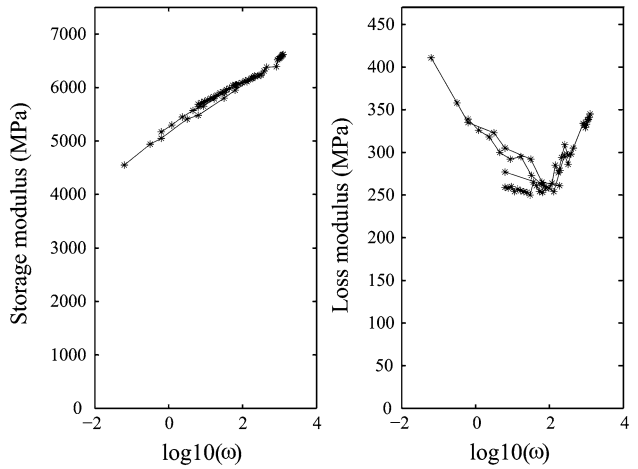

Fig. 7 Experimental data recorded during Dynamic Mechanical Analysis experiments (DMA). Storage modulus (*left*) and loss modulus (*right*) versus the logarithm of $2\pi f$, where f is the frequency

to a sinusoidal load with small amplitude ($\varepsilon_0 = 10^{-4}$), the linearity of the behavior being previously controlled. The range of frequencies goes from 0.004 to 200 Hz and the quadratic average strain rate range from 2×10^{-6} to 1×10^{-1} s^{-1}. Visco-elastic storage (E_{stor}) and loss (E_{loss}) modules were determined (Fig. 7).

The broad loops observed on Fig. 6 and the decrease of the stress (resp. the strain) during the relaxation (resp. recovery) conditions are attributed to visco-elasticity, assuming that irreversible mechanisms are locked during unloading. However, the asymmetry of the response obtained during a creep-recovery test suggests that another time-dependent mechanism must be added to linear visco-elasticity (Fig. 8).

Figure 9 shows a comparison between (1) a constant strain rate experiment and (2) a test with the same strain

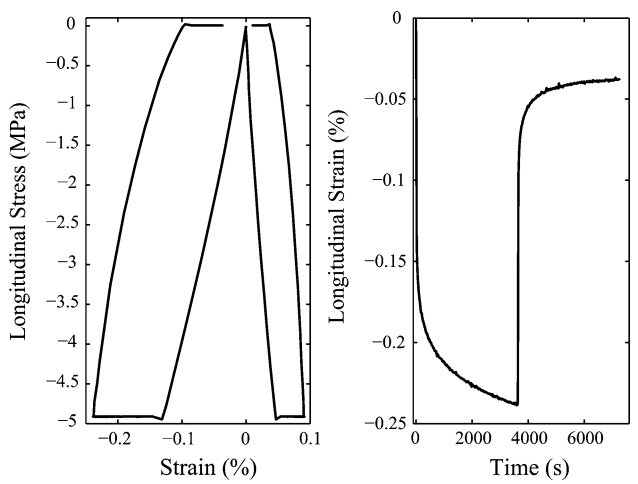

Fig. 8 Experimental data recorded during a creep-recovery test. Stress versus longitudinal and transversal strains (*left*) and strain versus time (*right*)

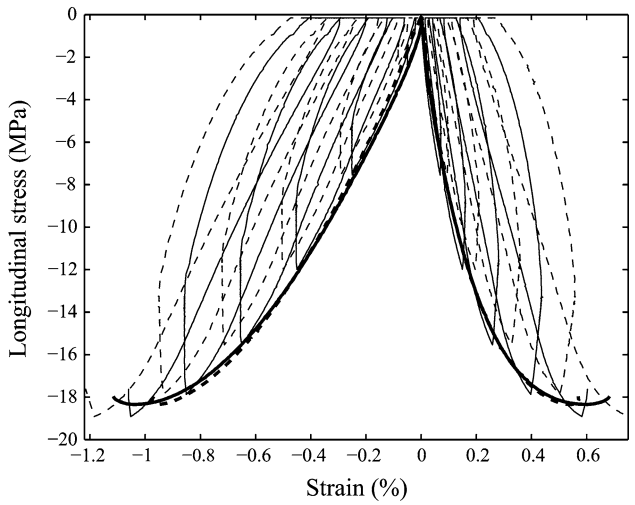

Fig. 9 Stress versus longitudinal and transversal strains for a constant strain rate equal to 3.3×10^{-5} s^{-1} (*bold lines*) and the same test interrupted by cycles (*line*). For each test, the two gauges glued on the lateral surface of the sample provided two longitudinal (respectively transversal) strain measurements (*dashed or not dashed lines*)

rate loading/unloading conditions and relaxation/recovery setup. The result of the second test is embedded below the first one, which will be referred to as the "cover curve" in this article. The same observation was done using different strain rate conditions or cycles without relaxation and recovery conditions.

In addition, the time-dependent stress can be drawn for three confining pressures during relaxation. The same strain amplitude is chosen for each test. Figure 10 shows the pressure dependence of the time-dependent stress. This phenomenon is consistent with the pressure dependence of the initial elastic modulus described later in this article (Fig. 15).

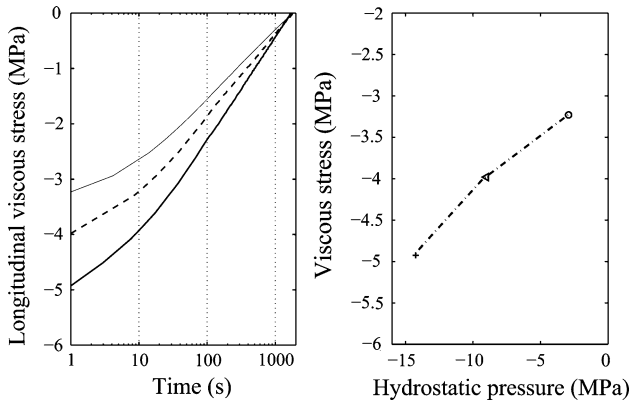

Fig. 10 Three relaxation curves recorded during compressive tests with the same strain but different confinements (compressive test: *line or circles*; confinement of 5 MPa: *dashed line* or Δ; confinement of 10 MPa: *bolded line* or +). Influence of the pressure on the time-dependent stress (*left*) and initial amplitude of the time-dependent stress (*right*)

The same analysis can be done using the recovery conditions. Figure 11 (left) gives a comparison between two records obtained for two confining pressures (5 and 10 MPa). These conditions were chosen because the level of the stress at the end of the relaxation and the residual strain were approximately the same. However, strain versus time curves are different. A dependence on the strain and/or the damage amplitudes is suspected (Fig. 11 right).

A master curve can be drawn for a given confinement but different strain rates, joining all the stress–strain data measured at the ends of relaxation times (Fig. 12). This observation shows that a hardening mechanism is at work. On the other hand, residual strains are used to observe the volumic and deviatoric parts of the behavior (Fig. 13). When the volume increases for tensile tests, a more complicated behavior is deduced from compressive experiments, showing an influence of the confining pressure. This

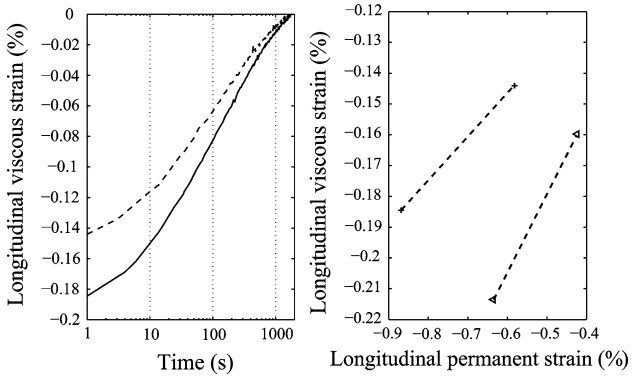

Fig. 11 Two recovery curves (*left*) recorded during a tri-axial experiment with a confinement of 10 MPa, for a residual strain after recovery equal to 0.58% (*dashed line*) or equal to 0.87% (*bold line*). The viscous strain is reported (*right*) versus residual strains for 5 and 10 MPa of confinement

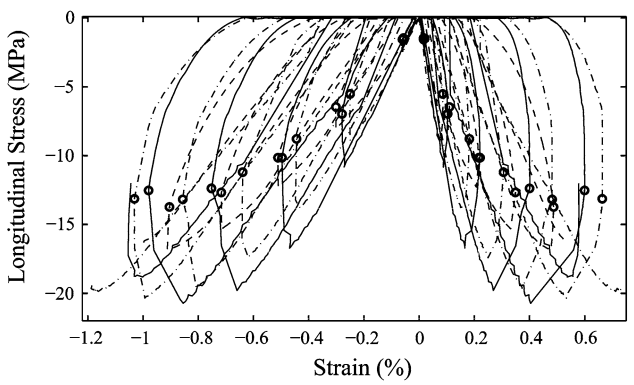

Fig. 12 Relaxed stress (*circles*) for each cycle and different strain rates (uniaxial compressive tests): 3.3×10^{-3} (——), 8.3×10^{-4} (— · —), and 3.3×10^{-6} s^{-1} (— —)

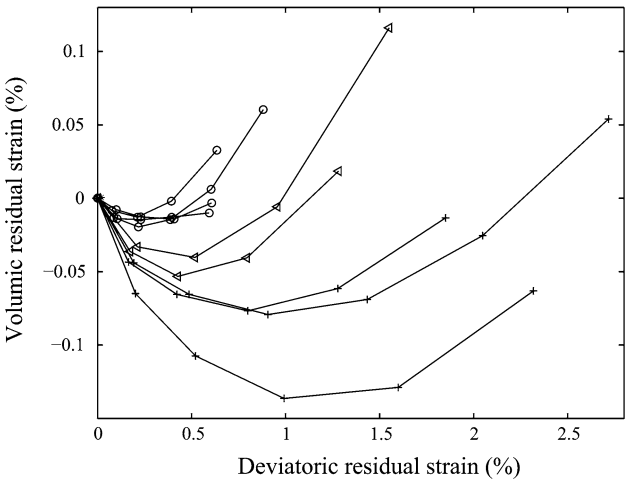

Fig. 13 Volumic versus deviatoric residual strains. Influence of the pressure: tensile experiment (∗), compressive experiment (o), and tri-axial experiments with a confining pressure of 5 (◁) and 10 MPa (+)

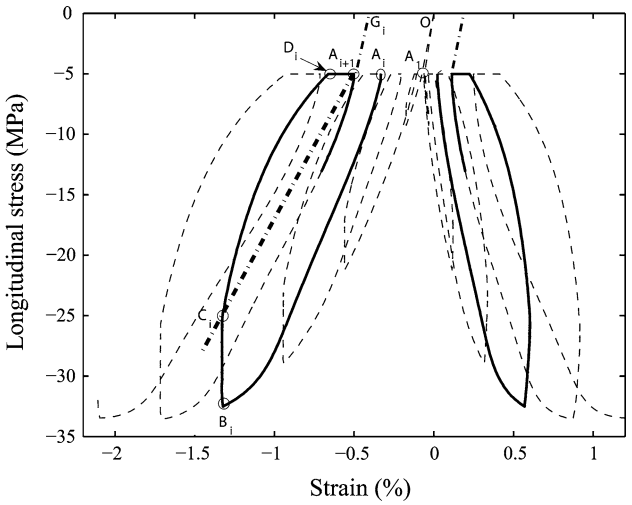

Fig. 14 Stress versus strains for a tri-axial experiment with a confining pressure of 5 MPa of pressure. Data were analyzed using dots A_i to D_i. *Bolded line* highlights a cyclic load involving loading (A_iB_i), relaxation (B_iC_i), unloading (C_iD_i), and recovery conditions (D_iA_{i+1})

mechanism, called here as the "compaction-dilatancy" phenomenon, is well-known for rocks, soils, and concrete-like materials.

Loops observed on Figs. 6, 9, or 12 can be described by a set of data $A_iB_iC_iD_iA_{i+1}$ as on Fig. 14. The slope of the line C_iA_{i+1} gives the current elastic modulus when the stress is relaxed. One can see on Fig. 15 a dependence of the initial modulus to the confining pressure. It can be due to the closing of a part of the residual porosity or of micro-cracks created during the process. Second, a decrease of the modulus is observed, pointing out to a damage mechanism usually associated to an increase of the positive strain.

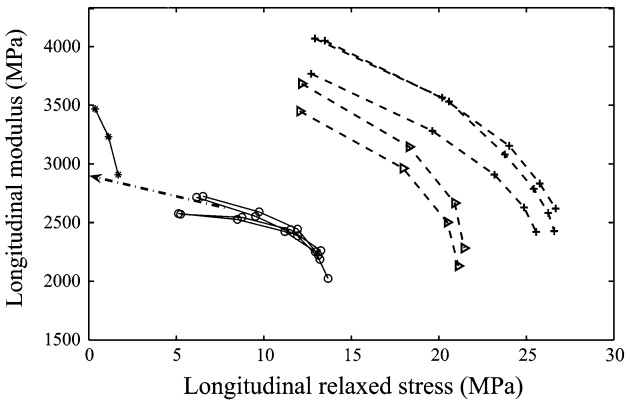

Fig. 15 Secant Young's modules (slope of the line C_iA_{i+1} on Fig. 14) for tensile experiment (*), compressive experiments (o), and tri-axial experiments with a confining pressure of 5 (◁) and 10 MPa (+). The modules decrease with the relaxed stress. There extrapolations to the origin of the graph give initial Young's modules

Many observations of the microstructure confirmed this deduction and shown that damage develops by micro-cracking during poorly confined pressure conditions.

This part of the article has shown that the behavior of pressed energetic materials is complicated. The constitutive law recently proposed for this energetic material was based on an elastic visco-plastic model. It takes into account the pressure and the damage dependences [18]. However, if the global trends of the behavior are reproduced, this model fails in representing the hysteretic behavior and the elastic time dependence. In this article, this constitutive law is modified. The visco-elastic data and the curve joining the relaxed data for all the strain rates (Fig. 12) guided us to a Maxwell's model incorporating an elasto-plastic component (Fig. 16). For the sake of simplicity, the dependence of the visco-elasticity on the pressure, the damage or the residual strain is omitted. The constitutive law is now detailed.

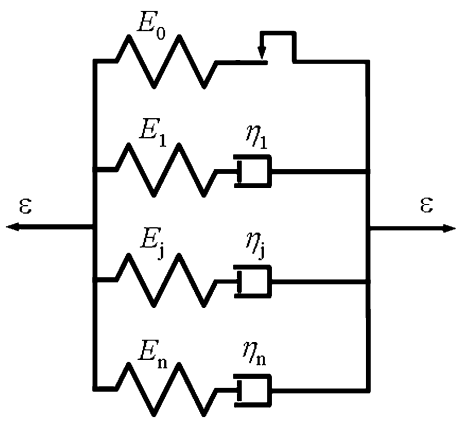

Fig. 16 A schematic diagram of the visco-elastic plastic model proposed in this article

Constitutive law

The macroscopic stress tensor $\boldsymbol{\sigma}$ is defined as the sum of the stress of the first time-independent elasto-plastic component ($\boldsymbol{\sigma}_{ep}$) and of the time-dependent components ($\boldsymbol{\sigma}_j$) using the following relation:

$$\boldsymbol{\sigma} = \boldsymbol{\sigma}_{ep} + \sum_{j=1}^{n} \boldsymbol{\sigma}_j, \quad \boldsymbol{\varepsilon} = \boldsymbol{\varepsilon}^{e}_{ep} + \boldsymbol{\varepsilon}^{p}_{ep} = \boldsymbol{\varepsilon}^{e}_{j} + \boldsymbol{\varepsilon}^{v}_{j} \tag{1}$$

An additive decomposition is assumed for the strain, denoted $\boldsymbol{\varepsilon}$, of each component between an elastic part and a plastic or time-dependent one. The model is now described in the following paragraphs. An analysis of thermodynamic requirements is proposed further (see "Annex").

Elasto-plastic component

A linear elastic behavior is supposed, with a dependence on the damage level d, using the following equation:

$$\boldsymbol{\sigma}_{ep} = (1-d)\boldsymbol{D}^{el}_{0} : \boldsymbol{\varepsilon}^{e}_{ep}, \tag{2}$$

where $\boldsymbol{D}^{el}_{0}$ is the initial elastic tensor. C_i on Fig. 14 defines the yield surface of the plastic component because the visco-elastic part is stress-free. C_iA_{i+1} gives the elastic modulus E_{ep}. $A_{i+1}G_i$, whose slope is assumed to be $E_{ep}/(1-2\nu)$, gives the plastic strain (measurements show a Poisson's ratio of 0.3 and a constant bulk modulus). A mean Young's modulus equal to 2,900 MPa is determined using unconfined compressive tests on Fig. 15. This assumption has some consequences on the damage determination (see later).

Due to the lack of data on the hardening mechanism, a unique isotropic hardening parameter, denoted k, is introduced in the constitutive law. The softening behavior observed during the compressive tests is ignored (tensile experiments have shown a brittle failure process). Consequently, a saturation of the hardening mechanism at the maximum stress is assumed.

A review of the main criteria used to describe isotropic plasticity was presented in [18]. The chosen non-linear plasticity criterion is given by the following relation (Fig. 17):

$$f(Q_{ep}, P_{ep}, k) = \sqrt{Q^2_{ep} + b(k)P_{ep}} - k, \quad b(k) = \frac{k^2}{X(k)},$$
$$X(k) = X_0 + (X_m - X_0)\frac{k-k_0}{k_m - k_0}, \tag{3}$$

where $Q_{ep} = \sqrt{(1/3)\boldsymbol{\sigma}^{D}_{ep} : \boldsymbol{\sigma}^{D}_{ep}}$ is the octahedral stress, $\boldsymbol{\sigma}^{D}_{ep}$ is the deviatoric stress and P_{ep} is the pressure. The

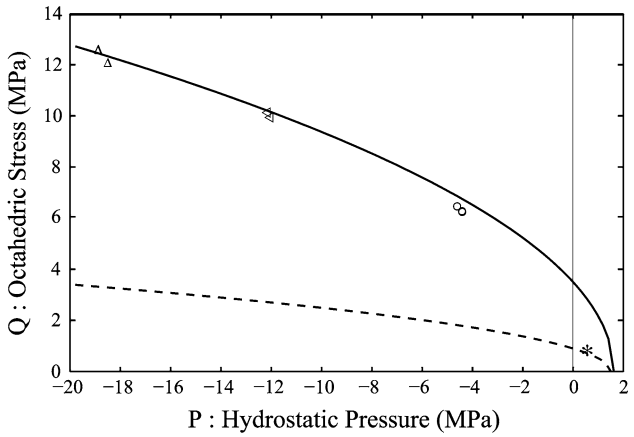

Fig. 17 Initial (*dashed line*) and saturated yield criterion (*bold line*) in the relaxed stress plane (P, Q). Symbols refer to tensile experiment ($*$), compressive experiment (o) and tri-axial experiments with a confining pressure of 5 ($\triangleleft$) and 10 MPa (Δ)

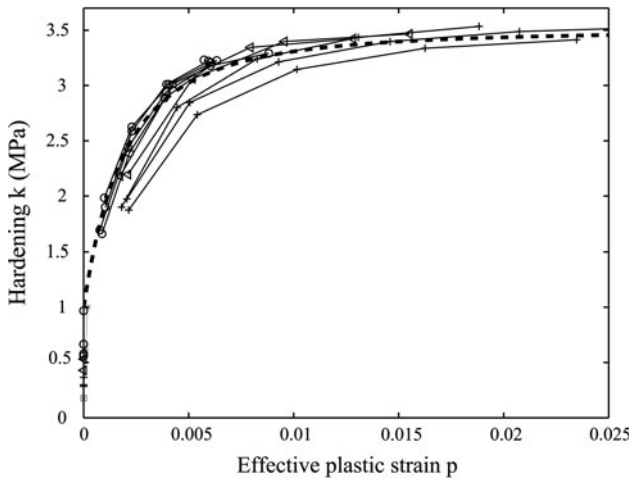

Fig. 18 Hardening parameter k versus the effective plastic strain p [tensile experiment ($*$), compressive experiment (o), and tri-axial experiments with a confining pressure of 5 ($\triangleleft$) and 10 MPa (+)]. Model is given using *dashed line*

following guidelines help for the determination of $X(k)$. The yield curves must not cross themselves in the P–Q plane, each one being embedded in those of higher levels, all of them being embedded in the maximum curve defined by the maximum relaxed stress recorded for several confining pressures.

Elementary algebra shows that the proposed relation satisfies the previous requirements. k_0, X_0, k_m, and X_m are four material parameters. The two parameters X_m and k_m are determined using the maximum yield stress curve. The following values are obtained: $X_m = 1.62$ MPa and $k_m = 3.45$ MPa.

The hardening parameter k is related to the effective plastic strain, denoted p. If it could be possible to take into account a plastic volumic part in p [18, 20], this solution couples hardening to dilatancy. As a consequence, an approximation in dilatancy prediction induces error on the hardening description. Such approach has not been adopted. The cumulated deviatoric plastic strain p is chosen to drive the hardening parameter k (Fig. 18). For the hardening law, the following hyperbolic empirical relation is used:

$$k = k_0 + (k_m - k_0)\left(1 - \frac{1}{1 + c_1 p + c_2 p^2}\right) \tag{4}$$

The four parameters c_1, c_2, k_0, and X_0 are determined using an optimization process applied to three sets of data: the response recorded during three-points bend tests, the compressive tests (with and without confinement) and the hardening curves shown in Fig. 18. The following values are obtained: $X_0 = 1.5$ MPa, $k_0 = 1$ MPa, $c_1 = 450$ and $c_2 = 1.4 \times 10^5$.

The flow rule is given by:

$$\dot{\boldsymbol{\varepsilon}}^{p}_{ep} = \dot{\lambda}\left(\frac{\boldsymbol{\sigma}^{D}_{ep}}{3Q_{ep}} + \frac{\beta}{3}\boldsymbol{I}\right)\cdot\sqrt{\frac{3}{(1+\beta^2)}}, \quad \beta = \frac{\dot{\boldsymbol{\varepsilon}}^{pV}_{ep}}{\dot{\boldsymbol{\varepsilon}}^{pD}_{ep}}, \quad \dot{\boldsymbol{\varepsilon}}^{pV}_{ep} = \mathrm{tr}(\dot{\boldsymbol{\varepsilon}}^{p}_{ep}), \quad \dot{\boldsymbol{\varepsilon}}^{pD}_{ep} = \sqrt{3\dot{\boldsymbol{\varepsilon}}^{pD}_{ep} : \dot{\boldsymbol{\varepsilon}}^{pD}_{ep}} \tag{5}$$

where $\dot{\lambda}$ is the plastic multiplier and $\dot{\boldsymbol{\varepsilon}}^{pD}_{ep}$ is the deviatoric plastic strain rate tensor. The parameter β is determined knowing the slopes of the curves shown on Fig. 13. A dependence on the cumulated deviatoric plastic strain p and on the pressure P_{ep} was observed and taken into account using the following equation:

$$\beta = C_0 + a_1\left(1 + e^{a_2 P_{ep}}\right) + a_3 P_{ep} + b\ln(1 + cp), \tag{6}$$

where C_0, a_1, a_2, a_3, b, and c are five parameters.

Visco-elastic components

The damage is assumed to influence all the components of the constitutive law. Moreover, relaxation times, denoted τ_j, are unchanged and the same values are used for spherical or deviatoric visco-elasticity. As a consequence, each visco-elastic component is described by the following linear first order differential equation:

$$\dot{\boldsymbol{\sigma}}^{ve}_{j} + \left(\frac{1}{\tau_j} + \frac{\dot{d}}{1-d}\right)\boldsymbol{\sigma}^{ve}_{j} = (1-d)\boldsymbol{K}^{ve}_{0j} : \dot{\boldsymbol{\varepsilon}}, \tag{7}$$

where $\boldsymbol{K}^{ve}_{0j}$ is the elastic tensor of each visco-elastic component. The Poisson's ratios of the elastic and time-dependent part of each component are equal to $\upsilon^{ve} = 0.42$.

For a one-dimensional application of the model (for example, to use DMA measurements), the material response can be split into an in-phase part (related to the storage modulus E_{stor}) and an out-phase part (related to the

loss modulus E_{loss}). These modules are related to Young's modulus and the visco-elastic parameters using the following relations:

$$E_{\text{stor}} = E_{\text{ep}} + \sum_{j=1}^{n} E_j \frac{(\tau_j \cdot \omega)^2}{1 + (\tau_j \cdot \omega)^2}, \qquad E_{\text{loss}} = \sum_{j=1}^{n} E_j \frac{(\tau_j \cdot \omega)}{1 + (\tau_j \cdot \omega)^2} \tag{8}$$

where $\tau_j = \eta_j/E_j$, η_j are the viscosities and ω is equal to 2π multiplied by the frequency. Ten visco-elastic components are used, the relaxation times τ_j being linearly distributed in the logarithmic time domain between 3,720 and 0.0005 s. The modulus E_0 previously determined ($E_0 =$ 2,900 MPa) is lower than the lowest storage modulus measured (around 4,500 MPa). E_0 is then supposed to be the long-term response of the material. Moreover, the relaxation curves obtained during compressive tests with cycles have been used to calibrate the short-term response of the model. Visco-elastic parameters are summarized in the Table 1.

Damage

Experimental data show that Young's modulus decreases as the positive principal strain increases (Fig. 19). The most probable damage mechanism is the nucleation and the growth of internal micro-defects (cavities, cracks) with extension [21–26]. In the proposed constitutive law, the damage amplitude d is defined as:

$$d = \frac{E_0 - E}{E_0}, \quad d = \left(d_1 \underbrace{\sup}_{\text{time}} \left(\underbrace{\max}_{I=1 \text{ to } 3} \langle \varepsilon_I \rangle_+ \right) + d_2 \right) \times \left(1 - \frac{1}{1 + d_3 . \underbrace{\sup}_{\text{time}} \left(\underbrace{\max}_{I=1 \text{ to } 3} \langle \varepsilon_I \rangle_+ \right)} \right), \tag{9}$$

where E_0 and E are the initial and current Young's modules. An hyperbolic relation is used to relate d to the maximum positive principal strain, denoted $\max\langle \varepsilon_I \rangle_+$. d_1, d_2, and d_3 are three parameters. A comparison between Eq. 9 and experimental data is shown in Fig. 19. One can see that the model is determined using the uniaxial compressive measurements. The pressure dependence of the initial Young's modulus is neglected for the sake of simplicity. We have determined the following values: $d_1 = 3$, $d_2 = 1$, and $d_3 = 100$.

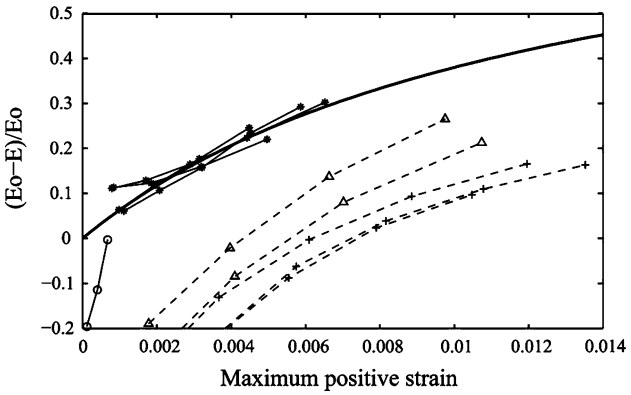

Fig. 19 Damage versus the maximum positive strain. Tensile experiment (∗), compressive experiment (o), and tri-axial experiments with a confining pressure of 5 (Δ) and 10 MPa (+)

Discussion

The constitutive law has been implemented into MATLAB software and the finite element code ABAQUS/Standard. Figure 20 shows a comparison between experimental data, the one-dimensional model, and simulations using ABAQUS. A detailed analysis outlines small differences which are attributed to the choice of equal Poisson's ratios for the elasto-plastic component and the visco-elastic ones. In the future, the three-dimensional interactions of the components should be carefully characterized to improve the model's accuracy.

Figures 21 and 22 show that the linear visco-elasticity is able to reproduce the material behavior for small strain amplitude. For compressive tests with and without confinement and with unloading cycles, relaxation and recovery conditions, the proposed flow rule is confirmed. The residual transversal strain is correctly reproduced. The hardening law and the plastic yield surface have been accurately fitted using these data. Loading and unloading behaviors are reproduced in the longitudinal direction but transversal loops are underestimated; thus, highlighting the influence of the internal friction or/and the damage.

Table 1 Visco-elastic parameters

j	1	2	3	4	5	6	7	8	9	10
τ (s)	5×10^{-4}	29×10^{-4}	168×10^{-4}	0.098	0.567	3.28	19.1	110	641	3,720
E_j (MPa)	546	336	240	348	492	384	492	552	492	288

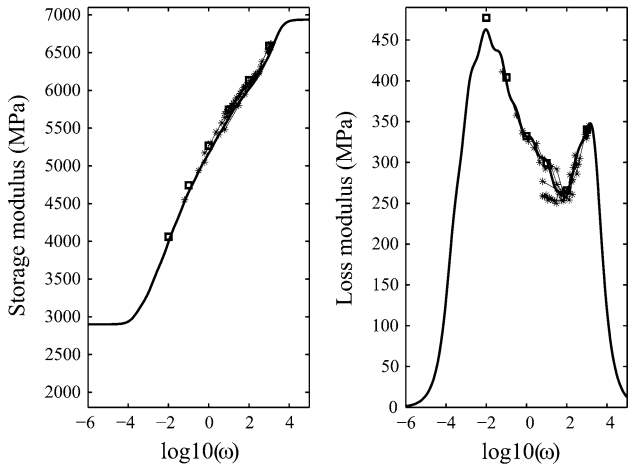

Fig. 20 Comparison between DMA data (∗) and the model with 10 components (*solid line* for a Matlab implementation of the model and *squares* for Abaqus finite element code implementation of the model)

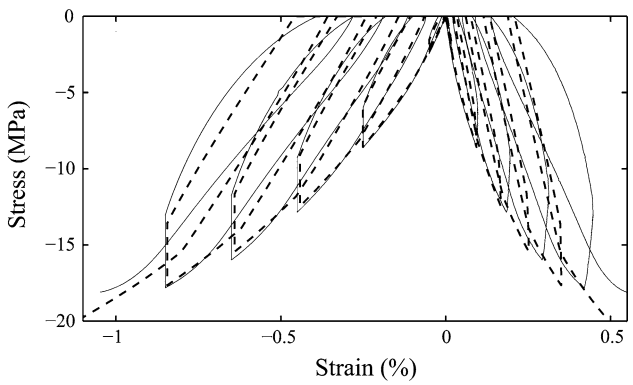

Fig. 21 Model (*dashed line*) versus data (*line*) for a compressive test

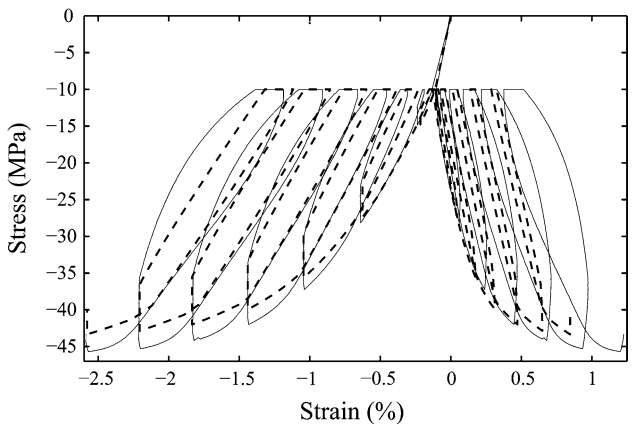

Fig. 22 Model (*dashed line*) versus experiment (*line*) for the compressive test with 10 MPa of confinement

The choice of an isotropic hardening mechanism is questionable.

Differences increase with the confinement or the high plastic strain level. The visco-elastic stress amplitude is

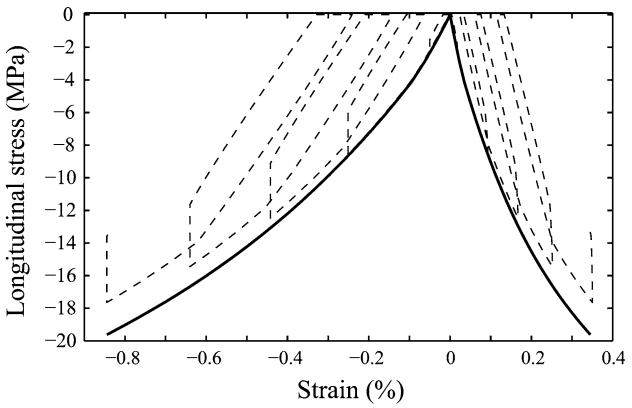

Fig. 23 Computed constant strain rate loading (*bolded line*) versus computed multiple cycled response (*dashed line*) for a compressive test

numerically underestimated. Both unloading–loading conditions and time response during recoveries are poorly reproduced. Finally, the model does not correctly describe the data shown on Fig. 9 (Fig. 23). Many parameter values were attempted to correct the constant strain rate prediction, but unsuccessfully. Our opinion is that it is now necessary to (1) characterize the different Poisson's ratios of the constitutive law, (2) to deduce how non-linear visco-elasticity could improve numerical results, and (3) to analyze different rheological approaches (for example, a Maxwell's model only for the deviatoric part of the behavior).

Conclusion

A new experimental protocol was carried out to characterize in depth the behavior of a pressed plastic-bonded explosive composition. The influence of the pressure, the viscosity, and the damage have been observed and discussed. This material behaves in a similar way than concrete-like materials, due to its high volume fraction of solid.

A visco-elastic plastic constitutive law has been proposed, based on a Maxwell's model associated to an elasto-plastic component. Comparisons between data and numerical results have shown that the material description proposed in [18] has been improved. However, the following remarks outline future works. The model reproduces the relaxed data. However, the constant strain rate data are not the cover curve of the corresponding cyclic tests, as was experimentally observed. The shape of the hysteretic loops, the behavior observed during creep-recovery experiments, the influence of the pressure on the material relaxation and the plastic strain dependence observed during recovery show the need of a non-linear visco-elasticity and/or a visco-plastic mechanism. It is

necessary to go into a detail characterization of the Poisson's ratios of the constitutive law to understand how longitudinal and transversal behaviors interact. A pressure dependence of Young's modulus must be incorporated as well as an anisotropic description of the induced damage. An isotropic plastic hardening mechanism has been proposed which is the simplest assumption. The case of kinematic hardening must be re-examined using alternating tensile-compressive tests.

Acknowledgments The authors would like to thank J. L. Brigolle for the contribution to this study, especially for the realization of the experiments, and to H. Trumel and P. Lambert for Fig. 1.

Appendix: Thermodynamical requirements

Only small strain amplitude is taken into account, leading to an assumed constant density of the material. As a consequence, the intrinsic dissipation reads, in a general way:

$$\omega = \boldsymbol{\sigma} : \dot{\boldsymbol{\varepsilon}} - \dot{\psi} \geq 0 \quad \forall \dot{\boldsymbol{\varepsilon}}, \ \forall \text{ state variables}$$

with $\dot{\psi}$ the per unit volume free energy. The following set of internal variables is proposed: $\{\boldsymbol{\varepsilon}, \boldsymbol{\varepsilon}^{\mathrm{p}}_{\mathrm{ep}}, \boldsymbol{\varepsilon}^{\mathrm{v}}_{j}, d, p\}$, given by:

$$\psi\left(\boldsymbol{\varepsilon}, \boldsymbol{\varepsilon}^{\mathrm{p}}_{\mathrm{ep}}, \boldsymbol{\varepsilon}^{\mathrm{v}}_{j}, d, p\right) = (1-d)\left(\frac{1}{2}(\boldsymbol{\varepsilon} - \boldsymbol{\varepsilon}^{\mathrm{p}}_{\mathrm{ep}}) : \boldsymbol{D}^{\mathrm{el}}_{0} : (\boldsymbol{\varepsilon} - \boldsymbol{\varepsilon}^{\mathrm{p}}_{\mathrm{ep}}) + \frac{1}{2}\sum_{j=1}^{n}(\boldsymbol{\varepsilon} - \boldsymbol{\varepsilon}^{\mathrm{v}}_{j}) : \boldsymbol{K}^{\mathrm{vel}}_{0j} : (\boldsymbol{\varepsilon} - \boldsymbol{\varepsilon}^{\mathrm{v}}_{j})\right) + \bar{\psi}(p) + \psi_0$$

Taking the assumption $\boldsymbol{\sigma} = \partial\psi/\partial\boldsymbol{\varepsilon}$ gives:

$$\varpi = (1-d)\boldsymbol{D}^{\mathrm{el}}_{0} : (\boldsymbol{\varepsilon} - \boldsymbol{\varepsilon}^{\mathrm{p}}_{\mathrm{ep}}) : \dot{\boldsymbol{\varepsilon}}^{\mathrm{p}}_{\mathrm{ep}} + (1-d) \times \sum_{j=1}^{n} \boldsymbol{K}^{\mathrm{vel}}_{0j} : (\boldsymbol{\varepsilon} - \boldsymbol{\varepsilon}^{\mathrm{v}}_{j}) : \dot{\boldsymbol{\varepsilon}}^{\mathrm{v}}_{j} - \bar{\psi}'(\boldsymbol{p})\dot{\boldsymbol{p}} + \left(\frac{1}{2}(\boldsymbol{\varepsilon} - \boldsymbol{\varepsilon}^{\mathrm{p}}_{\mathrm{ep}}) : \boldsymbol{D}^{\mathrm{el}}_{0} : (\boldsymbol{\varepsilon} - \boldsymbol{\varepsilon}^{\mathrm{p}}_{\mathrm{ep}}) + \frac{1}{2}\sum_{j=1}^{n}(\boldsymbol{\varepsilon} - \boldsymbol{\varepsilon}^{\mathrm{v}}_{j}) : \boldsymbol{K}^{\mathrm{vel}}_{0j} : (\boldsymbol{\varepsilon} - \boldsymbol{\varepsilon}^{\mathrm{v}}_{j})\right)\dot{d} \geq 0 \quad \forall\left(\boldsymbol{\varepsilon}, \dot{\boldsymbol{\varepsilon}}, \boldsymbol{\varepsilon}^{\mathrm{p}}_{\mathrm{ep}}, \boldsymbol{\varepsilon}^{\mathrm{v}}_{j}, d, p\right)$$

and

$$\boldsymbol{\sigma}_{\mathrm{ep}} : \dot{\boldsymbol{\varepsilon}}^{\mathrm{p}}_{\mathrm{ep}} - \dot{\bar{\psi}}(p) + \sum_{j} \boldsymbol{\sigma}_{j} : (\dot{\boldsymbol{\varepsilon}} - \dot{\boldsymbol{\varepsilon}}^{\mathrm{e}}_{j}) - \frac{\partial\psi}{\partial d}\dot{d} \geq 0$$

Plasticity, visco-elasticity, and damage are uncoupled. The two last terms of the previous equation are positive due to the quadratic form of ψ. Consequently, only the elasto-plastic dissipation must be studied. It comes from the model that:

$$Q_{\mathrm{ep}} + \beta(p, P_{\mathrm{ep}})P_{\mathrm{ep}} - k(p) + k_0 \geq 0$$

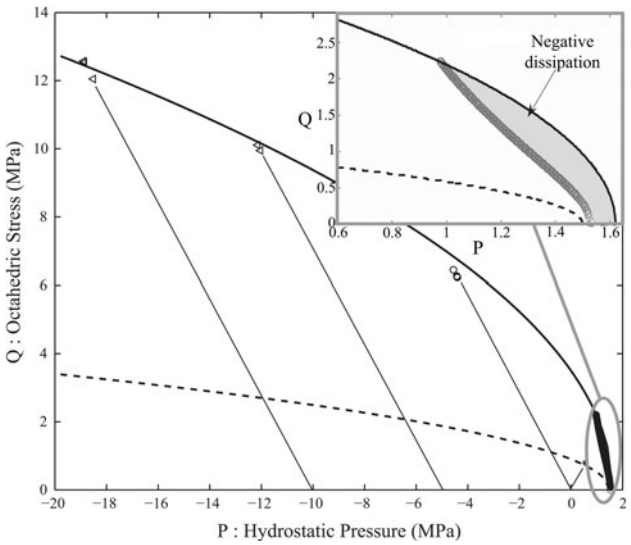

Fig. 24 Location of negative plastic dissipation in the (P, Q) stress plane. Negative dissipation occurs far from the failure stress recorded during tensile experiments

The analytical demonstration of this equation is hardly tractable due to the complicated forms of $\beta(p,P_{\mathrm{ep}})$ and $k(p)$. Thereby a numerical method has been chosen. Only a small negative dissipation zone appears on Fig. 24 in the extension domain. Failure is reached before this zone.

References

1. Belmas R, Reynaud J, Sorel J (2004) Propellants Explos Pyrotech 7:8
2. Wiegand DA (1998) In: Proceedings of the 11th international symposium detonation, Snowmass, USA, pp 744–750, ONR 333000-5
3. Wiegand DA (1999) In: APS topical conference on shock compression condensed matter. 2000 AIP conference proceedings, Snowbird, USA, pp 675–678
4. Wiegand DA, Reddingius B (2003) In: APS topical conference on shock compression condensed matter. 2004 AIP conference proceedings, Portland, USA, pp 812–815
5. Funk DJ, Laabs GW, Peterson PD, Asay BW (1995) In: APS topical conference on shock compressed condensed matter. 1996 AIP conference proceedings, Seattle, USA, pp 145–148
6. Gray III GT, Blumenthal WR, Idar DJ, Cady CM (1997) In: APS topical conference on shock compression condensed matter. 1998 AIP conference proceedings, Amherts, USA, pp 583–586
7. Gray III GT, Idar DJ, Blumenthal WR, Cady CM, Peterson PD (1998) In: Proceedings of the 11th international symposium detonation, Snowmass, USA, pp 76–84, ONR 333000-5
8. Idar DJ, Thompson DG, Gray III GT, Blumenthal WR, Cady CM, Peterson PD, Roemer EL, Wright WJ, Jacquez BL (2001) In: APS topical conference on shock compression condensed matter. 2002 AIP conference proceedings, Atlanta, USA, pp 821–824
9. Liu C (2002) In: APS topical conference on shock compression condensed matter. 2003 AIP conference proceedings, Portland, USA, pp 786–791

10. Bennett JG, Haberman KS, Johnson JN, Asay BW, Henson BF (1998) J Mech Phys Solids 46:2303
11. Dienes JK (1996) In: Lee D et al (eds) High pressure shock compression of solids II. Springer, New York
12. Dienes JK, Kershner JD (1998) In: Proceedings of the 11th international symposium detonation, Snowmass, USA, pp 717–724, ONR 333000-5
13. Asay BW, Dickson PM, Henson B, Fugard CS, Funk DJ, Idar DJ (1998) In: Proceedings of the 11th international symposium detonation, Snowmass, USA, pp 781–787, ONR 333000-5
14. Clancy SP, Johnson JN, Burkett MW (1998) In: Proceedings of the 11th international symposium detonation, Snowmass, USA, pp 3–11, ONR 333000-5
15. Scammon RJ, Browning RV, Middleditch J, Dienes JK, Haberman KS, Bennett JG (1998) In: Proceedings of the 11th international symposium detonation, Snowmass, USA, pp 111–118, ONR 333000-5
16. Hackett RM, Bennett JG (2000) Int J Numer Math Eng 49:1191
17. Dienes JK, Zuo QH, Kershner JD (2006) J Mech Phys Solids 54:1237
18. Rja Fi Allah S (2006) PhD thesis, Université François Rabelais de Tours (in French)
19. Williamson DM (2006) PhD thesis, Magdalene College, Cambridge
20. Nova R (1982) In: Proceedings of the international workshop on constitutive behavior of soils, Villard de Lans, France, pp 289–309, published in 1984
21. Dragon A, Halm D, Désoyer T (2000) Comput Methods Appl Mech Eng 183:331
22. Halm D, Dragon A (1998) Eur J Mech A 17:439
23. Mazars J (1981) In: Proceedings of the international conference of fracture, Cannes, France, pp 1499–1506
24. Mazars J (1984) PhD thesis, Université Pierre et Marie Curie–Paris 6 (in French)
25. Mazars J (1986) Eng Fract Mech 25:729
26. Mazars J, Ragueneau F, Pijaudier-Cabot G (2002) In: Allix O, Hild F (eds) Continuum damage mechanics of materials and structures. Elsevier Science Ltd, Oxford

2.4 MODÈLES À ANISOTROPIE INDUITE PAR L'ENDOMMAGEMENT (M1)

2.4.1 Choix du cadre de modélisation

A la suite des travaux menés dans le cadre de la thèse de V. D. Le, il était clair que le point principal à explorer concernait l'anisotropie induite par endommagement ainsi que son effectivité. Ces 2 points ont été mis en lumière par V.D. Le sur les deux figures suivantes :

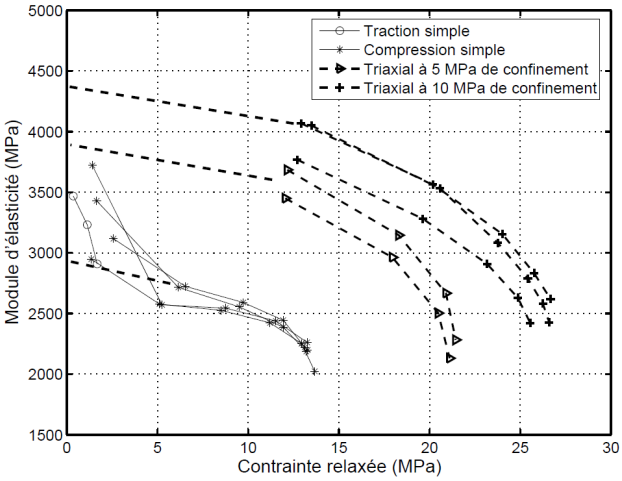

Figure 10 : Evolution du module d'élasticité et influence de la pression de confinement [Mémoire de V.D. Le].

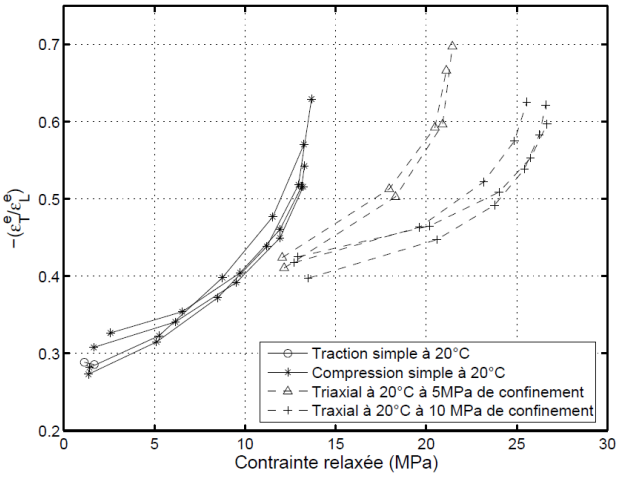

Figure 11 : Evolution du coefficient de Poisson et influence de la pression de confinement [Mémoire de V.D. Le].

L'effet de la pression de confinement sur le module d'élasticité initial (Figure 10) laisse penser à un endommagement initial plus ou moi actif selon le niveau de pression de confinement, via une refermeture des pores ou fissures ou une réorganisation de la matière. L'évolution du coefficient de Poisson (Figure 11) au-delà d'une valeur de 0.5 suggère une anisotropie de comportement induite, puisque le matériau est initialement isotrope.

Sur la base de ces observations, le travail mené dans le cadre de la thèse d'Abdelkibir Benelfellah a consisté dans un 1er temps en une étude bibliographique sur les approches permettant une modélisation de l'anisotropie induite avec 2 critères principaux :

- la possible introduction d'une variable d'effectivité de l'endommagement pilotée au moins en partie par la pression de confinement,
- la garantie d'une approche saine du point de vue de la thermodynamique

Le choix s'est tourné vers les modèles à somme de contributions d'endommagement exprimées suivant des directions fixées. Un gros effort de réécriture des modèles a été mené afin de pouvoir en comparer leurs effets sur les paramètres mesurables, en utilisant la base de représentation de Walpole. En conclusion de cette étude, le modèle retenu est basé sur une formulation microplans, avec décomposition Volumique / Déviatorique / Tangentielle (VDT). Il est le seul permettant une gestion de l'évolution du coefficient de contraction indépendante de celles des autres paramètres. Il permet de plus d'introduire un effet de la pression de confinement via une variable d'effectivité.

La comparaison des différentes approches retenues est exposée dans l'article référencé ACL11, présenté ci-après.

Engineering Fracture Mechanics 121–122 (2014) 28–39

Contents lists available at ScienceDirect

Engineering Fracture Mechanics

journal homepage: www.elsevier.com/locate/engfracmech

Analytical and numerical comparison of discrete damage models with induced anisotropy

A. Benelfellah [a,*], A. Frachon [b], M. Gratton [b], M. Caliez [b], D. Picart [c]

[a] Laboratoire de Mécanique et de Physique des Matériaux (UMR CNRS 6617), Ecole Nationale Supérieure de Mécanique et d'Aérotechnique, F-86961 Futuroscope Cedex, France
[b] Laboratoire de Mécanique et Rhéologie (E.A. 2640), ENI Val de Loire, Université François Rabelais de Tours, F-41034 Blois Cedex, France
[c] CEA, DAM, Le Ripault, F-37260 Monts, France

ARTICLE INFO

Article history:
Received 25 October 2013
Received in revised form 13 March 2014
Accepted 28 March 2014
Available online 18 April 2014

Keywords:
Damage effect
Microcracks
Induced anisotropy
Constitutive modeling
Microplane
Walpole basis

ABSTRACT

Quasi-brittle materials are modeled taking into account the anisotropic damage and its unilateral character. Among the models, proposed in the literature, a first selection has been made. The attention is thus restricted to models where the damage is managed by a discrete sum of its effects along fixed directions. The influence of the basic assumptions of the selected models are compared. Thus, models are at first expressed both into the Kunin and Walpole tensor decompositions to highlight the damage effects on each stiffness tensor component. A numerical study illustrates the effect of a damage effect on engineering parameters sensitivity and compares the versatility of those models. This work shows that the microplane framework is the most versatile, against Poisson's ratio damage, while using the Volumetric Deviatoric Tangential (VDT) decomposition.

1. Introduction

The influence of microcracking on the nonlinear behavior of quasi-brittle materials is widely recognized. This leads to a damage induced anisotropy, involving a sensitivity of the response to the cracks closure, which results in an increase of the transversal to longitudinal strain ratio during compression tests, and a strong dependence on the confining pressure. Continuum Damage Mechanics was originally introduced by Kachanov [16] and Rabotnov [24]. Isotropic damage were first considered by Lemaitre and Chaboche [10], Mazars [20], then anisotropic ones were proposed [18,13,21,15]. Despite continuous improvements, inconsistencies remained, as mentioned by Chaboche [9] or Carol and Willam [8].

A consistent thermodynamic formulation requires the conservativeness and existence of the free energy, *i.e.* the symmetry of the Hessian tensor. Moreover, the stress–strain response must be continuous and must not create any spurious dissipation. However, if discontinuity is introduced into the damage tensor using the strain eigenvalues, Challamel et al. [11] showed that conservation of free energy is obtained only if the principal directions of damage tensor coincide with those of strain tensor. Likewise, a thermodynamic potential based on the positive and the negative parts of the strain tensor often results in undesirable artificial dissipation [8]. Finally, Cormery [12] shows, for a given state, an example of loss of objectivity for such formulations and thus their inability to generate a potential.

Recent studies [4,22,27,1] have proposed solution for these kind of thermodynamic inconsistencies using a formulation based on a set of predetermined directions on which crack densities are defined, in a spherical distribution. These models can

* Corresponding author. Tel.: +33 549498207.
E-mail address: benelfellah@ensma.fr (A. Benelfellah).

http://dx.doi.org/10.1016/j.engfracmech.2014.03.022
0013-7944/

Nomenclature

Abbreviations

DM	Discrete Model
EM	Eshelby Model
RVE	Representative Volume Element
VD	Volumetric Deviatoric
VDT	Volumetric Deviatoric Tangential

Tensor notations

n	scalar
$\mathbf{n}$	vector
$\mathbf{N}$	second-order tensor
$\mathbb{N}$	fourth-order tensor
$\mathbf{1}$	second-order unit tensor
$\mathbb{I}$	fourth-order unit tensor
σ	Cauchy stress tensor
$\tilde{\sigma}$	effective stress tensor
η	strain tensor
$\mathbb{C}^{el}$	elastic stiffness tensor
$\mathbb{C}^{ed}$	elastic stiffness damaged tensor
$\mathbb{I}_V$	volumetric part of fourth-order identity tensor $\mathbb{I}$
$\mathbb{I}_D$	deviatoric part of fourth-order identity tensor $\mathbb{I}$

Tensor operations

$\cdot$	dot product
:	double dot product
$\otimes$	tensor product $(a \otimes b_{ijkl}) = a_{ij}b_{kl}$ $(a \underline{\otimes} b_{ijkl}) = a_{il}b_{jk}$ $(a \overline{\otimes} b_{ijkl}) = a_{ik}b_{jl}$ $(a \overline{\underline{\otimes}} b_{ijkl}) = \frac{1}{2}(a_{ik}b_{jl} + a_{il}b_{jk})$
$H(X)$	Heaviside function $H(x) = \frac{x+\lvert x\rvert}{2\lvert x\rvert}$

be classified into two categories: (1) phenomenological macroscopic constitutive laws, (2) macroscopic laws obtained from an homogenization process and assumptions at the mesoscale. This article proposes a method to compare formulation which describe the behavior of quasi-brittle materials, initially isotropic, satisfying thermodynamic requirements. Analysis of the damage effect highlights the differences between these models.

2. Selected models

In the selected models, microcracks fall into N sets, characterized by their density and normal orientation $\mathbf{n}_i$ which is described and fixed. The condition for opening/closure of crack can thus be postulated in these directions avoiding a spectral decomposition of the strain tensor. Considering the assumption of non-interacting microcracks, both behavior and closure effects are treated in each direction. The effect of several microcracks on the stiffness of an initially isotropic material is the sum of the contributions of each set of microcracks. A set of randomly distributed microcracks characterized by a common normal orientation induces a transverse isotropic behavior. The following models meet the requirements of the thermodynamics of irreversible processes framework. The Young's, shear and bulk moduli and the Poisson's ratio of the material are respectively E, μ, k, and v. For each direction, the second-order tensor $\mathbf{N}_i$ is defined as the tensor product $\mathbf{n}_i \otimes \mathbf{n}_i$ and the scalar angular weighting coefficient as w_i. $\otimes$ denotes the tensor product, and $\overline{\otimes}$ the symmetrized tensor product.

2.1. Discrete approach

Discrete Model (DM) is based on a previous model proposed by Halm and Dragon [15]. The damage tensor has been replaced by sets of microcracks with densities ρ_i^{Dis} associated with prescribed directions [1]. The resulting damaged stiffness tensor $\mathbb{C}^d$ is given in the Kunin [17] formalism by:

$$\mathbb{C}^d(\rho_i, \mathbf{N}_i) = \left(k - \frac{2}{3}\mu\right)\mathbf{1}\otimes\mathbf{1} + 2\mu\,\mathbf{1}\,\overline{\otimes}\,\mathbf{1} - \sum_{i=1}^{N}\rho_i^{Dis}\{\alpha[2\,\mathbf{1}\,\overline{\otimes}\,\mathbf{1} - \mathbf{1}\otimes\mathbf{1} + \mathbf{1}\otimes\mathbf{N}_i + \mathbf{N}_i\otimes\mathbf{1}] + 2\beta[\mathbf{1}\,\overline{\otimes}\,\mathbf{N}_i + \mathbf{N}_i\,\overline{\otimes}\,\mathbf{1}] - (3\alpha + 4\beta)H(-tr(\boldsymbol{\varepsilon}\cdot\mathbf{N}_i))\mathbf{N}_i\otimes\mathbf{N}_i\} \quad (1)$$

The two elastic moduli α and β are used to distribute damage effects *i.e.*: α multiplies both the isotropic and directional components of the model, while β affects only the directional component. The anisotropy ratio can be increased via β. Unilateraliy is introduced by a Heaviside function of the opening strain $H(\boldsymbol{\varepsilon} : \mathbf{N}_i)$.

2.2. Microplane models: V–D–T and V–D decomposition

Microplane models were originally introduced by Taylor [25]. They were first applied to plasticity [2], and also to brittle materials [3,5,7,19]. Each direction of the solid angle characterizes a microplane on which the strain is decomposed. Constitutive equations are defined in the microplane level where the existence of free energy is assumed. The stress tensor is determined by angular integration of the microplane stress vector over the whole solid angle. Recently, Leukart and Ramm [19] have suggested decomposing the projected strain tensor into its volumetric (ε_V) and deviatoric parts ($\boldsymbol{\varepsilon}_D$) (VD decomposition). In VDT decomposition [6], the normal strain is decomposed into volumetric (ε_V) and deviatoric parts (ε_D). The tangential part of the strain projection is $\boldsymbol{\varepsilon}_T$. By replacing the projection operators by their expressions in the Kunin tensor basis [17], the integral on the discretized unit sphere produces the following stiffness operator:

$$\mathbb{C}^d = \left(k - \frac{2}{3}\mu\right)\mathbf{1}\otimes\mathbf{1} + 2\mu\mathbf{1}\underline{\otimes}\mathbf{1} - \sum_{i=1}^{N} 3w_i\left\{d_V^{vdt}\frac{k}{3}\mathbf{1}\otimes\mathbf{1} + d_D^{vdt^i}\mu_D^{vdt}\left[\frac{1}{9}\mathbf{1}\otimes\mathbf{1} - \frac{1}{3}(\mathbf{N}_i\otimes\mathbf{1} + \mathbf{1}\otimes\mathbf{N}_i) + \mathbf{N}_i\otimes\mathbf{N}_i\right]\right.$$
$$\left. + d_T^{vdt^i}\mu_T^{vdt}\left[\frac{1}{2}(\mathbf{1}\underline{\otimes}\mathbf{N}_i + \mathbf{N}_i\underline{\otimes}\mathbf{1}) - \mathbf{N}_i\otimes\mathbf{N}_i\right]\right\} \tag{2}$$

where d_V^{vdt}, d_D^{vdt} and d_T^{vdt} are respectively the volumetric, deviatoric and tangential damage variables, and μ_D^{vdt} and μ_T^{vdt} are the deviatoric and tangential shear moduli. The global shear modulus μ is obtained by integrating the contributions of shear stiffness, and is defined from the μ_D^{vdt} and μ_T^{vdt} microplane shear moduli (Eq. (3)). In the VD decomposition, Leukart and Ramm [19] has chosen these two moduli as equal having a single modulus μ_D^{vd} (see Eq. (4), and equality between d_D^{vdt} and d_T^{vdt}). The VD stiffness tensor is thus quite similar to the VDT tensor.

$$\frac{2}{5}\mu_D^{vdt} + \frac{3}{5}\mu_T^{vdt} = 2\mu \tag{3}$$

$$\mu_D^{vd} = 2\mu \tag{4}$$

The volumetric parts of the VD and the VDT decompositions are similar. The volumetric damage variables d_V^{vdt} and d_V^{vd} are basically the global state variables. Both VD and VDT decompositions does not take into account the unilateral effect.

2.3. A micromechanical model based on the Eshelby's scheme

Micromechanical models are used to model macroscopic behavior considering the microstructure of the material of interest through a Representative Volume Element (RVE). The macroscopic equivalent behavior is deduced from a homogenization method with an assumption that the crack density is low and homogeneous on the RVE. Pensee and Kondo [22] has proposed a model based on the Eshelby scheme to describe the damage-induced anisotropy. Zhu et al. [27] completed this work by exploiting other homogenization schemes to take into account other microstructural mechanisms such as spatial distribution and interaction between microcracks using Ponte Castaneda and Willis Scheme [23]. For its intrinsic simplicity, the attention is focussed on the model using Eshelby's scheme denoted by EM. The stiffness tensor $\mathbb{C}^d$ associated with a material with N microcrack sets of normal $\mathbf{n}_i$ and density ρ_i^{Esh}, is given by:

$$\mathbb{C}^d = \left(k - \frac{2}{3}\mu\right)\mathbf{1}\otimes\mathbf{1} + 2\mu\,\mathbf{1}\underline{\otimes}\mathbf{1}$$
$$- \frac{32\mu(1-\nu)}{3}\sum_{i=1}^{N}\rho_i^{Esh}\left[\frac{H\nu^2}{(1-2\nu)^2}\mathbf{1}\otimes\mathbf{1} + \frac{1}{2-\nu}(\mathbf{1}\underline{\otimes}\mathbf{N}_i + \mathbf{N}_i\underline{\otimes}\mathbf{1}) + \frac{H\nu}{1-2\nu}(\mathbf{N}_i\otimes\mathbf{1} + \mathbf{1}\otimes\mathbf{N}_i) - \frac{H\nu + 2(1-H)}{2-\nu}\mathbf{N}_i\otimes\mathbf{N}_i\right] \tag{5}$$

where $H(\boldsymbol{\varepsilon} : \mathbf{N}_i)$ an Heaviside function used to take unilateral effect of damage into account. The detection of crack opening/closure is made using the sign of the normal deformation to the crack plane.

2.4. Constitutive law proposed by Dienes

Dienes model [14] has described the behavior of a particular class of high explosives. It is based on an additive decomposition of the strain rate into elementary strain rates associated with various mechanisms, whose compliances are postulated. This analysis is restricted to the damaged hypoelastic part of the model. The behavior is defined as the sum of the compliances associated with the matrix (undamaged material), opened (density F_i^o) and closed (density F_i^c) penny-shaped microcracks for a number of given directions. Open microcracks affect both normal and out-of-plane shear

responses, while the closed ones affect the shear properties, giving the model its unilateral nature. The total compliance of the damaged material $\mathbb{S}^d$ is given by:

$$\mathbb{S}^d = \frac{1}{2\mu}\mathbf{1}\,\overline{\otimes}\,\mathbf{1} + \left(\frac{1}{3k}-\frac{1}{2\mu}\right)\frac{1}{3}\mathbf{1}\otimes\mathbf{1} + \frac{8}{3\mu} \times \frac{1-\nu}{2-\nu}\sum_{i=1}^{N} w_i\left[(\mathbf{1}\,\overline{\otimes}\,\mathbf{N}_i + \mathbf{N}_i\,\overline{\otimes}\,\mathbf{1})\left(HF_i^o + (1-H)F_i^c\right) - \left(H\nu F_i^o + 2(1-H)F_i^c\right)\mathbf{N}_i\otimes\mathbf{N}_i\right] \tag{6}$$

Detection of crack opening/closure is made using the sign of the normal stress to the crack plane, $H(\boldsymbol{\sigma}:\mathbf{N}_i)$. The stiffness tensor can be deduced from Eq. (6) using inversion properties in Walpole basis. A first-order linearization with respect to a single open crack density leads to the same expression given for EM (Eq. (5)).

3. Analytical comparisons using Walpole's tensor decomposition

3.1. Walpole notations

A set of randomly distributed microcracks, characterized by a common normal orientation, induces transverse isotropic behavior. Thus, the previous models have been decomposed into the Walpole tensor basis for a single given set of microcracks [26]. The following tensors are defined as:

$$\begin{aligned}
\mathbb{E}_1 &= \frac{1}{2}(\mathbf{1}-\mathbf{N})\otimes(\mathbf{1}-\mathbf{N})\\
\mathbb{E}_2 &= \mathbf{N}\otimes\mathbf{N}\\
\mathbb{E}_3 &= (\mathbf{1}-\mathbf{N})\,\overline{\otimes}\,(\mathbf{1}-\mathbf{N}) - \frac{1}{2}(\mathbf{1}-\mathbf{N})\otimes(\mathbf{1}-\mathbf{N})\\
\mathbb{E}_4 &= \mathbf{N}\,\overline{\otimes}\,(\mathbf{1}-\mathbf{N}) + (\mathbf{1}-\mathbf{N})\,\overline{\otimes}\,\mathbf{N}\\
\mathbb{E}_5 &= \mathbf{N}\otimes(\mathbf{1}-\mathbf{N})\\
\mathbb{E}_6 &= (\mathbf{1}-\mathbf{N})\otimes\mathbf{N}
\end{aligned} \tag{7}$$

where $\mathbb{E}_1$ highlights the bulk behavior in the isotropy plane; $\mathbb{E}_2$ takes into account the stiffness along the isotropy direction; $\mathbb{E}_3$ and $\mathbb{E}_4$ respectively describe in-plane and out-of-plane behavior; $\mathbb{E}_5$ and $\mathbb{E}_6$ account for the Poisson's ratios defined between in-plane and out-of-plane directions.

3.2. Models in the Walpole notation

Analysis of the damage effects for each model after the angular summation implies understanding of the effects associated with a single set of microcracks. Thus, the stiffness tensors have been deduced in the Walpole basis assuming only one set associated with a normal direction $\mathbf{e}_1$. Only open cracks are considered. The vector $\mathbf{e}_2$, orthogonal to $\mathbf{e}_1$, is contained in the isotropy plane. All the selected models (as described in Section 2) can be written using the following general equation:

$$\mathbb{C}^d = 2\left(k+\frac{1}{3}\mu\right)(1-d_1)\mathbb{E}_1 + \left(k+\frac{4}{3}\mu\right)(1-d_2)\mathbb{E}_2 + 2\mu(1-d_3)\mathbb{E}_3 + 2\mu(1-d_4)\mathbb{E}_4 + \left(k-\frac{2}{3}\mu\right)(1-d_5)(\mathbb{E}_5+\mathbb{E}_6) \tag{8}$$

To obtain similar equations for all the models, the damage effects in DM and EM are expressed through the crack densities ρ_i^{Dis} and ρ_i^{Esh}. Table 1 summarizes the decomposition of the stiffness tensor into the Walpole basis. For the sake of simplicity,

Table 1
Damage effects for a given set of microcracks characterized by a normal direction $\mathbf{e}_1$. Models are expressed in the Walpole tensor basis. DM: Discrete Model, VDT: Volumetric–Deviatoric–Tangential, VD: Volumetric–Deviatoric, EM: Eshelby Model. The linearization of stiffness tensor Dienes model gives the same decomposition as given by EM.

Walpole notation	$\mathbb{E}_1$	$\mathbb{E}_2$	$\mathbb{E}_3$	$\mathbb{E}_4$	$\mathbb{E}_5+\mathbb{E}_6$
Stiffness					
Isotropy	$2k+\frac{2}{3}\mu$	$k+\frac{4}{3}\mu$	2μ	2μ	$k-\frac{2}{3}\mu$
Transverse isotropy	$2k_{e_2}$	$E_{e_1}+4k_{e_2}\nu_{e_2e_3}^2$	$2\mu_{e_2e_3}$	$2\mu_{e_1e_2}$	$2k_{e_2}\nu_{e_2e_3}$
Damage effects					
Walpole effect	$1-d_1$	$1-d_2$	$1-d_3$	$1-d_4$	$1-d_5$
DM	1	$1-\frac{(3\alpha+4\beta)}{k+\frac{4}{3}\mu}\rho^{Dis}$	$1-\frac{2\alpha}{2\mu}\rho^{Dis}$	$1-\frac{2(\alpha+\beta)}{2\mu}\rho^{Dis}$	1
VDT	$1-d_V^{vdt}\frac{2k}{2k+\frac{2}{3}\mu}-d_D^{vdt}\frac{\frac{2}{3}\mu_D^{vdt}}{2k+\frac{2}{3}\mu}$	$1-d_V^{vdt}\frac{k}{k+\frac{4}{3}\mu}-d_D^{vdt}\frac{\frac{4}{3}\mu_D^{vdt}}{k+\frac{4}{3}\mu}$	1	$1-d_T^{vdt}\frac{\frac{3}{2}\mu_T^{vdt}}{2\mu}$	$1-d_V^{vdt}\frac{k}{k-\frac{2}{3}\mu}+d_D^{vdt}\frac{\frac{2}{3}\mu_D^{vdt}}{k-\frac{2}{3}\mu}$
VD	$1-d_V^{vd}\frac{2k}{2k+\frac{2}{3}\mu}-d_D^{vd}\frac{\frac{4}{3}\mu}{2k+\frac{2}{3}\mu}$	$1-d_V^{vd}\frac{k}{k+\frac{4}{3}\mu}-d_D^{vd}\frac{\frac{8}{3}\mu}{k+\frac{4}{3}\mu}$	1	$1-\frac{3}{2}d_D^{vd}$	$1-d_V^{vd}\frac{k}{k-\frac{2}{3}\mu}+d_D^{vd}\frac{\frac{4}{3}\mu}{k-\frac{2}{3}\mu}$
EM	$1-\rho^{Esh}\frac{4(3k-2\mu)^2(3k+4\mu)}{9\mu(3k+\mu)^2}$	$1-\rho^{Esh}\frac{4(3k+4\mu)^2}{9\mu(3k+\mu)}$	1	$1-\rho^{Esh}\frac{16(k+4\mu)}{9(3k+2\mu)}$	$1-\rho^{Esh}\frac{4(3k+4\mu)^2}{9\mu(3k+\mu)}$

the angular weighting coefficient w_i has been omitted. E_{e_1}, $\mu_{e_1e_2}$ are the out-of-plane Young's and shear moduli, respectively and k_{e_2}, $\mu_{e_2e_3}$ and $v_{e_2e_3}$ are respectively the bulk modulus, shear modulus and Poisson's ratio in the isotropy plane.

In each model, damage variables are weighted by a dimensionless term determined from the elastic moduli and internal parameters. Moduli values may considerably change these coefficients and could even annihilate the effect of some damage variables. Table 1 shows that only one damage variable (*i.e.*: crack density) is used in DM and EM models. VD and VDT provides two or three independent damage variables for reproducing complex effects by phenomenological models. This advantage can be tempered by the lack of experimental data which could be decisive.

From Table 1 it is clear that the selected models affect the longitudinal stiffness carried by $\mathbb{E}_2$ as well as the out-of-plane shear modulus carried by the tensor $\mathbb{E}_4$. DM takes into account damage on the in-plane shear modulus ($\mathbb{E}_3$) but, unlike the other models, it does not influence in-plane bulk stiffness ($\mathbb{E}_1$), nor the out-of-plane Poisson's ratios ($\mathbb{E}_5+\mathbb{E}_6$). For VD and VDT, this effect is introduced by the volumetric damage d_V and, with an inverse impact, by the deviatoric damage d_D. Only these two models allow such an adjustment. With different weighting factors, these two damages affect the other tensors $\mathbb{E}_1$, $\mathbb{E}_2$ and $\mathbb{E}_5+\mathbb{E}_6$. However, the shear modulus ($\mathbb{E}_4$) is affected by only one damage variable, d_D or d_T.

EM and linearized Dienes models affect all the Walpole tensors by the opened crack density, except $\mathbb{E}_3$. The elastic parameters can thus only decrease when the crack density increases.

3.3. Analysis using engineering parameters

The contraction ratio must be adjusted carefully according to experimental data on quasi-brittle materials. Computation of damaged stiffness enables the determination of the compliance. The Young's modulus $E^d(\mathbf{m})$, shear modulus $\mu^d(\mathbf{m},\mathbf{p})$ and contraction ratio $v^d(\mathbf{m},\mathbf{p})$, is defined in Eq. (9) where $\mathbf{m}$ and $\mathbf{p}$ are two orthogonal vectors. Table 2(a)–(c) depicts the damage effects on these parameters on the normal direction $\mathbf{e}_1$ and orthogonal vector $\mathbf{e}_2$. The inversion of the stiffness tensor introduces a non-linearity. Linearized expressions versus the weighted damage parameters are given in Table 2.

$$\begin{aligned} E^d(\mathbf{m}) &= \left\{(\mathbf{m}\otimes\mathbf{m}):\mathbb{S}^d:(\mathbf{m}\otimes\mathbf{m})\right\}^{-1} \\ \mu^d(\mathbf{m},\mathbf{p}) &= \left\{4(\mathbf{m}\otimes\mathbf{p}):\mathbb{S}^d:(\mathbf{m}\otimes\mathbf{p})\right\}^{-1} \\ v^d(\mathbf{m},\mathbf{p}) &= -E^d(\mathbf{m})\left\{\mathbf{p}\otimes\mathbf{p}:\mathbb{S}^d:\mathbf{m}\otimes\mathbf{m}\right\} \end{aligned} \tag{9}$$

Along the direction $\mathbf{e}_1$ normal to the microcrack set, the Young's modulus can be affected in the four models, as well as the out-of-plane shear modulus. Table 2(a)–(c) shows that DM has only one damage variable and, one independent adjustment parameter (whereas no parameter is available in EM). In the isotropy plane, the two parameters α and β of DM being positive,

Table 2
(a)–(c) Linearized expressions with respect to damage, of the Young's modulus E, the shear modulus μ and the ratio of the transversal to the longitudinal strains v along $\mathbf{e}_1$ (a vector normal to the crack plane) and $\mathbf{e}_2$ (vector contained in the crack plane).

(a)	$\frac{E^d(\mathbf{e}_1)}{E}$	$\frac{E^d(\mathbf{e}_2)}{E}$
DM	$1-\frac{(3\alpha+4\beta)}{E}\rho^{Dis}$	$1-\rho^{Dis}\left(\frac{3\alpha+4\beta}{9k}+\frac{3\alpha+\beta}{3\mu}-\frac{3(\alpha+\beta)}{3k+\mu}\right)$
VD	$1-\left(\frac{E}{9k}d_V^{vd}+\frac{2E}{3\mu}d_D^{vd}\right)$	$1-\left(\frac{E}{9k}d_V^{vd}+\frac{E}{6\mu}d_D^{vd}\right)$
VDT	$1-\left(\frac{E}{9k}d_V^{vdt}+\frac{2E}{3\mu}\frac{\mu_D^{vdt}}{2\mu}d_D^{vdt}\right)$	$1-\left(\frac{E}{9k}d_V^{vdt}+\frac{E}{6\mu}\frac{\mu_D^{vdt}}{2\mu}d_D^{vdt}\right)$
EM	$1-\frac{12k(3k+4\mu)}{(3k+\mu)^2}\rho^{Esh}$	1

(b)	$\frac{\mu^d(\mathbf{e}_1,\mathbf{e}_2)}{\mu}=\frac{\mu^d(\mathbf{e}_2,\mathbf{e}_1)}{\mu}$	$\frac{\mu^d(\mathbf{e}_2,\mathbf{e}_3)}{\mu}$ (isotropic)	$\frac{v^d(\mathbf{e}_2,\mathbf{e}_3)}{v}$ (isotropic)
DM	$1-\rho^{Dis}\frac{\alpha+\beta}{\mu}$	$1-\rho^{Dis}\frac{\alpha}{\mu}$	$1-\rho^{Dis}\left(\frac{\beta}{\mu}-\frac{3(\alpha+\beta)}{(3k+\mu)}-\frac{3\alpha}{(3k-2\mu)}\right)$
VD	$1-\frac{3}{2}d_D^{vd}$	1	$1-\frac{E}{(3k-2\mu)}\left(d_V^{vd}-\frac{(3k+2\mu)}{2\mu}d_D^{vd}\right)$
VDT	$1-\frac{3}{2}\frac{\mu_T^{vdt}}{2\mu}d_T^{vdt}$	1	$1-\frac{E}{(3k-2\mu)}\left(d_V^{vdt}-\frac{(3k+2\mu)}{2\mu}\frac{\mu_D^{vdt}}{2\mu}d_D^{vdt}\right)$
EM	$1-\frac{16(3k+4\mu)}{9(3k+2\mu)}\rho^{Esh}$	1	1

(c)	$\frac{v^d(\mathbf{e}_1,\mathbf{e}_2)}{v}$	$\frac{v^d(\mathbf{e}_2,\mathbf{e}_1)}{v}$
DM	1	$1-\rho^{Dis}\left(-\frac{\beta}{\mu}-\frac{3(\alpha+\beta)}{(3k+\mu)}\right)$
VD	$1-\frac{E}{(3k-2\mu)}\left(d_V^{vd}-2d_D^{vd}\right)$	$1-\frac{E}{(3k-2\mu)}\left(d_V^{vd}-\frac{(3k+2\mu)}{2\mu}d_D^{vd}\right)$
VDT	$1-\frac{E}{(3k-2\mu)}\left(d_V^{vdt}-2\frac{\mu_D^{vdt}}{2\mu}d_D^{vdt}\right)$	$1-\frac{E}{(3k-2\mu)}\left(d_V^{vdt}-\frac{(3k+2\mu)}{2\mu}\frac{\mu_D^{vdt}}{2\mu}d_D^{vdt}\right)$
EM	$1-\frac{12k(3k+4\mu)}{(3k+\mu)^2}\rho^{Esh}$	1

it can be shown that $E^d(\mathbf{e}_2)$ can only decrease, while EM does not introduce such degradation. VD and VDT models also include a damage effect on $E^d(\mathbf{e}_2)$, but without introducing any effect on the in-plane shear modulus $\mu^d(e_2, e_3)$, unlike DM which includes an isotropic deviatoric damage (on $\mathbb{E}_3$, Table 1), affecting both the in-plane shear modulus and the in-plane contraction ratio.

In Table 2(c), DM does not include any damage effect on the contraction ratio $v^d(\mathbf{e}_1, \mathbf{e}_2)$. The same remark can be made concerning EM with regard to $v^d(\mathbf{e}_2, \mathbf{e}_1)$. Contrary to EM, DM permits an increase of the contraction ratio $v^d(\mathbf{e}_1, \mathbf{e}_2)$ which is consistent with experimental data. For VD and VDT, these ratios include a difference of two damage variables, which allows it to increase or decrease with respect to this difference. In VD, this Poisson's ratio evolution is managed by the relative values of d_V^{vd} and d_D^{vd}, where d_D^{vd} is constrained by the damage level on the shear modulus $\mu^d(\mathbf{e}_1, \mathbf{e}_2)$. The Poisson's damage effect may be negative or zero along the directions $\mathbf{e}_1$ and $\mathbf{e}_2$ verifying Eqs. (10) and (11) respectively.

$$\text{for } \mathbf{e}_1 \Rightarrow \quad d_V^{vd} \leq 2d_D^{vd} \tag{10}$$

$$\text{for } \mathbf{e}_2 \Rightarrow \quad d_V^{vd} \leqslant d_D^{vd} \frac{(3k + 2\mu)}{2\mu} \tag{11}$$

By introducing two additional elastic parameters μ_D^{vdt} and μ_T^{vdt} and another damage variable d_T^{vdt}, VDT allows an independant evolution of the shear modulus $\mu^d(\mathbf{e}_1, \mathbf{e}_2)$. Furthermore, additional weighting coefficients $\frac{\mu_D^{vdt}}{2\mu}$ and $\frac{\mu_T^{vdt}}{2\mu}$ allow further adjustment of the Poisson effect. The degree of "flexibility" of these models depends on the number of variables against the number of parameters. For EM, DM and VD, there are less number of variables than parameters. Therefore it is not possible to drive the three parameters independently with one or two variables. In case of VDT, there are more variables (*i.e.*: 4) than parameters (3) implying non-unique variables set for a given parameters set.

In the DM model, the two moduli α and β does not allow separate adjustment of the in-plane and out-of-plane Young's modulus, shear modulus and contraction ratios. Although DM and EM use the same terminology of density of microcracks from the difference in the numerical values, it appears that the crack density does not have the same interpretation in these two models. In VD, d_D can be used to adjust shear modulus, whereas the Young's modulus and contraction ratios is managed only with d_V. VDT (using d_T) provides an additional ability to adjust the shear modulus without altering the effects on the other elastic properties. VDT also provides access to the lateral strain in each plane often needed to drive the damage evolution law in quasi-brittle materials which is not possible with VD.

4. Numerical comparison of damage effect

The comparisons discussed in Section 3 can help and provide an understanding on the working of damage in various models and highlight some important differences. A numerical study is now presented to analyze these differences. As these models are based on a collection of mechanisms, it is difficult to conceptualize the effects of each damage parameter and its properties. To distinguish a particular damage effect, damage in only one direction in considered. This analysis is limited to the evolution of the three engineering parameters; Young's modulus, shear modulus and Poisson's ratio (Eq. (9)) and is carried out on Voges's sandstone material, whose isotropic elastic properties have already been identified ($\lambda = 3245$ MPa, $\mu = 5340$ MPa, $\alpha = 2500$ MPa and $\beta = 8100$ MPa [1]). DM parameters are used as a reference. This part concerns the effect of damage density oriented along the single direction ($\boldsymbol{e}_1$). For all models under consideration, the total solid angle is discretized into 42 sectors equally distributed and weighted ($w_2 = 4\pi/42$). In all selected models, this discretization is small enough to reproduce the isotropic behavior.

As the models do not consider crack coalescence, an arbitrary value of 25% is chosen for the damage variable of the normal Young's modulus in Walpole basis d_2 related to $\mathbb{E}_2$ tensor. This value is large enough to consider the damage effect, but not enough for rupture. It should also be noted that this value does not affect the sensitivity of the elastic properties since the sensitivity is dimensionless with respect to the damage value d_2 and discretization weight w_2 as show in Eq. (12). Fig. 1 explains the identification method of damage variables for compared models. α and β of DM model was identified by Bargellini et al. [1] for this quasi-brittle material, therefore the damage effect of DM model was considered as reference. Equating the Walpole damage effect $(1 - d_2)$ and damage effect in DM of the $\mathbb{E}_2$ stiffness component in Table 1, the crack density obtained is, $\rho^{DM} = 8.72\%$. Similarly, the crack density was obtained in the EM model which is, $\rho^{EM} = 4.4\%$. Using ρ^{DM}, it is thus possible to determine the damage parameters associated with the $\mathbb{E}_3$ ($d_3 = 4.08\%$) and $\mathbb{E}_4$ ($d_4 = 17.31\%$) components. By equating the damage effect of $\mathbb{E}_4$ component between DM and Walpole damage effect $(1 - d_4)$, one obtains the variable $d_D^{VD} = 11.55\%$ and $d_V^{VD} = 27\%$ is deduced. Initially, VDT parameters are set to obtain result similar to VD, therefore, microplane models can be compared to DM and EM. To ensure this similarity, the model parameters must verify $\mu_D^{VDT} d_D^{VDT} = \mu_T^{VDT} d_T^{VDT}$. By arbitrarily imposing $\mu_D^{VDT} = \mu_T^{VDT}$, we get $\mu_D^{VDT} = \mu_T^{VDT} = \mu_D^{VD} = \mu$ and $d_D^{VDT} = d_T^{VDT} = d_D^{VD}$. The variable $d_T^{VDT} = 11.55\%$ is thus obtained by equating the damage on $\mathbb{E}_4$ component from VD and VDT models.

The sensitivities of the elastic properties are deduced using Eq. (9) and isotropic Young's modulus, shear modulus and Poisson's ratio. To overcome this angular discretization and the damage amplitude, the sensitivities of Young's modulus, shear modulus and Poisson's ratio are divided by the damage variable d_2 which applies in $\boldsymbol{e}_1$ direction and the weight of each

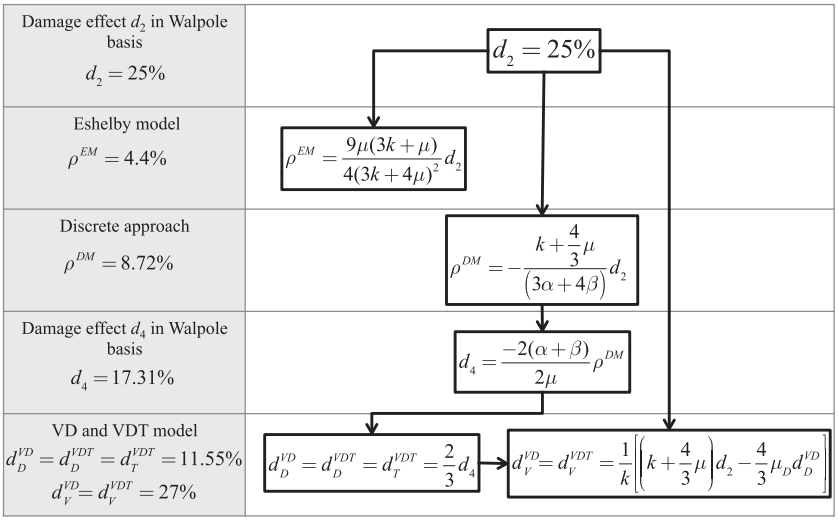

Fig. 1. Identification scheme of damage variables for comparing elastic properties sensitivity.

part of the total solid angle (w_2) as show in Eq. (12). Thus, the engineering parameters plotted in the plane $(\boldsymbol{e}_1, \boldsymbol{e}_2)$ (revolution symmetry around $\boldsymbol{e}_1$) are:

$$s^E(\boldsymbol{m}) = \frac{E - E(\boldsymbol{m})}{E w_2 d_2}, \quad s^\mu(\boldsymbol{m}) = \frac{\mu - \mu(\boldsymbol{m}, \boldsymbol{p})}{\mu w_2 d_2}, \quad s^\nu(\boldsymbol{m}) = \frac{\nu - \nu(\boldsymbol{m}, \boldsymbol{p})}{\nu w_2 d_2} \tag{12}$$

Numerical results are presented and analyzed in this section. In the first stage, the models are considered with the initial set of parameters (as defined in Section 4.1). In the second stage, a particular set of parameters of VD is chosen to ensure de negative sensitivity of Poisson ratio. Finally, the versatility of VDT is presented.

4.1. Comparison with initial set of parameters

The effect of damage on the Young's modulus (Fig. 2) is slightly attenuated for VD, VDT and EM along the $\boldsymbol{e}_1$ direction, whereas DM amplifies the effect of damage in the same direction. In the isotropy plane $(\boldsymbol{e}_1, \boldsymbol{e}_2)$, EM gives an effect of 15% whereas VD/VDT predict an amplitude of 42%. The ratio of these effects is proportional to the ratio between the volumetric component of DM ($-\rho\alpha$) and VDT/VD ($\frac{k}{3} d_V$).

Fig. 3 presents the angular distribution of the damage effect on the shear modulus. It shows that the DM and VD/VDT curves are superimposed and appear independent of direction. For EM, a slight attenuation of the modulus may be observed according to the bisector to $(\boldsymbol{e}_1, \boldsymbol{e}_2)$. Neither the low anisotropic sensitivity, nor isotropic sensitivity can be adjusted with

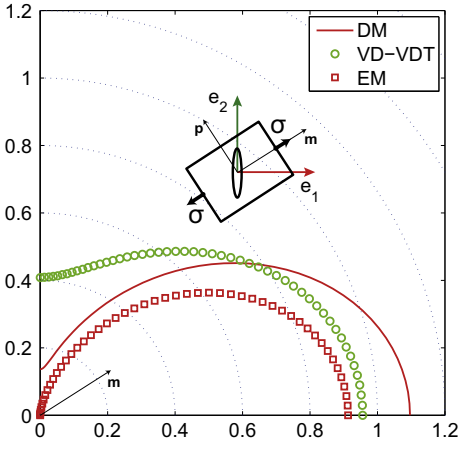

Fig. 2. Sensitivity of Young's modulus to damage d_2 : $s^E(\boldsymbol{m})$.

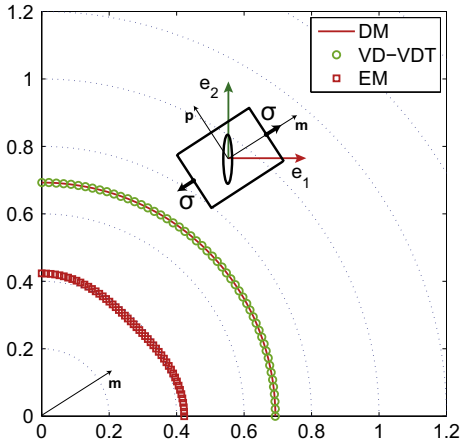

Fig. 3. Sensitivity of shear modulus to damage d_2 : $s^{\mu}(\boldsymbol{m})$.

internal parameter for EM. The same applies to VD, whereas the possibility for DM can be by adjusting α and β as seen in Table 2 ($\mu(\boldsymbol{e}_1, \boldsymbol{e}_2)$).

Fig. 4 presents the angular distribution of the contraction ratio sensitivity versus damage d_2. DM has a negative sensitivity along direction $\boldsymbol{e}_2$, *i.e.* an increasing effect on the Poisson ratio; there is no effect along direction $\boldsymbol{e}_1$. EM presents an assymmetrical behavior *i.e.* positive effect on direction $\boldsymbol{e}_1$ and no sensitivity along direction $\boldsymbol{e}_2$. This non-modifiable positive effect implies a decrease of the contraction ratio, which is in contradiction with experimental observations. Therefore, this model is not investigated any further in the rest of this paper. VD and VDT shows a maximum effect on $\boldsymbol{e}_2$. There is also a positive effect along the direction $\boldsymbol{e}_1$ and zero sensitivity along the bisector.

As explained in Section 3.3, the damage parameters of VD must satisfy two conditions (from Eqs. (10) and (11)) to ensure the negative effect of contraction ratio. One can observes in Fig. 4 that the chosen parameters set ($d_D^{VD} = 11.55\%$ and $d_V^{VD} = 27\%$) does not confirm the negativity of ratio sensitivity in direction $\boldsymbol{e}_1$, since the associated equation is not observed in direction $\boldsymbol{e}_1$ and also in $\boldsymbol{e}_2$.

4.2. Particular value to ensure negative sensitivity of Poisson's ratio

The borderline case (see Eq. (10)) related to the direction $\boldsymbol{e}_1$: ($d_V = 2d_D$), ensures a negative sensitivity of Poisson's ratio for any direction. This small modification of the ratio $d_V/2d_D$ has no effect on the shear modulus sensitivity (Fig. 6), and a small negative spherical one on Young's modulus sensitivity only for VD (Fig. 5). Similarly, the angular distribution of Poisson's ratio sensitivity is significantly changed only for VD, always being negative, and having no effect on DM (Fig. 7).

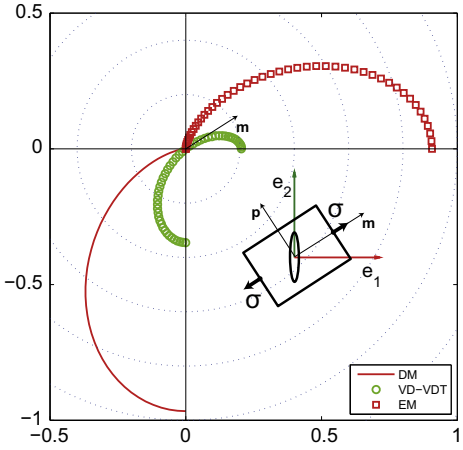

Fig. 4. Sensitivity of Poisson's ratio to damage d_2 : $s^{\nu}(\boldsymbol{m})$.

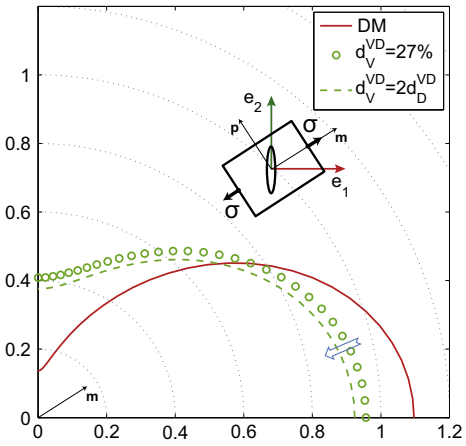

Fig. 5. Angular distribution of the Young's modulus sensitivity to damage d_2 : $s^E(\boldsymbol{m})$. $d_D = 11.55\%$.

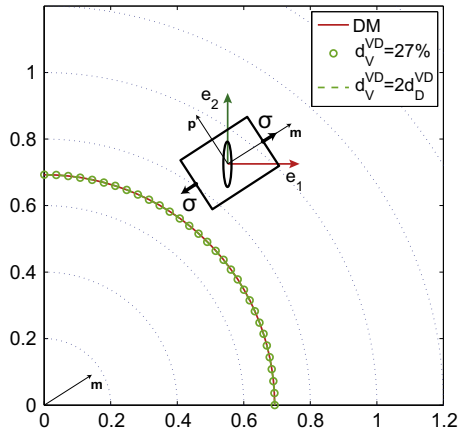

Fig. 6. Angular distribution of the shear modulus sensitivity to damage d_2 : $s^{\mu}(\boldsymbol{m})$. $d_D = 11.55\%$.

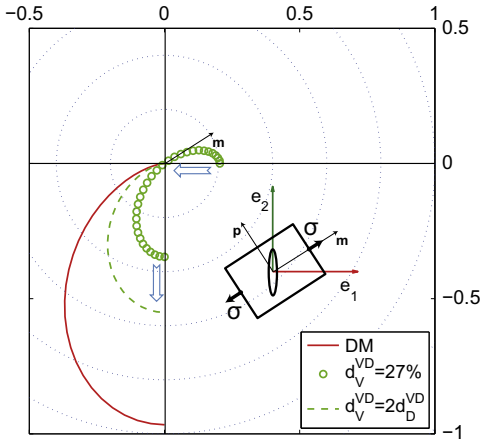

Fig. 7. Angular distribution of the Poisson's ratio sensitivity to damage d_2 : $s^{\nu}(\boldsymbol{m})$. $d_D = 11.55\%$.

This particular set of parameters highlights the versatility with regard to adjustment of the Poisson's effect on microplane models compared to DM. Moreover, one identifies that for DM, the sensitivity of Young's modulus cannot be zero on direction $\boldsymbol{e}_2$, even if $\alpha = 0$, but can be reduced to a smaller value. On the other hand, VD does not result in any marked decrease in this term while unaffecting the damage effect on the other directions and moduli, respectively.

4.3. Versatility of VDT model

VDT partition makes it possible to reach the lateral strain on the level of each microplane, necessary to meet the damage laws of brittle material responses. The set of parameters considered in this section is the one in Section 4.1. However, the relation $\mu_D^{VDT} = \mu_T^{VDT}$ is satisfied and Eq. (3) is restored. On the other hand, relation $\mu_D^{VDT} d_D^{VDT} = \mu_T^{VDT} d_T^{VDT}$ is no longer confirmed. This section concerns the influence of the ratio μ_D^{VDT}/μ_T^{VDT} on damage effect sensitivities.

Figs. 8–10 represents engineering parameter sensitivities with regard to the ratio μ_D^{VDT}/μ_T^{VDT}. The choice is made to vary this modulus ratio and not the damage ratio d_D^{VDT}/d_T^{VDT} to keep the same sensitivities as previously defined.

Fig. 8 shows invariant points for 33° and 73° directions, specific to this set of parameters. Between 0° and 33°, and 73° and 90°, Young's modulus sensitivity to damage d_2 increases, contrary to the directions between 33° and 73°. The amplitude of variation is more pronounced depending on the direction $\boldsymbol{e}_1$. The orientation of the maximum value of damage effect on the Young's modulus with respect to the normal of microcracks introduces a limit on the ratio $\mu_D/\mu_T > 0.4$.

Fig. 9 presents a symmetrical distribution of the invariant points between the bisector of the first quarter (20° and 70°). The symmetry compared to the bisector is recurrent and seems to be intrinsic to shear modulus. The greatest sensitivity variation amplitude for this modulus is on the bisector. In deviatoric part, the ratio μ_D/μ_T leads to adjust either the module associated with the opening and closing μ_D and the module associated with the slip μ_T. Only experimental results can help to conclude on this point.

Fig. 10 has two invariant points at 21° and 66° from axis $\boldsymbol{e}_1$. Maximum Poisson's ratio sensitivity is observed along the $\boldsymbol{e}_2$ direction. Moreover, it was found that there is zero sensitivity in direction $\boldsymbol{e}_1$ and $\boldsymbol{e}_2$ for the specific value of shear moduli ratio μ_D^{VDT}/μ_T^{VDT} (*i.e.* 0.2–2). In Fig. 10, two invariant points appear, which seems to depend on material parameters (modulus and damages). This represents a path to a better understanding of the model.

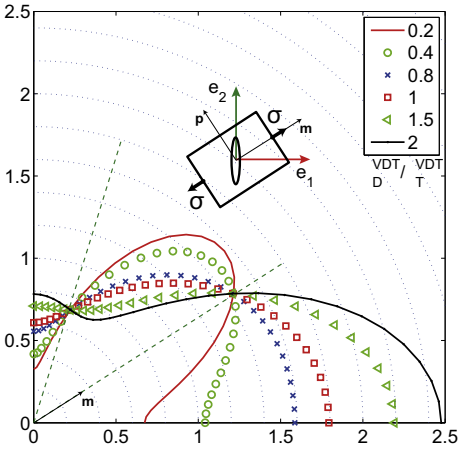

Fig. 8. Angular distribution of theYoung's modulus sensitivity to damage d_2 : $s^E(\boldsymbol{m})$ for different values of μ_D^{VDT}/μ_T^{VDT}.

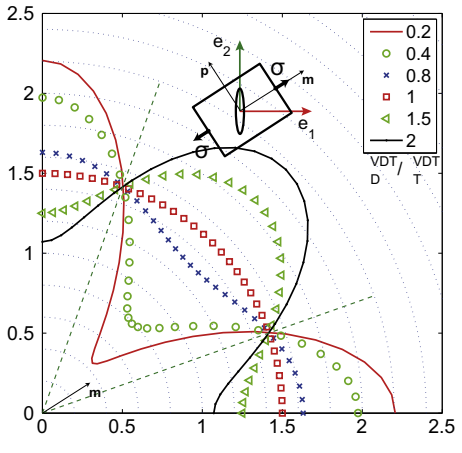

Fig. 9. Angular distribution of the sensitivity of shear modulus to sensitivity to damage d_2 : $s^{\mu}(\boldsymbol{m})$ for different values of μ_D^{VDT}/μ_T^{VDT}.

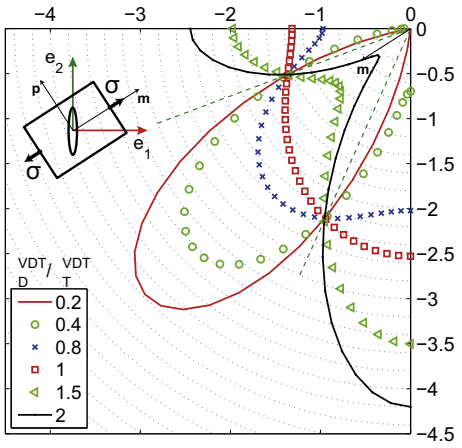

Fig. 10. Angular distribution of the Poisson's ratio sensitivity to damage d_2 : $s^{\nu}(\boldsymbol{m})$ for different values of μ_D^{VDT}/μ_T^{VDT}.

5. Conclusions

Thermodynamic considerations discussed in this paper have been used to select five models based on a summation of damage contributions defined in pre-established directions. Once reformulated in Walpole tensor basis, all the models appear similar. This tensor basis expands the choice of the variables that can drive damage, whether the thermodynamic framework is associated or not. The additive damage effects and the disconnection between the directions restrict the use of these models to low damage levels.

Considering one damaged direction means taking a rosette with singular damage. Rosettes effects of damage resulting from the fourth order tensors are "rather rounded" as based on "trigonometric functions in fourth degree." This confirms the judicious choice of 42 directions. The main differences come from the choice of the damage variables that affect the Walpole tensors. It was found that the VDT model is the only one which makes it possible to manage independently the evolution of the contraction ratio with respect to evolution of other parameters. It thus makes it possible to adjust the anisotropy ratio on the out-of-plane shear modulus and contraction ratio. The versatility of VDT comes from large number of model parameters compared to the moduli observed. The numerical study in this article provides an initial argument for understanding the sensitivity of engineering parameters which allows a better understanding of the influence of each parameters and simplify their identification.

The choice of a phenomenological framework to model the anisotropic induced damage remains difficult due to the lack of experimental data. The effect of crack opening/closure on the out-of-plane elastic modulus is relatively easy to consider, but is often insufficient to model all the unilateral phenomena. Indeed, one of the most difficult task is to model the coupling between shear damage and pressure.

The framework detailed here proposes a well defined formulation of damage effects. This framework is of interest in describing the pressure-dependence of quasi brittle (and thus pre-damaged) materials. It was observed that one of the major experimental and characterization difficulties is to separate damage from damage effectiveness, in an anisotropic and multidirectional context, to obtain their evolution. This new method can be used to analyze and select induced anisotropic model which introduces damage unilaterally, during opening and closing of cracks.

References

[1] Bargellini R, Halm D, Dragon A. Modelling of quasi-brittle behaviour: a discrete approach coupling anisotropic damage growth and frictional sliding. Eur J Mech A – Solids 2008;27(4):564–81.
[2] Batdorf SB, Budiansky B. A mathematical theory of plasticity based on the concept of slip, volume technical note no. 1871. National Advisory Committee for Aeronautics; 1949.
[3] Bazant ZP, Oh Byung H. Microplane model for fracture analysis of concrete structures. In: The interaction of non-nuclear munitions with structures: proc symp, vol. 2. Springs, Colorado: US Air Force Academy; 1983. p. 49–55.
[4] Bazant ZP, Caner FC, Carol I, Adley MD, Akers SA. Microplane model M4 for concrete. I: formulation with work-conjugate deviatoric stress. J Eng Mech – ASCE 2000;126(9):944–53.
[5] Beghini A, Bazant ZP, Zhou Y, Gouirand O, Caner FC. Microplane model M5f for multiaxial behavior and fracture of fiber-reinforced concrete. J Eng Mech – ASCE 2007;133(1):66–75.
[6] Carol I, Jirásek M, Bazant ZP. A thermodynamically consistent approach to microplane theory. Part I. Free energy and consistent microplane stresses. Int J Solids Struct 2001;38(17):2921–31.
[7] Carol I, Bazant ZP, Prat PC. Geometric damage tensor based on microplane model. J Eng Mech – ASCE 1991;117(10):2429–48.
[8] Carol I, Willam K. Spurious energy dissipation/generation in stiffness recovery models for elastic degradation and damage. Int J Solids Struct 1996;33(20–22):2939–57.
[9] Chaboche JL. Damage induced anisotropy: on the difficulties associated with the active/passive unilateral condition. Int J Dam Mech 1992;1(2):148–71.
[10] Chaboche JL, Lemaitre J. Aspect phénoménologique de la rupture par endommagement. J Mech Appl 1978(2):317–65.

[11] Challamel N, Halm D, Dragon A. On the non-conservativeness of a class of anisotropic damage models with unilateral effects. CR Acad Sci II B Mech 2006;334(7):414–8.
[12] Cormery F, Welemane H. A critical review of some damage models with unilateral effect. Mech Res Commun 2002;29:391–5.
[13] Chow CL, Wang J. An anisotropic theory of continuum damage mechanics for ductile fracture. Engng Fract Mech 1987;27(5):547–58.
[14] Dienes JK. Unified theory of flow, hot spots and fragmentation with an application to explosive sensitivity. In: Lee Davison et al., editors. High-pressure shock compression of solids II. Springer-Verlag New York, Inc.; 1996. p. 366–98.
[15] Halm D, Dragon A. An anisotropic model of damage and frictional sliding for brittle materials. Eur J Mech A – Solids 1998;17(3):439–60.
[16] Kachanov LM. On the time to failure under creep conditions. Izv AN SSR, Otd Tekhn Nauk 1958;8:26–31.
[17] Kunin IA. An algebra of tensor operators and its applications to elasticity. Int. J. of Engng Sci. 1981;19(12):1551–61.
[18] Ladevéze P. Inelastic strains and damage. In: Talreja R, editor. Composites materials series, 9: damage mechanics of composite materials. Elsevier; 1994. p. 117–38 [chapter 4].
[19] Leukart M, Ramm E. A comparison of damage models formulated on different material scales. Comput Mater Sci 2003;28(3–4):749–62.
[20] Mazars J. A description of micro- and macroscale damage of concrete structures. Engng Fract Mech 1986;25(5–6):729–37.
[21] Murakami S, Kamiya K. Constitutive and damage evolution equations of elastic-brittle materials based on irreversible thermodynamics. Int J Mech Sci 1997;39(4):473–86.
[22] Pensee V, Kondo D. Micromechanics of anisotropic brittle damage: comparative analysis between a stress based and a strain based formulation. Mech Mater 2003;35(8):747–61.
[23] Ponte Castaeda P, Willis JR. The effect of spatial distribution on the effective behavior of composite materials and cracked media. J Mech Phys Solids 1995;43(12):1919–51.
[24] Rabotnov YN. Progress in applied mechanics. Div Tech Sci 1968:307–15.
[25] Taylor GI. Plastic strain in metals. J Inst Met 1938;62:307–24.
[26] Walpole LJ. Elastic behavior of composite materials: theoretical foundations. Adv Appl Mech 1981;21:169–242.
[27] Zhu QZ, Shao JF, Kondo D. A micromechanics-based non-local anisotropic model for unilateral damage in brittle materials. CR Acad Sci II B Mech 2008;336(3):320–8.

2.4.2 Modèle microplans avec plasticité (M1)

La deuxième partie des travaux de thèse de A. Benelfellah a consisté en la définition d'essais permettant d'illustrer l'effectivité et la nature directionnelle de l'endommagement. Des essais de traction jusqu'à 85% de la contrainte à rupture puis compression ont été mis en œuvre au CEA et ont montré une reprise de raideur un peu après le passage en compression (-2MPa), illustrant un effet unilatéral. Après cette reprise de raideur, le comportement rejoint celui observé en compression simple, indiquant une absence d'effet de l'endommagement engendré en traction sur le comportement en compression. Le même type d'essai, avec une compression menée avant une phase de traction, montre en revanche un module beaucoup plus faible au passage en traction que celui mesuré en traction simple, accompagné d'une diminution de la contrainte à rupture. Les différences observées illustrent le caractère directionnel de l'endommagement.

Dans un souci de hiérarchisation de l'identification des paramètres et de simplification de l'approche, la partie élastique endommageable est extraite des courbes multicycles présentées dans les travaux précédents. Ces courbes reconstruites seront les seules exploitées pour caractériser l'endommagement et son effectivité. Dans cette 1ère approche, des fonctions d'effectivité sont introduites sur les parties volumiques et déviatoriques de l'endommagement. Afin de garantir de ne pas avoir de dissipation anormale, ces fonctions sont liées à leurs variables respectives. Ce choix a pour conséquence directe que le module de cisaillement soit indépendant de la pression de confinement. Ce point fera l'objet de la définition d'un essai de torsion sous confinement développé dans la thèse de Marwen Chatti.

L'effectivité volumique est gérée via une fonction d'Heaviside (endommagement totalement effectif pour une déformation volumique positive, non effectif sinon) et l'effet unilatéral est déclenché à déformation élastique nulle. Ce choix a pour avantage d'annuler un éventuel saut de contrainte, mais pour inconvénient de ne pas pouvoir régler la valeur de la contrainte correspondant au déclenchement de la reprise de raideur.

Les paramètres des lois d'évolutions sont identifiés à partir des essais sous pression hydrostatique puis des essais de compression simple. Les 1ères comparaisons essais/simulations (implantation du modèle dans une UMAT) montrent la difficulté et la nécessité de dissocier l'endommagement et son effet, ce qui est très difficile sans essai dédié. Néanmoins, la concordance est assez bonne. Cette approche est détaillée dans l'article ACL10 présenté ci-dessous.

Engineering Fracture Mechanics 131 (2014) 525–537

Contents lists available at ScienceDirect

Engineering Fracture Mechanics

journal homepage: www.elsevier.com/locate/engfracmech

Characterization and modeling of the anisotropic damage of a high-explosive composition

D. Picart [b,*], A. Benelfellah [c], J.L. Brigolle [b], A. Frachon [a], M. Gratton [a], M. Caliez [a]

[a] INSA Centre Val de Loire, Universite François Rabelais de Tours, Laboratoire de Mecanique et Rheologie, EA 2640, BP 3410, F-41034 Blois cedex, France
[b] CEA DAM Le Ripault, F-37260 Monts, France
[c] Institut Pprime UPR 3346 CNRS – ENSMA – Université de Poitiers, Département physique et Mécanique des matériaux, 1 Avenue Clément Ader, BP 40109, 86961 Futuroscope Chasseneuil cedex, France

ARTICLE INFO

Article history:
Received 19 March 2014
Received in revised form 3 September 2014
Accepted 9 September 2014
Available online 20 September 2014

Keywords:
Experiment
Constitutive law
Anisotropic damage
Unilateral effect

ABSTRACT

Modelling the behaviour of quasi-brittle materials requires dealing with the anisotropic damage evolution induced by the loading direction and the unilateral effect corresponding to the sudden opening/closure of defects. The latter was the cause deficiencies of some constitutive laws as a no continuous stress/strain response or spurious energy dissipation. In this paper, the behaviour of pressed high explosive is experimentally investigated. Evidences of a pre-existing damage, an anisotropic one developing during loading and the unilateral effect are detailed. The framework of the microplane constitutive laws previously proposed in the literature and based on the volumetric–deviatoric–tangential strain projections is used. Damage is introduced in the model and is affected by an "effectiveness" function weighting its influence with the loading direction. The calibration procedure is detailed and a discussion enables highlighting the strengths and weaknesses of the modelling approach.

1. Introduction

Modern numerical tools enable simulating operational life conditions of pyrotechnic structures as assembly/disassembly procedures or thermal cycles during storage. It requires an improved and accurate mechanical constitutive law of the explosive composition. A first difficulty comes from the complexity of the behaviour of such a material made of a high solid fraction of grains mixed with a polymeric binder. It gives a temperature and a strain rate dependencies as well as a dependence of the maximum stress with the confinement. A second difficulty comes from the experiments classically used to characterize such materials. Most of these are (1) monotonic ones with an increase of the load up to the failure and (2) strain measurement only made along the loading direction. These experimental set-ups hide some of the basic trends of the mechanical behaviour, and the calibration procedures of the models are questionable. Especially, the anisotropic nature of the damage cannot be observed, as well as the "unilateral" response of the material (for example the dependence of the Young's modulus with the loading direction) during tensile/compressive or compressive/tensile cyclic loadings.

The material studied in this paper is made of more than 95% by mass of octahydro-1,3,5,7-tetranitro-1,3,5,7-tetrazocine (HMX) grains mixed with a low percentage of a binder. The mixture is pressed using an isostatic process. The final product can be machined into solid samples of various shapes. It behaves as a quasi-brittle material with a maximum strain of 0.01

* Corresponding author.
E-mail address: didier.picart@cea.fr (D. Picart).

http://dx.doi.org/10.1016/j.engfracmech.2014.09.009
0013-7944/

Nomenclature

a_i	calibration parameters
d_V, d_D, d_T	volumetric and out-of plane and in-plane shear damage variables, initial values
E, v, K, μ	global Young's modulus, Poisson's ratio, bulk and shear moduli; experimental (resp. calibration) values with lowerscript "exp" (resp. "mod"), for compressive (resp. triaxial) tests with upperscript "H0" (resp. "H10")
E_L, E_T	longitudinal and transversal modules
F_V, F_D, F_T	volumetric, deviatoric and tangential forces associated to the damage variables
κ_V, μ_D, μ_T	volumetric and out-of plane and in-plane shear modulii
$\mathbf{n}$	microplane normal
q	state variable
$\mathbf{t}_\varepsilon$	strain vector
α_V, α_D	effectiveness parameters
ε_V, ε_D, $\boldsymbol{\varepsilon}_T$	volumetric, deviatoric and tangential strain
$\boldsymbol{\varepsilon}$	strain tensor
ψ, ψ^n	global and microplane free energies
ρ_0	density
$\boldsymbol{\sigma}$	stress tensor
σ_V, σ_D, $\boldsymbol{\sigma}_T$	volumetric, deviatoric and tangential stress

(respectively 0.001) recorded at the maximum stress during a compressive experiment (resp. a tensile one). During its operational life, this material is submitted to a hydrostatic pressure ranging between 0 and 10 MPa and few tensile/compressive loading cycles. The temperature and strain rate loading conditions being out of the scope of this paper, measurements will be reported below at ambient temperature and low strain rates (approx. 10^{-5} s^{-1}).

The microstructure of the material (Fig. 1 left) shows the distribution of the grain which sizes ranging from approximately 500 μm to less than a micron. It highlights the high density of pre-existing discontinuities (and thus defects) between grains. Porosity is mainly located between the smallest grains (dark zones in Fig. 1 come from optical aberrations due to small particles remaining at the surface of the polished sample). Due to the high pressure used to compact the aggregate, grains have been forced each to the other leading to intense stress at the contact zones. Intra-granular micro-cracks are observed as a consequence of this process. Randomly orientated grains, discontinuities and micro-cracks provide an isotropic response of the material confirmed by macroscopic measurements of the elastic modules whatever the direction the sample has been machined into a rough piece.

The sample has been submitted to a reverse edge-on compression test using the set-up described by Picart et al. [1]. This experiment enables observations at the surface of the sample during its deformation around a fixed wedge. Fig. 1 right shows (1) debonding between grains as the dominant mechanism of deformation at low confinement, (2) new intra-granular micro-cracks, (3) inelastic deformation of some grains along straight bands and (3) reorganization of the "matrix" (made by the smallest grains, the binder and the porosity). Damage is dominated by local tensile loadings, few shear strain being

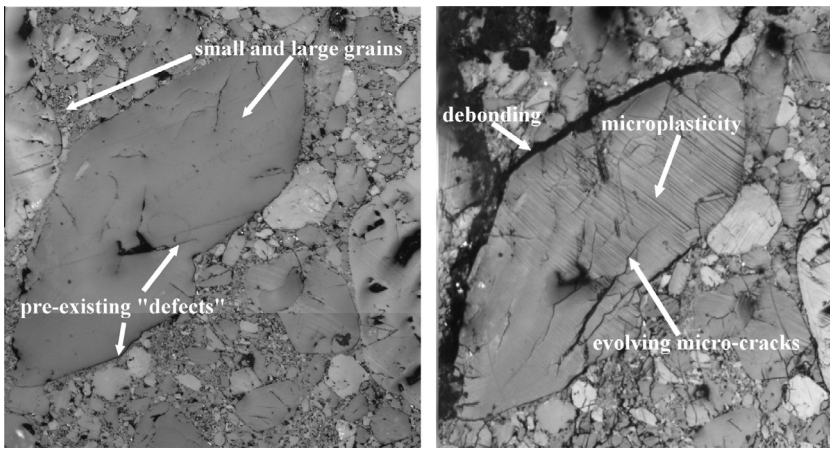

Fig. 1. Microstructural observations of a sample before (left) and after (right) a deformation at a low confinement. The first image highlights the dispersed sizes of the grains, pre-existing intra-granular micro-cracks due to the pressing process used to compact the powder and a lot of grain–grain surface contacts. The second one shows new micro-cracks due to debonding between grains, induced intra-granular micro-cracking and straight bands related to the inelastic deformation of some grains.

observed. Unfortunately, measurement of the anisotropy of the damage is hardly tractable, even with sophisticated software, at that scale and for quasi-static loadings. Evidence of microstructural anisotropy has been mentioned by Trumel et al. [2] as a result of a dynamic uniaxial compression made using a split Hopkinson pressure set-up.

If the previous microstructural observations have shown a pre-existing damage and its anisotropic increase with the loading, an in-depth analysis of experimental data gives the consequences on the macroscopic response of the material. Eliminating the viscous and the inelastic components of the measured stress–strain curves enables characterizing the "elastic" response of the material. A pressure-dependence of the elastic modules as well as of the damage rate is observed. Data are reported and analysed in Sections 2 and 3.

An experimental set-up has been developed to submit a sample to a tensile and then a compressive load or vice-versa. The recovery (respectively the loss) of the stiffness, here called the "unilateral effect of the damage", is observed and is attributed to micro-crack closing (resp. micro-crack re-opening). These tests are reported in the Section 4 of this paper.

Constitutive laws based on micromechanical assumptions and homogenization methods were proposed to model the induced anisotropic damage of an explosive composition [3,4] or for other quasi-brittle materials (see for example [5–7]). These approaches start with the behaviour of a single penny-shaped micro-crack which contribution to continuum constitutive law is deduced by applying an averaging rule. Based on orientated micro-cracks, their contributions are summed over the unit sphere. Sophisticated constitutive laws were proposed taking into account the micro-crack opening/closure mechanism or friction between the lips of closed micro-cracks. However, many efforts remain to determine the micromechanical variables from experimental data.

The now well-known continuum damage mechanic provides another useful framework for the development of models. Damage was described using vectors [8] or on a second order tensor [9–13]. Some authors [14–17] have shown some persistent thermodynamical inconsistencies in some of these models. To maintain the Hooke's tensor symmetries, a non dissipative free energy and its uniqueness, and continuous stress–strain behaviour at the opening/closure of micro-cracks, constitutive laws formulated as a summation of directional contributions, and thus a summation of symmetric tensors, must be adopted. In Section 5, a microplane approach is used with a volumetric–deviatoric–tangential decomposition of the strain tensor [18,19]. Volumetric and deviatoric damage variables are weighted by a function of their respective projected strain to account for the unilateral effect. This model satisfies all of the thermodynamical requirements and its strengths and weaknesses are discussed in Section 5 and 6. In the latter, a method is proposed to calibrate the model.

Sections 7 and 8 are devoted to the simulations of a microplane behaviour and to comparisons between the model and macroscopic data.

2. Existence of an initial damage and its influence

The influence of an initial damage has been characterized for sandstones for example in [20,21]. Applying a hydrostatic confinement, an increase of the bulk modulus is observed till the pressure reaches approximately 15 MPa.

A set of triaxial experiments have been made to observe the influence of the confinement on the mechanical response of our material. A cylindrical sample is submitted first to an isostatic compression and then to a uniaxial loading, the lateral confinement being maintained. Samples have been equipped by two bidirectional gauges. Data published for our material

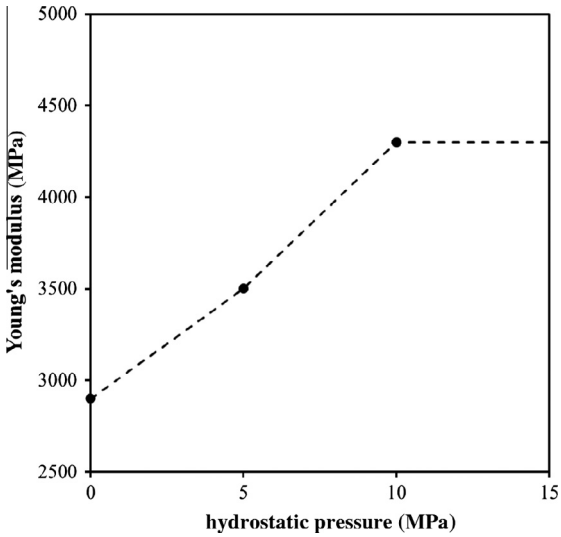

Fig. 2. Evolution of the Young's modulus deduced from triaxial experiments with different hydrostatic confinements. The influence of the pre-existing damage is eliminated above 10 MPa [22]. Data available at 20, 60 and 100 MPa are not reported here.

have been summarized in [22]. Stress–strain curves have been obtained for hydrostatic pressure ranging from 0 to 800 MPa, and the elastic Young's modulus can be deduced versus the confinement. Fig. 2 shows a modulus evolving from 2.9 GPa without confinement to 4.3 GPa if the confinement ranges between 10 MPa and the manufacturing pressure. In the scope of this paper we are interested in moderate confinement well below the manufacturing one. The pressure does not delete the microstructural defects as grain/grain interfaces or intra-granular micro-cracking, but it closes and eliminates their influences on the macroscopic response. This phenomenon will be called here "the effectiveness of the damage". It means that damage can exist or increase, but its influence on the macroscopic response depends on the loading.

3. Evidences of an anisotropic damage induced by the loading

During the uniaxial part of the triaxial experiments, cyclic loadings are applied to the sample including relaxations at fixed longitudinal strain and recovery at few Newtons above the applied hydrostatic pressure [23]. Joining the relaxed stress difference and the residual strain at the given confinement gives the elastic modules, the elastic behaviour of the material being determined (Fig. 3). Below, elastic strain will be called "strain" for the sake of simplicity. Experiments reported here have been made at a strain rate of $3.3\ 10^{-5}\ s^{-1}$ and 20 °C. One can observe the difference on the maximum stress between the tensile and all the compressive loadings.

Although an initial damage is eliminated by the confinement of 10 MPa, a non-linear behaviour is observed due to the evolution of the damage. The contraction ratio (ratio of the transversal to the longitudinal modules in the stress–strain diagram) increases along the loading (it is the case for all the compressive experiments [23]). Evidence of anisotropic damage is observed using the elastic degradations determined on the longitudinal (Young's modulus) and the transversal modules (Fig. 4). A higher degradation is obtained on the transverse modulus than on the longitudinal one.

The influence of the pressure on the damage is observed in Fig. 4. Pressure limits the damage rate for the same positive strain. As observed at the microstructural scale, tensile strain influences the evolution of the damage. Each last dot on the curves refers to the last cycle. These cycles have been made not at but close to the maximum stress. The damage determined at that level is far from 1.

As for quasi-brittle rocks or concretes, the behaviour under a tensile loading differs drastically from those under compressive stress. An explanation comes from the direct increase of the positive strain during tensile experiments when the Poisson's ratio determines the positive strain for compressive ones. We will see below that it is not the only reason. Moreover, there is no clear evidence of damage anisotropy during the tensile test.

If an anisotropic evolution of the damage is macroscopically observed, its cause remains impossible to characterize in-situ and at the real time. We therefore limit ourselves to interpret the anisotropy as the consequence of an orientated micro-cracking process of damage, the orientation being due to the loading direction and thus the local tensile strain.

4. Evidences of the unilateral effect

Previous sections have shown evidences of damage by micro-cracking (here referring to intra-granular micro-cracking as well as inter-granular debonding) into the microstructure and the influence of the pressure and the loading direction on the macroscopic behaviour. One can suspect that tensile loading normal to a micro-crack leads to its opening and for compressive loading to its closure. The latter would be accompanied by an increase of the material strength. This phenomenon has

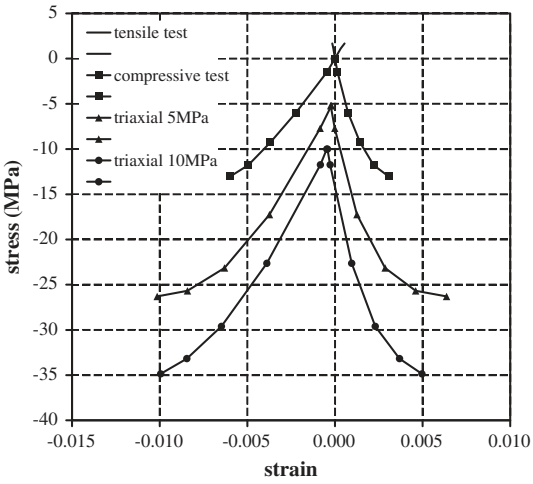

Fig. 3. Stress versus the elastic longitudinal and transversal strains for a tensile (short lines above 0 MPa), a compressive (square) and two compressive experiments respectively with a confinement of 5 (triangle) and 10 MPa (dot). The module drawn between the ends of the relaxation phases and of the recovery loadings gives the elastic strain versus the relaxed stress. Thus each dot refers to a cycle during the corresponding test.

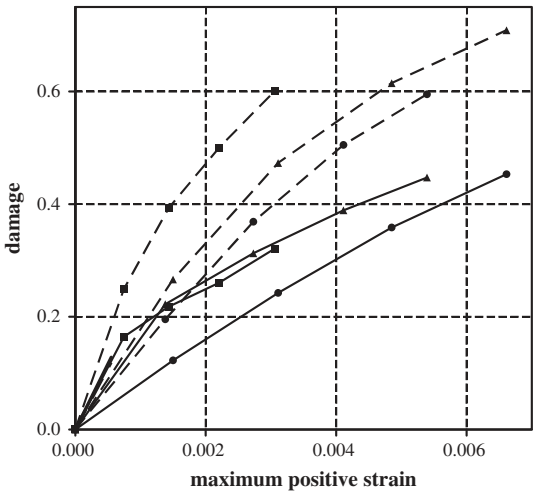

Fig. 4. Damage versus the tensile strain during the uniaxial part of the experiments. Damage is determined as the ratio of the difference of the actual modulus minus the initial modulus to the initial modulus. This ratio is determined either for the longitudinal (line) modules and the transversal ones (dashed lines). Same symbols as for the previous figure.

been previously observed for example for a concrete [24] and a composite [11,25]. We now report a set of experiments providing data for our material.

Double belt-shaped samples have been used (Fig. 5 right) with a central volume of $10 \times 10 \times 20$ mm^3 to avoid buckling. Samples have been equipped with two opposite pairs of strain gauges Vishay CEA13-062UT-350 glued with the M200 glue. Samples have also been glued (M200) between two plates. These plates are parts of two rigid assemblies (Fig. 5 left) made by two plates and three columns each. Thus, a removal of the set-up ends using an electro-mechanical machine leads to a compressive loading of the sample and vice versa.

Experiments have been made at a cross-head speed of 12 μm/min and 20 °C. The displacement is controlled using three LVDT fixed between the two assemblies. The behaviour of the material characterised using this set-up has been compared to standard compressive (made on cylinders of diameter equal to 10 mm and a height of 20 mm) and tensile (made on belt-shaped samples with a working volume of $10 \times 10 \times 50$ mm^3) experiments. The maximum stress and strains compare very well with the results published [23], the recorded maximum stress being equal to 2.92 MPa here for tensile loading (respectively 15.3 MPa for compressive one) compared to 3.13 MPa (resp. 17.8 MPa). The low decrease of the stress comes from the low strain rate applied here, and thus a lower viscous stress.

A first test alternating a tensile and a compressive loading has been made (Fig. 6). During the first stage, a maximum stress of 2.72 MPa has been applied, representing 0.93 of the maximum stress. Then, the sample has been unloaded and uniaxially pressed up to the failure. An increase of the stiffness (the slope is multiplied by 1.35) is observed around −2.5 MPa. The curve previously obtained for the compressive loading is recovered. The maximum stress of 14.9 MPa is close to the one obtained without a previous tensile loading. It proves that the damage created during tensile loading does not affect the compressive response. Micro-cracks which have been created and opened, mainly orientated along a plane perpendicular to the load direction, close at −2.5 MPa after unloading. A new set of micro-cracks develops during the compressive load parallel to the load direction.

Fig. 7 shows the behaviour of a sample submitted to a compressive load followed by a tensile one. During the first stage, a maximum stress of 13.8 MPa has been applied, corresponding to 0.90 of the maximum compressive stress. During unloading, a rapid decrease of the slope of the stress–strain curve is observed approximately at −2.5 MPa. Failure is recorded at 2.50 MPa i.e. at 0.85 of the maximum tensile stress, when the unloading curve joins the monotonic tensile response. Results highlight a dependence of the effectiveness of the damage during a tensile loading following a compressive one. Conversely it has not been the case in Fig. 6.

Some experiments have been made at lower stress for the same cross-head velocity. Two cycles have been made between 0.75 of the maximum stress in compressive and tensile loading conditions (respectively −11.5 and 2.23 MPa), followed by a cycle between 0.85 of the maximum stress (respectively −13.1 and 2.43 MPa). The same trends being observed whatever the direction of the first load, Fig. 8 reports the results obtained during one of these experiments. For the sake of simplicity, only one of the two measurement gauges is reported in this figure and the stress is shifted artificially between each cycle. The experiment starts in the compression direction. During the second cycle (respectively the third one), the monotonic response is reached for a higher stress of −11 MPa (resp. −12.5 MPa). The unloading phases following the compressions show again a rapid decrease of the slope of the curve at −2.5 MPa, or a recovery of the stiffness during loading. Failure has always been obtained during the tensile loading of these cyclic tests.

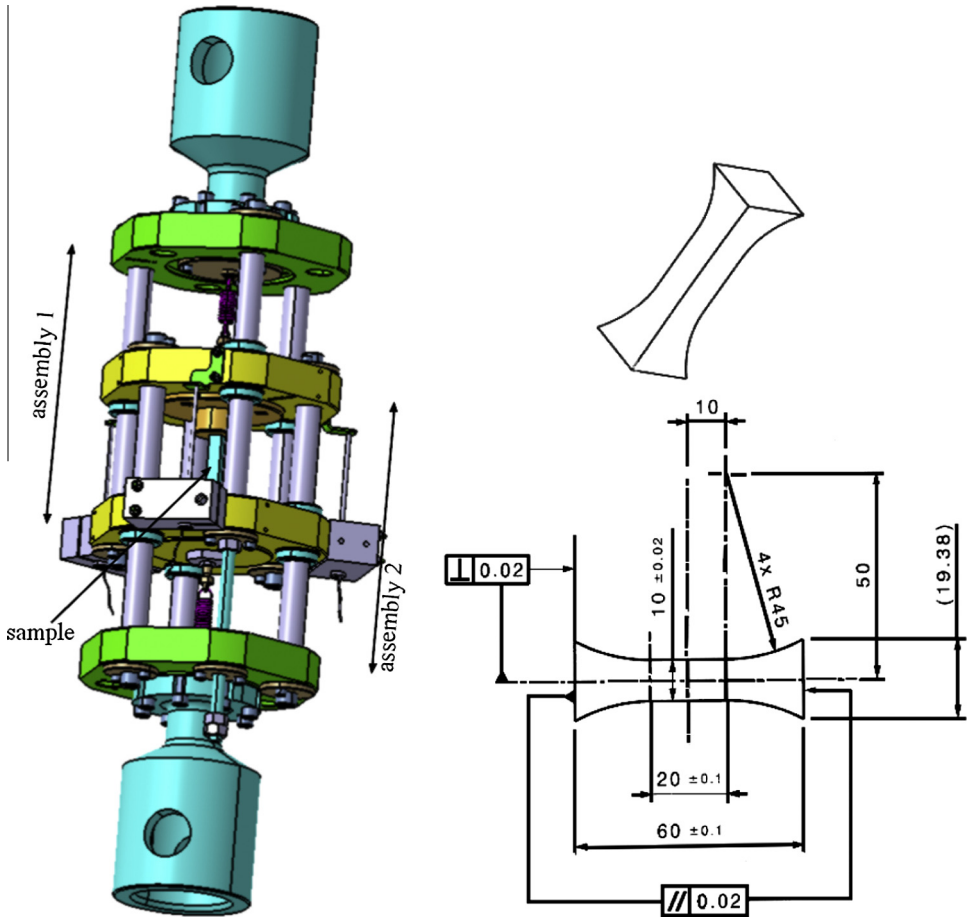

Fig. 5. Experimental set-up (left) inspired from [26] and sample (right) used for tensile/compressive tests. The two rigid assemblies are fixed to the machine. Extremities of the set-up must be hanging over to yield a tensile loading one.

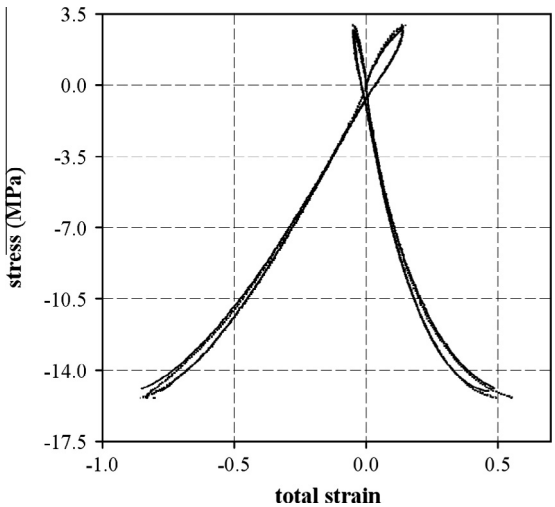

Fig. 6. Tensile loading followed by a compressive one. Dashed lines are the responses recorded during monotonic tensile or compressive loadings. The curve shows the stiffness recovery at −2.5 MPa and the same maximum stress during the last stage.

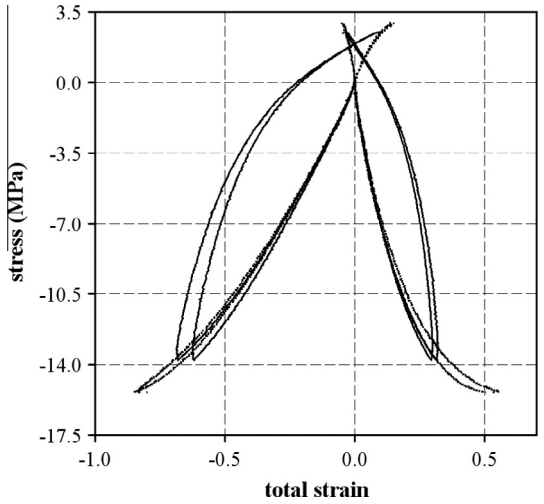

Fig. 7. Compressive loading followed by a tensile one. Dashed lines are the responses to monotonic tensile or compressive loadings. The curve shows the stiffness loss at −2.5 MPa and a lower maximum stress at failure obtained during the last stage.

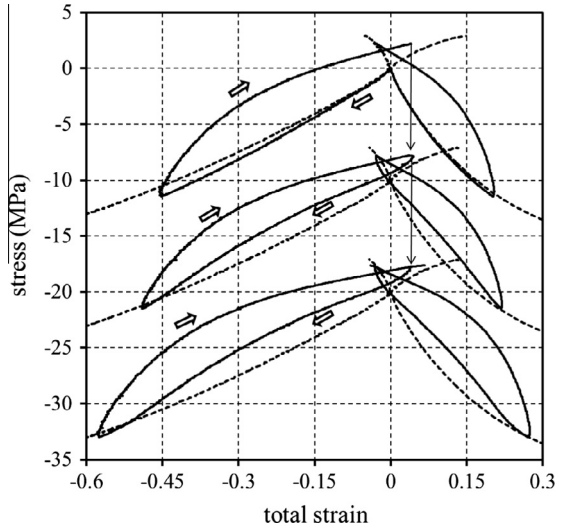

Fig. 8. Compressive load followed by a tensile one and repeated three times. The first two cycles have been made at 0.75 of the maximum stress, the following one at 0.85. To improve the graph, only one of the two gauges is reported and a vertical shift (vertical harrows) of −10 MPa (respectively of −20 MPa) has been applied at the second cycle (resp. the third one). Dashed lines are the responses to monotonic tensile or compressive loadings. Failure occurs during the last cycle and the tensile loading.

Unfortunately, Fig. 3 cannot be directly compared to Figs. 6–8 due to remaining viscous stress in the latters and because cyclic experiments do not involved relaxation and recovery stages. However, it demonstrates the existence of stiffness loss and recovery.

5. Constitutive law

Among the constitutive laws proposed to model the anisotropic damage induced by the loading and satisfying the thermodynamic requirements, the microplane approach provides a powerful framework to implement complex laws. Particularly, the introduction of a unilateral effect is possible keeping a no dissipative free energy, a continuous stress–strain response or a symmetrical stiffness tensor. The lines below give the notations used for the volumetric–deviatoric–tangential, denoted VDT, split of the strain tensor. The way the effectiveness of the damage has been introduced in the model is detailed. The evolution laws and the model calibration will be detailed in the next section.

The stress $\boldsymbol{\sigma}$ is defined by the strain (denoted $\boldsymbol{\varepsilon}$) partial derivative of the free energy ψ. The microplane approach states that the free energy is equal to the angular integral over the entire solid angle Ω of the angular free energy density, expressed as $\psi^n/4\pi$, associated to each plane defined by its normal $\mathbf{n}$. The following definition yields:

$$\boldsymbol{\sigma} = \frac{\partial \rho_0 \psi}{\partial \boldsymbol{\varepsilon}} = \frac{3}{4\pi} \int_\Omega \frac{\partial \rho_0 \psi^n(\mathbf{t}_\varepsilon, q)}{\partial \boldsymbol{\varepsilon}} d\Omega \quad \text{with} \quad \mathbf{t}_\varepsilon = \boldsymbol{\varepsilon} \cdot \mathbf{n} \tag{1}$$

where q is a set of state variables. The strain tensor is decomposed into its volumetric, deviatoric and tangential components by the following equations:

$$\varepsilon_V = \frac{1}{3}\mathbf{1} : \boldsymbol{\varepsilon} = \mathbf{V} : \boldsymbol{\varepsilon} \quad \varepsilon_D = \left(\mathbf{n} \otimes \mathbf{n} - \frac{1}{3}\mathbf{1}\right) : \boldsymbol{\varepsilon} = \mathbf{D} : \boldsymbol{\varepsilon} \quad \boldsymbol{\varepsilon}_T = (\mathbf{n} \cdot \mathbf{U} - \mathbf{n} \otimes \mathbf{n} \otimes \mathbf{n}) : \boldsymbol{\varepsilon} = T : \boldsymbol{\varepsilon} \tag{2}$$

with $\mathbf{1}$ and $\mathbf{U}$ respectively the second and fourth unit tensors. It gives the relation:

$$\boldsymbol{\sigma} = \frac{\partial \rho_0 \psi}{\partial \boldsymbol{\varepsilon}} = \frac{3}{4\pi} \int_\Omega \left[\frac{\partial \rho_0 \psi^n(\mathbf{t}_\varepsilon, q)}{\partial \varepsilon_V} \mathbf{V} + \frac{\partial \rho_0 \psi^n(\mathbf{t}_\varepsilon, q)}{\partial \varepsilon_D} \mathbf{D} + \frac{\partial \rho_0 \psi^n(\mathbf{t}_\varepsilon, q)}{\partial \boldsymbol{\varepsilon}_T} \cdot T \right] d\Omega \tag{3}$$

The stress associated to the energy of the microplane is thus defined with the following relations:

$$\sigma_V = \frac{\partial \rho_0 \psi^n(\mathbf{t}_\varepsilon, q)}{\partial \varepsilon_V} \quad \sigma_D = \frac{\partial \rho_0 \psi^n(\mathbf{t}_\varepsilon, q)}{\partial \varepsilon_D} \quad \boldsymbol{\sigma}_T = \frac{\partial \rho_0 \psi^n(\mathbf{t}_\varepsilon, q)}{\partial \boldsymbol{\varepsilon}_T} \tag{4}$$

To model the induced anisotropic damage of the material, let us define the microplane free energy as follow:

$$\psi^n = \frac{1}{2}\kappa_V(1 - \alpha_V(\varepsilon_V)d_V)\varepsilon_V^2 + \frac{1}{2}\mu_D(1 - \alpha_D(\varepsilon_D)d_D)\varepsilon_D^2 + \frac{1}{2}\mu_T(1 - d_T)\boldsymbol{\varepsilon}_T.\boldsymbol{\varepsilon}_T \tag{5}$$

Three damage variables d_V, d_D and d_T are introduced to damage the corresponding elastic modules denoted k_V, μ_D and μ_T. These modules can be related to the bulk and the shear global ones K and μ: $k_V = 3\,\mathrm{K}$ and $2\mu_D + 3\mu_T = 10\mu$. We have seen above that the influence of the pre-existing damage disappears as the pressure increases, justifying the bulk damage effectiveness variable α_V. To obtain a simple volumetric constitutive law and to avoid a dissipative free energy [17], α_V is dependent on its associated strain component. Moreover, it has been defined as a Heaviside's function centred on a zero elastic volumetric strain to provide continuous stress–strain behaviour. It yields:

$$\begin{cases} \varepsilon_V < 0 \Rightarrow \alpha_V(\varepsilon_V) = 0 \\ \varepsilon_V \geqslant 0 \Rightarrow \alpha_V(\varepsilon_V) = 1 \end{cases} \tag{6}$$

We have shown above that even for a high confinement, damage can develop. The influence of the damage could be set on the deviatoric and the tangential components of the microplane model. However, it is not clear how the latter could be adjusted using only $\boldsymbol{\varepsilon}_T$. One can find in the literature some models with d_T weighted by a function of the normal strain ($\varepsilon_N = \varepsilon_V + \varepsilon_D$). These models require the definition of a "stored energy" readjusted at the crack closure [11,25,27] to avoid discontinuous stress–strain responses. Here, choice has been made to relate α_D only to its associated strain component, leaving d_T unaffected. The consequences of these assumptions are discussed below. A hyperbolic tangent function could have replaced the Heaviside one to regularize the effectiveness. To highlight the effectiveness effect, the latter is used. The following relations yield the stress components:

$$\begin{aligned} \sigma_V &= \kappa_V(1 - \alpha_V(\varepsilon_V)d_V)\varepsilon_V - \frac{1}{2}\frac{\partial \alpha_V(\varepsilon_V)}{\partial \varepsilon_V} d_V \kappa_V \varepsilon_V^2 \\ \sigma_D &= \mu_D(1 - \alpha_D(\varepsilon_D)d_D)\varepsilon_D - \frac{1}{2}\frac{\partial \alpha_D(\varepsilon_D)}{\partial \varepsilon_D} d_D \kappa_D \varepsilon_D^2 \\ \boldsymbol{\sigma}_T &= \mu_T(1 - d_T)\boldsymbol{\varepsilon}_T \end{aligned} \tag{7}$$

and the forces associated to each damage variable:

$$\begin{aligned} F_V &= -\frac{\partial \rho_0 \psi^n}{\partial d_V} = \frac{1}{2}\kappa_V \alpha_V(\varepsilon_V)\varepsilon_V^2 \\ F_D &= -\frac{\partial \rho_0 \psi^n}{\partial d_D} = \frac{1}{2}\mu_D \alpha_D(\varepsilon_D)\varepsilon_D^2 \\ F_T &= -\frac{\partial \rho_0 \psi^n}{\partial d_T} = \frac{1}{2}\mu_T \boldsymbol{\varepsilon}_T.\boldsymbol{\varepsilon}_T \end{aligned} \tag{8}$$

In the simulations below, the whole solid angle has been meshed using 42 directions. Studies not detailed here have shown no dependencies of the response on the number of directions.

6. Calibration of the model

6.1. Initial damage and elastic modules

At the beginning of the compressive tests with or without a confinement of 10 MPa (respectively denoted by superscripts H10 and H0), modules at the microplane level can be analytically related to the global ones and to the pre-existing damages by the following equations:

$$k_V(1-d_V^0) = 3K_{\text{mod}}^{H0} \quad k_V = 3K_{\text{mod}}^{H10} \tag{9}$$

$$2\mu_D(1-d_D^0) + 3\mu_T(1-d_T^0) = 10\mu_{\text{mod}}^{H0} = 10\mu_{\text{mod}}^{H10}$$

For the H0 test, the initial volumetric damage is taken into account ($\alpha_V = 1$) when, for H10, the pressure cancels its influence ($\alpha_V = 0$). Fig. 3 enables determining the experimental elastic modules given in Table 1 and thus $k_V = 21.5$ GPa. The bulk damage value d_V^0 is discussed below.

The influence of the deviatoric damage d_D being related to the deviatoric strain ε_D, which is zero at the beginning of H0 and H10, the model imposes the same shear modulus on the microplane. Thus, the global shear modulus in the model μ_{mod} is not dependent on the confinement pressure when the experimental one μ_{exp} shows a difference (Table 1). This difficulty could have been solved using a dependence of α_D on ε_V but again it would have required a more sophisticated model to avoid a dissipative free energy. Thus, we will use a pressure-dependent damage evolution rule for the deviatoric damage d_D. The model will give a unique shear modulus at the beginning of the uniaxial part of the different tests, for any confining pressure.

Knowing the experimental bulk and shear modules for H10 and assuming $\mu_{\text{mod}}^{H0} = \mu_{\text{mod}}^{H10}$, the longitudinal and transversal modules (denoted with subscripts "L" and "T") of the stress-strain curves must satisfy the following inequalities:

$$E_{L_{mod}}^{H0} \leqslant E_{L_{mod}}^{H10} \quad \text{and} \quad E_{T_{mod}}^{H0} \leqslant E_{T_{mod}}^{H10} \tag{10}$$

It yields for the model $K_{\text{mod}}^{H0} \in [5740; 7220]$ MPa. To maximize the pressure dependence, we arbitrary have chosen $K_{\text{mod}}^{H0} = 5740$ MPa and $K_{\text{mod}}^{H10} = K_{\text{exp}}^{H10} = 7167$ MPa. It gives the initial bulk damage $d_V^0 = 1 - K_{\text{mod}}^{H0}/K_{\text{mod}}^{H10} = 0.2$ (another choice could have been $K_{\text{mod}}^{H0} = K_{\text{mod}}^{H10} = K_{\text{exp}}^{H10} = 7176$ MPa which would have given $d_V^0 = 0$).

The determination of the initial deviatoric and tangential damage d_D^0 and d_T^0 is also an open question. How could they be experimentally determined without shear experiment with and without confinement? Due to the lack of data, we assume at the microplane level (1) that $\mu_D = \mu_T$ and $d_D^0 = d_T^0$ and (2) that $d_D^0 = d_V^0/2$. The latter comes from a property of the VDT formulation. It can be demonstrated that, for a given direction, an increase of the contraction ratio is obtained if the inequality $d_V^0/d_D^0 \leq 2$ is satisfied. Thus, it results the following parameters:

$$d_V^0 = 0.2 \quad d_D^0 = d_T^0 = 0.1 \quad \mu_D = \mu_T = \frac{10\mu_{\text{exp}}^{H10}}{5\left(1-d_D^0\right)} = 3411 \text{ MPa} \tag{11}$$

6.2. Evolution of the damage

Another difficulty comes from the impossibility to access to the experimental effect of each orientated micro-cracks family on the global response of the material. Constitutive law must be assumed and calibrated comparing the numerical global behaviour to experiments. A dependence of the damage variables to their forces is assumed. As shown in Fig. 3, a pressure-dependence is also introduced, the following phenomenological relation being proposed:

$$d_i(F_i,p) = \max\left(d_i^0, 1-\exp\left[-p(a_3F_i)^{a_4}\right]\right)_t \quad \text{with} \quad 0 \leq d_i \leq 1 \tag{12}$$

$$p = 1 + \left[a_5.H(-\varepsilon_V) + a_5'.H(\varepsilon_V)\right]k_V\left\langle \varepsilon_V - \varepsilon_V^{0\_H10}\right\rangle_+$$

with the subscript i replacing the subscripts V, D or T and a_j four parameters. For the tangential damage law, the associated force is not divided. The pressure dependence is carried out through the function p where $\varepsilon_V^{0\_H10}$ is a third of the negative volumetric strain reached after a hydrostatic compaction at 10 MPa. As the pressure decreases, p increases accelerating the damage rate. The same laws and parameters are used whatever the damage components. The a_3 and a_4 parameters

Table 1
Elastic modules determined using experiments and Fig. 3.

	Young's modulus E_{exp} (MPa)	Poisson's ratio ν_{exp}	Bulk modulus K_{exp} (MPa)	Shear modulus μ_{exp} (MPa)
H0	2900	0.3	2416	1115
H10	4300	0.4	7167	1535

are determined by a fit on the H10 response. Then, a_5 is calibrated on the H0 one and a'_5 on the tensile test. These two last parameters illustrate a damage mechanism depending on the volumetric strain sign as has been observed during the tensile/compressive loading path (Figs. 6–8).

6.3. Stiffness recovery

In the literature, the closure of the micro-cracks during tensile/compressive experiments is related to the sign of the strain normal to the plane which is the sum of the volumetric and the deviatoric strains in our model. Here, the two components ε_v and ε_D have been separated and the effectiveness of the damage cannot be determined using a non associated strain component. Another Heaviside function is thus introduced for the deviatoric one ε_D. The influence of the damage d_D is complete at the micro-crack opening ($\alpha_D = 1$ for $\varepsilon_D \geqslant 0$) and partial ($\alpha_D = a_6$ for $\varepsilon_D < 0$) at the micro-crack closure. The a_6 parameter has been calibrated on the cyclic experiment. The parameters of model are listed in Table 2.

Let us ask two remarks. (1) The microplane constitutive laws being given, data cannot be used to explicitly calibrate the model which requires the use of the global response computed from the 42 microplanes. (2) This model imposes a sudden but partial stiffness recovery when the elastic volumetric and deviatoric strains vanish. But, the previously detailed tensile/compressive tests have shown a recovery of the modules at −2.5 MPa. Unfortunately, these curves do not tell us the magnitude of the elastic strain at that moment. Experimental data must be obtained just above and below this characteristic stress by the use of relaxation and recovery loadings to eliminate the viscous-dependence of the data and to measure the elastic unloading.

7. Numerical results for a single microplane

The volumetric and the confined or not deviatoric responses are plotted on Fig. 9 when a microplane is submitted to a positive strain then unloaded and submitted to a negative one. For the volumetric stress versus the volumetric strain, a non linear response due to the damage growth is observed (on Fig. 9, the volumetric strain has been multiplied by 5). After a linear unloading due to a constant damage, a recovery of the modulus is observed as α_V changes with the strain sign. Lastly, high negative volumetric stress results in a no damage growth.

For the deviatoric component, the same response is observed at the beginning of the tensile loading, whatever the confinement. The pressure-dependence of the damage law yields two non linear softening responses. The softener is associated to the unconfined condition and a rapid increase of the damage (no volumetric strain in p) when the other is for a volumetric strain equal to $\varepsilon_V^{0\_H10}$ in p. A partial recovery of the modulus is obtained after unloading, its amplitude being given by a_6. Lastly, damage growths again with the compressive load.

Table 2
Elastic modules, initial damages and parameters of the damage law.

k_V (MPa)	$\mu_D = \mu_T$ (MPa)	$d_V^0 = 2d_D^0 = 2d_T^0$	a_3 (MPa^{-1})	a_4	a_5 (MPa^{-1})	a'_5 (MPa^{-1})	$\varepsilon_V^{0\_H10}$	a_6
21,500	3411	0.2	12	0.66	0.25	1.5	$-4.65 \cdot 10^{-4}$	0.5

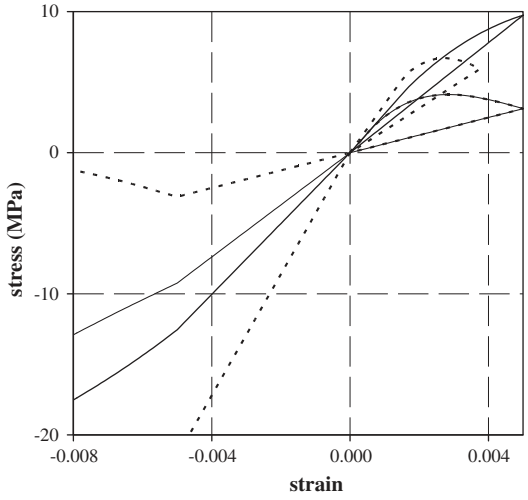

Fig. 9. Volumetric response (dashed line), unconfined deviatoric response (small line), confined (10 MPa) deviatoric response (bold line) and tangential (dot) response of a single microplane. The volumetric strain is multiplied by 5 to highlight the stiffness recovery.

A non linear response is also observed for the tangential constitutive law as d_T growths. During unloading, a constant modulus is observed till the maximum absolute strain value over time is reached again. As for the deviatoric behaviour, the pressure increases the stiffness of the microplane, decreasing the damage growth for a given strain (not plotted on Fig. 9).

8. Experiments versus simulations

Simulations have been made using the finite element code ABAQUS and a Fortran subroutine UMAT. To avoid any mesh-dependence due to the damage and the resulting softening behaviour, the loading paths have been applied to a unique C3D8 finite element. Fig. 10 shows a comparison between numerical results and data. A good agreement is obtained for the tensile test. If the longitudinal data of H10 have been used to calibrate the model, this figure shows that a good agreement is also obtained for the transversal ones and for the unconfined compressive test which also have been used to calibrate the damage rule. However, improvement is needed for the triaxial experiment made at a confinement of 5 MPa. The linear volumetric strain dependence introduced in p could be replaced by a non linear one to obtain a better fit.

The model over-estimates the maximum stress for all the loading conditions. More data are needed to improve the calibration as, for example, cyclic loading including relaxation and recovery stages realized as close as possible to the maximum stress.

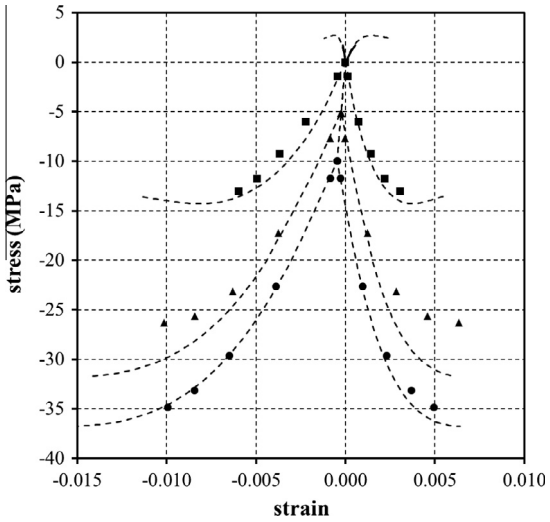

Fig. 10. Stress–strain computed curves for the tensile test, the compressive one and a compression with a confinement of 5 and 10 MPa. Same symbols as in Fig. 3 for experimental data.

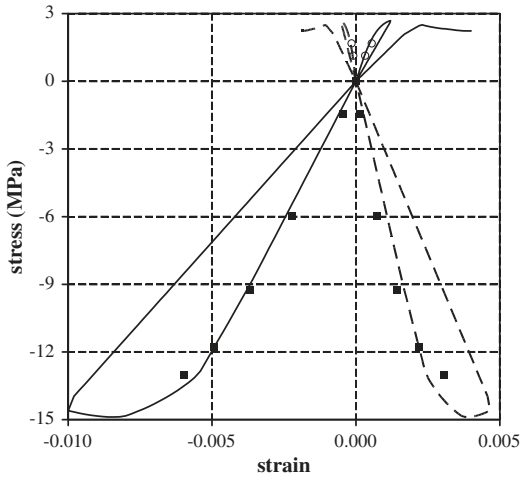

Fig. 11. Stress–strain computed curves for a tensile loading followed by an unloading, a compression and a traction. Experimental data (symbols) refers to Fig. 3 (tensile – white circle – or compressive – black square-loading up to failure) due to the absence of relaxation and recovery phases during the cyclic experiments.

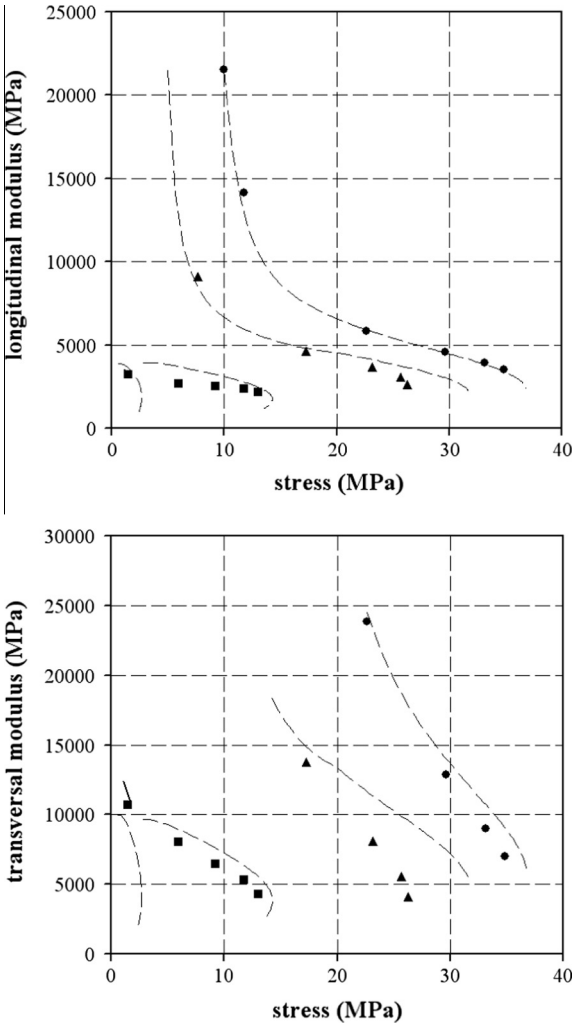

Fig. 12. Numerical evolution of the modulus (longitudinal and transversal) versus the stress. Experimental data (symbols) refers to Fig. 3: tensile – dark line, compressive – square, and triaxial experiment with a 5 MPa – triangle – or 10 MPa – circle – confinement. For the longitudinal modulus, the data for the tensile experiment are masked by the first compressive square.

The tensile/compressive/tensile loading has been simulated using the model. Dots reported on Fig. 11 have been deduced from Fig. 3 due to the lack of data allowing suppressing the viscous stress and the residual strain of the tensile/compressive data. Both the effect of the damage growth in tensile phase, the secant stiffness during unloading and a partial stiffness recovery in compressive loading should be pointed out. A quite good agreement is observed between the experimental and the numerical curves.

Fig. 12 shows quite well fitted longitudinal and transversal computed responses. The latter associated to the Poisson's ratio effect matches the experimental results. The model enables the increase of the Poisson's ratio due to damage, as observed during experiments. To the authors' knowledge, only the VDT split of the microplane models enables to adjust this evolution (see [28] for a comparison of some induced damage anisotropy constitutive laws).

9. Conclusion

During their operational life, pressed high explosives are submitted to heterogeneous and cyclic loadings. The modelling of their quasi-brittle behaviour must take into account the non linear and anisotropic elasticity due to damages driven by the loading directions. An experimental procedure has been proposed (1) to extract the elastic response of the material from stress/strain curves, (2) to characterize the influence of the pre-existing isotropic damage of the elastic modules depending on the confining pressure and (3) to quantify the anisotropic damage. A set-up has been proposed also to apply tensile/compressive loadings highlighting the stiffness loss or recovery.

Future experimental works are devoted to the development of a shear test with or without a confinement to determine the pressure-dependence of the initial shear modulus. The reverse edge-on compression test developed by some of the authors of this paper has given qualitative indications of the deformation mechanism and kinetic at the micro-scale level. Deducing quantitative data as the orientation of the damage remains hardly tractable. Post-mortem analyses are time consuming and destructive and the high solid fraction and thus the low contrast at that scale prevents the use of 3D X-ray microtomographs.

The microplane model previously proposed in the literature enables modelling the unilateral effect while satisfying the thermodynamical requirements. Cautions have been taken to model the effectiveness of the volumetric and the deviatoric damages using functions only related to their associated strain. As a consequence of this simplifying assumption, no pressure-dependence of the shear modulus has been described, this dependence being rejected into the damage evolution rule. The same rule is used for the three damage variables to reduce the number of parameter. The calibration procedure has been detailed. Despite some compromises, a quite agreement is obtained between data and the model.

Future works will improve the model considering a sliding mechanism on the tangential part of the microplane allowing a stiffness recovery at any stress level. The modelling of the inelastic response is another goal. Irreversible strains can be introduced at the microplane level or, more-widely used, by means of standard isotropic effective plasticity. Whatever the choice, the anisotropy effectiveness described in this paper will yield an anisotropic plasticity in the true stress space. Data will be necessary to make the choice.

Acknowledgement

Authors thank H. Trumel for the surface preparation of the sample shows on Fig. 1.

References

[1] Picart D, Damiani D, Doucet M. The reverse edge-on impact test: a small scale experiment for non-shock ignition studies. In: AIP conference proc shock comp condensed matter, vol. 1426(1); 2012. p. 497–500.
[2] Trumel H, Lambert P, Belmas R. Mesoscopic investigations of the deformation and initiation mechanisms of a HMX-based pressed composition. In: Proc fourteenth int. detonation symp. Coeur d'Alene (USA); 2010. p. 1096–105.
[3] Dienes J, Zuo Q, Kershner J. Impact initiation of explosives and propellants via statistical crack mechanics. J Mech Phys Solids 2006;54(6):1237–75.
[4] Tan H, Huang Y, Liu C, Ravichandran G, Paulino GH. Constitutive behaviors of composite with interface debonding: the extended Mori–Tanaka method for uniaxial tension. Int J Fract 2007;146:139–48.
[5] Pensee V, Kondo D. Une analyse micromécanique 3-D de l'endommagement par mésofissuration. CR Acad Sci Paris Série IIb 2001;329:271–6.
[6] Zhu Q, Shao J, Kondo D. A micromechanics-based non-local anisotropic model for unilateral damage in brittle materials. CR Méc 2008;336(3):320–8.
[7] Zhu Q, Kondo D, Shao J. Micromechanical analysis of coupling between anisotropic damage and friction in quasi-brittle materials: role of the homogenization scheme. Int J Solids Struct 2008;45(5):1385–405.
[8] Krajcinovic D, Fonseka GU. The continuous damage theory of brittle materials, part I and II. J Appl Mech 1981;48:809–24.
[9] Ladeveze P. Sur la théorie de l'endommagement anisotrope. Rapport interne n°34. Laboratoire de Mécanique et Technologie, Cachan; 1983.
[10] Chow CL, Wang J. An anisotropic theory of continuum damage mechanics for ductile fracture. Engng Fract Mech 1987;27(5):547–58.
[11] Chaboche JL, Maire JF. A new micromechanics based CDM model and its application to CMC's. Aerospace Sci Technol 2002;6(2):131–45.
[12] Murakami S, Kamiya K. Constitutive and damage evolution equations of elastic-brittle materials based on irreversible thermodynamics. Int J Mech Sci 1997;39(4):473–86.
[13] Halm D, Dragon A. An anisotropic model of damage and frictional sliding for brittle materials. Eur J Mech – A/Solids 1998;17(3):439–60.
[14] Chaboche JL. Damage induced anisotropy: on the difficulties associated with the active/passive unilateral condition. Int J Damage Mech 1992;1(2):148–71.
[15] Cormery F, Welemane H. A critical review of some damage models with unilateral effect. Mech Res Com 2002;29(5):391–5.
[16] Challamel N, Halm D, Dragon A. On the non-conservativeness of a class of anisotropic damage models with unilateral effects. CR Méc 2006;334(7):414–8.
[17] Carol I, Willam K. Spurious energy dissipation/generation in stiffness recovery models for elastic degradation and damage. Int J Solids Struct 1996;33(20–22):2939–57.
[18] Bazant ZP, Oh BH. Microplane model for progressive fracture of concrete and rock. J Engng Mech 1985;111(4):559–82.
[19] Leukart M, Ramm E. Identification and interpretation of microplane material laws. J Engng Mech 2006;132(3):295–305.
[20] Dautriat J. Comportement hydromécanique de roches réservoir sous contraintes. Relations entre évolution de la perméabilité et échelles des mécanismes d'endommagement. PhD thesis. Laboratoire de Mécanique des Solides, Ecole Polytechnique, Palaiseau (France); 2009 [in French].
[21] Pecqueur G. Etude expérimentale et modélisation du comportement d'une craie et d'un gré en torsion. PhD thesis. université de Lille 1 (France); 1995 [in French].
[22] Vial J, Picart D, Bailly P, Delvare F. Numerical and experimental study of the plasticity of HMX during a reverse edge-on impact test. Model Simul Mater Sci Engng 2013;21:045006.
[23] Le VD, Gratton M, Caliez M, Frachon A, Picart D. Experimental mechanical characterization of plastic-bonded explosives. J Mater Sci 2010;45:5802–13.
[24] Ramtani S. Contribution à la modélisation du comportement multiaxial de béton endommagé avec description du caractère uniaxial. PhD thesis. université Paris 6 (France); 1990 [in French].
[25] Maire JF, Chaboche JL. A new formulation of continuum damage mechanics (CDM) for composite materials. Aerospace Sci Technol 1997;1(4):247–57.
[26] Gagliardi FJ, Cunningham BJ. Creep testing plastic-bonded explosives in uni-axial compression. In: Proc of the XIth international congress and exposition, June 2–5, 2008. Orlando (Florida USA): Society for Experimental Mechanics In; 2008.
[27] Bargellini R, Halm D, Dragon A. Modelling of quasi-brittle behaviour: a discrete approach coupling anisotropic damage growth and frictional sliding. Euro J Mech A/Solids 2008;27(4):564–81.
[28] Benelfellah A, Frachon A, Gratton M, Caliez M, Picart D. Analytical and numerical comparison of discrete damage models with induced anisotropy. Engng Fract Mech 2014;121–122:28–39.

A des fins de prospection, un modèle complété par une partie plasticité a été proposé dans le cadre des travaux de A. Benelfellah. Afin de profiter des travaux déjà effectués, le modèle de plasticité est repris de la thèse de V. D. Le avec quelques aménagements. Par souci de simplification, l'endommagement est calculé avec la déformation élastique connue en début de pas de temps et la UMAT est écrite en contrainte effective, autorisant en découplage entre l'endommagement et la plasticité et une implantation de cette dernière en dehors des microplans. L'utilisation de la UMAT requiert donc de s'assurer d'avoir des incréments de déformations faibles entre deux instant successifs. Les comparaisons entre calculs et expériences permettent d'illustrer l'influence de certains paramètres sur la réponse globale, mais une optimisation finale des paramètres serait nécessaire pour ajuster notamment la reprise de raideur lors de la prise en compte de l'effet unilatéral.

En conclusion des travaux issus de la thèse de A. Benelfellah, il est clair que le principal verrou concerne la mesure directionnelle de l'endommagement (par des essais multiaxiaux ou par observation de densité et d'orientation de fissures) et de son effectivité via la pression de confinement, notamment sur le module de cisaillement. De plus, il est nécessaire de compléter le modèle par une partie modélisant la viscosité du matériau.

2.4.3 Modèle microplans avec viscoélasticité (M1)

Les premiers travaux entrepris dans la thèse de Marwen Chatti, suite à celle de A. Benelfellah, ont concerné le développement d'un modèle viscoélastique endommageable intégré au niveau des microplans. L'objectif était ici d'explorer la possibilité de modéliser le comportement du matériau M1 sans introduire de déformation permanente via un mécanisme de plasticité. En effet, des essais de relaxation réalisés au CEA sur des temps longs ont montré que la contrainte n'était pas encore stabilisée après 2 mois (Cf. Figure 12). L'existence même d'une contrainte stabilisée, interprétée dans notre modèle comme caractérisant l'état d'écrouissage, peut donc être remise en cause. Un mécanisme viscoélastique pourrait donc peut-être suffire à modéliser la non entière recouvrance des déformations.

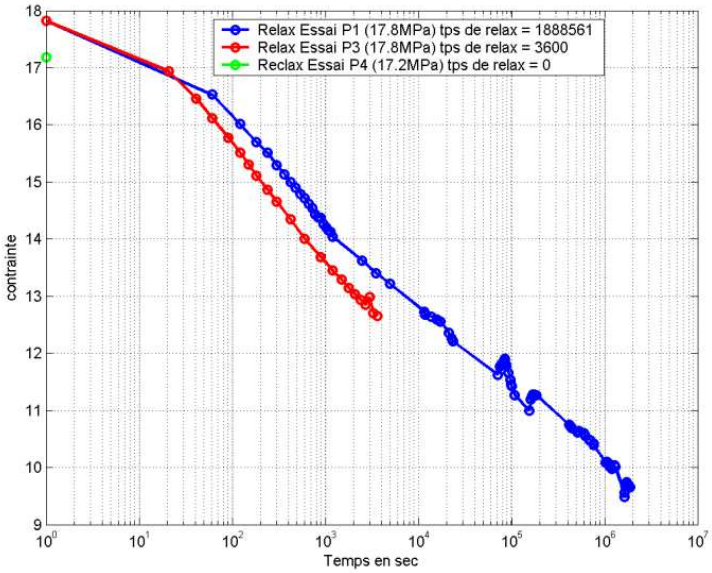

Figure 12 : Essais de relaxation temps longs [rapport AP10].

A ce stade, 2 choix sont possibles : intégrer la viscoélasticité au niveau des microplans après projection du tenseur de déformations (approche qualifiée d'« intérieure »), ou l'intégrer de manière non directionnelle

comme cela avait été fait pour la plasticité dans le cadre de la thèse de A. Benelfellah (approche qualifiée d'« extérieure »). Dans les 2 cas, un modèle de type Maxwell généralisé, basé sur les travaux menés précédemment est considéré.

Une approche « intérieur » a été adoptée car elle présente notamment l'avantage de gérer l'anisotropie via des scalaires alors que l'approche « extérieur » amène à gérer l'anisotropie via des tenseurs d'ordre 4 (on reste ici sur l'hypothèse que l'endommagement affecte tous les modules élastiques). Elle est aussi plus simple à programmer. Le respect de la relation entre module visqueux et module élastique de chaque branche au travers de leur temps de relaxation entraîne un choix. Nous avons préféré garder un module visqueux constant (ne dépendant pas de l'endommagement directionnel) ce qui entraîne une évolution directionnelle des temps de relaxation, dont nous n'avons pas formellement étudié les conséquences. Ces 1ers travaux sont retranscrits ci-après avec l'article référencé ACL6.

International Journal of Solids and Structures 168 (2019) 13–25

Contents lists available at ScienceDirect

International Journal of Solids and Structures

journal homepage: www.elsevier.com/locate/ijsolstr

Modelling of the viscoelastic behaviour with damage induced anisotropy of a plastic-bonded explosive based on the microplane approach

M. Chatti[a,*], A. Frachon[a], M. Gratton[a], M. Caliez[a], D. Picart[b], N. Aït Hocine[a]

[a] INSA CVL, University Tours, University Orléans, LaMé, 3 rue de la Chocolaterie, BP 3410, Blois Cedex 41034, France
[b] CEA DAM Le Ripault, Monts F-37260, France

ARTICLE INFO

Article history:
Received 26 March 2018
Revised 16 July 2018
Available online 21 August 2018

Keywords:
Plastic-bonded explosive
Microplane model
Damage induced anisotropy
Viscoelasticity

ABSTRACT

In this work, a mechanical constitutive law is proposed for a plastic-bonded explosive (PBX) which is a quasi-brittle energetic aggregate material, submitted to quasi-static loadings. Such material, sensitive to hydrostatic pressure, presents viscoelastic behaviour with damage induced anisotropy and irreversible strains. Previous models developed for this kind of material were mainly devoted for transient dynamic behaviour. The few existing quasi-static models considered the mechanical behaviour either isotropic or only elastoplastic. So, a new viscoelastic Microplane model with the damage induced anisotropy is proposed and implemented in commercial Finite Element software. The viscoelasticity was taken into account using a Maxwell generalized model with Microplane approach. The model consists in implementing the viscoelasticity inside the microplanes defining thus a Maxwell model on every direction. The sensitivity of the model to the strain increment magnitude and to the loading direction was analysed. As main conclusion, the experimental behaviour of the studied material was successfully predicted by this model.

1. Introduction

Pyrotechnic structures constituted of plastic-bonded explosives (PBX) are commonly used in applications under quasi-static loadings, like storage and transportation. These applications induce high stress levels due to mechanical and/or thermal loadings that affect the material behaviour, which requires improved and accurate constitutive laws to simulate this behaviour. Many models were developed in the last two decades for PBX materials, especially for dynamic and high-pressure loading conditions leading to ignition. The most popular is Visco–Scram (viscoelastic statistical crack mechanics) model (Bennett et al., 1998). This model is a combination of the fragmentation theory proposed by Dienes from the early 80′s (Dienes, 1996, 1982) (SCRAM) for brittle materials and viscoelastic Maxwell model (visco). The SCRAM approach consists of an isotropic model with the damage related to the mean crack radius, in which the growth rate is limited to a maximum value. An update was proposed afterward by Hackett & Bennett (Hackett and Bennett, 2000). They modified the crack growth law to consider the influence of the hydrostatic pressure on the damage and on the tensile and compressive responses. Recently, Xiao et al. (2017) described the dynamic mechanical behaviour of PBX1314 as a function of aspect ratio and inclusion concentration. They modelled the viscoelastic behaviour of the polymer binder using a generalized Maxwell model, with a Prony series representation for the stress relaxation functions. Another damage constitutive model with viscoelastic response and statistical fracture was developed by Xiao et al. (2017) to model low velocity impact experiment, for PBX. This model is based on SCRAM approach of Dienes et al. (2006) with a generalized Maxwell scheme. An isotropic constitutive relation is employed to describe the damage response of the material. For quasi-static loadings, Gratton et al. (2009) developed an isotropic model assuming the material as damageable elastic viscoplastic. Then, an additional isotropic model that account for damageable viscoelasticity and plasticity was proposed by Le et al. (2010) and Caliez et al. (2014). The viscoelasticity was modelled using a generalized Maxwell chain model. Recently, Benelfellah et al. (2014) and Picart et al. (2014) proposed an elastoplastic model with damage induced anisotropy, without considering the material viscosity. The authors illustrated the effect of the damage on engineering parameters and compared existing models based on the different aspects of the material behaviour. This investigation revealed that, among the constitutive laws proposed to model the anisotropic damage induced by the loading and satisfying the thermodynamic requirements, the Microplane approach, initially developed for

* Corresponding author.
E-mail address: marwen.chatti@insa-cvl.fr (M. Chatti).

https://doi.org/10.1016/j.ijsolstr.2018.08.018
0020-7683/

concrete by Bazant and Gambarova (1984), provides a powerful framework to implement complex laws. Particularly, the introduction of a unilateral effect is possible keeping a non-dissipative free energy, a continuous stress–strain response or a symmetrical stiffness tensor (Benelfellah et al., 2014). The Microplane-based models were successfully used to predict viscoelastic behaviour of uncracked concrete, creep, rate dependence of crack growth, aging creep and creep-cracking interaction (Di Luzio and Cedolin, 2007; Di Luzio, 2009; Ozbolt and Reinhardt, 2001; Ozbolt and Bazant, 1992; Hasegawa and Bazant, 1993; Bazant et al., 2000a). These models were developed following two approaches: "internal approach", where the viscoelasticity is integrated inside the microplanes (Zi and Bazant, 2002), and "external approach", where the viscoelasticity is defined in series with a damaged elastic Microplane model (Di Luzio and Cedolin, 2007; Di Luzio, 2009). In the present paper, a constitutive law for a quasi-brittle energetic material submitted to quasi-static loadings, is proposed. This constitutive law accounts simultaneously for the viscoelasticity and the anisotropic nature of the damage, based on the Microplane approach.

Numerical aspects of microplane models didn't have the same interest as constitutive laws. Previous studies show an influence of strain increment magnitude and loading direction on the simulation results. In addition, the integration formula (number and weight of the microplanes for the spatial partition) has an important impact on the predictions of the models and depending on the number and the distribution of the integration points used, the influence can be very distinct (Badel and Leblond, 2004; Ehret et al., 2010; Huang, et al., 2017; Levasseur et al., 2013; Nemecek et al., 2002; Verron, 2015; Qiu and Crouch, 1997). Thus, the sensitivity of the proposed model to the strain increment magnitude and to the loading direction is analysed using different integration formulas.

Numerical simulations achieved in this work are based on experimental data performed on a Plastic Bonded Explosive (PBX) and published in Le et al. (2010). This data includes monotonic and cyclic compression and tension, carried out at a strain rate of 3.3×10^{-5}/s, and monotonic compression, performed at strain rates of 8.3×10^{-4}/s and 4.4×10^{-6}/s. Experimental results showed a quasi-brittle nonlinear behaviour and a high dependency on the strain rate, hydrostatic pressure and temperature, which makes difficult the experimental investigation and modelling of the PBX behaviour.

2. Experimental investigation

The studied PBX material is made of more than 95% of energetic crystals (octahydro-1,3,5,7-tetranitro-1,3,5,7-tetrazocine, HMX) mixed with a low percentage of a polymer binder. The mixture is pressed using an isostatic compaction process that aims to eliminate the initial porosity of the powder. The final product was machined into solid samples of various shapes (Picart et al., 2014). Optical microscopy observations showed the high solid fraction of crystals whose size varies from a few tens of microns to a few hundred of microns, with an average size of 200 µm. The crystals have different forms and are randomly orientated in the material (Picart et al., 2014). On the pristine material, optical microscopy observations highlighted the presence of a lot of pre-existing intragranular microcracks and a lot of grain–grain surface contacts. However, after submitting the material to a low confinement, optical micrographs revealed loading induced intergranular and intragranular microcracks, and straight bands related to inelastic deformation of some grains (Picart et al., 2014; Le et al., 2010). PBX material presents a nonlinear behaviour, whatever the loading conditions, with asymmetry between tension and compression. A quasi-brittle behaviour is obtained during tensile tests while a more ductile one is observed during compression and triaxial tests. Due to the presence of polymer binder, the material presents strain rate and temperature dependencies (Le et al., 2010; Caliez et al., 2014). Also, a dependency of the material behaviour, particularly the initial elastic modulus, on the confinement pressure is observed. This could be related to the closure of a part of initial porosity and the evolution of contact conditions between crystals with increasing hydrostatic pressure, as suggested by Caliez et al. (2014) and Picart et al. (2014). Residual strains are registered after unloading and recovery and a hysteretic response are highlighted for cyclic loading. The observed broad loops and the decrease of the stress (respectively the strain) during the relaxation (respectively the recovery) conditions are attributed to viscoelastic behaviour of the material and probably internal friction (Picart et al., 2014). The observations above prove that the studied material behaves like a concrete, due to its quasi-compact aggregate microstructure. The main difference with concrete is the strong temperature and strain-rate dependencies. The literature contains some studies on the strain rate dependent behaviour of PBXs (Ellis et al., 2005; Chen et al., 2007; Liu et al., 2009; Williamson et al., 2008; Le et al., 2010). Viscoelastic behaviour of the material was characterized using DMA experiments allowing the determination of the storage and loss moduli (Le et al., 2010). Analysing the results of cyclic compression and cyclic confined compression at hydrostatic pressure levels of 5 MPa and 10 MPa, Le et al. (2010) suggested that the studied PBX displays linear viscoelastic behaviour. Using these tests, and comparing the viscous stress at two levels of isovalues of global stress, Le et al. (2010) concluded that the viscoelastic part does not depend on the pressure. In some recent models, the behaviour of PBX materials was considered as anisotropic. Using a dynamic compression test on a Hopkinson bar Trumel et al. (2010) showed the presence of a network of cracks that induces an anisotropic degradation of the mechanical properties of the material. Unfortunately, the anisotropic nature of the damage could not yet be directly observed. Evidence of anisotropic damage is highlighted by the degradation observed on the longitudinal modulus and the called "transversal elastic modulus". Picart et al. (2014) reported the results of tension and compression experiments where the "transversal stiffness" of the studied PBX evolves faster in compression than in tension, which is in accordance with the idea of an anisotropic damage that preferentially occurs in mode I. This has been proved also using the evolution of the contraction ratio defined as the ratio of the transversal elastic strain and the longitudinal elastic strain $-\varepsilon_T^e/\varepsilon_L^e$. It appeared that this ratio varies from 0.28 to 0.75 for the studied PBX (Le et al., 2010), while it should not exceed 0.5 in the isotropic framework. An explanation presented by Pecqueur (1995) after studying sandstone and then adopted by Dragon et al. (Bargellini, 2006) invokes damage induced anisotropy. If such anisotropic damage is macroscopically observed, its causes remain difficult to be identified. Nevertheless, this phenomenon was explained as the consequence of oriented microcracking process (Picart et al., 2014). Previous works by Benelfellah et al. (2014) and by Picart et al. (2014) also highlighted the damage effectivity of the PBX. In fact, tensile loading and compressive loading applied in the direction perpendicular to a "micro-crack" surface lead, respectively, to opening and closing of such a crack, which allows the recovery of the stiffness in the compression case.

3. Constitutive laws

In what follows, the Microplane approach and the damage evolution laws are presented. Then, the procedures and schemes used to model the viscoelasticity with the anisotropic damage are detailed. Finally, the identification procedure of the model material parameters is described.

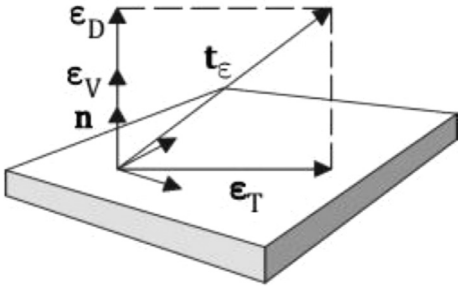

Fig. 1. VDT decomposition in Microplane directions (Kuhl et al., 2001).

3.1. Microplane approach and damage evolution law

As mentioned above, the material presents an evolving damage with induced anisotropy. Some procedures have been developed in the literature to model such damage (Maire and Chaboche, 1997; Zhu et al., 2008; Bargellini et al., 2008; Murakami and Kamiya, 1997). However, despite continuous improvements of these procedures, inconsistencies remained in the used methods (Challamel et al., 2006; Cormery and Welemane, 2002; Carol and Willam, 1996). The background of the Microplane approach can be traced back to Taylor (1938). The basic idea is that the stress-strain relations can be defined independently on various planes in the material. It was applied first to model the plasticity (Batdorf and Budiansky, 1949). The Microplane approach was proposed by Bazant and Gambarova (1984) to simulate concrete material behaviour. This approach states that each direction of the solid angle characterizes a microplane on which the strain is decomposed (Fig. 1). It should be noted that Microplane approach is not a micro-macro homogenisation model but rather a spatial partition. Constitutive equations are defined in the microplane level where the existence of free energy is assumed. The global stress tensor is determined by angular integration of the microplane stress vector over the whole solid angle. The global free energy ψ^{glo} is equal to the angular integral over the entire solid angle Ω of the angular free energy density, expressed as $\psi^i/4\pi$ and associated to each plane defined by its normal vector $\underline{n}^i$:

$$\psi^{glo} = \frac{3}{4\pi}\int_{\Omega}\psi^i(\underline{t}_\varepsilon, q)d\Omega, \tag{1}$$

where the subscript i denotes the microplane orientation, $\underline{t}_\varepsilon = \underline{\underline{\varepsilon}}.\underline{n}^i$ represents a deformation vector and q is a set of state variables.

The global stress tensor $\underline{\underline{\sigma}}$ is defined by the partial derivative of the free energy ψ^{glo} with respect to the strain tensor $\underline{\underline{\varepsilon}}$:

$$\underline{\underline{\sigma}} = \frac{\partial\rho_0\psi^{glo}}{\partial\underline{\underline{\varepsilon}}} = \frac{3}{4\pi}\int_{\Omega}\frac{\partial\rho_0\psi^i(\underline{t}_\varepsilon, q)}{\partial\underline{\underline{\varepsilon}}}d\Omega$$

It should be noted that variables underlined with one line are vectors, those underlined with two lines are twice rank tensors and those underlined with four lines are fourth rank tensors. Many different Microplane formulations exist in the literature, based on the strain decomposition (Normal-shear, volumetric-deviatoric, etc). Carol et al. (2001) proposed a thermodynamically consistent Microplane model with a Volumetric–Deviatoric–Tangential (V-D-T) split i.e. with a decomposition of the strain tensor to volumetric, deviatoric and tangential components respectively noted ε_V, ε_D and $\underline{\varepsilon}_T$ and expressed as follows in each microplane:

$$\varepsilon_V = \frac{1}{3}\underline{\underline{1}} : \underline{\underline{\varepsilon}} = \underline{\underline{V}} : \underline{\underline{\varepsilon}} \tag{2}$$

$$\varepsilon_D = \left(\underline{n}\otimes\underline{n} - \frac{1}{3}\underline{\underline{1}}\right) : \underline{\underline{\varepsilon}} = \underline{\underline{D}} : \underline{\underline{\varepsilon}} \tag{3}$$

$$\underline{\varepsilon}_T = \left(\underline{n}\cdot\underline{\underline{I}} - \underline{n}\otimes\underline{n}\otimes\underline{n}\right) : \underline{\underline{\varepsilon}} = \underline{\underline{T}} : \underline{\underline{\varepsilon}} \tag{4}$$

Eqs. (2), (3) and (4) define the projection of the global strain tensor on a microplane. It should be noted that ε_V is isotropic in the material. These strains allow the determination of stresses in a microplane with the following state laws:

$$\sigma_V = \frac{\partial\rho_0\psi^i(\underline{t}_\varepsilon, q)}{\partial\varepsilon_V} \tag{5}$$

$$\sigma_D = \frac{\partial\rho_0\psi^i(\underline{t}_\varepsilon, q)}{\partial\varepsilon_D} \tag{6}$$

$$\underline{\sigma}_T = \frac{\partial\rho_0\psi^i(\underline{t}_\varepsilon, q)}{\partial\underline{\varepsilon}_T} \tag{7}$$

The global stress tensor is then evaluated from the stresses defined in microplanes by an integral over the solid angle Ω, using the following equation:

$$\underline{\underline{\sigma}} = \frac{3}{4\pi}\int_{\Omega}\left\{\sigma_V.\underline{\underline{V}} + \sigma_D.\underline{\underline{D}} + \underline{\sigma}_T.\underline{\underline{T}}\right\} \tag{8}$$

We should note that the operators used to get the global stress are the same used during the decomposition of the strain into the microplanes.

When the Microplane approach is used to model only damageable elasticity, a global potential can be expressed by integration by taking into account a damaged elastic global anisotropic operator. Microplane approach can be used in this case only to define this operator without introducing all the variables at the level of microplanes. To model the induced anisotropic damage of the material, the free energy is defined as follows (Picart et al., 2014):

$$\psi^i = \frac{1}{2}E_V(1-\alpha_V(\varepsilon_V)d_V)\varepsilon_V^2 + \frac{1}{2}E_D(1-\alpha_D(\varepsilon_D)d_D)\varepsilon_D^2 + \frac{1}{2}E_T(1-d_T)\underline{\varepsilon}_T.\underline{\varepsilon}_T \tag{9}$$

In this equation, three damage variables d_V, d_D and d_T, that affect the corresponding elastic moduli denoted, respectively, E_V, E_D and E_T, are introduced. These moduli are related to the bulk and shear global parameters K and μ as follows: $E_V = 3K$ and $2E_D + 3E_T = 10\,\mu$ Carol et al., 2001). The damage is calculated at the level of microplanes. d_V is the same for all microplanes since ε_V is isotropic. d_D and d_T are calculated individually for each microplane, based on ε_D and $\underline{\varepsilon}_T$ (Eqs. (2), ((3) and (4)). α_V *and* α_D are the effectivity functions defined, respectively, in terms of volumetric strain and deviatoric strain for each microplane. These effectivity functions manage the opening/closure of microcracks, asymmetry of the behaviour between tension and compression and the effect of hydrostatic pressure. It has been assumed that d_T is not affected by the effectivity. To avoid a spurious dissipation and discontinuity in the model responses and to obtain simple constitutive laws, α_V and α_D depend on their associated strain components. In the proposed model the damage depends on the total strain. The assumed relationships between damage variables and their associated forces F_V, F_D and F_T are given in terms of ε_V, ε_D and $\underline{\varepsilon}_T$ respectively for each microplane:

$$F_V = -\frac{\partial\rho_0\psi^i}{\partial d_V} = \frac{1}{2}E_V\alpha_V(\varepsilon_V)\varepsilon_V^2 \tag{10}$$

$$F_D = -\frac{\partial\rho_0\psi^i}{\partial d_D} = \frac{1}{2}E_D\alpha_D(\varepsilon_D)\varepsilon_D^2 \tag{11}$$

$$F_T = -\frac{\partial\rho_0\psi^i}{\partial d_T} = \frac{1}{2}E_T\underline{\varepsilon}_T.\underline{\varepsilon}_T \tag{12}$$

Taking into account the effect of the pressure on the damage evolution and the dependency of this damage on strain, the following phenomenological relations have been proposed by Picart et al. (2014) in a microplane:

$$d_{V,D,T}(F_{V,D,T}, p) = \max\left(d^0_{V,D,T}, 1 - \exp\left[-p(a_1 F_{V,D,T})^{a_2}\right]\right)_t, \quad 0 \le d_{V,D,T} \le 1 \tag{13}$$

where:

$$p = 1 + [a_3.H(-\varepsilon_V) + a_4.H(\varepsilon_V)]E_V\left\langle \varepsilon_V - \varepsilon_V^{0-H10}\right\rangle_+ \tag{14}$$

The effectivity functions are defined as follows:

$$\begin{cases} \varepsilon_V \ge 0 \rightarrow \alpha_V(\varepsilon_V) = 1 \\ \varepsilon_V < 0 \rightarrow \alpha_V(\varepsilon_V) = 0 \\ \varepsilon_D \ge 0 \rightarrow \alpha_D(\varepsilon_D) = 1 \\ \varepsilon_D < 0 \rightarrow \alpha_D(\varepsilon_D) = 0.5 \end{cases}$$

In the previous equations, a_j are four material parameters. a_1 and a_2 manage the evolution of the damage versus the strain, and a_3 and a_4 manage the dependency of the damage on the pressure. The pressure dependency is carried out through the function p given by Eq. (14), where ε_V^{0-H10} is a third of the negative volumetric strain reached after hydrostatic compaction of 10 MPa. In this model (Picart et al., 2014), the four material parameters a_j are the same for d_V, d_D and d_T. Nevertheless, the evolution law offers the possibility to use different values of a_1 and a_2 for d_V, d_D and d_T. The main limit of the models based on an additivity of oriented damages comes from the impossibility to experimentally identify the effect of each oriented microcracks group on the global mechanical response of the material. Thus, the parameters related to the damage evolution should be calibrated by comparing the numerical predictions of the material global behaviour to the test data.

3.2. Viscoelastic microplane model

Many viscoelastic models exist in the literature. One of the commonly used models is based on the nonlinear viscoelastic model of Schapery identified for solid propellants which that have many similarities to PBX materials (Ha and Schapery, 1998). Belmas et al. (1982) have modelled both linear and non-linear viscoelasticity of an explosive material composed of 90% wt of crystals. Linear viscoelasticity is generally defined in the low strain range while nonlinear viscoelasticity is defined in the large one. Based on the studies of Le et al. (2010), Caliez et al. (2014) and Belmas et al. (1982), the linear viscoelasticity would be convenient for the material studied in the present work. The generalized Maxwell model corresponds to a Prony series development for the relaxed moduli. It is considered as a sum of contributions or elements, each one consisting of a spring and a dashpot in series. In this context, the Maxwell chain is more effective than the Kelvin chain (Zi and Bazant, 2002). As mentioned above, two approaches exist to take into account such a kind of viscoelasticity with a Microplane model: external and internal approaches.

The external approach consists on defining in series the Maxwell model with a damaged elastic Microplane model. The damage is calculated with the Microplane model, whereas the elastic strains and stresses are obtained for viscoelastic elements and elastic element from the Maxwell chain model defined with the Microplane model. The Microplane model is used to generate the 11 damaged elastic operators. No other state variables but damage variables are introduced in the microplanes. The Microplane model yields a fourth rank damaged stiffness tensor $\underline{\underline{\underline{\underline{C}}}}^d$ calculated using elastic and viscoelastic moduli that affect all the mechanisms in the Maxwell model. Each mechanism contributing to the global behaviour is defined by an elastic strain tensor and its corresponding stress tensor. In this approach, elastic strains in the elements of the Maxwell model are not projected on the microplanes and, so, they do not depend on Microplane directions.

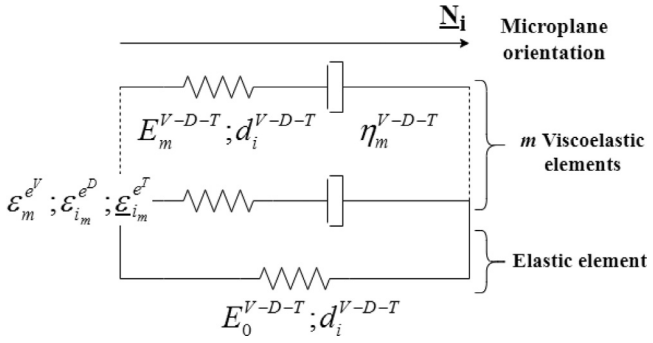

Fig. 2. Internal approach scheme.

The internal approach states that a viscoelastic law is integrated inside the microplanes, i.e each microplane contains a Maxwell chain model. The viscoelastic model is integrated in each microplane, following V-D-T decomposition, i.e a Maxwell chain model is defined along every direction, containing 10 viscoelastic elements and one elastic element. Defining the behaviour inside the microplanes requires the determination of the elastic strain and the elastic stress for every microplane direction and every element. By analogy with asphalt materials (Saadeh, 2005), the anisotropy of stiffness matrix due to damage is supposed to imply the anisotropy of relaxation times, while viscous moduli are considered to be constant through the time and through the solid angle. Only one set of damage variables (d_V, d_D and d_T) is introduced for the whole multi branch model (for the elastic and the viscoelastic parts). The damage evolution laws of d_V, d_D and d_T, in the viscoelastic model are non-associated: the damage depends only on the contribution of the associated force within the purely elastic element (total strain projected on the microplanes with VDT decomposition and properties of the elastic element) and not on the contributions of viscoelastic elements. The damage evolution laws are expressed in the same manner as Eq. (13) for each microplane, but in which $F_{V,D,T}$ don't represent the associated forces to the damage variables. This calculated damage affects all the modules of all the branches in the same manner.

Due to its simplicity and various capabilities, the internal approach is used in the present work. The viscoelasticity will be integrated using an implicit forward scheme. A scheme of the used approach is shown in Fig. 2.

The Maxwell chain model used for the viscoelasticity yields the following equations (stress additivity, element equilibrium and behaviour):

$$\underline{\underline{\sigma}}^{tot} = \sum_m \underline{\underline{\sigma}}_m \tag{15}$$

For each viscoelastic element m, the strain is decomposed into elastic strain $\underline{\underline{\varepsilon}}^e_m$ and viscous strain $\underline{\underline{\varepsilon}}^v_m$, as follows:

$$\underline{\underline{\varepsilon}} = \underline{\underline{\varepsilon}}^e_m + \underline{\underline{\varepsilon}}^v_m \tag{16}$$

The stress continuity imposes:

$$\underline{\underline{\sigma}}_m = \underline{\underline{\sigma}}^e_m = \underline{\underline{\sigma}}^v_m \tag{17}$$

The behaviour inside the elements is described by:
$\underline{\underline{\sigma}}^e_m = \underline{\underline{\underline{\underline{C}}}}^d_m : \underline{\underline{\varepsilon}}^e_m$ and $\underline{\underline{\sigma}}^v_m = \eta_m : \dot{\underline{\underline{\varepsilon}}}^v_m$ for the elasticity and viscosity respectively.

Using the previous equations, the following development was made for every element m:

$$\underline{\underline{\varepsilon}}_{n+1} = \underline{\underline{\varepsilon}}_{n} + \Delta\underline{\underline{\varepsilon}}$$

From (Eq. (16)), we can write:

$$\underline{\underline{\varepsilon}}_{n+1} = \underline{\underline{\varepsilon}}^{e}_{n+1} + \underline{\underline{\varepsilon}}^{v}_{n+1} = \underline{\underline{\varepsilon}}^{e}_{n} + \Delta\underline{\underline{\varepsilon}}^{e} + \underline{\underline{\varepsilon}}^{v}_{n} + \Delta\underline{\underline{\varepsilon}}^{v}$$
$$\Rightarrow \Delta\underline{\underline{\varepsilon}}^{v} = \underline{\underline{\varepsilon}}_{n} + \Delta\underline{\underline{\varepsilon}} - \left(\underline{\underline{\varepsilon}}^{e}_{n} + \Delta\underline{\underline{\varepsilon}}^{e}\right) - \underline{\underline{\varepsilon}}^{v}_{n}$$

Also, we obtain from (Eq. (17)):

$$\begin{aligned} &\underline{\underline{\sigma}}_{n+1} = \eta\frac{\Delta\underline{\underline{\varepsilon}}^{v}}{\Delta t} = \frac{\eta}{\Delta t}\left(\underline{\underline{\varepsilon}}_{n} + \Delta\underline{\underline{\varepsilon}} - \underline{\underline{\varepsilon}}^{e}_{n+1} - \underline{\underline{\varepsilon}}^{v}_{n}\right) = \underline{\underline{\underline{\underline{C}}}}^{d}_{n+1} : \underline{\underline{\varepsilon}}^{e}_{n+1} \\ &\Rightarrow \underline{\underline{\varepsilon}}^{e}_{n+1} = \left(\underline{\underline{\underline{\underline{C}}}}^{d}_{n+1} + \frac{\eta}{\Delta t}\underline{\underline{\underline{\underline{I}}}}\right)^{-1} \times \frac{\eta}{\Delta t}\left(\underline{\underline{\varepsilon}}^{e}_{n} + \Delta\underline{\underline{\varepsilon}}\right) \end{aligned} \tag{18}$$

where n and $n+1$ denote respectively the beginning and the end of an increment. To integrate the viscoelasticity inside the microplanes, as stated by the internal approach, the expression of the elastic strain in each viscoelastic element (Eq. (18)) is projected on the microplanes i following V-D-T decomposition:

$$\varepsilon^{e^{Volumetric}}_{m_{n+1}} = \left(\frac{\eta^{Volumetric}_{m}}{\Delta t \times E^{Volumetric}_{m} \times \left(1 - \alpha^{Volumetric} \times d^{Volumetric}\right) + \eta^{Volumetric}_{m}}\right) \times \left(\varepsilon^{e^{Volumetric}}_{m_n} + \Delta\varepsilon^{Volumetric}\right), \tag{19}$$

$$\varepsilon^{e^{Deviatoric}}_{i_{m_{n+1}}} = \left(\frac{\eta^{Deviatoric}_{m}}{\Delta t \times E^{Deviatroic}_{m} \times \left(1 - \alpha^{Deviatoric}_{i} \times d^{Deviatoric}_{i}\right) + \eta^{Deviatoric}_{m}}\right) \times \left(\varepsilon^{e^{Deviatoric}}_{i_{m_{n+1}}} + \Delta\varepsilon^{Deviatoric}_{i}\right), \tag{20}$$

$$\underline{\varepsilon}^{e^{Tangential}}_{i_{m_{n+1}}} = \left(\frac{\eta^{Tangential}_{m}}{\Delta t \times E^{Deviatroic}_{m} \times \left(1 - \alpha^{Tangential}_{i} \times d^{Tangential}_{i}\right) + \eta^{Tangential}_{m}}\right) \times \left(\underline{\varepsilon}^{e^{Tangential}}_{i_{m_{n+1}}} + \underline{\Delta\varepsilon}^{Tangential}_{i}\right), \tag{21}$$

with η denoting the viscosity and $\eta^{Deviatoric}_{m} = \eta^{Tangential}_{m} \neq \eta^{Volumetric}_{m}$.

The Microplane model is very computationally demanding, mainly because it deals with all microstress components. In the literature, some authors presented a comprehensive study on the numerical aspects of a class of microplane constitutive models for concrete with emphasis on the most popular one, i.e., the model M4 (Bazant et al., 2000b; Caner and Bazant, 2000).

It was observed that the Microplane model leads to numerical results that are sensitive to the strain increment magnitude (Huang, et al., 2017; Nemecek et al., 2002), which can cause an excessive lateral expansion on the macroscale level instead of contraction in the evaluated uniaxial tension tests (Nemecek et al., 2002). The algorithm gives different responses for small and large strain increments especially in the softening branches of macroscopic stress–strain curves.

Many studies (Qiu and Crouch, 1997; Nemecek et al., 2002; Badel and Leblond, 2004; Ehret et al., 2010; Levasseur et al., 2013; Verron, 2015) examined also the effect of the integration formula, number and distribution of the integration points on the unit sphere, on the performance of different Microplane models. It was found that the integration formula has an important impact on the predictions of the models and this effect depends on the number and the distribution of the integration points. The integration scheme usually adopted is a Gaussian integration with 21 or 28 points, developed by Bazant and Oh (1986).

Di Luzio (2007) and Huang et al. (2017) reported that the numerical predictions of the Microplane model M4 depend on the loading directions when rotating the axes defining the position of the microplanes on the unit sphere. With a uniaxial compression test, in which displacements were applied in three orthogonal directions respectively, Di Luzio (2007) obtained different stress-strain curves. Huang et al. re-examined the influence of the loading direction on the response of the model using a more general approach, in which the axes (x, y, z) defining the position of the microplanes on the unit sphere are subjected to rotation while the loading direction remains constant. The following 21, 28, 37 and 61-points integration formulas and 4 different orientations were considered. For each considered integration formula, different loading directions lead to different stress-strain curves (Huang, et al., 2017). The dependence of the model responses on the loading direction mainly results from the directional behaviour of the used integration formula induced by the uneven distribution of the microplanes over the unit sphere (Huang, et al., 2017). This numerical sensitivity of the Microplane models can affect their ability to reflect the isotropy or anisotropy of the considered constitutive equation and its ability to integrate non-smooth functions (Badel and Leblond, 2004; Verron, 2015; Ehret et al., 2010). With the increase of the number of the integration point, the difference with the predicted stress–strain curves generally decreases. Among the most classical integration formulas, the 61-point one is recommended to be used in numerical simulations. Some authors suggested that the best strategy to numerically integrate functions of one variable exhibiting quick variations is not to use high-order Gaussian integration, but simply to subdivide the integration interval into many sub-intervals and use low-order Gaussian integration over each of them. Transposed to integration over some surface, this strategy consists in meshing this surface (Badel and Leblond, 2004; Levasseur et al., 2013). Unfortunately, the price to pay for is an increase of the number of integration points (120 points seem necessary to converge well in the proposed problem), imposing an increase of the number of state variables that need to be stored and updated at each loading step.

In this study, in one hand, the influence of the strain increment on the predictions from our model is examined in uniaxial compression using finite element simulations on a cube. Four step increment values are used: 10, 1, 0.1 and 0.01. In the other hand, to evaluate the influence of the loading direction, uniaxial compression simulations were run with 26 different orientations over the ¼ of the hemisphere. The 26 different orientations of solicitation are extracted from a sphere surface meshed with 162 directions (same weight), keeping only those contained in ¼ of the hemisphere. The simulated cube is rotated with the loading direction while the axes (x, y, z) remain constant. The cube is rotated by an angle α along the axis y, followed by a second rotation by an angle β along the new axis z. For the loading direction sensitivity, three different integration formulas were considered from the literature (Bazant and Oh, 1986; Badel and Leblond, 2004). The details and the results are presented and analysed in Section 5.

3.3. Parameters identification

The viscoelastic parameters could be identified with the previously fixed damage parameters. These damage parameters were identified by fitting the curve "extended experimental relaxed points" with elastic damaged Microplane model predictions (Figs. 3 and 4). Extended experimental relaxed points were obtained by

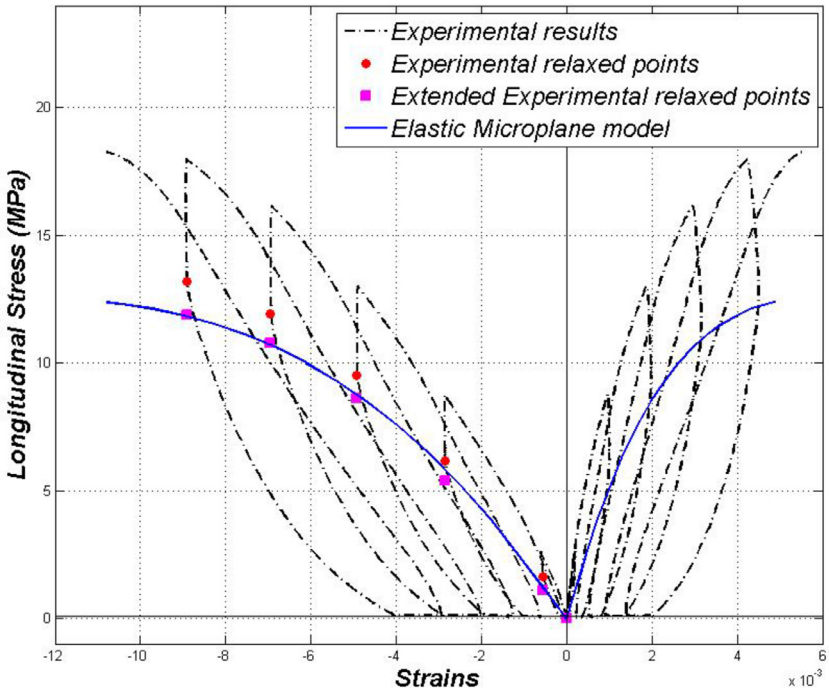

Fig. 3. Calibrating damage parameters based on extended experimental relaxed points of cyclic compression.

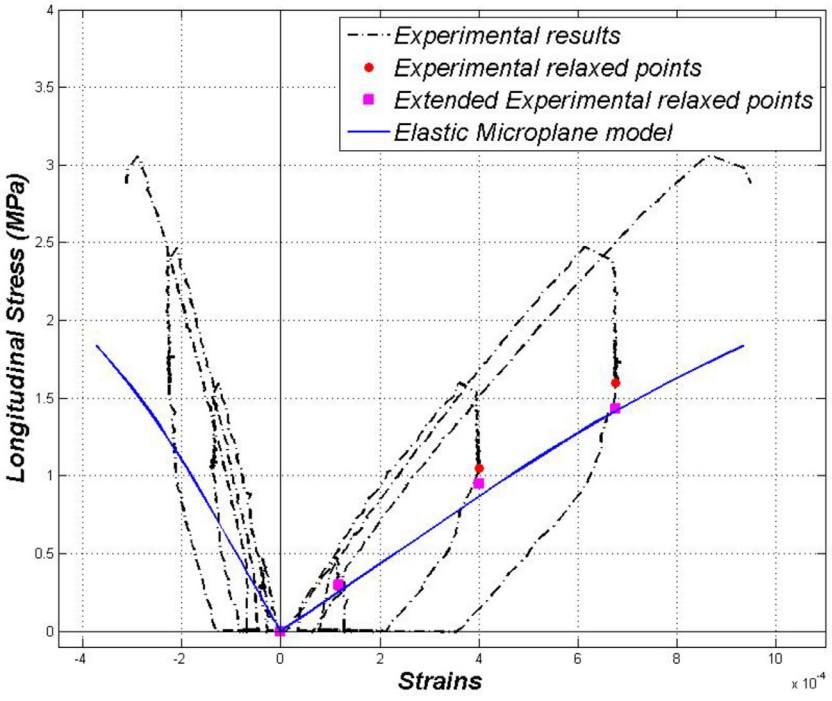

Fig. 4. Calibrating damage parameters based on extended experimental relaxed points of cyclic tension.

eliminating temporal contributions, so the resulted points are supposed to represent an elastic damaged behaviour. The initial viscoelastic modules were obtained from (Le, et al. 2010) and then were iteratively adjusted to fit the relaxation steps, in tension and compression (Figs. 7 and 8). To simplify the parameters identification process, values already used in Picart et al. (2014), Le et al. (2010) and Caliez et al. (2014) were considered in the beginning. The initial experimental elastic modulus and viscous moduli of the material were identified from DMA tests, at 20 °C (Le et al., 2010). This initial elastic modulus was adjusted, based on the comparison between simulation results obtained using the damaged elastic Microplane model and the reconstructed experimental stress-strain (σ-ε) curves obtained by extending the relaxation steps. In fact, to insure a complete stress relaxation, the time step was extended from 1800 s, for cyclic compression, and from 3000 s, for cyclic tension, to 10^4 s. Figs. 3 and 4 show the original

Table 1
Damage parameters used in the model.

$a_1^{V,D}$	a_1^T	a_2	a_3	a_4	ε_V^{0-H10}
6	7.8	0.5	0.3	1.5	-8.309×10^{-4}

relaxed points and the extended relaxed points for compression and tension tests performed at a strain rate of 3.3×10^{-5}/s. The elastic modulus was adjusted to better fit both tension and compression experimental data. The obtained value is E = 2400 MPa. Experimentally, initial Poisson's ratio ranges between 0.25 and 0.4 for tension and compression tests (Le et al., 2010; Caliez et al., 2014). A value of 0.4 was considered for this model. Damage parameters were also adjusted to capture experimental extended relaxed points with the damaged elastic Microplane model. The obtained values are given in Table 1.

After calibrating initial elastic modulus and damage parameters with the damaged elastic Microplane model, viscous moduli initially obtained from DMA tests (Le et al., 2010) are adjusted regarding the best fit between predictions for cyclic compression and tension obtained with the developed viscoelastic Microplane model and experimental results, in terms of longitudinal stress in relaxation steps. Relaxation times are kept identical as in (Le et al., 2010) without adjustment. It is to be noted that the first four viscous moduli do not significantly affect the simulations results for the strain rates considered in this paper. The viscous moduli and the relaxation times used in our model are reported in Table 2. Relaxation times were defined to guarantee an almost complete relaxation of the stress from quasi-static to slow dynamic solicitations (Le et al., 2010).

4. Validation of the viscoelastic microplane model

The viscoelastic behaviour was taken into account in the Microplane approach and the resulting model was successfully implemented in the commercial finite element software "Abaqus", using Umats and following the internal approach described above. The standard 21 symmetric directions on a hemisphere, proposed by Bazant and Oh (1986), were used to define the directions of microplanes. A 3-dimensional, 8 nodes element with a reduced integration (element C3D8R) was considered. The model is simple and fast to be implemented, since variables are projected on the microplanes and, so, only scalar variables or vectors are managed. However, it requires many state variables to be saved (~900 SDV in this study), which makes the simulation times consuming. Cyclic σ-ε curves are reported in Figs. 5 and 6, globally showing a good agreement between experimental results and numerical simulations, in both longitudinal and transversal directions. However, the proposed model still lacks accuracy when simulating unloading paths and strain evolution in recovery steps, in compression loadings, even if the experimental tendencies are well predicted.

Figs. 7 and 8 show experimental and numerical longitudinal stress evolutions, in relaxation steps, respectively, in cyclic compression and cyclic tension. The numerical predictions are globally consistent with experimental data with a better fit being obtained in compression. This is probably due to the fact that the compres-

Table 2
Viscous parameters used in the model.

Element m	1	2	3	4	5	6	7	8	9	10
τ_m *(sec)*	5×10^{-4}	29×10^{-4}	168×10^{-4}	0.098	0.567	3.28	19.05	110.5	640.7	3715
E_m *(MPa)*	546	336	240	348	60	40	692	752	392	588

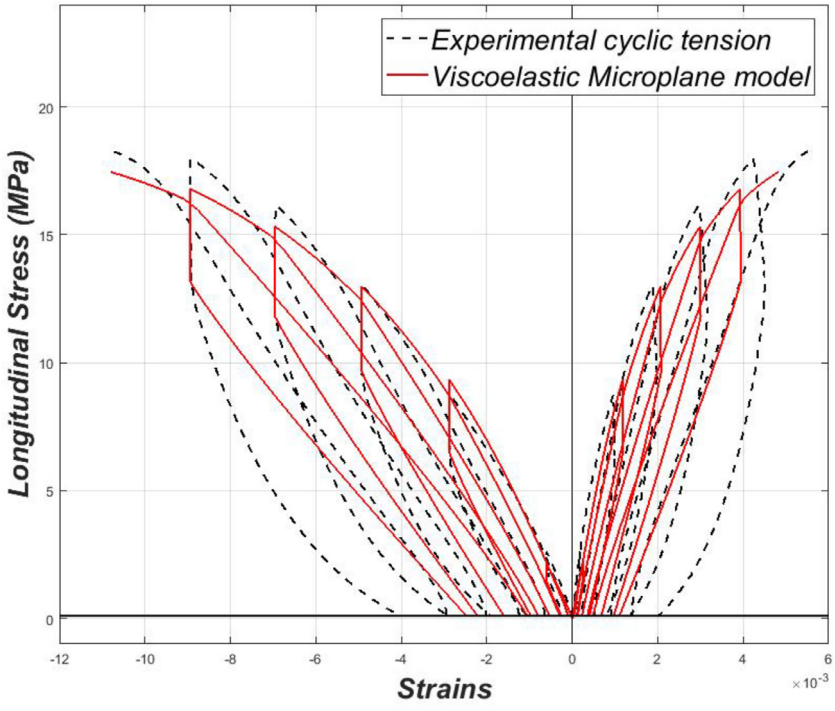

Fig. 5. Experimental and numerical σ-ε curves of cyclic compression results.

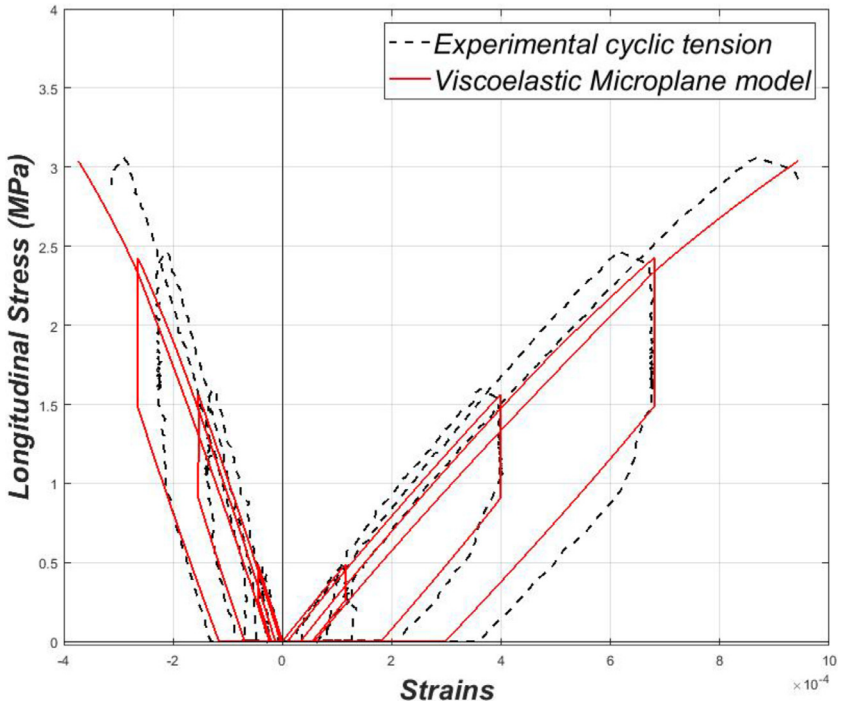

Fig. 6. Experimental and numerical σ-ε curves of cyclic tension results.

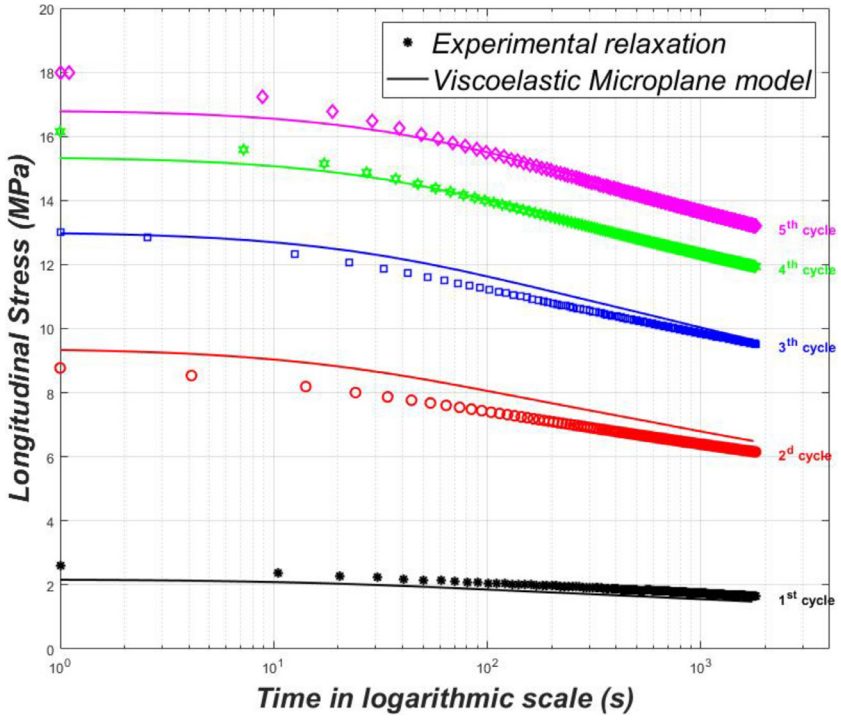

Fig. 7. Experimental and numerical evolutions of longitudinal stress in relaxation steps of cyclic compression.

sion experimental results were favoured in the adjustment process of the damage parameters (Figs. 3 and 4).

To evaluate the model at different strain rates, monotonic compression tests with strain rates of 8.3×10^{-4} s^{-1}, 3.3×10^{-5} s^{-1} and 4.4×10^{-6} s^{-1} were simulated and the results are compared to experimental data, respectively to the strain rate, in Figs. 9–11. Despite some slight divergence, reaching a maximum of ~11% between numerical and experimental curves, the proposed viscoelastic Microplane model reproduces the strain rate effect.

5. Numerical aspects of the model

To test the sensitivity of the proposed Microplane model on the strain increment, four simulations of the monotonic compression

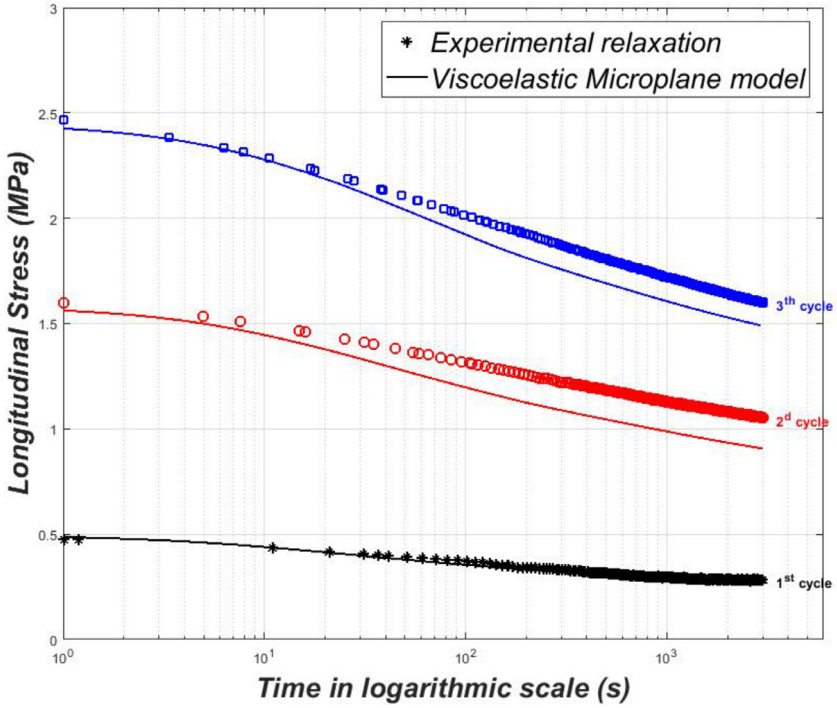

Fig. 8. Experimental and numerical evolution of longitudinal stress in relaxation steps of cyclic tension.

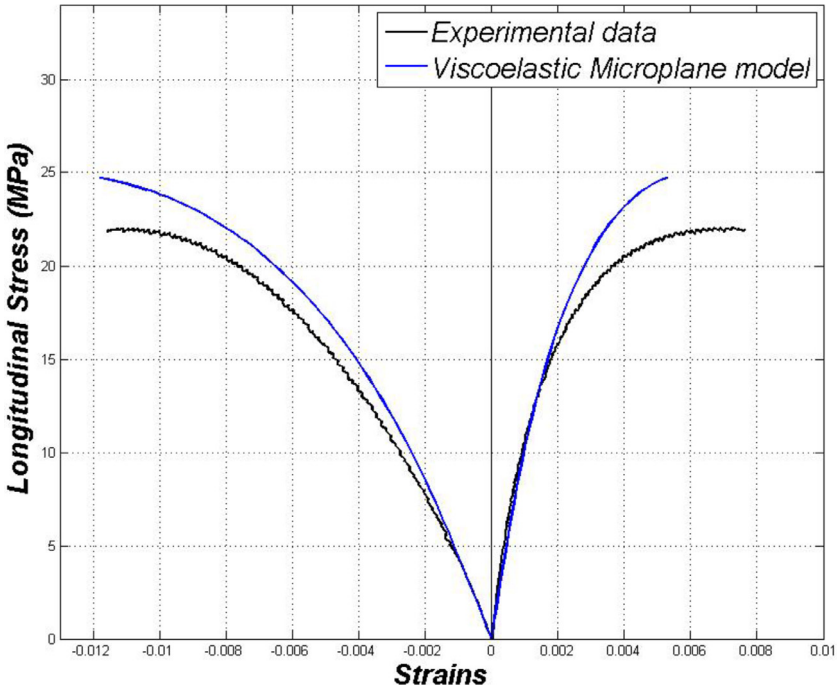

Fig. 9. Experimental and numerical σ-ε curves of monotonic compression test, strain rate $= 8.3 \times 10^{-4}$/s.

test were run at a strain rate of 3.3×10^{-5} with four different step increments: 10, 1, 0.1, and 0.01 corresponding respectively to strain increments of 3.3×10^{-4}, 3.3×10^{-5}, 3.3×10^{-6} and 3.3×10^{-7}. The model was reduced to only one viscoelastic element and one elastic element so as to reduce CPU time. For this study, the standard 21 symmetric directions on a hemisphere, proposed by Bazant and Oh (1986), were used to define the directions of microplanes. The simulations were stopped at the peak of the stress since the behaviour of the material at the softening phase is out of the focus of the present work. The results presented in Fig. 12 do not show any remarkable sensitivity to the strain increment, particularly in the linear regime.

An almost perfect convergence is obtained between the simulations at strain increments of 3.3×10^{-6} and 3.3×10^{-7} which is consistent with the finding of Nemecek et al. (2002). The strain increment of 3.3×10^{-6} seems to be the critical value that ensures

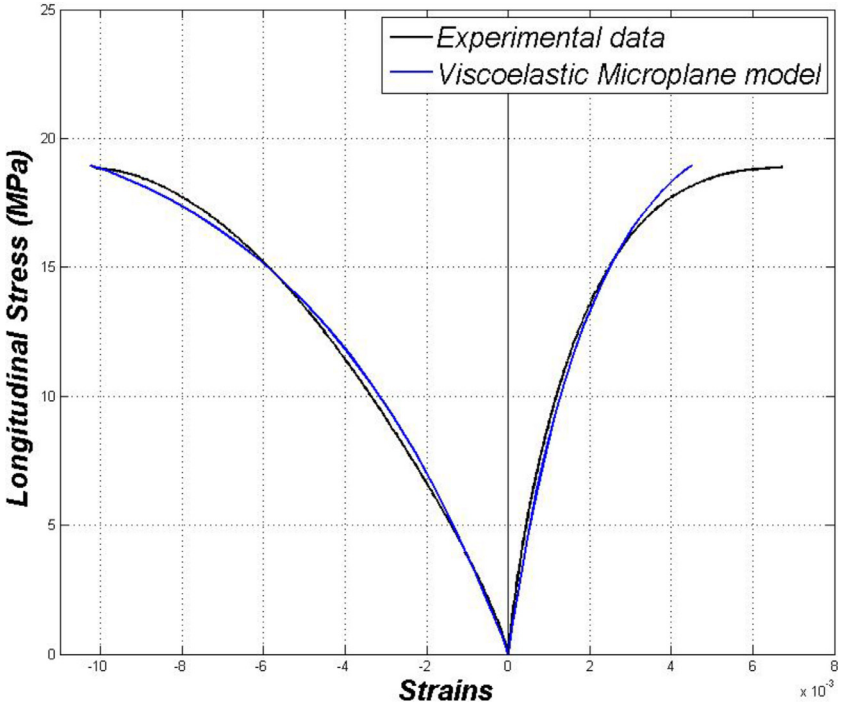

Fig. 10. Experimental and numerical σ-ε curves of monotonic compression test, strain rate $= 3.3 \times 10^{-5}$/s.

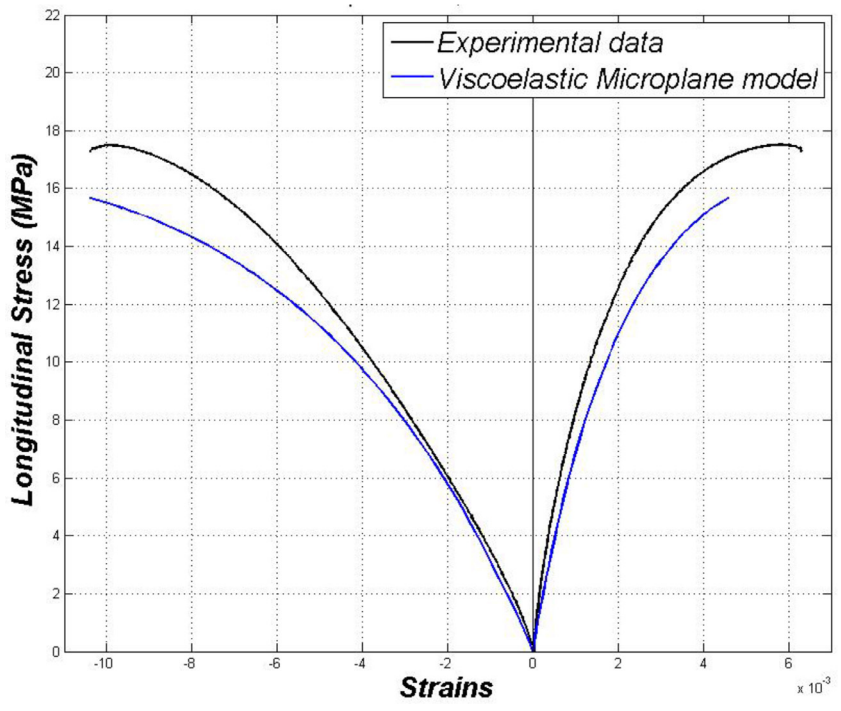

Fig. 11. Experimental and numerical σ-ε curves of monotonic compression test, strain rate $= 4.4 \times 10^{-6}$/s.

the best convergence and the stability of the model. In our study however, bigger step increments are acceptable since the behaviour of the material in the softening phase is not important.

The literature already highlighted the sensitivity of the Microplane models to the loading orientation as mentioned above. In this study, we performed simulations with 26 different orientations over the ¼ of the hemisphere, where the simulated cube is rotated with the loading direction while the axes (*x, y, z*) remain constant using integration formulas with 21-, 61-points, as proposed by Bazant and Oh (1986), and 362 points obtained from a sphere surface meshing, as proposed by Badel and Leblond (2004). With 21 points, a maximal divergence of 3.6% is obtained between

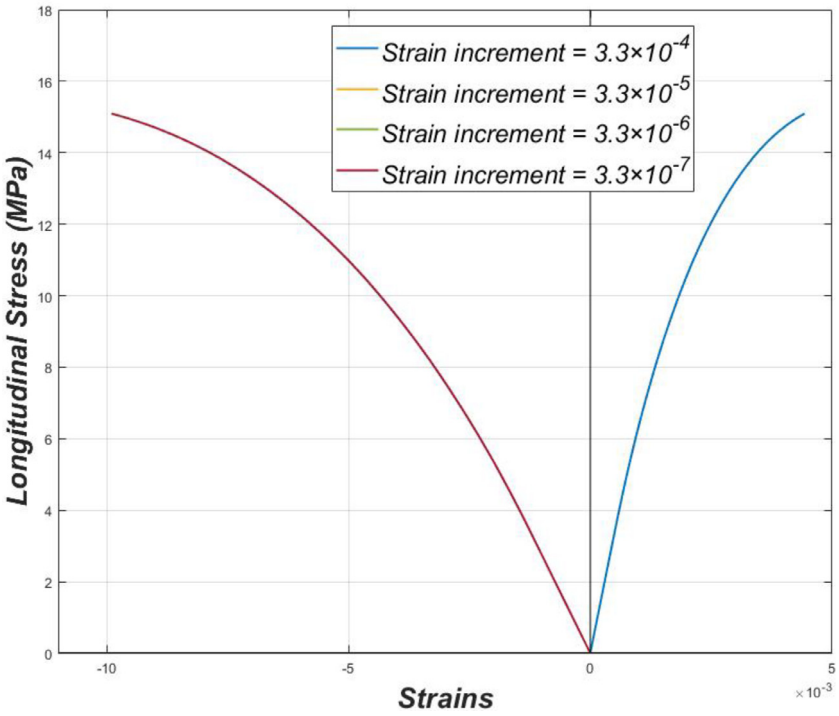

Fig. 12. Dependence on the strain increment magnitude.

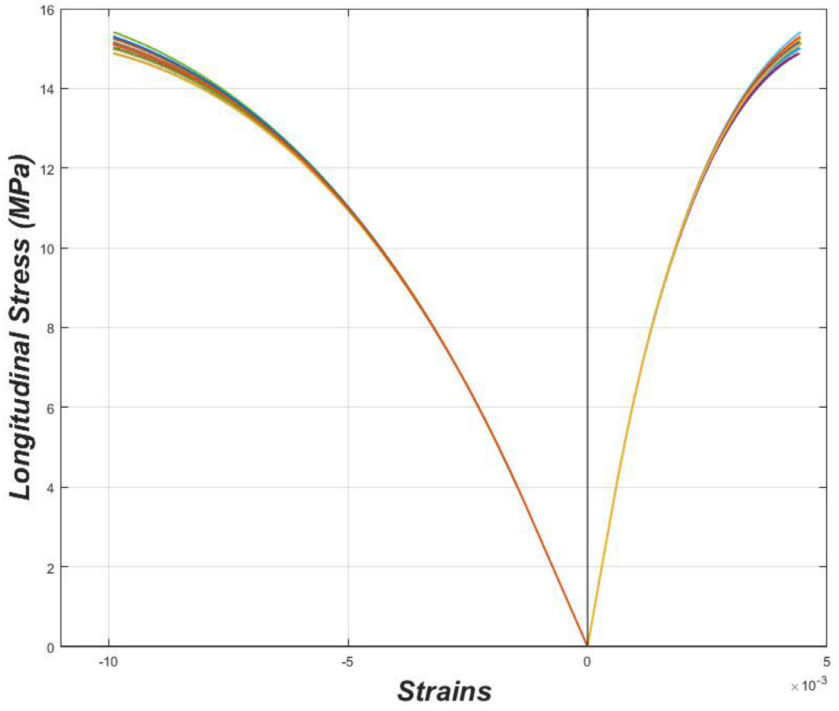

Fig. 13. Impact of loading direction on the simulation results in compression with 21 microplanes.

the maximum and the minimum longitudinal stresses, in the last increment of the simulation (Fig. 13). This divergence could be greater when simulating structures with many elements. Using the 61-point integration formula, the maximal divergence is reduced to 0.64% (Fig. 14). In Fig. 15, stress–strain curves were obtained with 362-points integration formula. All the Microplanes have the same weight ($w = 1/362$). The maximal divergence is of 0.26%. The results mentioned above indicate the following findings:

- Different loading directions lead to more or less dispersion in the predicted stress-strain curves for the used integration schemes;
- When increasing the number of the integration point, the dispersion of the stress-strain curves is reduced;
- The 61-point integration formula seems to be adequate for our model and extending to the 362-point configuration is unnecessary based on the obtained results.

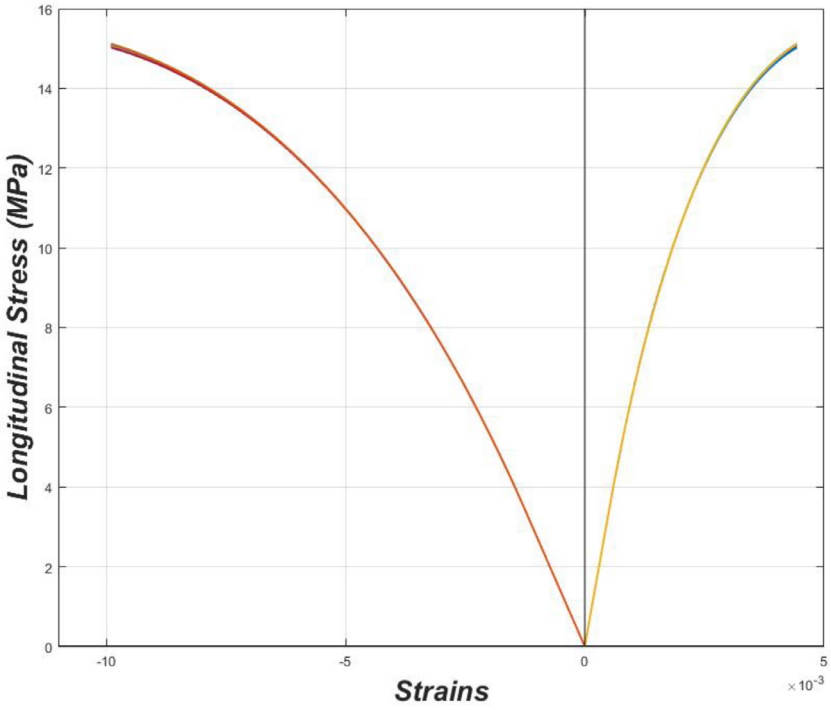

Fig. 14. Impact of loading direction on the simulation results in compression with 61 microplanes.

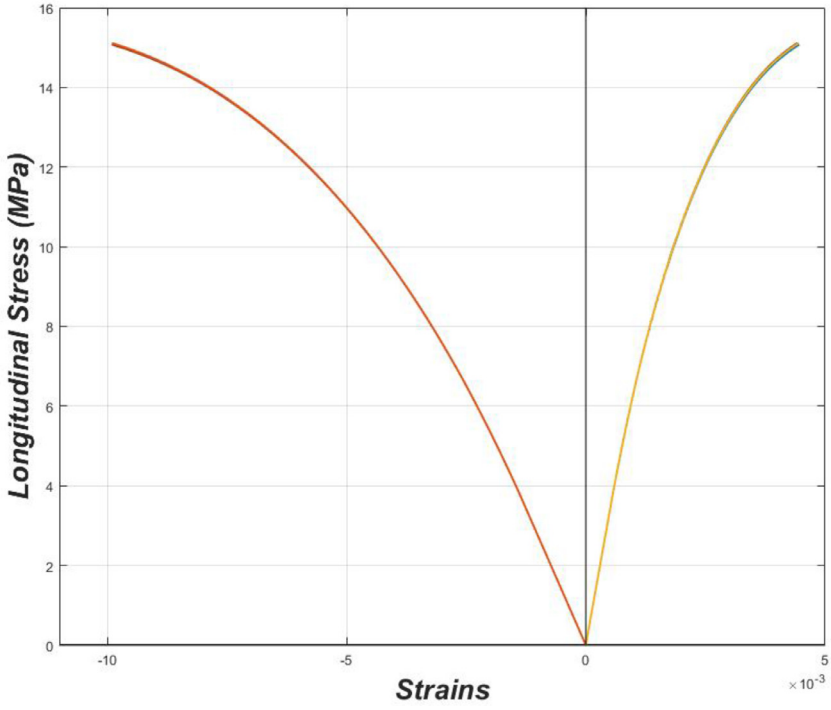

Fig. 15. Impact of loading direction on the simulation results in compression with 362 microplanes.

6. Conclusion

A new viscoelastic Microplane model has been proposed to simulate the behaviour of quasi-brittle PBX materials, using a Maxwell chain model and the Microplane approach. The integration of both the viscoelasticity and the damage induced anisotropy represents one of the new contributions of this work for such kinds of materials.

The modelling approach consists in integrating a viscoelastic model in each microplane where the components of elastic strains are projected on the microplane directions following a V-D-T decomposition.

It appeared that the numerical predictions reasonably fitted experimental data, when considering the envelope curve, the transversal strain and the relaxation steps. Moreover, the effect of the strain rate on the material mechanical response seems to be

quite well supported by the model. However, the proposed model still lacks accuracy when simulating unloading path in compression and strain evolution in recovery steps. As a perspective of this study, irreversible strain will be considered in our future investigations (plasticity or friction between microcracks lips).

The model shows a small sensitivity to the strain increment though a good convergence is globally obtained. Different loading directions lead to more or less dispersion in the predicted stress-strain curves for the used integration formulas. The 21-point integration formula is insufficient to minimize the influence of the loading direction on the results. The 61-point configuration seems to be a good compromise between the accuracy of the results, state variables and the CPU time.

Acknowledgments

Authors thank "Région Centre Val de Loire, France" and "INSA Centre Val de Loire, France" for funding this project.

References

Badel, P.B., Leblond, J.B., 2004. A note on integration schemes for the microplane model of the mechanical behaviour of concrete. Commun. Numer. Methods Eng. 20, 75–81.
Bargellini, R., 2006. Contribution d'une approche discrète à la modélisation de l'endommagement de matériaux microfissurés. Poitiers: Ecole nationale supérieure de mécanique et d'aérotechnique.
Bargellini, R., Halm, D., Dragon, A., 2008. Modelling of quasi-brittle behaviour: a discrete approach coupling anisotropic damage growth and frictional sliding. Eur. J. Mech. 27 (4), 564–581.
Batdorf, S.B., Budiansky, B., 1949. A Mathematical Theory of Plasticity Based on The Concept of Slip. s.l.: National Advisory Committee for Aeronautics.
Bazant, Z.P., Caner, F.C., Adley, M.D., Akers, S.A., 2000a. Fracturing rate effect and creep in Microplane model for dynamics. J. Eng. Mech. 126 (9), 962–970.
Bazant, Z.P., et al., 2000b. Microplane Model M4 for concrete. I: formulation with work-conjugate deviatoric stress. J. Eng. Mech. 126 (9), 944–953.
Bazant, Z.P., Gambarova, P.G., 1984. Crack shear in concrete: crack band microplane model. J. Struct. Eng. 110, 2015–2035.
Bazant, Z.P., Oh, B.H., 1986. Efficient numerical integration on the surface of a sphere. ZAMM J. Appl. Math. Mech. Zeitschrift für Angewandte Mathematik und Mechanik 66 (1), 37–49.
Belmas, R., Reynaud, J., Sorel, J., 1982. Simulation numérique du comportement viscoélastique non-linéaire d'un matériau explosif. Propellants Explos. Pyrotech. 7 (1), 8–11.
Benelfellah, A., et al., 2014. Analytical and numerical comparison of discrete damage models with induced anisotropy. Eng. Fract. Mech. 121, 28–39.
Bennett, J.G., Haberman, K.S., Johnson, J.N., Asay, B.W., 1998. A constitutive model for the non shock ignition and mechanical response of high explosives. J. Mech. Phys. Solids 46 (12), 2303–2322.
Caliez, M., et al., 2014. Viscoelastic plastic model and experimental validation for a granular energetic material. Int. J. Energetic Mater. Chem. Propul. 13 (4), 339–371.
Caner, F.C., Bazant, Z.P., 2000. Microplane Model M4 for concrete. II: algorithm and calibration. J. Eng. Mech. 126 (9), 954–961.
Carol, I., Jiràsek, M., Bazant, Z.P., 2001. A thermodynamically consistent approach to microplane theory. Part I. Free energy and consistent microplane stresses. Int. J. Solids Struct. 38 (17), 2921–2931.
Carol, I., Willam, K., 1996. Spurious energy dissipation/generation in stiffness recovery models for elastic degradation and damage. Int. J. Solids Struct. 33 (20–22), 2939–2957.
Challamel, N., Halm, D., Dragon, A., 2006. On the non-conservativeness of a class of anisotropic damage models with unilateral effects. C.R. Mec. 334 (7), 414–418.
Chen, P., Huang, F., Ding, Y., 2007. Microstructure, deformation and failure of polymer bonded explosives. J. Mater. Sci. 42 (13), 5272–5280.
Cormery, F., Welemane, H., 2002. A critical review of some damage models with unilateral effect. Mech. Res. Commun. 29 (5), 391–395.
Di Luzio, G., 2007. A symmetric over-nonlocal microplane model M4 for fracture in concrete. Int. J. Solids Struct. 44 (13), 4418–4441.
Di Luzio, G., 2009. Numerical model for time-dependent fracturing of concrete. J. Eng. Mech. 135 (7), 632–640.
Di Luzio, G., Cedolin, L., 2007. Numerical model for time-dependent fracturing of concrete structures and its application. In: New Trends in Fracture Mechanics of Concrete, Proceedings of International Conference on Fracture Mechanics of Concrete and Concrete Structures, Catania, Italy, pp. 175–180.
Dienes, J.K., 1982. Permeability, Percolation and Statistical Crack Mechanics. Berkeley, California American Rock Mechanics Association.
Dienes, J.K., 1996. A Unified Theory of flow, Hot Spots, and Fragmentation With an Application to Explosive Sensitivity. Dans: High-Pressure Shock Compression of Solids II. Springer, New York, pp. 366–398.
Dienes, J.K., Zuo, Q.H., Kershner, J.D., 2006. Impact initiation of explosives and propellants via statistical crack mechanics. J. Mech. Phys. Solids 54 (6), 1237–1275.
Ehret, A.E., Itskov, M., Schmid, H., 2010. Numerical integration on the sphere and its effect on the material symmetry of constitutive equations - a comparative study. Int. J. Numer. Methods Eng. 81 (2), 189–206.
Ellis, K., Leppard, C., Radesk, H., 2005. Mechanical properties and damage evolution of a UK PBX. J. Mater. Sci. 40 (23), 6241–6248.
Gratton, M., et al., 2009. Mechanical characterization of a viscoplastic material sensitive to hydrostatic pressure. Eur. J. Mech. A. Solids 28 (5), 935–947.
Hackett, R.M., Bennett, J.G., 2000. An implicit finite element material model for energetic particulate composite materials. Int. J. Numer. Methods Eng. 49 (9), 1191–1209.
Ha, K., Schapery, R.A., 1998. A three-dimensional viscoelastic constitutive model for particulate composites with growing damage and its experimental validation. Int. J. Solids Struct. 35 (26-27), 3497–3517.
Hasegawa, T., Bazant, Z.P., 1993. Nonlocal microplane concrete model with rate effect and load cycles. I: general formulation. J. Mater. Civ. Eng. 5 (3), 372–393.
Huang, L.C., et al., 2017. Numerical aspects of microplane constitutive models for concrete. Appl. Math. Modell. 41, 530–548.
Kuhl, E., Steinmann, P., Carol, I., 2001. A thermodynamically consistent approach to microplane theory. Part II. Dissipation and inelastic constitutive modeling. Int. J. Solids Struct. 38, 2933–2952.
Levasseur, S., Collin, F., Charlier, R., Kondo, D., 2013. On micromechanical damage modeling in geomechanics: Influence of numerical integration scheme. J. Comput. Appl. Math. 246, 215–224.
Le, V.D., et al., 2010. Experimental mechanical characterization of plastic-bonded explosives. J. Mater. Sci. 45 (21), 5802–5813.
Liu, Z.W., et al., 2009. Fracture behavior of PBX simulant subject to combined thermal and mechanical loads. Polym. Test. 28 (6), 627–635.
Maire, J.F., Chaboche, J.L., 1997. A new formulation of continuum damage mechancis (CDM) for composite materials. Aerosp. Sci. Technol. 1 (4), 247–257.
Murakami, S., Kamiya, K., 1997. Constitutive and damage evolution equations of elastic-brittle materials based on irreversible thermodynamics. Int. J. Mech. Sci. 39 (4), 473–486.
Nemecek, J., Patzak, B., Rypl, D., Bittnar, Z., 2002. Microplane models: computational aspects and proposed parallel algorithm. Comput. Struct. 80 (27-30), 2099–2108.
Ozbolt, J., Bazant, Z.P., 1992. Microplane model for cyclic triaxial behavior of concrete. J. Eng. Mech. 118 (7), 1365–1386.
Ozbolt, J., Reinhardt, H.-W., 2001. Sustained loading strength of concrete modelled by creep-cracking interaction. Otto Graf J. 12 (9).
Pecqueur, G., 1995. Étude Expérimentale et Modélisation du Comportement d'une Craie et d'un Grès en Torsion. Lille: Université de Lille 1.
Picart, D., et al., 2014. Characterization and modeling of the anisotropic damage of a high-explosive composition. Eng. Fract. Mech. 131, 525–537.
Qiu, Y., Crouch, R.S., 1997. Spurious compaction in the microplane model and a new adaptative framework. In: Computational Plasticity. CIMNE, Barelona, pp. 493–499.
Saadeh, S.A.R., 2005. Characterization of Asphalt Concrete Using Anisotropic Damage Viscoelastic-Viscoplastic Model. College Station. A&M University, Texas: Texas.
Taylor, G.I., 1938. Plastic strains in metals. J. Inst. Met. 62, 307–324.
Trumel, H., Lambert, P., Belmas, R., 2010. Mesoscopic Investigations of the Deformation and Initiation Mechanisms of a Hmx-Based Pressed Composition. Coeur d'Alene (ID), USA s.n..
Verron, E., 2015. Questioning numerical integration methods for microsphere (and microplane) constitutive equations. Mech. Mater. 89, 216–228.
Williamson, D.M., et al., 2008. Temperature-time response of a polymer bonded explosive in compression (EDC37). J. Phys. D Appl. Phys. 41 (8).
Xiao, Y., Sun, Y., Yang, Z., Guo, L., 2017a. Study of the dynamic mechanical behaviour of PBX by Eshelby theory. Acta Mech. 228 (6), 1993–2003.
Xiao, Y., et al., 2017b. Characterization, modeling and simulation of the impact damage for polymer bonded explosives. Int. J. Impact Eng. 103, 149–158.
Zhu, Q.Z., Shao, J.F., Kondo, D., 2008. A micromechanics-based non-local anisotropic model for unilateral damage in brittle materials. Comptes Rendus Mécanique 336 (3), 320–328.
Zi, G., Bazant, Z.P., 2002. Continuous relaxation spectrum for concrete creep and its incorporation into Microplane model M4. J. Eng. Mech. 128 (12), 1331–1336.

2.5 DÉVELOPPEMENTS EXPÉRIMENTAUX ET CRITÈRE DE RUPTURE MULTIAXIAL (I1)

Le second apport principal des travaux de M. Chatti concerne le développement d'essais permettant d'accèder qualitativement et quantitativement à l'endommagement et son effectivité. La fourniture par le CEA d'un matériau simulant non explosif (matériau I1), dans le cadre du financement institutionnel de la thèse, nous a permis de pouvoir effectuer les essais en interne. Ce matériau a sensiblement le même comportement que M1 en terme de contrainte et déformation à rupture. En revanche, le comportement en compression cyclique montre une évolution quasi-linéaire jusqu'à environ 60% de la contrainte à rupture. Le cyclage montre de plus une reprise de raideur lors de la charge, peut-être due à un taux de porosité beaucoup plus important que M1, de l'ordre de 28% contre 5%.

Une campagne de caractérisation complète, avec essais de traction et compression multicycles, a été entreprise avec une attention particulière concernant les mesures de déformation. Aucun essai n'ayant été effectué au CEA avec une mesure par jauges sur ce matériau, 2 colles ont été testées avec la vérification de la non-influence du collage des jauges sur le comportement, une rigidification par la colle pouvant être suspectée sous les jauges vue la porosité importante du matériau. Des essais de compression sous confinement ont été menés avec une enceinte développée et fabriquée en interne dans le cadre de projets de fin d'études étudiants. Enfin, des essais permettant de mettre en lumière l'évolution de l'effectivité d'endommagement (essais de Compression/Traction/Compression ou Traction/Compression/traction), l'aspect directionnel de l'endommagement (essais 0°/90°/0°) et l'effet de la pression sur le module de cisaillement (essai de torsion sous confinement) ont été développés et menés. Enfin, des essais multiaxiaux (essais couloir et compression/torsion) ont été développés et mis en œuvre afin d'identifier un critère de rupture unique, compatible avec tous les types de sollicitations.

Cette base très riche est détaillée dans l'article référencé ACL1 présenté ci-après.

Mechanics of Materials 172 (2022) 104388

Contents lists available at ScienceDirect

Mechanics of Materials

journal homepage: www.elsevier.com/locate/mechmat

Experimental investigation of the behaviour of a simulant material for plastic-bonded explosives and modelling of the effectivity and damage induced anisotropy

Marwen Chatti [a,*], Michel Gratton [a], Michael Caliez [a], Arnaud Frachon [a], Didier Picart [b], Nourredine Aït Hocine [a]

[a] INSA CVL, Univ. Tours, Univ. Orléans, LaMé, 3 Rue de la Chocolaterie, 41000, Blois, France
[b] CEA DAM Le Ripault, F-37260, Monts, France

ARTICLE INFO

Keywords:
Plastic-bonded explosives
Simulant
Experiments
Damage induced anisotropy
Effectivity
Viscoelasticity
Plasticity

ABSTRACT

This paper presents an original experimental investigation and modelling of the behaviour of a simulant material for Plastic-Bonded Explosives (PBXs). The conducted tests are tension, compression, alternated tension/compression, confined compression, channel-die, and DMA. The experimental dispositive and protocols are presented and detailed. Monotonic and cyclic tests are conducted in addition to alternated and non-proportional tests. The obtained results are presented and discussed. A special focus was put on the damage induced anisotropy and the effectivity in the material behaviour. Also, hydrostatic pressure and strain rate dependencies and the presence of hysteresis loops and irreversible strains, are highlighted.

Based on the experimental results, damage evolution laws and novel effectivity functions are proposed to model the material behaviour in the quasi-static domain.

1. Introduction

Plastic-Boded Explosives (PBXs) used for pyrotechnic structures are commonly subjected to quasi-static loadings during storage and transportation which can induce high stress levels affecting the material behaviour. These stress levels can generate the ignition of the explosive due to a local hot spot released by friction and/or the reactive decomposition (combustion or deflagration) influenced by the permeation of hot gas into the damaged material and the microcracks network (Picart and Pompon, 2016) (You et al., 2015). The PBX material is an HMX (octahydro-1,3,5,7-tetranitro-1,3,5,7-tetrazocine) based energetic material. Its microstructure is composed of more than 95 wt% of energetic crystals mixed with a low percentage of a polymer binder. The mixture is pressed using an isostatic compaction process, which reduces the void of the material but induces inter- and intra-granular microcracks due to the high volume fraction of the solid phase (Le et al., 2010) (Picart et al., 2014).

Many experimental works were published about different types of PBX materials (PBX9501, PBX9502, EDC37 or LX-14) submitted to quasi-static loadings (Plassart et al., 2020) (Belmas, 1994) (Idar et al., 1998) (Wiegand, 2000) (Ellis et al., 2005) (Williamson et al., 2008) (Le et al., 2010) (Picart et al., 2014). The energetic material presents a nonlinear behaviour, whatever the loading conditions, with an asymmetry between tension and compression. Tension tests show a quasi-linear and quasi-brittle behaviour, unlike compression and triaxial tests that display more ductile and nonlinear behaviour (Rja Fi Allah, 2006) (Le, 2007) (Ellis et al., 2005) (Benelfellah, 2013). Strain rate, temperature and hydrostatic pressure dependencies were also observed (Le et al., 2010) (Caliez et al., 2014). Aggregate materials show commonly, a hydrostatic pressure dependency because of its quasi-compact microstructure. For PBXs, the initial stiffness strongly depends on the hydrostatic pressure which shows the effect of the damaged initial microstructure. Picart et al. (Picart et al., 2012) analysed the evolution of the microstructure of a PBX during an instrumented reverse edge-on impact test. New microcracks and shear bands in the grains were observed in addition to debonding. Ravindran et al. (Ravindran et al., 2016) performed dynamic compression tests on a polymer bonded sugar (a known simulate for PBXs). It was observed that the local strain distribution is highly heterogeneous with large strain localization occurring between the crystal boundaries. The

* Corresponding author.
E-mail address: chatti.marwen@hotmail.fr (M. Chatti).

https://doi.org/10.1016/j.mechmat.2022.104388
Received 17 January 2021; Received in revised form 26 March 2022; Accepted 2 June 2022
Available online 11 June 2022

microstructure shows crushed crystals areas. Most of the crystals deformations are minimal, and usually realign themselves with large deformation of the binder by rigid rotation and sliding. Using also dynamic compression, Parab et al. (Parab et al., 2016) observed that most of the cracking in the crystals was due to the tensile stress generated by the diametral compression applied from the contacts between the crystals. Tensile stress driven cracking was also observed for some of the crystals due to the transverse deformation of the binder and superior bonding between the crystal and the binder. Trumel et al. (Trumel et al., 2010), in a Hopkinson test, observed a preferred orientation for microcracks. They showed a common normal to the direction of extension. Picart et al. (Picart et al., 2014) presented a uniaxial tension test followed by compression test. The damage generated in tension doesn't seem to affect the behaviour of the material in compression. Also, the material stiffness is progressively recovered. The opposite test was performed also. The prior loading in compression, seems to affect the behaviour in tension and to yield a brittle failure. Recently, Benelfellah et al. (Benelfellah et al., 2014) (Picart et al., 2014) suggested the presence of damage anisotropy induced by loading and that the material shows unilateral effect caused by the opening and the closure of microcracks. This observation is relatively recent, and these phenomena weren't studied experimentally in the literature. The published tests were only monotonic, and mostly uniaxial and proportional, and the evolution of the damage and the anisotropy weren't investigated. The mentioned conclusions, thus, need to be further studied and analysed experimentally.

To investigate these behavioural aspects, multiaxial and non-proportional tests, not existing in the literature, were developed, carried out and analysed. Also, microstructural observations were carried out to highlight, first, the initial state of the material microstructure and then the different damage and failure mechanisms.

As mentioned above, the presence of irreversible strains was highlighted at the end of recovery in cyclic tests (loading, relaxation, unloading and recovery) (Picart et al., 2014) (Le et al., 2010). Hysteresis loops were also observed in these tests. In the literature, this phenomenon is attributed to cracks opening in unloading along with a dissipative friction between microcracks lips in addition to viscoelasticity of the material. Unfortunately, these behavioural aspects, irreversible strains, and viscoelasticity, were rarely mentioned or analysed in the literature. Additionally, most published constitutive laws neglect these phenomena. In the present work, plasticity and viscoelasticity were studied and analysed in uniaxial, multiaxial, and non-proportional tests in addition to the DMA test.

Due to costs and security constrains, it would be very complicated and difficult to first, access the PBX material and to carry new experimental protocols directly. Following the CEA (French Atomic Energy Commission) recommendation, a simulant material, presenting the same behavioural aspects as the PBX, is used in this experimental campaign.

To model the behaviour of such complex material, a constitutive law considering all this physical phenomenon needs to be developed and identified based on this experimental investigation. Many models were developed in the last two decades for PBX materials, especially for dynamic and high-pressure loading conditions leading to ignition. The most popular model is ViscoScram (viscoelastic statistical crack mechanics) (Bennett et al., 1998). This model is a combination of the fragmentation theory proposed by Dienes in the early 80s for brittle materials (Dienes, 1982) (Dienes, 1996) (SCRAM) and viscoelastic Maxwell model (Visco). The SCRAM approach consists of an isotropic model with the damage related to the mean crack radius, in which the growth rate is limited to a maximum value. An update was proposed afterward by Hackett and Bennett (2000). They modified the crack growth law to consider the influence of the hydrostatic pressure on the damage and on the tensile and compressive responses. Recently, Xiao et al. (Xiao et al., 2017) described the dynamic mechanical behaviour of PBX1314 as a function of aspect ratio and inclusion concentration. They modelled the viscoelastic behaviour of the polymer binder using a generalized Maxwell model, with a Prony series representation for the stress relaxation functions. Another damage constitutive model with viscoelastic response and statistical fracture was developed by Xiao et al. (Xiao et al., 2017) to model low velocity impact experiment, for PBX. This model is based on SCRAM approach of Dienes et al. (Dienes et al., 2006) with a generalized Maxwell scheme. An isotropic constitutive relation is employed to describe the damage response of the material.

For quasi-static loadings, Gratton et al. (Gratton et al., 2009) developed an isotropic model assuming the material as damageable elastic viscoplastic. An additional isotropic model that accounts for damageable viscoelasticity and plasticity was proposed by Le et al. (Le et al., 2010) and Caliez et al. (Caliez et al., 2014). The viscoelasticity was modelled using a generalized Maxwell chain model. Recently, Liu et al. (Liu et al., 2020) presented a mechanical constitutive model, for PBX, that combines a porosity model and a viscoelastic–viscoplastic damage model with consideration of pressure and strain rate dependencies. The model is calibrated and tested only in compressive loading modes, specifically under hydrostatic cyclic compression, uniaxial compression at various strain rates, and triaxial compression with hydrostatic confining pressure.

As mentioned above, the most recent observation suggests that the material presents an evolving damage with induced anisotropy. Some approaches have been developed in the literature to model such damage (Maire and Chaboche, 1997) (Zhu et al., 2008) (Bargellini et al., 2008) (Murakami and Kamiya, 1997).

Benelfellah et al. (Benelfellah et al., 2014) and Picart et al. (Picart et al., 2014) proposed an elastoplastic model with damage induced anisotropy and effectivity. The authors illustrated the effect of the damage on engineering parameters and compared existing models based on the different aspects of the material behaviour. This investigation revealed that, among the constitutive laws proposed to model the anisotropic damage induced by the loading and satisfying the thermodynamic requirements, the Microplane approach, initially developed for concrete by Bazant and Gambarova (Bazant and Gambarova, 1984), provides a powerful framework to implement complex laws. Particularly, the introduction of a unilateral effect is possible keeping a non-dissipative free energy, a continuous stress–strain response or a symmetrical stiffness tensor (Benelfellah et al., 2014).

The proposed model is the first to introduce damage induced anisotropy and effectivity functions. The damage evolution laws were rather simple, and the effectivity functions were defined using Heaviside functions. The latter functions are unable to model the gradual stiffening of the behaviour and the nonlinearity of the unloading (Hysteresis loops). Also, the proposed model didn't account for viscoelasticity.

Based on the experimental results and the analysis of the damage and effectivity, new damage evolution laws and effectivity functions are proposed. In addition, viscoelasticity and plasticity will be analysed using relaxation and recovery steps in tension and compression, in addition to DMA test to characterize, in the future, a viscoelastic plastic constitutive law with effectivity and damage induced anisotropy.

2. Experiments

2.1. Material

The simulant material is an aggregate composite constituted of inert crystals and polymeric binder. The crystals are composed of 29.3 wt% of barium meal (BaSO4) and 65.2 wt% of melamine. The crystals size ranges from 1 to 100 μm (Bailly et al., 2011). The binder is of small amount, 5.5 wt%. It is made of an epoxy resin and a blue pigment. The material is manufactured by hot hydrostatic press moulding. The manufacturing process induces an initial damage in the simulant, like in PBXs. The resulting material has a mean density of 1.73 with a high residual porosity of 28% (Bailly et al., 2011). The morphology and the mechanical properties of this simulant are similar to those of a PBX and

both materials show the same behavioural aspects (Le et al., 2010) (Picart and Brigolle, 2010) (Bailly et al., 2011) (Caliez et al., 2014) (Liu et al., 2009) (Yeom et al., 2012) (Zhou et al., 2011) (Park et al., 2013).

2.2. Test protocols and strain acquisition techniques

Microstructure observations were carried out on the pristine material and on the failure surfaces for each test using a scanning electron microscope.

Monotonic and cyclic tests were conducted, at an imposed strain rate of 2×10^{-5}/s, using a tension-compression electromechanical MTS machine. These tests consist of tension, compression, alternated tension-compression, channel-die and triaxial compression.

In tension and alternated tension/compression, strains were measured with general-purpose 90° tee rosettes, glued in the middle of the specimen, on opposite sides (two longitudinal gauges L_1 and L_2 and two transversal gauges T_1 and T_2). In compression and triaxial compression tests, three general-purpose 90° tee rosettes, glued in the middle of the specimen and spaced by 120°, were used. One longitudinal gauge was connected directly to the MTS machine to drive the test.

In cyclic tests, each cycle contains 4 steps: loading, relaxation, unloading until zero force and, finally, recovery by maintaining the zero force value. The 3 first steps are driven by the strain measured by the gauge L_1, while the last step is controlled by the load cell signal.

Previous studies (Le et al., 2010) (Caliez et al., 2014) showed that experimental stress-strain $(\sigma - \varepsilon)$ curves of cyclic tests are embedded below the corresponding $\sigma - \varepsilon$ experimental curves of monotonic tests, and that both tests present almost the same failure points, as observed in concrete materials (Burlion, 2010).

The test protocol and strain acquisition for the channel-die test are detailed in the correspondent section.

2.3. Uniaxial tension and compression

Dog-bone shaped specimens were used for uniaxial tension tests, with a cross-section of 9×10 mm^2 and a total length of 150 mm. A specific gripping fixture was designed, to ensure the homogeneous loading during the test (Fig. 1). It is worth noting that tension tests are delicate to achieve because of the quasi-brittle behaviour of the studied material.

In compression, cylindrical samples of 10 mm diameter and 20 mm height were used. The specimen was pressed between two compression platens through the intermediate of two hard papers of 10.4 mm diameter and 1 mm thickness to prevent misalignment and geometric defaults (Fig. 2). Monotonic and cyclic tension and compression tests were conducted. Relaxation and recovery steps last 1800 s in uniaxial experiments.

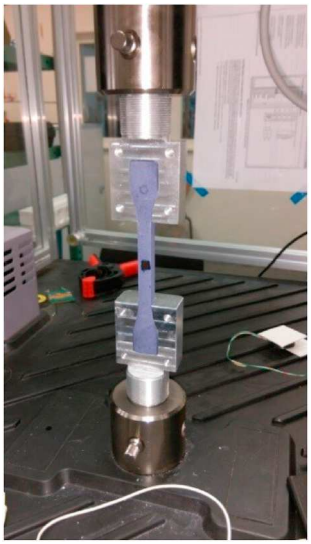

Fig. 1. Tension experimental dispositive.

2.4. Alternated tension-compression tests

The alternated tests: tension-compression-tension (TCT) and compression-tension-compression (CTC) were conducted using the tension experimental dispositive and dog-bone specimens. The cross-section has been adjusted to 8.5×8.5 mm^2 to guarantee a relatively homogeneous stress in the central zone of the specimen, while avoiding buckling in compression. The TCT test (resp. CTC), consists first, on performing few cycles in tension (resp. compression in CTC) approaching failure (80%). At the end of the recovery of the last cycle, a cyclic compression (resp. cyclic tension in CTC) is applied without reaching failure also. Finally, the specimen is again subjected to cyclic tension (resp. cyclic compression in CTC) until failure. Four general-purpose 90° tee rosettes were glued in the middle of the specimen, on opposite sides to detect a possible buckling. Relaxation and recovery steps last 1800 s in uniaxial experiments.

2.5. Triaxial compression

Cyclic triaxial compression tests were performed using compression specimens, at hydrostatic pressure levels of 5 MPa and 10 MPa. Fig. 3 presents the experimental dispositive. The specimen was glued inside a pressure vessel filled with distilled water. A pressure system group and a sensor mounted on the vessel were used to control the hydrostatic pressure level. A rod compressing the specimen inside the vessel was mounted on the MTS machine to apply the longitudinal load. The specimen and the wires were coated by a silicone gel to ensure their impermeability. Three general-purpose 90° tee rosettes were glued in the middle of the specimen spaced by 120°. Relaxation and recovery steps last 1200 s in triaxial compression.

2.6. Channel-die

Channel-die tests consist of a biaxial monotonic loading performed on cubic specimens of $15 \times 15 \times 15$ mm^3. These experiments enable obtaining several biaxial compression points by varying the ratio between transversal and longitudinal loadings, using a specific experimental setup. Fig. 4 presents the designed experimental dispositive and test details. The specimen is loaded in the longitudinal direction, using the MTS machine, and in the transversal direction T_1, using an additional load cell, while the transversal direction T_2 is left free. Two strain gauges were glued on the two opposite free sides of the cube to measure the longitudinal strain ε_L and the transversal strain ε_{T1}. The second transversal strain ε_{T2}, in the free direction T_2, was measured using two

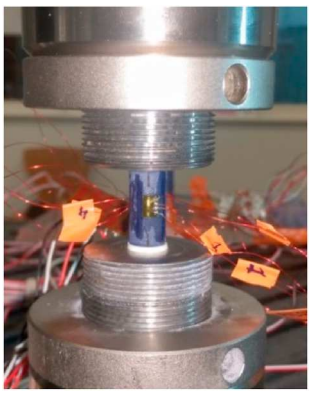

Fig. 2. Compression experimental dispositive.

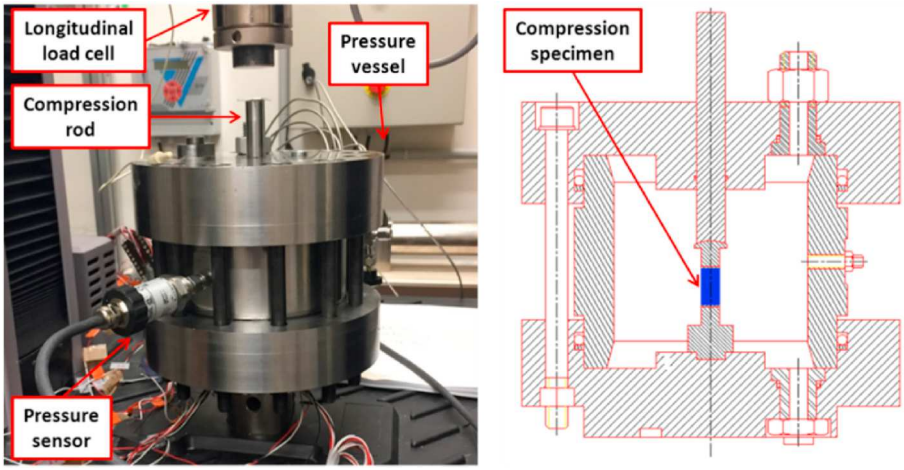

Fig. 3. Triaxial compression experimental dispositive.

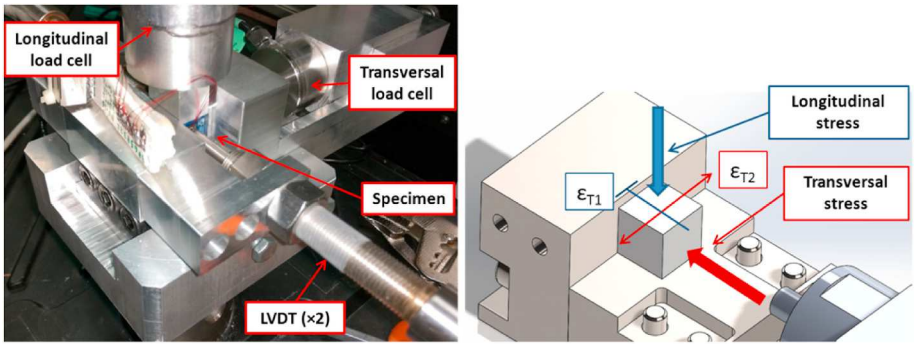

Fig. 4. Channel-die experimental dispositive.

opposite LVDT. All the specimen-setup interfaces were lubricated using a teflon-grease-teflon hard paper sandwich to avoid friction and conical fracture (Picart and Pompon, 2016), and to limit the geometric default effects.

Five monotonic channel-die tests were performed. One test consisted of applying an initial transversal loading ($\sigma_{T-initial} = 1$ MPa), then left free during the test, and applying a longitudinal loading until failure. In two other tests, the initial transversal loading was kept constant during the test ($\sigma_T = 2$ MPa and $\sigma_T = 10$ MPa), while applying the longitudinal loading until failure. The two last tests consisted of simultaneously applying longitudinal and transversal loadings, keeping respectively a ratio of 0.5 and 1 between σ_T and σ_L until failure.

2.7. Dynamic mechanical analysis DMA

Dynamic Mechanical Analysis (DMA) allows the study of the visco-elastic properties of the material as a function of the strain or the frequency, by loading the specimen under cyclic loads with very low amplitudes. This test allows to determine the storage modulus E' which characterizes the elastic part, the loss modulus E'' which characterizes the viscous part and the damping factor $tan\delta$ which characterizes the damping of the material.

The first test consists of dynamic strain sweep until a maximal value of $\varepsilon_{dyn} = 3 \times 10^{-4}$ at a frequency of 1 Hz and initial static strain in compression $\varepsilon_{stat} = -3 \times 10^{-4}$. The second test consists of a frequency sweep between 1 and 520 Hz, with a dynamic strain of $\varepsilon_{dyn} = 3 \times 10^{-4}$ but without initial static load ($\varepsilon_{stat} = 0$). The same test is then repeated with a static load in compression of $\varepsilon_{stat} = -3 \times 10^{-4}$.

A rectangular specimen of 4×4 mm^2 in section and 50 mm length is glued between 2 plates. The tests were carried out only at room temperature since the time-temperature equivalence is out of the focus of this paper. The specimen self-heating should be negligeable based on the material constituents thermal properties and the number of cycles during the DMA test.

3. Experimental characterisation of the material behaviour

Given the diversity of the conducted tests, it is necessary to adopt a common strategy for the results post-processing. Fig. 5 presents the points A_i, B_i, C_i, D_i and A_{i+1} in the strain-stress plane $(\sigma - \varepsilon)$ allowing the post processing of the different behavioural aspects at each cycle:

- when it exists, represents the hydrostatic pressurization phase.
- and $[C_iD_i]$ represent, respectively, loading and unloading phases.
- and $[D_iA_{i+1}]$ represent, respectively, the relaxation and recovery phases. During post processing, these steps are linearly extended, in a Log time scale, up to 10^4 s for a real estimation of the relaxed stress in relaxation (point C_i) and irreversible strain in recovery (point A_i, longitudinally and transversally).
- The slope of $[C_iA_{i+1}]$ describes the secant elastic modulus (damaged), noted E.
- For the unconfined tests, the final point of recovery A_{i+1} represents the residual plastic strain: $\varepsilon_p = [A_1A_{i+1}]$. In this case, $O \equiv A_1$.
- Confined tests require a virtual hydrostatic unloading to obtain the point G_{i+1} corresponding to the residual strain. To simplify the identification process, it is assumed that the hydrostatic unloading is from the undamaged isotropic compressibility module K_0 (the slope of $[A_{i+1}G_{i+1}]$ is therefore equal to 3 K_0). With this hypothesis, a common approach to identify the current residual strain is obtained $\varepsilon_p = [OG_{i+1}] = [A_1A_{i+1}]$.

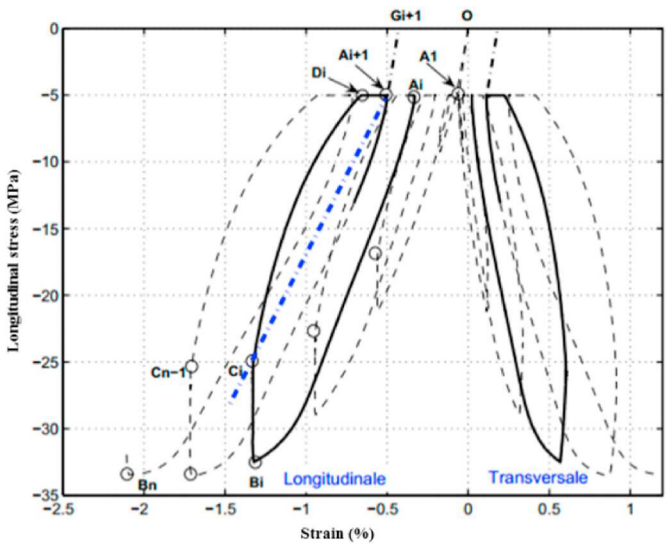

Fig. 5. Characteristic points of a load-relaxation-unloading-recovery cycle for triaxial compression test (5 MPa) and strain rate of 2×10^{-5}/s.

3.1. Microstructural observations of the material damage

Fig. 6 show the different constituents of the pristine material. The brilliant phases correspondents probably to the Barium crystals $BaSO_4$. High solid fraction of crystals is observed in the microstructure. The binder cannot be identified clearly. The initial microstructure reveals the presence of initial microcracks generated by the manufacturing process.

Fig. 7 shows the microstructure of the material loaded in tension. Barium meal crystals appear to be grey. A clearer material is observed between these crystals, that may contain melamine crystals and binder. It's very hard to distinguish only the binder because of its small amount.

The observation of the failure surfaces in tension shows long microcracks developed in the interface binder-crystals and, to a lesser extent, inside the crystals. The microcracks orientations are random, and the damage seems to propagate in all directions. Despite the presence of some broken crystals, this failure mode doesn't seem dominant.

Based on the aspect of the microstructure, failure surfaces observed in compression show clearly higher levels of damage and a different failure mode compared to tension, as observed in Fig. 8. In addition to intergranular cracks, some regions in the microstructure present a high concentration of small crystals due to a violent fracture of big crystals. Some shear bands are observed also proving the presence of friction and irreversible strains. Same as tension, microcracks are randomly orientated, and the damage propagates in all directions.

Failure surfaces of specimens loaded under biaxial compression were also observed and analysed. The microstructure of the material is presented in Fig. 9 ($\sigma_{T-initial} = 1$ MPa) and Fig. 10 ($\sigma_L = \sigma_T$). The microstructure presents the same debonding and fractured crystals, like compression but in a more concentrated manner. However, an unexpected phenomenon consisting of the presence of voids in the microstructure was observed. This phenomenon seems to be due to crystals tearing under the high stress levels in biaxial compression.

3.2. Behaviour asymmetry between tension and compression

Stress-Strain $(\sigma - \varepsilon)$ curves obtained from tension, compression, CTC and TCT are reported, respectively in Fig. 11, Fig. 12, Fig. 13 and Fig. 14. It's noticed, first, that the curves of monotonic tension and monotonic compression constitute the master curves (envelope curves) for the cyclic tests. It seems that unloading-loading steps don't influence the material global behaviour. In tension, a tensile strength of 2.75 MPa and longitudinal and transversal strains of 0.26% and −0.053% are obtained respectively. In compression, the material behaviour is more ductile. In fact, the material fails at −18.84 MPa of compressive strength and −1.62% and 0.97% of longitudinal and transversal strains respectively.

The material clearly presents an asymmetry of behaviour between tension and compression which could indicate the presence of two different damage evolutions.

The tension curves present a nonlinearity related, partially, to a damage starting from the beginning of the test, at low level of stress. The failure is quasi-brittle and happens too quickly compared to the compression. The evolution of the compression curves shows mainly two phases: a quasi-linear evolution until ~60% of the compressive strength followed by a strong nonlinearity.

The study of the evolution of the stiffness and the damage in the material is necessary to understand this asymmetry in the material behaviour.

3.3. Hydrostatic pressure dependency

Stress-Strain $(\sigma - \varepsilon)$ curves obtained from triaxial compression at 5 and 10 MPa of hydrostatic pressure are shown below in Fig. 15. The material response is more ductile than uniaxial compression. Two phases are observed, quasi-linear behaviour followed by a nonlinear one, same as seen in compression. At 5 MPa (resp. 10 MPa) of hydrostatic pressure, the material fails at a compressive strength of −29.8 MPa (resp. −45.9 MPa), a longitudinal strain of −2.7% (resp. −3.2%) and a transversal strain of 1.73% (resp. 1.65%). The ultimate strength and strains increase with increasing hydrostatic pressure. A type of consolidation phenomena seems to appear.

3.4. Directional damage and effectivity

3.4.1. Tension, compression and triaxial compression

Fig. 16 and Fig. 17 show the evolution of longitudinal and transversal secant stiffnesses as a function of the relaxed stress (stress at the end of

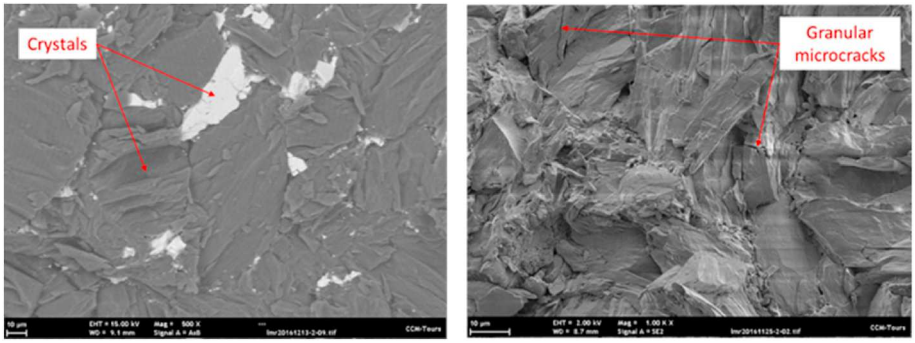

Fig. 6. Microstructure of the pristine material.

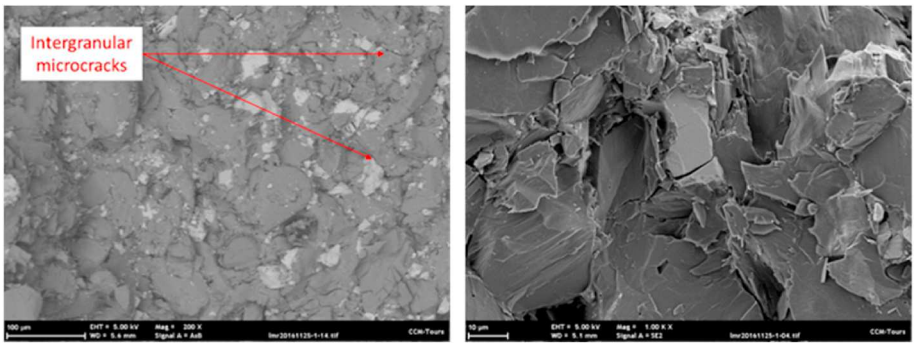

Fig. 7. Microstructure of the material loaded in tension.

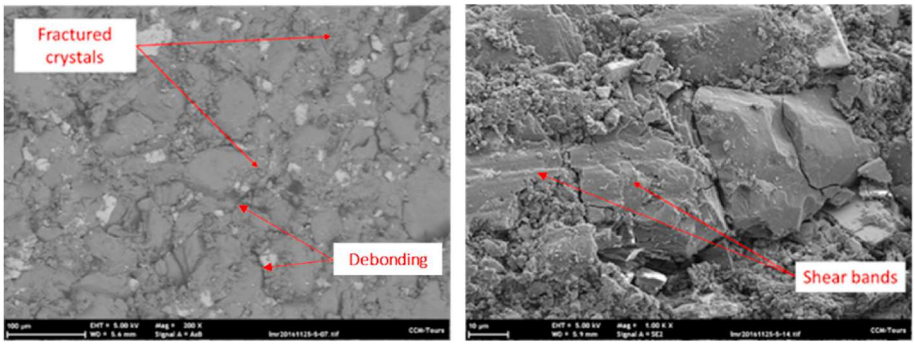

Fig. 8. Microstructure of the material loaded in compression.

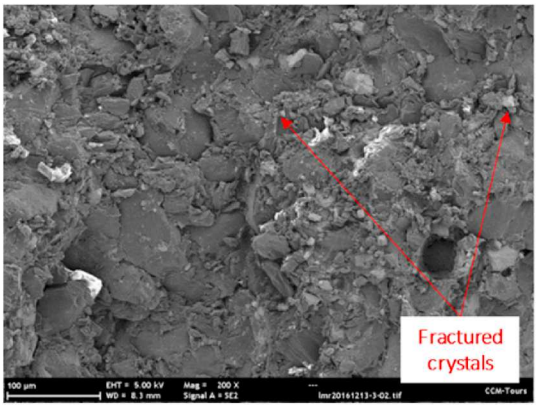

Fig. 9. Microstructure of the material loaded in channel die ($\sigma_{T-initial} = 1$ MPa).

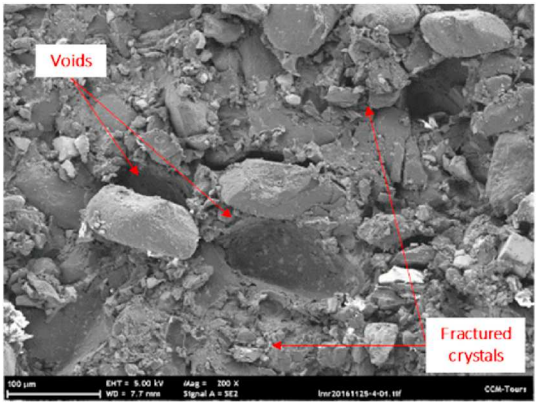

Fig. 10. Microstructure of the material loaded in channel die ($\sigma_L = \sigma_T$).

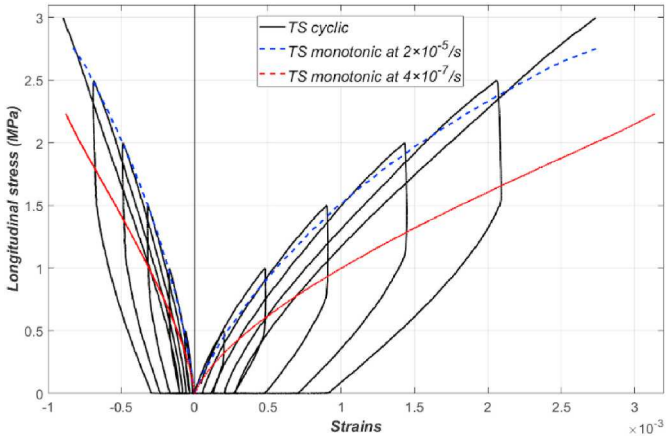

Fig. 11. Monotonic and cyclic tension at $\dot{\varepsilon} = 2 \times 10^{-5} s^{-1}$ and.$\dot{\varepsilon} = 4 \times 10^{-7} s^{-1}$

relaxation steps and without hydrostatic pressure). The behaviour difference between tension and compression can be observed clearly.

In tension, the longitudinal stiffness decreases from the beginning of the test, when, at the same time in compression, it increases first (until 60–70% of ultimate stress) and then decreases. For triaxial compression, the latter phenomenon is more pronounced: the stiffening happens in the confinement step yielding higher initial stiffness. The stiffness decreases, then, throughout the loading.

Taking into account the initial pre-damage in the microstructure, the direct opening of the microcracks, perpendicular to the solicitation, in tension, yields a quick brittle failure. In compression and triaxial compression, the initial microcracks tend to close first inducing a linear global material behaviour and later a ductile failure with irreversible strains.

The extrapolation of the stiffness curves to zero stress allows an

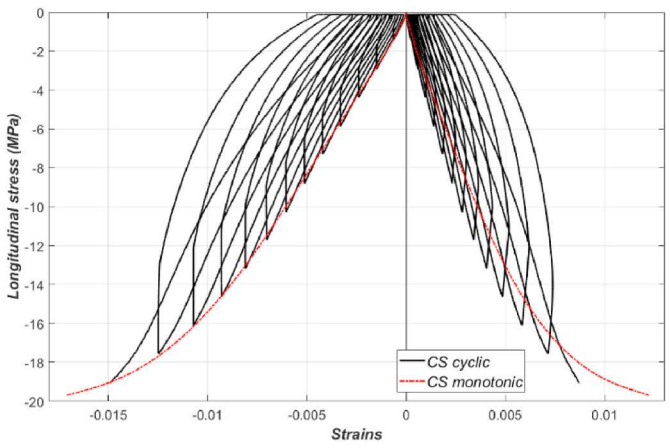

Fig. 12. Monotonic and cyclic compression at.$\dot{\varepsilon} = 2 \times 10^{-5} s^{-1}$

estimation of the initial secant stiffness E_0 for each test as seen in Table 1.

3.4.2. Tension-compression-tension and compression-tension-compression

The alternated tests, TCT and CTC, were developed and carried out to highlight the effectivity and the suspected phenomenon of the stiffness recovery during changes of stress or strain signs. The master stress–strain $(\sigma - \varepsilon)$ curves of the cyclic CTC and TCT are compared with those of CS and TS and shown in Fig. 18 and Fig. 19. The longitudinal and transversal strains are initialized to zero at the start of steps 2 and 3 in TCT and CTC. The analysis of the different evolutions revealed the following observations:

– The material responses in compression and in the first step of CTC (CTC/1) are relatively the same.
– The material response in the second step of TCT (TCT/2: compression preceded by tension) presents a lower stiffness in the beginning and a higher recovery than in compression. This is interpreted by a generated damage in tension (TCT/1). The damage is visible in the beginning of the test but rapidly "deactivated" by the closing of the microcracks throughout the loading.
– The material response in the third step of TCT (TCT/3: tension preceded by tension and then compression) is quasi-linear, contrary to a simple tension. The stiffness in TCT/3 is, from the beginning of the

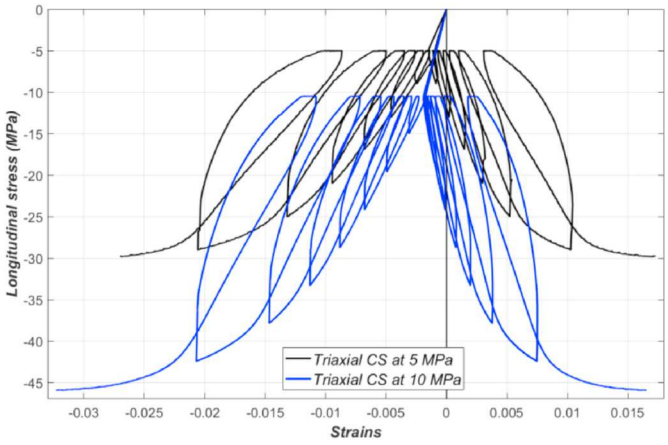

Fig. 15. Cyclic triaxial compression 5 MPa and 10 MPa at.$\dot{\varepsilon} = 2 \times 10^{-5} s^{-1}$

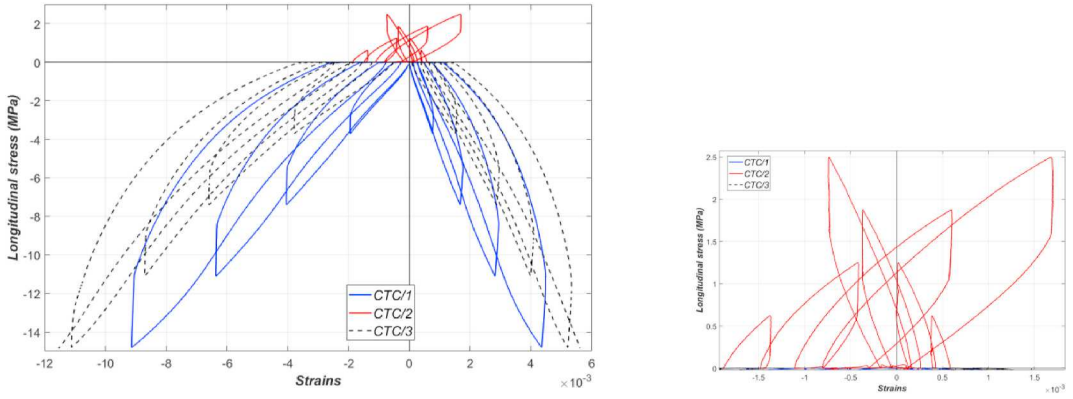

Fig. 13. Cyclic compression-tension-compression at.$\dot{\varepsilon} = 2 \times 10^{-5} s^{-1}$

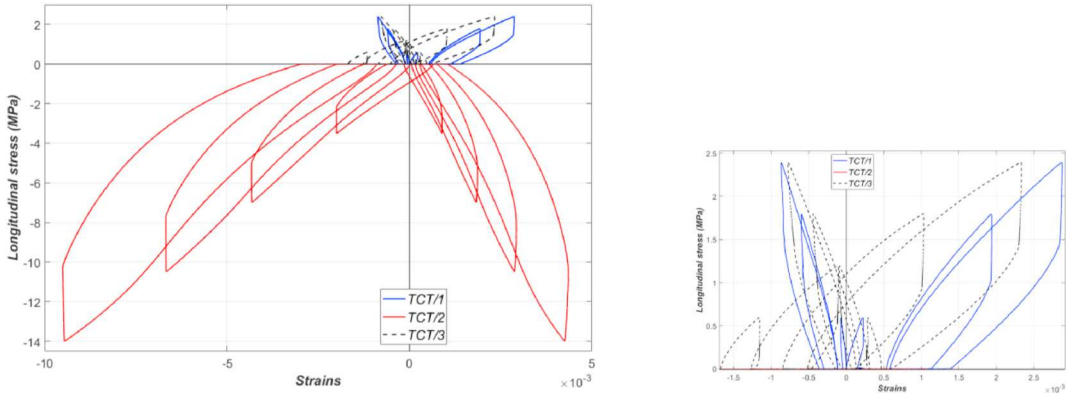

Fig. 14. Cyclic tension-compression-tension at.$\dot{\varepsilon} = 2 \times 10^{-5} s^{-1}$

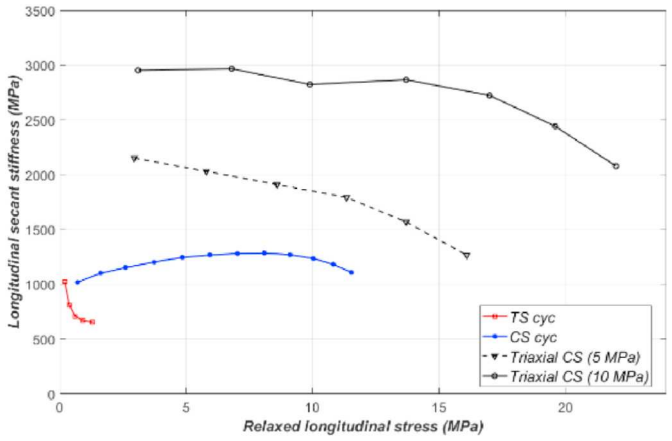

Fig. 16. Evolution of the longitudinal secant stiffness in function of relaxed longitudinal stress in tension, compression and triaxial compression.

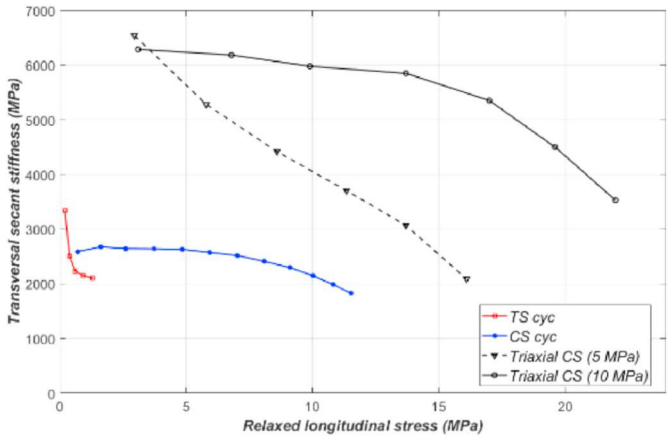

Fig. 17. Evolution of the transversal secant stiffness in function of relaxed longitudinal stress in tension, compression and triaxial compression.

Table 1
Initial longitudinal and transversal stiffnesses for tension, compression and triaxial compression (at 5 and 10 MPa).

Tests	E_L (MPa)	E_T (MPa)
Uniaxial tension	1000	3300
Uniaxial compression	1000	2600
Triaxial compression at 5 MPa	2150	6500
Triaxial compression at 10 MPa	3000	6300

test, is twice as low as those observed in simple tension, and contrariwise not decreasing throughout the rest of the test. It seems that the material had been degraded in the compression step (TCT/2) even if it isn't visible in the evolution of the stiffness; effectivity seems to prevent seeing the damage in compression, although visible in tension responses in CTC/2 and TCT/3.

– These observations can be seen in the evolution of longitudinal stiffness and especially in the transversal stiffness (see Figs. 20 and 21).

3.5. Contraction ratio

In the isotropic framework, the Poisson's ratio is defined from the ratio of the transversal elastic strain and the longitudinal elastic strain as, $\nu = -\varepsilon_T^e/\varepsilon_L^e$. Considering that irreversible strains don't develop during unloading and recovery, it's possible to plot the evolution of this

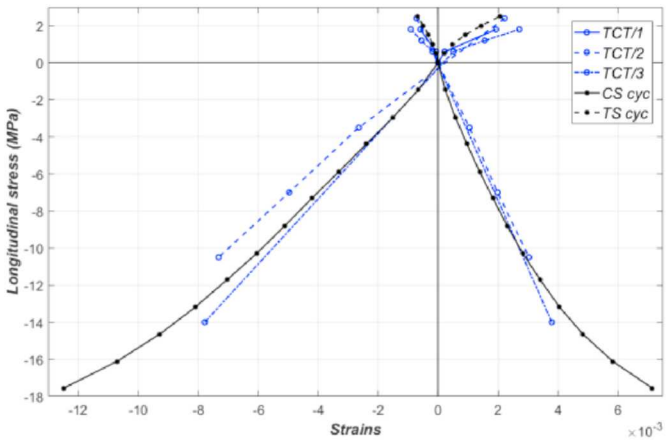

Fig. 18. Master curves for cyclic TCT, CS and TS.

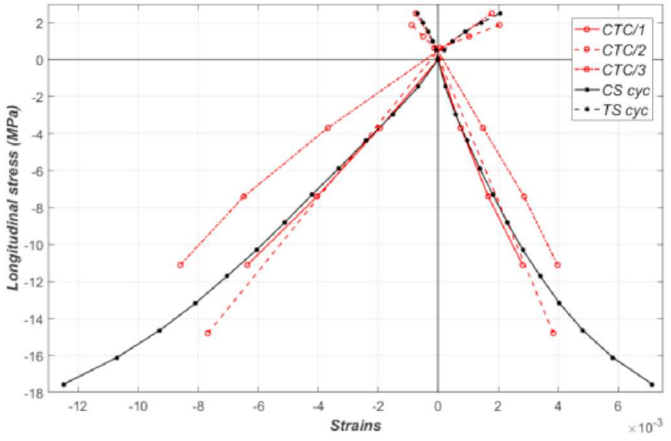

Fig. 19. Master curves for cyclic CTC, CS and TS.

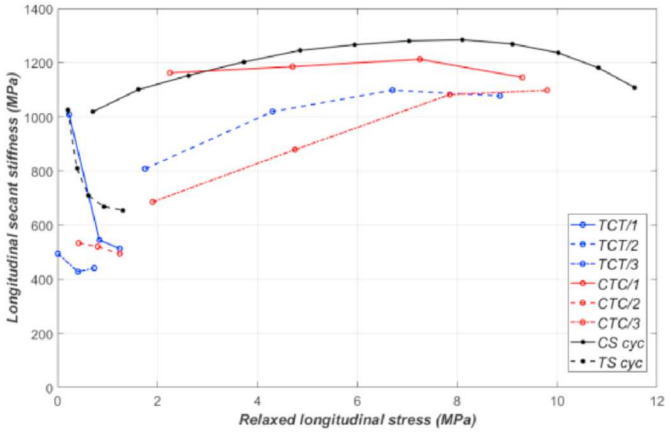

Fig. 20. Evolution of the longitudinal secant stiffness in function of relaxed longitudinal stress in cyclic TCT, CTC, compression and tension.

ratio for each test (Fig. 22). The obtained values are between 0.26 and 0.61. In the isotropic framework, this value shouldn't exceed 0.5. An explication of this phenomenon was advanced by Pecqueur (1995) and adopted with Dragon et al. (Bargellini et al., 2007) (Bargellini et al., 2008) for brittle aggregate materials invoking induced anisotropic damage by loading.

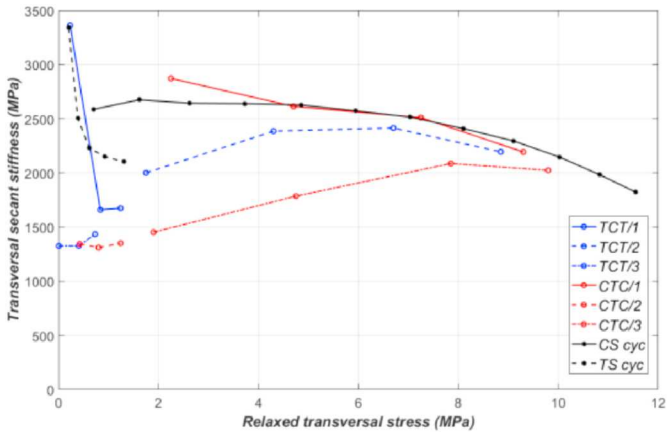

Fig. 21. Evolution of the transversal secant stiffness in function of relaxed longitudinal stress in cyclic TCT, CTC, compression and tension.

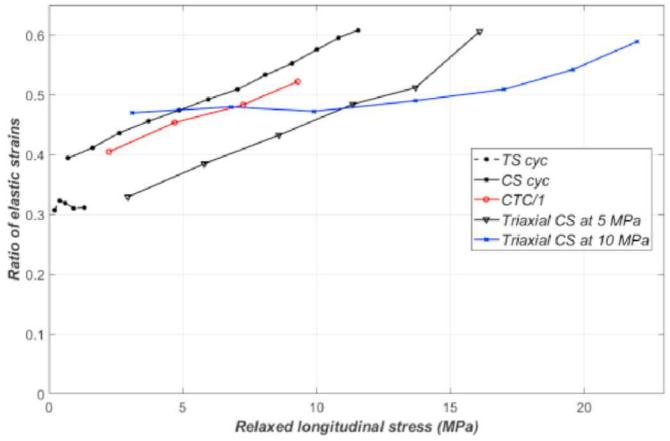

Fig. 22. Evolution of the contraction ratio in tension, compression, CTC/1 and triaxial compression at 5 and 10 MPa.

3.6. Strain rate dependency

The studied material presents a sensitivity to the strain rate, thus a viscoelasticity coming essentially from the polymeric binder. In cyclic tension, irreversible strains are very low and, so, the behaviour is considered mainly viscoelastic (Fig. 11). Two monotonic tension tests at two different strain rates 2.10^{-5}/s and 4.10^{-7}/s were carried out. The stress-strain $(\sigma - \varepsilon)$ curves, presented in the figure above (Fig. 11), clearly show a dependency of the response to the strain rates. Cyclic tests, at 2.10^{-5}/s, present relaxation and recovery steps that can be used to identify and analyse viscoelasticity. In Fig. 23, the evolution of longitudinal stress in relaxation steps at low stress levels in tension and compression is shown. The curves don't seem to present a difference, meaning that there isn't an effect of the opening/closing of microcracks between tension and compression at low stress levels.

At higher stress levels, in compression, it seems that the hydrostatic pressure doesn't have much effect on the stress in relaxation (Fig. 24). At the same level of stress in the beginning of relaxation, there is a very small difference between the response in compression and both responses in hydrostatic at 5 and 10 MPa. It should be noted that viscous phenomena can have viscoelastic part and a viscoplastic part because of the irreversible strains present at the end of recovery. Although ignoring this distribution during the relaxation phases, experimental results can still be analysed.

Curves showing the evolution, in time, of the ratio between longitudinal stress in relaxation steps σ_L and the stress at the beginning of the relaxation steps σ_0, are shown in Fig. 25. A nonlinearity, with respect to the stress level, is observed: curves are not superposed and with the increase of the stress level, the relaxation is slower.

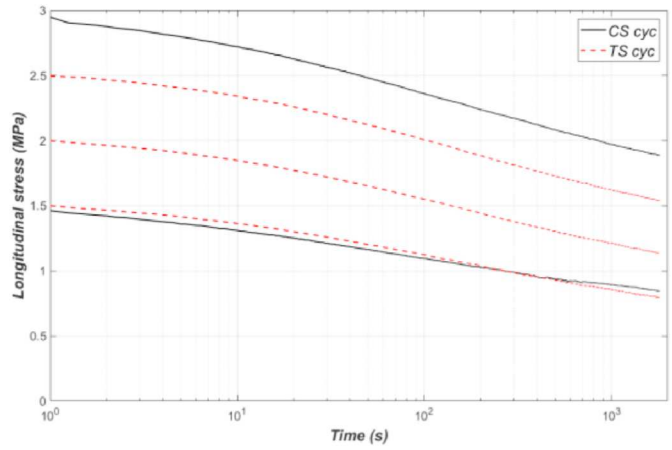

Fig. 23. Evolution of σ_L in relaxation steps at low stress levels in tension and compression.

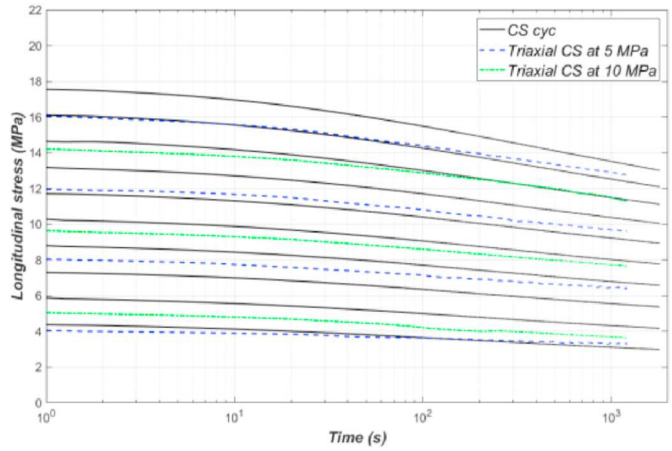

Fig. 24. Evolution of σ_L in relaxation steps in compression and triaxial compression at 5 and 10 MPa – Hydrostatic pressure effect.

Fig. 26 shows the first cycle of tension, TCT/3 and CTC/2. The material response in tension on a pristine material is different from tension

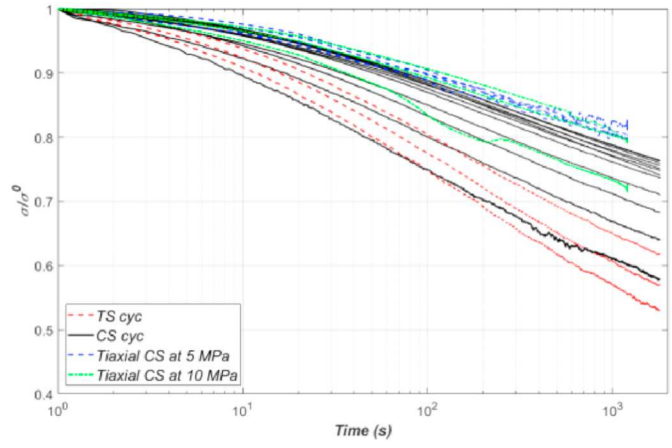

Fig. 25. Evolution of the ratio of σ_L and σ_0 (stress at the beginning of relaxation) in relaxation steps in tension, compression and triaxial compression – Stress level effect.

preceded with compression, which generates a lot of damage. In TCT/3 and CTC/2, the material relaxes more, thus reducing the relaxed stress approaching zero. The nonlinearity with respect to the stress level is more pronounced. Contrary to relaxation step, the material recovers very little yielding important irreversible strain even at low level of stress.

In order to cover a large range of strain rates, and to better analyse the viscoelastic behaviour, DMA tests were carried out on the material. Frequency sweeps between 1 and 520 Hz at two different amplitudes of dynamic strain (ε_{dyn}), respectively 10^{-4} and 2.10^{-4}. The tests cover a range of strain rate from 6.10^{-4}/s and 6.10^{-1}/s. The first test was made without a preload and therefore alternates tension and compression, for a maximum stress of 0.6 MPa. The second test was carried out with a static preload of -3.10^{-4}, which allows the specimen to be compressed with a stress of -2 MPa. The first step consisted in verifying the absence of nonlinearity for this level of solicitation. To do this, the specimen is loaded at a frequency of 1 Hz and a strain varying from 0 to 3×10^{-4}. A slight nonlinearity of the bulk modulus vis-à-vis the strain level appears. It decreases slightly (about 15%) while the loss modulus increases slightly (Fig. 27). No clear nonlinearity appears during the increasing sweep, relatively linear, and moreover, no irreversibility appears during the decreasing sweep which is superimposed on the increasing sweep and joins the starting point of the pristine material. The second step consists on performing frequency sweep. The dependency of the storage modulus and the loss modulus is important, since for the swept range, the variation is around 60–70% (Fig. 28). Finally, the tangent modulus at the origin of the two tensile tests (4.10^{-7}/s and 2.10^{-5}/s) and the compression test (2.10^{-5}/s) are reported on the curves describing the dynamic modules (Fig. 29). It can be noted that in all tests, the failure stress increases with increasing strain rate, as expected.

3.7. Biaxial strength

The developed experimental dispositive, called "Channel-die", allow to level up the absence of biaxial test machine. Those tests are mainly carried out to calibrate a failure criterion based on stress plane responses and to study the behaviour under biaxial loading. An example of a channel die test with $\sigma_T/\sigma_L = 0.5$, is presented in Fig. 30. The evolution of the longitudinal stress is plotted in function of the 3 measured strains. The transversal strain is close to the longitudinal strain observed in triaxial compression at 10 MPa, for a level of pressure, in terms of $Tr()$, slightly inferior. Table 2 presents the ultimate stresses and strains at break for all carried channel die tests corresponding to the following biaxiality levels, $\sigma_T/\sigma_L = \{0.083; 0.17; 0.34; 0.48; 0.92\}$. The tests are monotonic, so the measured stresses contain a viscous part.

It can be noted, the high level of positive transversal strain associated

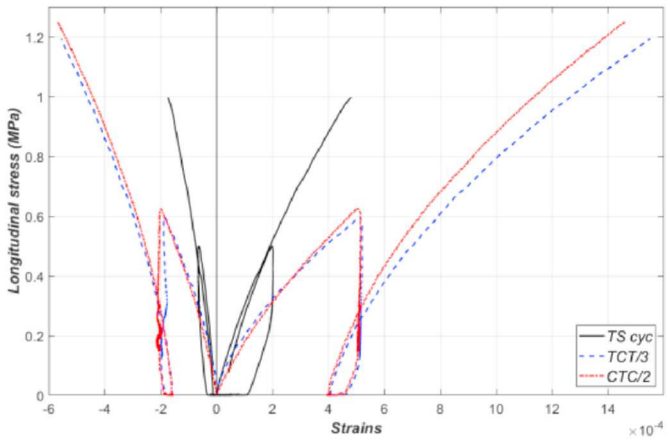

Fig. 26. First step in tension and tension preceded with compression (TCT/3 and CTC/2).

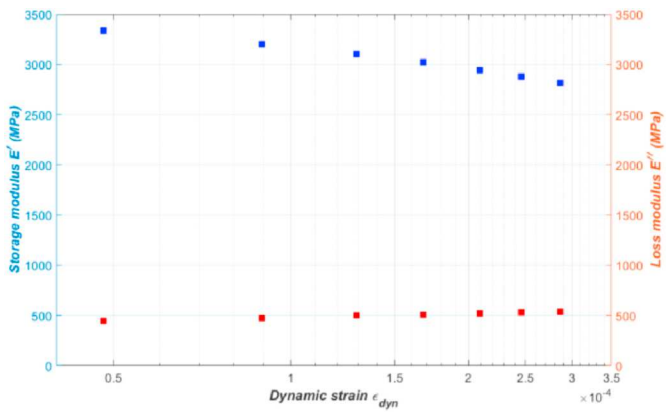

Fig. 27. Evolution of E′ and E″ in function of ε_{dyn} in DMA test with an amplitude sweep, $\varepsilon_{stat} = -3 \times 10^{-4}$ and f = 1 Hz.

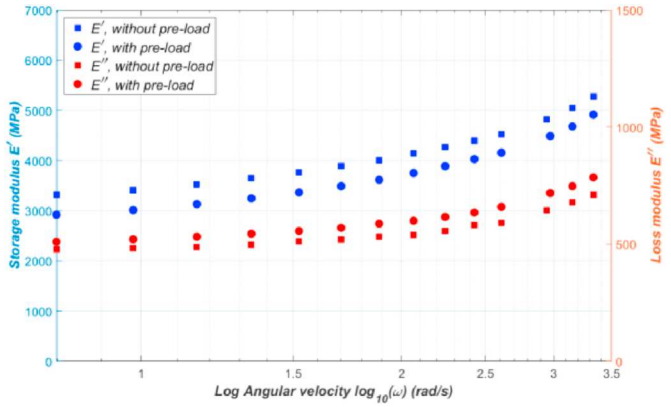

Fig. 28. Evolution of E′ and E″ in function of ω in DMA test with a frequency sweep without preload ($\varepsilon_{stat} = 0$ et $\varepsilon_{dyn} = 10^{-4}$) and with preload ($3 \times 10^{-4}$ et $\varepsilon_{dyn} = 2 \times 10^{-4}$).

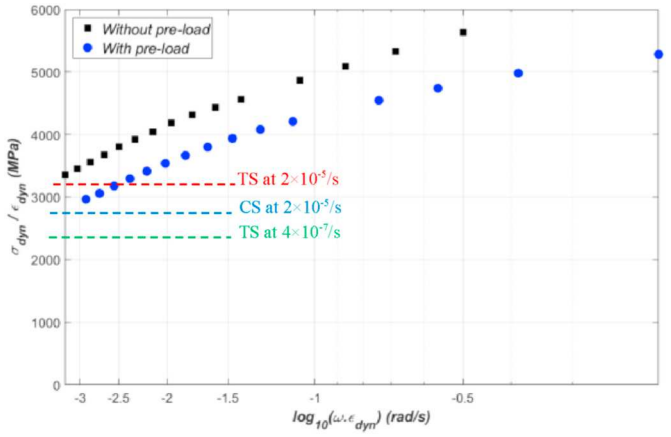

Fig. 29. Evolution of the ratio ($\sigma_{dyn}/\varepsilon_{dyn}$) in function of ($\omega \times \varepsilon_{dyn}$) in DMA test with a frequency sweep without preload ($\varepsilon_{stat} = 0$ and $\varepsilon_{dyn} = 10^{-4}$) and with preload ($\varepsilon_{stat} = -3 \times 10^{-4}$ and $\varepsilon_{dyn} = 2 \times 10^{-4}$).

to the free transversal direction translating thus, the dilatant character of the material.

The material strength under biaxial loading is clearly higher than under uniaxial compression: in fact, the strength increases with increasing biaxiality ratio, reaching 70% growth in the equibiaxial compression $\sigma_T/\sigma_L \approx 1$. To highlight this phenomenon, the failure

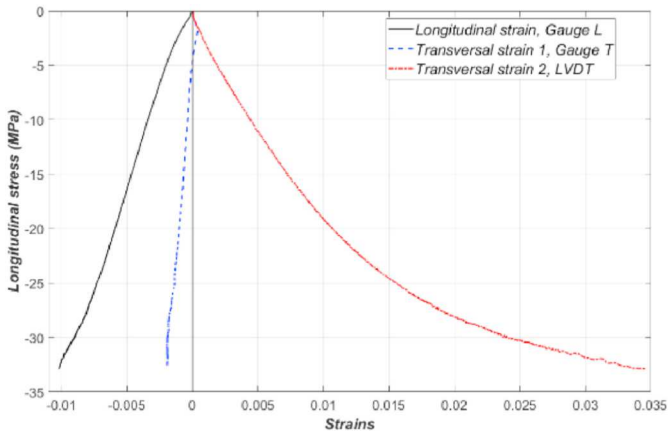

Fig. 30. Evolution of the longitudinal stress in function of the strains in channel die test with $\sigma_T/\sigma_L = 0.5$.

Table 2
Ultimate stresses and strains at break for channel die tests.

Channel-die	σ_L (MPa)	σ_{T1} (MPa)	σ_{T2} (MPa)	ε_L (%)	ε_{T1} (%)	ε_{T2} (%)
$\sigma_{T-initial} = 1$ MPa	−26.47	−4.42	0	−1.072	0.537	3.792
$\sigma_T = 2$ MPa	−24.76	−2.054	0	−1.416	0.561	2.283
$\sigma_T = 10$ MPa	−31.51	−10.8	0	−0.679	−0.063	2.739
$\sigma_T/\sigma_L = 0.5$	−32.88	−15.67	0	−1.021	−0.196	3.453
$\sigma_T = \sigma_L$	−34.98	−32.2	0	−0.564	−0.418	3.838

stresses of compression test and channel die tests are plotted in the plane $(\sigma_1/|\sigma_{uc}|, \sigma_2/|\sigma_{uc}|)$ (Fig. 31). The failure stresses are normalized by the uniaxial compressive strength σ_{uc}.The failure points present an increasing nonlinear evolution with an opening envelope translating thus the previous observations.

This behaviour can be interpreted from the increase of the contact surfaces between the crystals in compression and thus the resulting cohesion from friction. More, the biaxial compression generated in this type of tests leads to blocking or compressing the transversal strain (ε_{T1}), which prevents the propagation of the damage, thus increasing the apparent resistance by confinement effect.

3.8. Irreversible strains

Unloading steps followed by recovery steps highlight the presence of irreversible strains of plasticity or inter-granular friction type. The curves in Fig. 32 show the evolution of the relaxed Von Mises stress as a function of irreversible longitudinal and transversal strains, for tension, compression and triaxial compression tests. In tension, irreversible strains are very low, and the behaviour is mainly viscoelastic. In compression, the levels of irreversible strains are higher: as mentioned above, in compression, the contact surface between crystals becomes important and a shear is developed in the microstructure of the material. This phenomenon is even more pronounced in triaxial compression where the material is consolidated under hydrostatic pressure.

It is difficult to find, at the same time, an internal variable of irreversible strain and an equivalent stress that could, by means of plasticity law, describe all tests with the same hardening curve.

In Fig. 33, the relaxed Von Mises stress is plotted in function of the deviatoric plastic strain $\dot{\varepsilon}^p_{Dev} = \sqrt{\frac{2}{3}\dot{\varepsilon}^p_{Dev} : \dot{\varepsilon}^p_{Dev}}$. The differences between the curves suggest that the deviatoric strain can't be linked to the same level of Von Mises stress for the different tests.

An eventual consolidation effect is inspected. For this, the deviatoric irreversible strain is plotted in function of the deviatoric stress increased by the triaxial pressure weighted by a consolidation term c, $\sigma^{Mises} + c.\frac{1}{3}Tr(\sigma)$ in Fig. 34. The curves are dispersed, and one consolidation parameter is not enough to obtain a representative model for the conducted tests, especially for low stress levels.

A concept of an effective quantity in plasticity could also be explored with a view to establish a hardening law.

Fig. 35 shows the evolution of the irreversible volumetric strain $\varepsilon^p_{Vol} = Tr(\varepsilon^p)$ in function of the deviatoric strain ε^p_{Dev}. It's noticed first that the level of the volumetric strain remains low compared to the deviatoric strain. The triaxial compression at 10 MPa presents the highest irreversible volumetric strain. Tension presents a dilatant behaviour from the beginning and stays very low. In compression, the behaviour becomes quasi deviatoric. When a hydrostatic pressure of 5 MPa is applied, the material seems highly dilatant from the beginning of the test. This observation is not expected for this test and probably coming from the high transversal strain observed at 5 MPa of hydrostatic pressure.

The channel die test with ratio 0.5, being monotonous, doesn't allow reporting points associated to the dilatancy. However, the 3 strains, in Fig. 30, show an important positive volumetric strain, same as in triaxial compression at 5 MPa. It seems that the hydrostatic pressure consolidates, in terms of stress and stiffness, without generating negative volumetric flow as seen in triaxial compression at 10 MPa.

In the latter test, triaxial compression at 10 MPa, the presence of an important initial porosities allows a first step of contraction depending on the reached pressure level. It seems that the material presents different physical phenomena in test with low level of confinement at

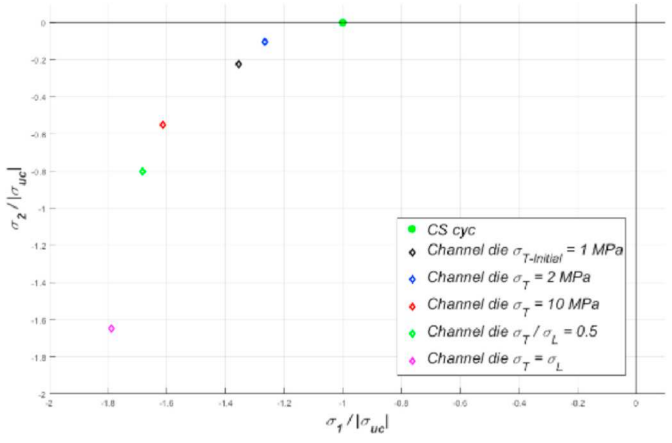

Fig. 31. Failure stresses plotted in the stress plane.

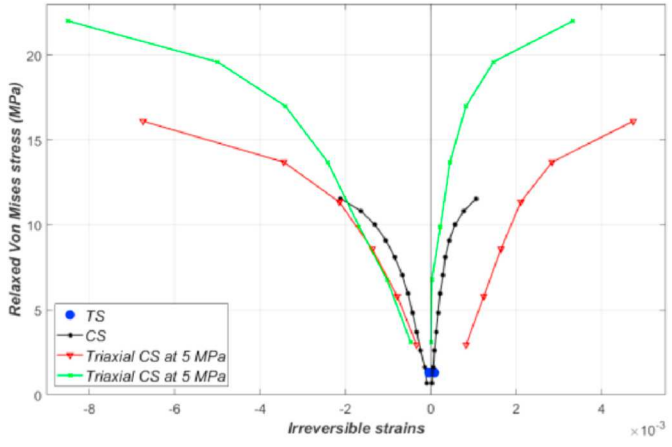

Fig. 32. Evolution of relaxed Von Mises stress in function of irreversible strains in tension, compression and triaxial compression at 5 and 10 MPa.

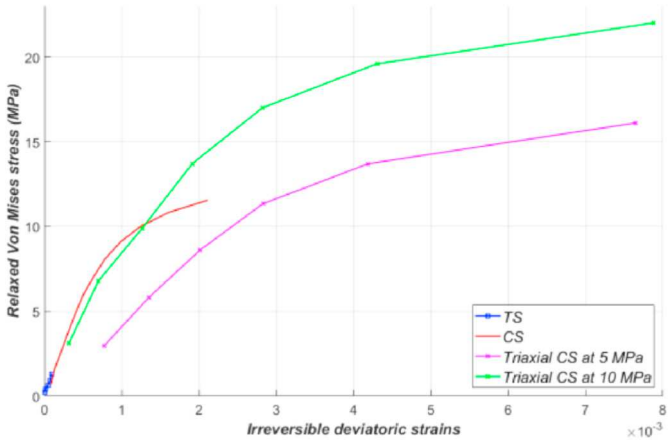

Fig. 33. Evolution of relaxed Von Mises stress in function of deviatoric irreversible strains in tension, compression and triaxial compression at 5 and 10 MPa.

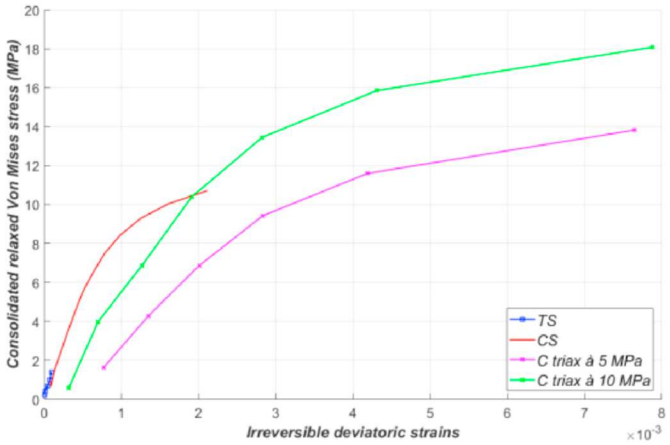

Fig. 34. Evolution of consolidated relaxed Von Mises stress in function of irreversible strains in tension, compression and triaxial compression at 5 and 10 MPa.

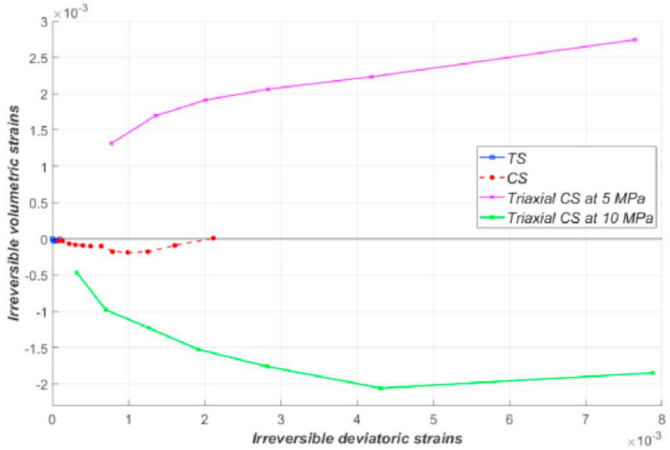

Fig. 35. Evolution of irreversible volumetric strains in function of deviatoric irreversible strains in tension, compression and triaxial compression at 5 and 10 MPa.

high level of confinement. This response is difficult to interpret but suggests the need to do additional tests at intermediate hydrostatic pressure levels and arouses the question of the flow limit under only spherical confinement that exceeds 10 MPa.

4. Modelling of the damage induced anisotropy and effectivity functions

4.1. Microplane model for plastic-bonded explosives

This approach states that each direction of the solid angle characterizes a microplane on which the strain is decomposed. It should be noted that Microplane approach is not a micro-macro homogenisation model but rather a spatial partition. Constitutive equations are defined in the microplane level where the existence of free energy is assumed. The global stress tensor is determined by angular integration of the microplane stress vector over the whole solid angle. The global free energy Ψ^{glo} is equal to the angular integral over the entire solid angle Ω of the angular free energy density, expressed as $\Psi^i/4\pi$ and associated to each plane defined by its normal vector $\underline{n}^i$:

$$\psi^{glo} = \frac{3}{4\pi}\int_{\Omega} \psi^i\left(\underline{t}_{\varepsilon}, q\right) d\Omega \qquad \text{(Eq. 1)}$$

where the subscript i denotes the microplane orientation, $\underline{t}_{\varepsilon} = \underline{\underline{\varepsilon}}.\underline{n}^i$ represents a deformation vector and q is a set of state variables. The global stress tensor $\underline{\underline{\sigma}}$ is defined by the partial derivative of the free energy Ψ^{glo} with respect to the strain tensor $\underline{\underline{\varepsilon}}$:

$$\underline{\underline{\sigma}} = \frac{\partial \rho_0 \psi^{glo}}{\partial \underline{\underline{\varepsilon}}} = \frac{3}{4\pi}\int_{\Omega} \frac{\partial \rho_0 \psi^i\left(\underline{t}_{\varepsilon}, q\right)}{\partial \underline{\underline{\varepsilon}}} d\Omega \qquad \text{(Eq. 2)}$$

It should be noted that variables underlined with one line are vectors, those underlined with two lines are twice rank tensors and those underlined with four lines are fourth rank tensors.

Many different Microplane formulations exist in the literature, based on the strain decomposition (Normal-shear, volumetric-deviatoric, etc.). Carol et al. (Carol et al., 2001) proposed a thermodynamically consistent Microplane model with a Volumetric-Deviatoric-Tangential (V-D-T) split, i.e., with a decomposition of the strain tensor to volumetric, deviatoric and tangential components respectively noted ε_V, ε_D and $\underline{\varepsilon}_T$ and expressed as follows in each microplane:

$$\varepsilon_V = \frac{1}{3}\underline{\underline{1}} : \underline{\underline{\varepsilon}} = \underline{\underline{V}} : \underline{\underline{\varepsilon}} \qquad \text{(Eq. 3)}$$

$$\varepsilon_D = \left(\underline{n} \otimes \underline{n} - \frac{1}{3}\underline{\underline{1}}\right) : \underline{\underline{\varepsilon}} = \underline{\underline{D}} : \underline{\underline{\varepsilon}} \qquad \text{(Eq. 4)}$$

$$\underline{\varepsilon}_T = \left(\underline{n} \cdot \underline{\underline{I}} - \underline{n} \otimes \underline{n} \otimes \underline{n}\right) : \underline{\underline{\varepsilon}} = \underline{\underline{T}} : \underline{\underline{\varepsilon}} \qquad \text{(Eq. 5)}$$

Equations (3)–(5) define the projection of the global strain tensor on a microplane. It should be noted that ε_V is isotropic in the material. These strains allow the determination of stresses in a microplane with the following state laws:

$$\sigma_V = \frac{\partial \rho_0 \psi^i\left(\underline{t}_{\varepsilon}, q\right)}{\partial \varepsilon_V} \qquad \text{(Eq. 6)}$$

$$\sigma_D = \frac{\partial \rho_0 \psi^i \left(\underline{\varepsilon}, q \right)}{\partial \varepsilon_D} \quad \text{(Eq. 7)}$$

$$\underline{\sigma}_T = \frac{\partial \rho_0 \psi^i \left(\underline{\varepsilon}, q \right)}{\partial \underline{\varepsilon}_T} \quad \text{(Eq. 8)}$$

The global stress tensor is then evaluated from the stresses defined in the microplanes by an integral over the solid angle Ω, using the following equation:

$$\underline{\underline{\sigma}} = \frac{3}{4\pi} \int_{\Omega} \left\{ \sigma_V . \underline{\underline{V}} + \sigma_D . \underline{\underline{D}} + \underline{\sigma}_T . \underline{\underline{T}} \right\} \quad \text{(Eq. 9)}$$

When the Microplane approach is used to model only damageable elasticity, a global potential can be expressed by integration by taking into account a damaged elastic global anisotropic operator. Microplane approach can be used in this case only to define this operator without introducing all the variables at the level of microplanes. To model the induced anisotropic damage of the material, the free energy is defined as follows (Picart et al., 2014):

$$\psi^i = \frac{1}{2} E_V (1 - \alpha_V(\varepsilon_V) d_V) \varepsilon_V^2 + \frac{1}{2} E_D (1 - \alpha_D(\varepsilon_D) d_D) \varepsilon_D^2 + \frac{1}{2} E_T (1 - d_T) \underline{\varepsilon}_T . \underline{\varepsilon}_T \quad \text{(Eq. 10)}$$

In this equation, three damage variables d_V, d_D and d_T that affect the corresponding elastic moduli denoted, respectively, E_V, E_D and E_T, are introduced. These moduli are related to the bulk and shear global parameters K and μ as follows: $EV = 3K$ and $2ED + 3ET = 10\mu$ (Carol et al., 2001). The damage is calculated at the level of microplanes. d_V is the same for all microplanes since ε_V is isotropic. d_D and d_T are calculated individually for each microplane, based on ε_D and $\underline{\varepsilon}_T$.

α_V and α_D are the effectivity functions defined, respectively, in terms of volumetric strain and deviatoric strain for each microplane. These effectivity functions manage the opening/closure of microcracks, asymmetry of the behaviour between tension and compression and the effect of hydrostatic pressure. It has been assumed that d_T is not affected by the effectivity. To avoid a spurious dissipation and discontinuity in the model responses and to obtain simple constitutive laws, α_V and α_D depend on their associated strain components. In the proposed model, the damage depends on the total strain. Volumetric and deviatoric damages are supposed effective when volumetric strain and deviatoric strain are positive, respectively. In the opposite case, the volumetric strain is supposed deactivated. For the deviatoric strain, a partial recovery of the deviatoric model is considered with $\alpha_D(\varepsilon_D) = 0.5$.

The assumed relationships between damage variables and their associated forces F_V, F_D and F_T are given in terms of ε_V, ε_D and $\underline{\varepsilon}_T$ respectively for each microplane:

$$F_V = -\frac{\partial \rho_0 \psi^i}{\partial d_V} = \frac{1}{2} E_V \alpha_V(\varepsilon_V) \varepsilon_V^2 \quad \text{(Eq. 11)}$$

$$F_D = -\frac{\partial \rho_0 \psi^i}{\partial d_D} = \frac{1}{2} E_D \alpha_D(\varepsilon_D) \varepsilon_D^2 \quad \text{(Eq. 12)}$$

$$F_T = -\frac{\partial \rho_0 \psi^i}{\partial d_T} = \frac{1}{2} E_T \underline{\varepsilon}_T . \underline{\varepsilon}_T \quad \text{(Eq. 13)}$$

Considering the effect of the pressure on the damage evolution and the dependency of this damage on strain, the following phenomenological relations have been proposed by (Picart et al., 2014) in a microplane:

$$d_{V,D,T}\left(F_{V,D,T}, p\right) = \max\left(d^0_{d^{V,D,T}}, 1 - \exp\left[-p\left(a_1 F_{V,D,T}\right)^{a_2} \right] \right)_t, \; 0 \le d_{d^{V,D,T}} \le 1 \quad \text{(Eq. 14)}$$

where:

$$p = 1 + [a_3 . H(-\varepsilon_V) + a_4 . H(\varepsilon_V)] E_V \langle \varepsilon_V - \varepsilon_V^{0-H10} \rangle_+ \quad \text{(Eq. 15)}$$

The effectivity functions are defined as follows:

$$\begin{cases} \varepsilon_V \ge 0 \rightarrow \alpha_V(\varepsilon_V) = 1 \\ \varepsilon_V < 0 \rightarrow \alpha_V(\varepsilon_V) = 0 \end{cases} \quad \begin{cases} \varepsilon_D \ge 0 \rightarrow \alpha_D(\varepsilon_D) = 1 \\ \varepsilon_D < 0 \rightarrow \alpha_D(\varepsilon_D) = 0.5 \end{cases} \quad \text{(Eq. 16)}$$

In the previous equations, d^0_{VDT} is the initial damage in the material. The material parameters a_1 and a_2 manage the evolution of the damage versus the strain, and a_3 and a_4 manage the dependency of the damage on the pressure. The pressure dependency is carried out through the function p given by Eq. (14), where ε_V^{0-H10} is a third of the negative volumetric strain reached after hydrostatic compaction of 10 MPa. Thus, $p = 1$ in the beginning of the compression phase in the triaxial compression at 10 MPa ($\varepsilon_V = \varepsilon_V^{0-H10}$) and $p \gg 1$ in the beginning of the uniaxial compression.

Two damage evolution laws were integrated to manage the asymmetry between tension and compression based on ε_V in Eq. (15). Fig. 36 shows the effect of the parameters on the damage evolution.

The main limit of the models based on an additivity of oriented damages comes from the impossibility to experimentally identify the effect of each oriented microcracks group on the global mechanical response of the material. Thus, the parameters related to the damage evolution should be calibrated by comparing the numerical predictions of the material global behaviour to the test data.

4.2. New damage evolution laws and effectivity functions

4.2.1. Pre-damage

The pre-damage defined above allows the stiffness in tension to be properly adjusted since the damage is effective from the beginning. For compression and triaxial compression, this does not seem sufficient. A stiffening effect is therefore introduced into the model; the pressure acts both on the compressibility modulus K and on the shear modulus μ, but in two different ways.

4.2.2. Nonlinear volumetric elasticity

For the compressibility modulus K, the stiffening is considered as a non-linear function of the volumetric strain with a stiffening coefficient r_K as shown below. This parameter allows to describe the observed stiffening at the end of the pressurization cycles in triaxial compression tests. Heaviside-type effectivity functions alone can't describe this evolution. Thus, the compressibility modulus is defined as follows:

$$K_{ref} = \frac{E}{3(1 - 2\upsilon)} \quad \text{(Eq. 17)}$$

If

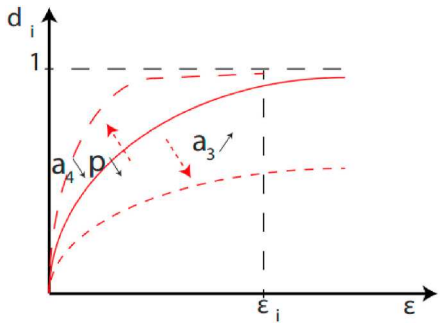

Fig. 36. Damage evolution law (Benelfellah et al., 2014).

$$\varepsilon_V \leq 0 : K = \frac{K_{ref}}{(1 + r_K \varepsilon_V)^2} \text{ with } (\varepsilon_V < 0 \text{ in compression}) \quad \text{(Eq. 18)}$$

–If not: $K = K_{ref}$

with υ is Poisson's ratio.

4.2.3. Elastic parameters

It has been observed that the modulus of the materials varies approximatively between around 1000 MPa in the beginning of uniaxial compression to 3000 MPa in the beginning of triaxial compression at 10 MPa of hydrostatic pressure. The Young's modulus of the material, considered not damaged, will be taken as observed in the beginning of the triaxial compression. An important level of pre-damage allows then, via an effectivity parameter, to find the initial modulus (lower) in uniaxial compression. The effectivity which allows this stiffness recovery is related to the shear moduli and is a function of the volumetric strain.

4.2.4. Damage evolution laws

Damage evolution laws are driven by the total deformation (and not the elastic deformation). In fact, the material response under triaxial compression presents a stress plateau during which the product of the elastic deformation by the Young's modulus is constant (ε^eE), which will lead to blocking the damage if it has been driven by ε^e, not observed experimentally.

To adjust the evolution of the damage, the two parameters a_1 and a_2 of Eq. (14) must be identified. These two parameters are chosen identical in Benelfellah's model for the three damage variables, even if the model gives us the possibility of having different parameters for d_V, d_D and d_T, and therefore to adjust their evolutions separately. It is assumed in the model that the three damage variables do not evolve in the same way. In tension, the normal to the failure surface is oriented according to the direction of the load. This suggests that it's the deviatoric damage d_D that predominantly develops there. In addition, we observed experimentally that the damage evolves as a function of the positive deformation, therefore as a function of the longitudinal deformation in tension, and transverse in compression. This encourages us to define the force that drives the deviatoric damage with a positive part, replacing Eq. (12):

$$F_D = \frac{1}{2}\alpha_D E_D \varepsilon_{D_+}^2 \quad \text{(Eq. 19)}$$

In compression, it is rather the tangential damage d_T which is predominant since the failure is manifested according to the 45° failure surface. For the tangential strain, there is no effectiveness in Benelfellah's model. Also, the force which drives the evolution of tangential damage is defined as a replacement for Eq. (13):

$$F_T = \frac{1}{2}\alpha_T E_T \boldsymbol{\varepsilon}_T . \boldsymbol{\varepsilon}_T \quad \text{(Eq. 20)}$$

The volumetric pre-damage is conserved. The force driving the volumetric damage is defined same as in Eq. (11). The damage evolution laws contain a function p defined as a function of the positive part and the negative part of the volumetric deformation, which reflects the effect of pressure on the evolution rate of damage. This function slows down (resp. accelerates) the evolution of damage under the effect of negative volumetric strain (resp. positive volumetric strain). This is redundant with the effectivity functions that deactivate (resp. activate) the effect of the damage according to the sign of the volumetric deformation. In our model, it's supposed that the effectivity with manage this effect in compression and only on the case of positive volumetric deformation, the damage evolution is accelerated by p. We therefore suggest defining the pressure the pressure function p only as a function of the positive volumetric deformation, replacing Eq. (15) as follows:

$$p = 1 + a_3 E_V \varepsilon_{V+} \quad \text{(Eq. 21)}$$

Considering the mentioned observations above, three damage evolution laws are defined, for the three different damage variables for each microplane, replacing Eq. (14):

$$d_{V,D,T}\left(F_{V,D,T}, p\right) = max\left(d^0_{V,D,T}, 1 - exp\left[-p\left(a_{1V,D,T} F_{V,D,T}\right)^{a_2}\right]\right)_t \quad \text{(Eq. 22)}$$

with $0 \leq d_V, d_D, d_T \leq 1$.

4.2.5. Effectivity functions

To have a thermodynamically consistent model, the effectivity functions α_V, α_D and α_T must be defined in functions of their respective deformations ε_V, ε_D and ε_T. This does not seem sufficient to model the stiffening of the behaviour in function of the pressure and the nonlinearity in unloading steps. We will, thus, propose an effectivity function defined exclusively in function of the volumetric deformation ε_V. For the relatively proportional loading paths, it seems that the thermodynamics is relatively respected. During simulations, an energy balance will allow to assess this assumption. The effectivity functions initially defined, are based on Heaviside functions. The sudden variation of such a function does not correspond to what we want to describe, namely a gradual recovery of rigidity. We state that the damage is gradually deactivated by passing from a positive volume strain to a negative volume strain. A tabulated law was thus proposed and defined between the responses of compression and triaxial compression at 5 MPa and a function between the triaxial compressions at 5 MPa and at 10 MPa. The damage is supposed to be completely deactivated, i.e., $\alpha_T = 0$, for a volumetric strain value, ε_V^{0-H10} to which it is considered that all the microcracks are closed. Nevertheless, there exist two different cases of loading with negative volumetric strain, compression and triaxial compression at two levels of pressure. The evolution of the effectivity function cannot be the same for a uniaxial test and a triaxial test. Fig. 37 shows the change in tangential effectivity as a function of the volume deformation.

The equations below define the function of tangential effectivity in the model:

– If $\varepsilon_V \geq 0$, $\alpha_T = 1$
– If $0 \geq \varepsilon_V \geq \varepsilon_V^{0-H5}$: $\alpha_T = 1 - \frac{1}{\beta \varepsilon_V^{0-H10}} \varepsilon_V$

If

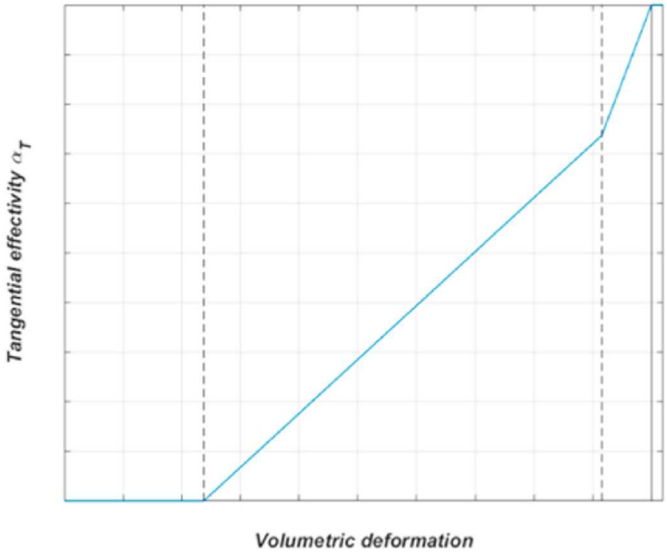

Fig. 37. Evolution of the tangential effectivity in function of the volumetric deformation.

$$\varepsilon_V^{0-H5} \geq \varepsilon_V \geq \varepsilon_V^{0-H10} : \alpha_T = \delta_a \varepsilon_V + \delta_b \quad \text{(Eq. 23)}$$

With

$$\delta_a = \frac{1 - \frac{1}{\beta}\frac{\varepsilon_V^{0-H5}}{\varepsilon_V^{0-H10}}\varepsilon_V}{\varepsilon_V^{0-H5} - \varepsilon_V^{0-H10}} \quad \text{(Eq. 24)}$$

with $\delta_b = -\delta_a \varepsilon_V^{0-H10}$ and β is a parameter to identify.

ε_V^{0-H10} is the volumetric deformation at which the damage is no longer effective, i.e, $\alpha_T(\varepsilon_V^{0-H10}) = 0$. ε_V^{0-H5} is the volumetric deformation that defines the slope change of the tangential effectivity function.

Due to the complexity of the identification, we will simplify the model here by assuming that the deviatoric effectiveness evolves in the same way as the tangential effectiveness:

$$\alpha_D = \alpha_T \quad \text{(Eq. 25)}$$

The difficulty of such model is the calibration. The parameters of the model drive the rate of evolution of the damage and the effectivity that evolve progressively at the same time. The combination of these two physical phenomena should give the desired material behaviour and especially the desired damaged modulus evolution.

The calibration and the simulations of all the tests will be detailed in future works.

This research work gave many interesting perspectives. Two major points will be discussed in the future works. Two additional non-proportional tests, 0°–90° compression, torsion and confined torsion will give an additional insight on the material behaviour. The 0°–90° compression test will give an additional light as to the longitudinal stiffness associated with the transverse direction. This information isn't available in all the previous tests. The torsion and confined torsion tests will allow the analysis of the damage and the effectivity in different planes under positive and negative strains evolving at the same time.

Also, an anisotropic viscoelastic-plastic model is needed to model the studied behaviour. The material presents an important viscous component that should be taken into account in an anisotropic framework. Also, the evolution of irreversible strains seems complex and could be modelled using multiple load surfaces defined in the different microplanes.

5. Conclusion

An original experimental study of a simulant material for Plastic-Bonded explosives composed of uniaxial, cyclic, alternated, and non-proportional tests was presented in this article.

Microstructural observations show an initial pre-damage in the pristine material generated by the manufacturing process. The microstructure is initially considered isotropic in the sense that it doesn't have a preferred microcracks orientation. These microcracks evolve randomly under loading with different failure mechanisms. In tension, binder-crystals debonding is observed with inter-granular cracks. Granular cracks and fracture crystals are still present but rarely observed. Compression presents a more violent damage with fractured crystals and shear bands.

These different phenomena yield a complex macroscopic behaviour. The opening/closing of microcracks in tension/compression under the longitudinal strains induces an asymmetry of behaviour. In tension, the behaviour is brittle, and the damage evolves rapidly unlike compression where the material shows a stiffening behaviour at the beginning and then softening. The alternated tests highlight the presence of damage effectivity which plays a role of the same order or even predominant, in the evolution of stiffness in terms of degradation, and in recovery.

Under biaxial compression, higher strengths than in uniaxial compression were shown. In the triaxial compression, the sensitivity of the material to pressure was observed. The confinement of the material increases its rigidity, as well as the stress and the strain at break.

Regarding the sensitivity of the behaviour to the strain rate, the cyclic tests with relaxation and recovery steps and the DMA tests show a viscoelasticity which can be considered linear and independent of the pressure.

Finally, the evolution of irreversible deformations in the various tests was underlined. Its evolution seems complex. A single load surface controlling the evolution of the load surface using simplifying assumptions seems a strong hypothesis. A complex dilating nature has been observed also.

This experimental investigation highlighted the complexity of the damage evolution and effectivity phenomena in the material. The existing models are simplistic and enable to model the evolution of the damaged stiffness of the material. The proposed evolution stipulated a directional damage following microplanes orientation with volumetric, deviatoric and tangential components. Volumetric effectivity is defined with Heaviside functions while the deviatoric and tangential effectivity functions are a linear function with two different slopes based on the level of hydrostatic pressure ensuring thus a progressive closure of microcracks in function of the negative volumetric deformation.

This experimental investigation will be used to develop and identify a constitutive material model taking into account damage induced anisotropy, effectivity, viscoelasticity and plasticity. The proposed model will be completed with viscoelasticity (as in (Chatti et al., 2019)) and plasticity embedded in the microplanes. The available experimental data will be used to calibrate the material parameters and then simulate the cyclic uniaxial, multiaxial, proportional, and non-proportional tests.

Author statement

Conception and design of study: M. Chatti, M. Gratton, M. Caliez, A. Frachon, D. Picart; Acquisition of data: M. Chatti, M. Gratton, M. Caliez, D. Picart; Analysis and/or interpretation of data: M. Chatti, M. Gratton, A. Frachon, N. AitHocine; Drafting the manuscript: M. Chatti, A. Frachon, N. AitHocine; Revising the manuscript critically for important intellectual content: , M. Gratton, N. AitHocine, D. Picart.

Declaration of competing interest

The authors declare that they have no known competing financial interests or personal relationships that could have appeared to influence the work reported in this paper.

Acknowledgements

Authors thank "la Région Centre Val de Loire, France" and "INSA Centre Val de Loire" for funding this project.

References

Bailly, P., et al., 2011. Dynamic behavior of an aggregate material at simultaneous high pressure and strain rate: SHPB triaxial tests. Int. J. Impact Eng. 38, 73–84.
Bargellini, R., Halm, D., Dragon, A., 2007. Discrete approach for modelling quasi-brittle damage : conditions on the set of directions. Compt. Rendus Mec. 335 (12), 781–786.
Bargellini, R., Halm, D., Dragon, A., 2008. Modelling of quasi-brittle behaviour: a discrete approach coupling anisotropic damage growth and frictional sliding. Eur. J. Mech. 27 (4), 564–581.
Bazant, Z.P., Gambarova, P.G., 1984. Crack shear in concrete: crack band microplane model. J. Struct. Eng. 110, 2015–2035.
Belmas, R., 1994. Mechanical Behaviour of Passed Explosives. International Symposium of Engineering Material Technology, Orlando, USA.
Benelfellah, A., 2013. Contribution à la modélisation de l'anisotropie induite par endommagement d'un materiau aggrégataire energétique. Université François Rabelais de Tours, Tours.
Benelfellah, A., et al., 2014. Analytical and numerical comparison of discrete damage models with induced anisotropy. Eng. Fract. Mech. 121–122, 28–39.
Bennett, J.G., et al., 1998. A constitutive model for the non shock ignition and mechanical response of high explosives. J. Mech. Phys. Solid. 46 (12), 2303–2322.
Burlion, N., 2010. Test techniques and experimental characterization. Dans. In: Torrenti, J., Pijaudier-Cabot, G., Reynouard, J. (Eds.), *Mechanical behavior of Concrete.* s.l.:ISTE. WILEY.
Caliez, M., et al., 2014. Viscoelastic plastic model and experimental validation for a granular energetic material. Int. J. Energ. Mater. Chem. Propuls. 13 (4), 339–371.

Carol, I., Jiràsek, M., Bazant, Z.P., 2001. A thermodynamically consistent approach to microplane theory. Part I. Free energy and consistent microplane stresses. Int. J. Solid Struct. 38 (17), 2921–2931.
Chatti, M., et al., 2019. Modelling of the viscoelastic behaviour with damage induced anisotropy of a plastic-bonded explosive based on the microplane approach. Int. J. Solid Struct. 168, 13–25.
Dienes, J.K., 1982. Permeability, Percolation and Statistical Crack Mechanics. American Rock Mechanics Association, Berkeley, California.
Dienes, J.K., 1996. A unified theory of flow, hot spots, and fragmentation with an application to explosive sensitivity. In: Davison, L., et al. (Eds.), Dans: *High-Pressure Shock Compression of Solids II*. Springer, New York, pp. 366–398.
Dienes, J.K., Zuo, Q.H., Kershner, J.D., 2006. Impact initiation of explosives and propellants via statistical crack mechanics. J. Mech. Phys. Solid. 54 (6), 1237–1275.
Ellis, K., Leppard, C., Radesk, H., 2005. Mechanical properties and damage evolution of a UK PBX. J. Mater. Sci. 23, 6241–6248.
Gratton, M., et al., 2009. Mechanical characterization of a viscoplastic material sensitive to hydrostatic pressure. Eur. J. Mech. Solid. 28 (5), 935–947.
Hackett, R.M., Bennett, J.G., 2000. An implicit finite element material model for energetic particulate composite materials. Int. J. Numer. Methods Eng. 49, 1191–1209.
Idar, D.J., Peterson, P.D., Scott, P.D., Funk, D.J., 1998. Low Strain Rate Compression Measurements of PBXN-9, PBX9501 and Mock9501. *Shcok Compression of Condensed Matter*, p. 587.
Le, V.D., 2007. Modélisation et identification du comportement plastique visco-élastique endommageable d'un matériau agrégataire. Université François Rabelais, Tours.
Le, V.D., et al., 2010. Experimental mechanical characterization of plastic-bonded explosives. J. Mater. Sci. 45, 5802–5813.
Liu, M., et al., 2020. Modeling of the deformation and damage of plastic-bonded explosive in consideration of pressure and strain rate effects. Int. J. Impact Eng. 146.
Liu, Z.W., et al., 2009. Fracture behavior of PBX simulant subject to combined thermal and mechanical loads. Polym. Test. 28 (6), 627–635.
Maire, J.F., Chaboche, J.L., 1997. A new formulation of continuum damage mechancis (CDM) for composite materials. Aero. Sci. Technol. 1 (4), 247–257.
Murakami, S., Kamiya, K., 1997. Constitutive and damage evolution equations of elastic-brittle materials based on irreversible thermodynamics. Int. J. Mech. Sci. 39 (4), 473–486.
Parab, N.D., et al., 2016. High speed X-ray phase contrast imaging of energetic composites under dynamic compression. Appl. Phys. Lett. 109.
Park, C., Jeong, S., Huh, H., Park, J., 2013. Material behaviors of PBX simulant with various strain rates. Key Eng. Mater. 117–120.
Pecqueur, G., 1995. Étude expérimentale et modélisation du comportement d'une craie et d'un grès en torsion, vol. 1. Lille: Université de Lille.
Picart, D., et al., 2014. Characterization and modeling of the anisotropic damage of a high-explosive composition. Eng. Fract. Mech. 131, 525–537.
Picart, D., Brigolle, J.L., 2010. Characterization of the viscoelastic behaviour of a plastic bonded explosives. Mater. Sci. Eng. A 527, 7826–7831.
Picart, D., Damiani, D., Doucet, M., 2012. *The Reverse Edge-on Impact Test; a Small Scale Experiment for Non-shock Ignition Studies*. s.L. AIP Conference Proceedings, American Institute of Physics, pp. 497–500.
Picart, D., Pompon, C., 2016. Experimental characterization of the multiaxial failure of plastic bonded explosive. Int. J. Energ. Mater. Chem. Propuls. 15 (2), 141–165.
Plassart, G., et al., 2020. Quasistatic mechanical behavior of HMX- and TATB-based plastic-bonded explosives. Mech. Mater. 150.
Ravindran, S., Tessema, A., Kidane, A., 2016. Local Deformation and Failure Mechanisms of Polymer Bonded Energetic Materials Subjected to High Strain Rate Loading, vol. 2, pp. 146–156.
Rja Fi Allah, S., 2006. Modélisation du comportement mécanique d'un matériau agrégataire. Université François Rabelais, Tours.
Trumel, H., Lambert, P., Belmas, R., 2010. Mesoscopic Investigations of the Deformation and Initiation Mechanisms of a Hmx-Based Pressed Composition. Coeur d'Alene (ID), USA, s.n.
Wiegand, D.A., 2000. Mechanical failure of composite plastic bonded explosives and other energetic materials. Proceedings of the 11, 744. *detonation symposium*.
Williamson, D.M., et al., 2008. Temperature-time response of a polymer bonded explosive in compression (EDC37). J. Phys. D Appl. Phys. 85404–85414.
Xiao, Y., et al., 2017. Characterization, modeling and simulation of the impact damage for polymer bonded explosives. Int. J. Impact Eng. 103, 149–158.
Yeom, K.S., Jeong, S., Huh, H., Park, J., 2012. New pseudo-elastic model for polymer-bonded explosive simulants considering the Mullins effect. J. Compos. Mater. 47 (27), 3401–3411.
You, S., Chen, M.-W., Dlott, D.-D., Suslick, K.-S., 2015. Ultrasonic hammer produces hot spots in solids. Ultrasonic hammer produces hot spots in solids 6 (6581).
Zhou, Z., Chen, P., Huang, F., Liu, S., 2011. Experimental study on the micromechanical behavior of a PBX simulant using SEM and digital image correlation method. Opt Laser. Eng. 49, 366–370.
Zhu, Q.Z., Shao, J.F., Kondo, D., 2008. A micromechanics-based non-local anisotropic model for unilateral damage in brittle materials. Compt. Rendus Mec. 336 (3), 320–328.

La base expérimentale présentée ci-avant a permis de développer de nouvelles lois d'évolution d'endommagement. Des approches dont nous savions qu'elles n'étaient thermodynamiquement pas acceptables, comme la gestion de l'effectivité déviatorique via la déformation volumique, ont aussi été testées. Un modèle complet avec viscoélasticité et plasticité intégrées au niveau des microplans a été programmé dans une UMAT. Les résultats, s'ils sont encourageants, montrent que les paramètres proposés mériteraient d'être parfois affinés, pour mieux reproduire les réponses expérimentales. Le calage n'est pas direct et la méthodologie d'identification proposée a montré des limites dans le cadre d'un modèle microplans. De plus, l'écriture en contraintes effectives offre l'avantage de découpler l'intégration de la plasticité de l'endommagement mais présente l'inconvénient d'en coupler l'identification des paramètres. On peut néanmoins noter que le modèle permet de retrouver les tendances expérimentales concernant l'évolution de la rigidité, notamment pour les essais avec retournement et les essais alternés (Cf. Figure 13).

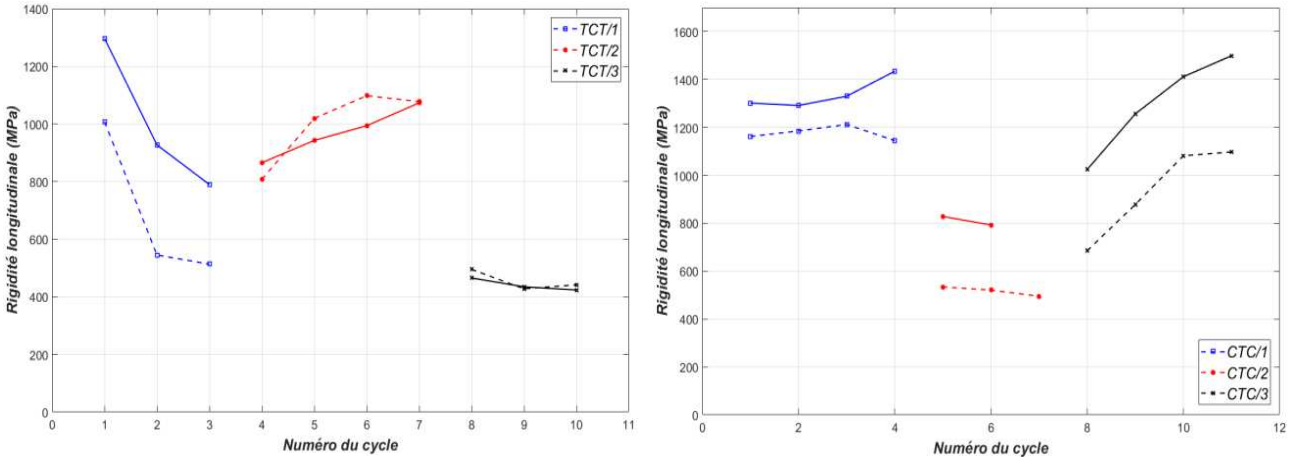

a/ b/

Figure 13 : Evolution des rigidités dans le cas d'essais alternés a/ Traction-Compression-Traction, b/ Compression-Traction-Compression (pointillés = essais) [Mémoire de M. Chatti].

Enfin, les essais réalisés ont permis d'ajouter des points de rupture expérimentaux originaux dans le plan des 2 plus grandes contraintes principales. La surface résultante montre des caractéristiques similaires à celle du béton : une rupture fragile en traction, une évolution non-linéaire de la surface de rupture dans le quadrant traction-compression, une rupture relativement ductile en compression et une contrainte à rupture plus importante en compression biaxiale qu'en compression simple. 2 critères de rupture initialement développés pour le béton ont donc été étudiés et identifiés. Le critère d'Ottosen est le plus adapté car il offre la possibilité de gérer la surface tracée dans le plan pression-déviateur le long du méridien de compression via un point de rupture dont nous disposons via les essais de compression sous confinement.

Les travaux concernant l'identification du critère de rupture pour I1 sont développés dans l'article référencé ACL3. Celui-ci n'est pas présenté dans le corps du manuscrit afin de ne pas en alourdir le contenu, mais est disponible en Annexe B. Le critère d'Ottosen a aussi été identifié à partir des essais disponibles pour le matériau M1 dans le manuscrit de thèse de M. Chatti.

2.6 MODÈLE A ANISOTROPIE INDUITE PAR LA PLASTICITÉ (M2)

Les travaux effectués durant la thèse de Gaëtane Plassart concernent la modélisation du comportement du matériau M2. L'objectif était de capitaliser sur l'expérience acquise précédemment sur M1 afin de mettre en œuvre la campagne d'essais nécessaire et suffisante pour une identification complète du modèle de comportement. Celui-ci devait permettre de modéliser le comportement de M2 et M1 en supposant à priori des mécanismes comportementaux identiques entre les deux matériaux.

Une base de données expérimentale complète, reprenant des essais développés dans le cadre des thèses de V.D. Le et M. Chatti, a été construite. Il est à noter que la doctorante était physiquement présente au CEA, ce qui a permis de grandement accélérer la mise en œuvre des essais. Les premiers essais à 20°C ont montré que M2 s'endommage très peu. La perte de rigidité mesurée est par exemple d'environ 10% à la rupture en compression simple, soit environ 3 fois moins important que pour M1. On observe de plus que le module d'élasticité ne dépend pas de la pression de confinement, et aucune reprise de raideur en compression n'est constatée après une traction. Aucun effet unilatéral n'est donc observé. Ces mêmes constatations ont été effectuées sur I2 dans le cadre du post-doctorat de Clément Touzeau.

Les essais 0°/90°/0° mettent cependant en lumière le développement d'une anisotropie induite par le chargement, mais dont l'endommagement n'est pas le moteur principal. L'hypothèse d'un écrouissage cinématique engendrant une anisotropie induite par la plasticité a été avancée, confirmée par un essai de cyclage entre 2 contraintes fixes montrant une évolution de la déformation.

Un modèle viscoélastique viscoplastique avec endommagement a été proposé, toujours avec l'objectif de l'identifier pour M2 puis pour M1. Dans le modèle rhéologique, la viscoplasticité est placée en série par rapport à la viscoélasticité. Cette structure a été étudiée dans le cadre d'un contrat de collaboration mené entre 2009 et 2011 portant sur le développement d'un modèle rhéologique pour M1 (résultats non publiés à ce jour). Elle permet de mieux reproduire l'unicité de la courbe enveloppe du comportement sous sollicitations cyclique et monotone.

Il est clair que cette structure de modèle ne facilite pas l'implantation numérique. De plus l'identification des paramètres de comportement peut difficilement être découplée, et leur ajustement fin doit obligatoirement être réalisé par méthode inverse. Comme pour M1, les paramètres matériau ont été identifiés dans un premier temps à 20°C. Six essais sont utilisés (DMA, compression simple monotone et cyclée à la vitesse de référence, traction, torsion et compression triaxiale monotones à la vitesse de référence). L'ensemble des essais quasi-statiques de la base de données sont ensuite simulés à titre de validation, en explorant donc plusieurs chemins de chargement. Les résultats montrent une bonne corrélation avec les essais en reproduisant très correctement les courbes contrainte-déformation et les courbes temporelles en compression, sur le domaine de vitesses et de pressions confinement considéré. Un problème est néanmoins soulevé lors de la simulation de l'essai de fatigue entre 2 contraintes, à priori dû à la présence de dilatance dans le modèle.

L'extension en température a été effectué dans une plage plus vaste que pour M1, de -30 à 80°C. Une équivalence temps-température est utilisée pour la viscoélasticité, et l'identification des autres paramètres est effectuée à partir d'essais à 4 températures : -30°C, 0°C, 50°C et 80°C. On constate une évolution du comportement du matériau à 80°C , correspondant à la température de transition vitreuse. On constate de plus le module réel à 20°C plus faible après un passage à -30°C, suggérant un endommagement à froid. Des essais de dilatométrie confirment la création d'une déformation résiduelle après passage à 30°C.

Ces travaux sont présentés dans l'article référencé ACL2 présenté ci-dessous.

Mechanics of Materials 170 (2022) 104318

Contents lists available at ScienceDirect

Mechanics of Materials

journal homepage: www.elsevier.com/locate/mechmat

Quasistatic anisotropic induced behaviour of a tatb-based plastic-bonded explosive

Gaëtane Plassart [a,b,*], Didier Picart [a], Michel Gratton [b], Arnaud Frachon [b], Michaël Caliez [b]

[a] CEA DAM Le Ripault, F-37260, Monts, France
[b] INSA Centre Val de Loire, Univ. Orléans, Univ. Tours, LaMé, EA 7494, F-41000, Blois, France

ARTICLE INFO

Keywords:
Plastic-bonded explosives
Constitutive law
Quasistatic mechanical behaviour
Load-induced anisotropy
Non-linear kinematic hardening
anisotropic damage
Viscoelasticity
Viscoplasticity

ABSTRACT

The constitutive law of a plastic-bonded explosive (PBX) based on TATB crystals is studied in the quasistatic loading range. The experimental data highlight a viscoelastic behaviour with damage, and an anisotropy induced by plastic flow. The existing models for PBXs being not appropriate, a constitutive law accounting for the observed mechanisms is proposed. The linear viscoelasticity is integrated in a microplane model describing an effective anisotropic damage. A multilayer viscoplasticity is used to yield a non-linear kinematic hardening. A von Mises yield criterion is defined on each surface and a dilatancy function describes the volumetric plastic yield. This law is implemented in the Abaqus/Standard finite element code in the form of a UMAT subroutine. The model is calibrated on ten tests. The simulations performed to compare the model to each experimental test correctly reproduce the behaviour of the studied explosive composition.

1. Introduction

When designing a pyrotechnic structure, simulations must be performed to assess mechanical strength. This step consists, in particular, in developing and implementing a constitutive law for the energetic material. In addition, the thermomechanical stresses that such a material undergoes during its life cycle can alter its microstructure. It can potentially modify its mechanical and/or reactive behaviour. To guarantee the safety and reliability of pyrotechnic structures, understanding and modelling the thermomechanical behaviour of these materials is essential. The CEA (Commissariat à l'Energie Atomique et aux Energies Alternatives – French Alternative Energies and Atomic Energy Commission) has developed several explosive compositions. In this paper, the plastic-bonded explosive (PBX) of interest is called M2. It is made of more than 95 wt% TATB crystals (1,3,5-triamino-2,4,6-trinitrobenzene), mixed with a polymeric binder. Other TATB-based PBXs frequently mentioned in the literature are PBX-9502 (95 wt% TATB, 5 wt% Kel-F 800 binder), LX-17-1 (92.5 wt% TATB, 5 wt% Kel-F 800 binder). In the literature, many studies have also been carried out on HMX (octahydro-1,3,5,7-tetranitro-1,3,5,5,7-tetrazocine)-based PBXs as PBX9501 (95 wt% HMX, 2.5 wt% estane, and 2.5 wt% nitro-plasticizer) or M1 (approximately 95 wt% of HMX mixed with a binder). Compaction of these TATB-or HMX-based compositions is obtained by hot isostatic compression (Picart, 1993; Thompson and Wright, 2004). The residual porosity is less than 5%. They are isotropic in their initial state.

Quasistatic constitutive laws have been developed for PBXs since the 1980s. A distinction is made between macroscopic and micromechanical models. The micromechanical models capture the mechanisms at the grain scale. They help understand the influence of the different components on the macroscopic response (Clements and Mas, 2004; Tan et al., 2005, 2007; Wu and Huang, 2009; Ambos et al., 2015; Arora et al., 2015; Gasnier et al., 2018; Trumel et al., 2019). However, these models cannot be used in industrial context because of their prohibitive cost. The macroscopic quasistatic models proposed for PBXs have been compared by Plassart et al. (2020). These models are:

- the SCRAM model (Statistical CRAcks Mechanics) (Dienes, 1978, 1996; Dienes et al., 2006), an elasto-plastic model with anisotropic damage, for PBX-9501,
- the ViscoSCRAM model (Bennett et al., 1998; Hackett and Bennett, 2000), an isotropic version of SCRAM adding a viscoelastic component, for PBX-9501,
- the model of Liu et al. (2019), a viscoplastic version of the Visco-SCRAM model, for PBX-9502,

* Corresponding author. CEA DAM Le Ripault, F-37260, Monts, France.
E-mail addresses: gaetane.plassart@gmail.com (G. Plassart), didier.picart@cea.fr (D. Picart), michel.gratton@insa-cvl.fr (M. Gratton), arnaud.frachon@insa-cvl.fr (A. Frachon), michael.caliez@insa-cvl.fr (M. Caliez).

https://doi.org/10.1016/j.mechmat.2022.104318
Received 6 July 2021; Received in revised form 5 April 2022; Accepted 7 April 2022
Available online 10 May 2022

- the model of Buechler (2012b, 2013), a viscoelastic-viscoplastic model with isotropic damage, for PBX-9501,
- the model of Zubelewicz et al. (2013), an elasto-viscoplastic model with anisotropic damage, for PBX-9502.

Unfortunately, the modelling choices were not based on experimental evidence. For example, the calibration of an anisotropic damage law was only done by observing the longitudinal response during compression tests, without measuring the transverse one. It explains the multitude of models without one of them emerging to describe the behaviour of this class of materials. Therefore, an in-depth characterization of the mechanical behaviour of M1 and M2 have been made. For the composition M1 (Picart and Brigolle, 2010; Le et al., 2010; Picart et al., 2014; Picart and Pompon, 2016), it yields a viscoelastic-plastic model with isotropic damage (Le, 2007, 2010; Caliez et al., 2014) or an elasto-plastic model with anisotropic damage (Benelfellah, 2013; Benelfellah et al., 2014, 2017; Picart et al., 2014). These models have better reproduced the behaviour of M1 than the previous one. However, they poorly reproduce the hysteresis observed during loading/unloading cycles. The model proposed below for the M2 composition allows to understand the cause.

The experimental quasistatic behaviour of the TATB-based PBX M2 has been extensively characterized in Plassart et al. (2020) and is summarized in section 2. The authors showed that HMX- and TATB-based PBXs have quite similar macroscopic properties: a quasi-brittle response with tensile/compressive asymmetry; strain rate-, temperature- and pressure dependencies; inelastic strains; a load-induced anisotropy. Therefore, a unique constitutive law is attainable for this class of materials in the quasistatic loading range. This is the aim of this paper. Each explosive composition would have its own set of parameters reinforcing the influence of particular deformation mechanisms.

For the explosive composition M2, the main deformation mechanism is the plasticity flow. In section 3, a viscoelastic-viscoplastic model, with effective load-induced anisotropic damage and a non-linear kinematic hardening, is developed and implemented. It is calibrated on M2. To the authors' point of view, the scientific novelty is based on the following key points. The first one is the strong link between the experimental study (described in Plassart et al., 2020) and the model proposed here. The phenomena have been isolated and studied in detail. Numerous simulations performed with various loading paths are compared to the corresponding data. The agreement between the simulations and this large database strongly validates the approach (see section 4). The second key point concerns unloadings. The study of loadings/unloadings has required to reject the popular Armstrong-Fredericks model. The older approach of Mroz allows reproducing correctly the hysteresis as well as monotonic tests. This suggests a good ability of the model to describe alternating loadings. In addition, it is uncommon in the literature to calibrate a kinematic strain hardening to model unloadings, without any isotropic strain hardening. The third key point concerns the consideration of pressure. The behaviour of explosive compositions, commonly pressure-dependent, often leads to a Drucker-Prager yield flow stress. However, despite the very high granular solid fraction of the M2 material, both the independence of the plasticity threshold to pressure and the plastic viscosity evolving with pressure have been experimentally demonstrated. Those choices are rarely found in the literature.

2. Characterization of the TATB-based material M2

2.1. Material

M2 is composed of about 95% by weight of TATB grains bonded by a thermoplastic binder. The mean diameter of TATB grains is about 50 μm. The material is obtained by coating the grains with a thin layer of polymeric binder. A granulation process leads to millimetric metagrains. The granules are then subjected to several isostatic compression cycles at a temperature of about 150 °C and a pressure cycle of 200 MPa (Picart, 1993). After cooling, a coherent material is obtained, and samples can be manufactured. Due to the compaction process, the residual porosity is only a few percent. Fig. 1 shows a micrograph of the material M2. The colour variations are due to a strong anisotropy of the TATB grains on the microscale. However, as the orientation of the grains and the binder are randomly distributed, the material is initially isotropic on a macroscale. All the tests described in this paper were performed on the same batch.

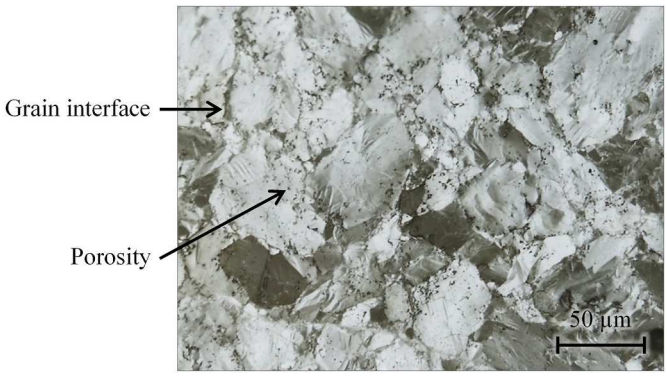

Fig. 1. Micrograph of material M2. The color variations are due to the anisotropy of the TATB grains. Porosity is mainly located inside the grains (small black dots) and at the grain/grain interfaces.

2.2. Experimental observations, guidelines for model

A complete experimental characterization of M2 has been presented by Plassart et al. (2020). In the following, the key features of the behaviour are summarized. We refer the reader to the original paper for details on test procedures and their repeatability. All the mechanical tests performed on the material M2 are listed in Table 1. The

Table 1
Mechanical tests performed on the material M2 (from Plassart et al., 2020).

Uniaxial compression	Longitudinal/ transversal strains	✓/✓
	Temperature	−30 °C to 80 °C
	Strain rate	10^{-6} s^{-1} to 10^{-4} s^{-1}
	Creep/relaxation	✓
	Load – unload cycles	✓
Uniaxial tensile	Longitudinal/ transversal strains	✓/✓
	Temperature	−30 °C to 80 °C
	Strain rate	10^{-6} s^{-1} to 10^{-4} s^{-1}
	Creep/relaxation	✓
	Load – unload cycles	✓
Torsion	Shear strains	✓
	Temperature	20 °C
	Strain rate	0.01°.s^{-1}
	Creep/relaxation	×
	Load – unload cycles	✓
Triaxial compression	Longitudinal/ transversal strains	✓/✓
	Pressure	2.5, 5 and 10 MPa
	Temperature	20 °C
	Strain rate	10^{-5} s^{-1}
	Creep/relaxation	✓
	Load – unload cycles	✓
Alternating loading	Longitudinal/ transversal strains	✓/✓
	Temperature	20 °C
	Strain rate	10^{-5} s^{-1}
	Creep/relaxation	✓
	Load – unload cycles	✓
Other tests	DMA	0 °C to +90 °C
	Multiaxial tests	Brazilian test, channel-die, equibiaxial compression, three-point bending

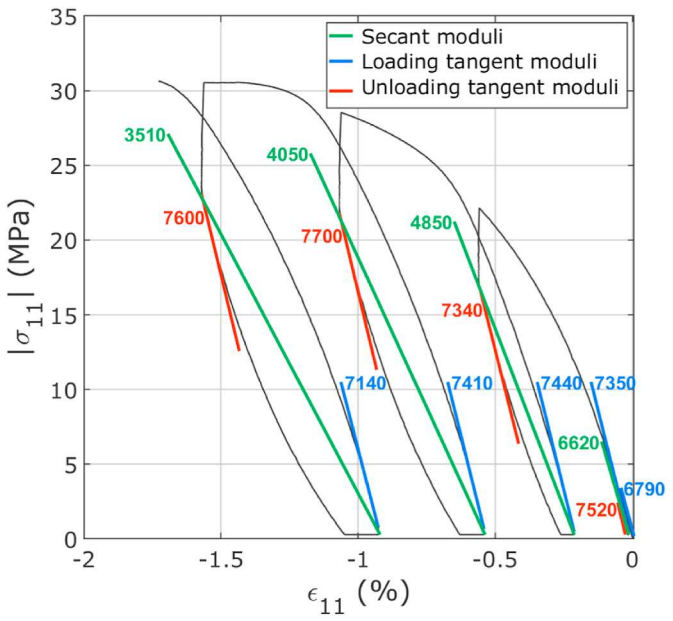

Fig. 2. Secant and tangent longitudinal modules for a cyclic compression test (from Plassart et al., 2020). Secant modules decrease can not be interpreted as a damage effect since the tangent modules do not show any evolution.

corresponding curves (stress-strain or waveforms) are in the article and the supplementary materials of Plassart et al. (2020).

In this paper, the influence of temperature is not considered. The analysis of the behaviour is limited to a temperature of 20 °C. For details on the temperature influence, see Plassart et al. (2020) and Plassart (2020).

Among the key points of the behaviour, an asymmetry between the tensile and compression responses is observed. This is common for quasi-brittle granular materials (see Mazars et al., 1990 for concrete; Thompson et al., 2010 for PBX-9502; Buechler, 2012a for PBX-9501; and Picart et al., 2014 for M1). There is no clear transition to plasticity. The Young's modulus is independent of the stress sign (compression or tensile), the strain rate and the pressure from 0 to 10 MPa. These observations differ from that made on HMX-based PBXs (Wiegand et al., 2011; Picart et al., 2014). The ratio of the transversal to the longitudinal strain (Poisson's ratio at low strain) is independent of the strain rate and the stress sign, but there is a non-linear effect of pressure. It decreases below 5 MPa and then increases. In addition, dynamic mechanical analysis (DMA) tests highlighted the linear viscoelastic behaviour of M2 at low stress levels (1 MPa).

Cyclic compression and tensile tests were also performed on M2. Fig. 2 shows an example of cyclic compression. Each cycles had four phases: (1) a strain rate controlled load, (2) a stress relaxation at fixed longitudinal strain, (3) a strain rate controlled unload, (4) a strain recovery at rest. These tests are inspired by those performed on M1 (Gratton et al., 2009; Le et al., 2010). The relaxation and recovery steps enable removing the viscous trends of M2. The amount of the stress that relaxes during the dwell is denoted as the "relaxed stress". The strains at the end of the recovery step highlight the irreversible strains suffered by the material. As for M1 (Le et al., 2010), the comparison between cyclic and monotonic curves shows that the cyclic test envelope corresponds to the monotonic test one. Adding cycles does not influence the envelope behaviour of M2.

Moreover, the transversal strain grows faster than the longitudinal one. So, M2 develops a load-induced anisotropy. The latter could be due to damage. The evolution of the elastic modules during loading/unloading has been studied. An elastic stress state is assumed at the beginning of each load and unload. Tangent modules are calculated in load (Fig. 2, in blue) and unload (Fig. 2, in red). They are determined by linear regression over a strain window of 0.05%. All modules being similar, no damage is visible. Moreover, the influence of the stress level on the elastic modules is negligible. So, the assumption of a linear viscoelasticity is possible.

Fig. 3 shows the evolution of longitudinal (left), and transversal (right) modules measured under cyclic loading in uniaxial compression (black lines), triaxial compression at 10 MPa pressure (blue line) and uniaxial tensile (red lines) at 20 °C. The three rates applied in uniaxial loading are distinguished (lines, dotted and dashed lines). For each condition, the test leading to the maximum modulus degradation is

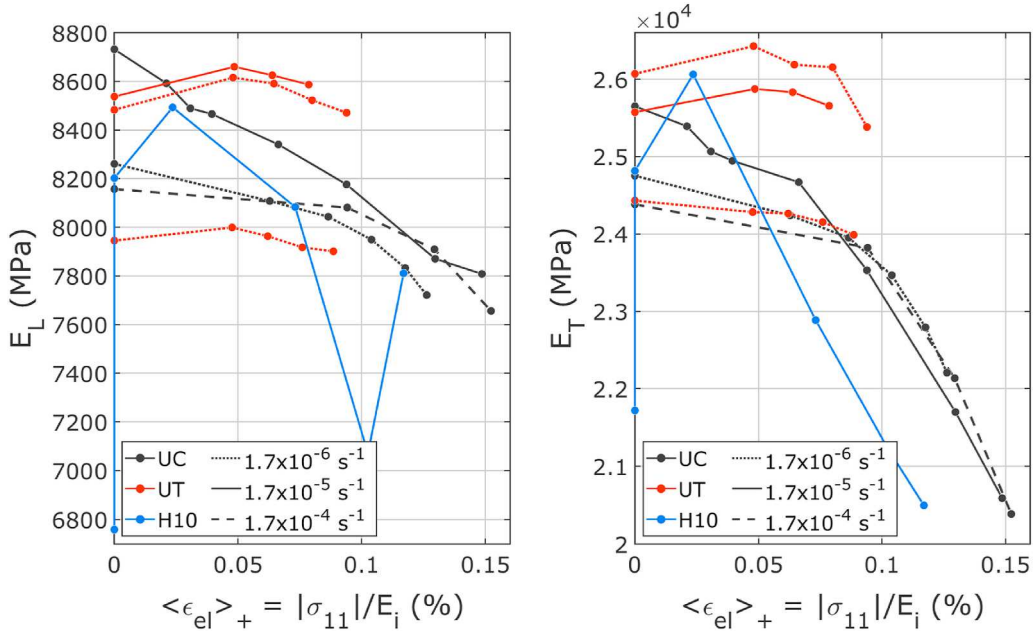

Fig. 3. Evolution of elastic modules in uniaxial compression (« UC »), uniaxial tensile test (« UT ») and triaxial compression at 10 MPa pressure (« H10 ») at 20 °C as a function of the positive elastic strains at three strain rates. The positive strains are calculated from the elastic transversal modulus (i = T) in compression, and elastic longitudinal modulus in tensile loading (i = L).

shown. In uniaxial compression, a decrease about 500 MPa (respectively 5000 MPa) is observed for the longitudinal (resp. transversal) modulus. These degradations are independent of the strain rate because line and dotted curves show a similar decrease. Using the samples tested at 20 °C (independently of the strain rate), the 95% confidence interval of the initial longitudinal modulus is 900 MPa. It is 3000 MPa for the transversal modulus. Since the decrease in longitudinal modulus is within its confidence interval, no significative longitudinal damage is observed. Conversely, since the decrease of the transversal modulus is larger than its confidence interval. Therefore, a slight transversal damage is developing (less than 20% at failure). This results in zero volumetric damage and a maximum deviatoric damage of 12%. About the triaxial test, the modules evolution is not linear. The slope of the last four transversal modules is the same as in uniaxial compression. Therefore, damage is pressure-independent. The tensile tests did not reveal any considerable damage. They fail at a strain corresponding to the beginning of the modules degradation in compression. The damage of the TATB-based PBX M2 at 20 °C thus develops late. Its influence on the global behaviour of the material is limited.

Damage evolution is usually estimated assuming an elastic unloading (see for concrete, Benouniche, 1979; Gotuwka, 1999) and for HMX-based PBXs (Gratton et al., 2009; Le et al., 2010; Picart et al., 2014). For each cycle, the secant modulus between the end of the relaxation and the end of the recovery is presumed elastic (Fig. 2, in green). The secant modules measured on M2 strongly decreases during the loading when the tangent modules remain unchanged. The variations of the secant modules cannot be due to damage. The evolution of the secant modules could be due to plasticity. This interpretation is discussed below.

An experimental campaign of alternating tensile/compression was also performed on M2. Two kinds of tests were conducted: (1) a compression up to ~0.95 σ_{max} (σ_{max} is the peak stress in compression) followed by a tensile loading to failure, and (2) a traction up to ~0.95 σ_{max} (σ_{max} is the peak stress in tensile test) followed by a compression loading to failure. When quasi-brittle granular materials are submitted to alternating tensile/compression, a stiffness recovery is commonly observed at the beginning of compression (Mazars et al., 1990; Picart et al., 2014). This phenomenon is called unilateral effect and is related to damage by microcracking. For M2, no recovery of stiffness is observed. This is consistent with the negligible damage of the material.

A linear viscoelastic model based on the DMA data has been developed. It cannot by itself reproduce the non-linear response of the material up to failure nor the whole relaxation of the stress (respectively recovery of the strain) when the longitudinal strain (resp. the stress) is constant. During relaxation, only 20% of the stress evolution can be obtained using the linear viscoelastic model based on DMA data. Therefore, a plastic strain mechanism is added in series with the viscoelastic model.

The analysis of the uniaxial compression, triaxial compression, uniaxial tensile and torsion curves shows that the behaviour is non-linear starting from about 4 MPa of equivalent von Mises stress, whatever the strain rate. These observations show that the initial yield surface of M2 is pressure- and strain-independent. It could be represented by a von Mises criterion.

The experimental campaign providing the most information on M2 is an alternating compression test. Two compressions at 30 MPa were performed successively to highlight the load-induced anisotropy of M2, the latter being observed during a second loading in a different direction (Cambou and Lanier, 1988; Lanier et al., 1991). The curves are compared in Fig. 4. The first compression is in red, the 0° reloading is in blue, the 90° reloading is in green and all the inversed unloadings are in grey (see Plassart et al., 2020 for details). The blue and green curves are clearly different. The green curve shows more strain than the red one.

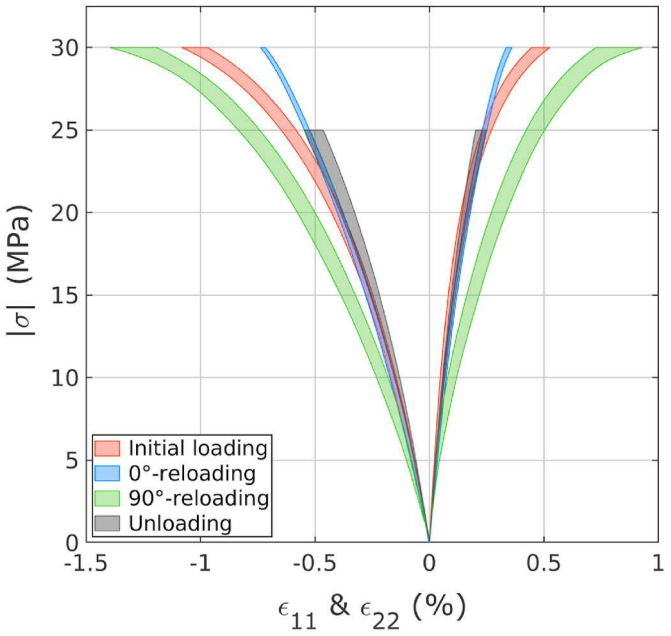

Fig. 4. Comparison of the loading and unloading curves of the 0°–0° and 0°–90° tests (from Plassart et al., 2020). The response depends on the reloading direction highlighting a load-induced anisotropy during the first loading.

Lastly, the maximum strain for the blue curve is half that of the green curve. So, the 90° direction (in green), stretched during the first loading, is more ductile than initially. Conversely, the 0° direction (in blue), compressed during the first loading, is more rigid above a stress of 15 MPa. The anisotropy induced by the first load is obvious. This induced anisotropy cannot be attributed to a negligible damage, as previously demonstrated. This observation is confirmed by the fact that the elastic modules (the initial slope of the curves) are not influenced by the first load. Furthermore, the unloading curves (in grey) match with the 0° reloading one (in blue). Also, the 0° reloading and the initial loading (in red) are overlapped up to 15 MPa. The behaviour revealed by these observations can be interpreted using a kinematic hardening plasticity model (Plassart et al., 2020). An isotropic strain hardening would fail to reproduce these phenomena.

The kinematic hardening should be non-linear to reproduce the strong non-linearity observed in compression. A popular non-linear kinematic hardening is the Armstrong-Frederick model (Armstrong and Frederick, 1966, 2007). A cumulative plasticity term is added to the linear Prager strain hardening. Therefore, the strain hardening modulus is related to the accumulated plastic strain. The total strain at a given stress is dependent on the number of cycles previously performed. Consequently, a monotonic curve is necessarily different from the envelope curve of a cyclic test. This is not the case for the M2 composition. Cyclic and monotonic tests have the same envelope behaviour. The Armstrong-Frederick model also leads to stiffer unloading than reloading, which is not observed during experiments on M2. Chaboche et al. (1979) proposed a model based on "parallel" mechanisms in the sense of stress (and hardening) additivity. The non-linearity is due to an evanescent strain memory which is a cumulative plasticity. Therefore, for the same reasons as the Armstrong-Frederick model, this model does not meet our expectations.

A multilayer model (Mroz, 1967) is preferred to reproduce the experimental observations. Several linear Prager hardening modules are added in series. So, there is a strain additivity. It is equivalent to nest several yield surfaces. The global hardening modulus is non-linear

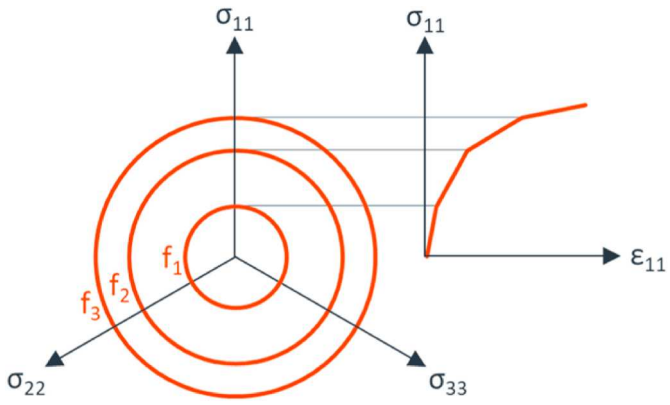

Fig. 5. Scheme of the multilayer model of Mroz (Mroz, 1967) with three yield surfaces. f_i are the yield criterion of each surface. When a surface is reached, it moves to the next one, then the two move together. The global hardening modulus decreases when a surface is activated.

because each surface has a different kinematic modulus and yield strength. The activation of a new surface decreases the global hardening modulus. This model can be qualified as "multilinear". It is schematically described in Fig. 5.

A repeated torsional cycling test, no presented in Plassart et al., (2020) was performed on M2. The angular rate was controlled up to a torque corresponding to a stress of ±6 MPa on the average radius of the sample. The test was stopped after twenty cycles without reaching failure. It was carried out with the same procedure as the monotonic torsion tests (Plassart et al., 2020). The second and twentieth cycles are identical. Fig. 6 shows that the material has an immediate accommodation in cyclic test at zero mean stress. Since there is no cyclic softening nor strain hardening in alternating torsion, adding isotropic strain hardening is inappropriate. It would increase the apparent yield strength over several cycles due to viscoplastic flow.

Another point to focus is the pressure-dependence. The yield criterion and the elastic modules are pressure independent. The same is assumed for the viscoelastic characteristic times. Two constitutive laws

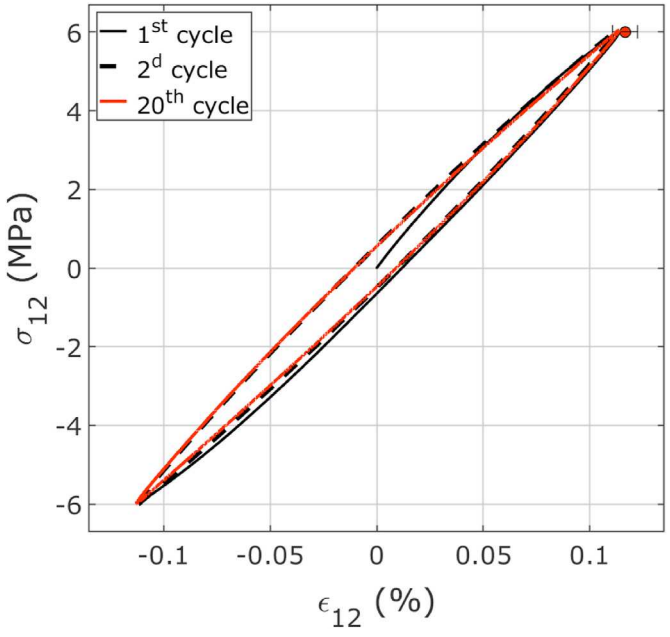

Fig. 6. Alternating torsion test performed at $0.015°.s^{-1}$ and cycled twenty times.

are then possible: integrating the pressure effect on the kinematic hardening or on the viscoplastic flow. Rinaldi (2006) and Dasriaux (2013) showing that pressure slows down the plastic flow of polymers, the latter is adopted.

Lastly, during a compression test a strong non-linearity of the volumetric behaviour is observed, with a transition from contraction to dilatation (Plassart et al., 2020). A similar observation was made for many granular materials (Green and Swanson, 1973; Van Mier, 1984; 1986; Homand-Etienne et al., 1998; Hu et al., 2010). Therefore, viscoplastic flow and kinematic hardening must address the volumetric component of the behaviour. With a von Mises criterion, a non-associated flow rule is needed. The determination of a flow potential being thermodynamically complicated, an indirect method is followed: the volumetric part is related to the deviatoric one by a dilatancy function.

To conclude, the explosive composition called M2 shows strain rate-, temperature- and pressure-dependence, inelastic strain, and a load-induced anisotropy. The strain additivity is justified, as is the use of a linear viscoelastic component. Damage being not the main deformation mechanism for the composition M2, the non-associated viscoplastic flow governs the material "ductility". The load-induced anisotropy can be reproduced using a non-linear kinematic strain hardening. Isotropic strain hardening must be avoided.

The temperature dependence is out of the scope of this paper. The modelling only focuses on the strain rate and pressure dependencies at 20 °C. For information on the integration of the temperature dependence, the reader will see Plassart (2020).

3. Modelling

The relevance of the models from the literature for HMX- and TATB-based PBXs is questionable due to their insufficient experimental justification (Plassart et al., 2020). For this class of materials, only M1 (an HMX-based PBX) and M2 (a TATB-based PBX) have been deeply characterized to highlight deformation mechanisms (Picart et al., 2014; Plassart et al., 2020). The main difference is their level of damage (Benelfellah, 2013; Picart et al., 2014). M2 develops a load-induced anisotropy attributed to plastic flow when the load-induced anisotropy of M1 is due to damage. For the latter, the transversal to the longitudinal strains ratio can exceed 0.5 and a unilateral effect was observed. In addition, its Young's modulus is pressure-dependent. Despite these differences, the two explosive compositions M1 and M2 have quite similar

Table 2
Summary of the state variables and their associated variables defined in the model. The corresponding mechanism and the level of definition of each variable are given.

Mechanisms	Observable and internal state variables	Associated variables	Definition level (state var./associated var.)
Viscoelasticity	$\underline{\underline{\varepsilon}}$	$\underline{\underline{\sigma}}$	global
	$\varepsilon_{ve}{}^{V}$	σ^{V_b}	global/branch
	$\underline{\underline{\varepsilon_{ve}{}^{D}}}^{mic}$	$\underline{\underline{\sigma^{D_b}}}^{mic}$	microplane/ microplane branch
	$\varepsilon_{ve}{}^{V_{b,elast}}$	$\sigma^{V_{b,elast}} = \sigma^{V_b}$	branch
	$\underline{\underline{\varepsilon_{ve}{}^{D_{b,elast}}}}^{mic}$	$\underline{\underline{\sigma^{D_{b,elast}}}}^{mic} = \underline{\underline{\sigma^{D_b}}}^{mic}$	microplane branch
	$\varepsilon_{ve}{}^{V_{b,visc}}$	$-\sigma^{V_{b,visc}} = -\sigma^{V_b}$	branch
	$\underline{\underline{\varepsilon_{ve}{}^{D_{b,visc}}}}^{mic}$	$-\underline{\underline{\sigma^{D_{b,visc}}}}^{mic} = -\underline{\underline{\sigma^{D_b}}}^{mic}$	microplane branch
Damage	d_V	$-Y_V$	global
	$d_{D^{mic}}$	$-Y_{D^{mic}}$	microplane
Viscoplasticity	$\varepsilon_{vp\ s}{}^{V}$	$-\sigma^{V}$	surface/global
	$\underline{\underline{\varepsilon_{vp\ s}}}^{D}$	$-\underline{\underline{\sigma}}^{D}$	surface/global
	$\underline{\underline{\xi_s}}$	$\underline{\underline{X_s}}$	surface

macroscopic properties. It gives confidence on the rise of a single constitutive law for this class of materials.

Giving the discussion on section 2 and the model proposed by Benelfellah et al. (Benelfellah, 2013; Picart et al., 2014) for M1, the constitutive law must incorporate a viscoelastic part in series with a viscoplastic one. A load-induced anisotropy by damage and a non-linear kinematic strain hardening mechanisms must be incorporate. The single law proposed for this class of materials is detailed in the next paragraphs.

3.1. Formulation

A new macroscopic constitutive law is now proposed and calibrated on the TATB-based PBX M2. The proposed model is written in the framework of generalized standard materials. The formalism is that of Lemaître et al. (2020). The specific Helmholtz free energy ψ is chosen as the state potential. It is a function of the observable variable $\underline{\underline{\varepsilon}}$ and the internal variables defining the material history (Table 2). The viscoelastic and viscoplastic components are in series. Assuming they are uncoupled, the state potential can be decomposed in a viscoelastic potential ψ_{ve} and a viscoplastic one ψ_{vp} (Lemaître et al., 2020). The viscoelastic potential is split in volumetric ψ_{ve}^{V} and deviatoric ψ_{ve}^{D} parts. The decomposition of the free energy and its expression are summarized in Fig. 8. A rheological scheme of the behaviour law is given Fig. 9.

3.1.1. Viscoelastic part

The viscoelastic behaviour is described by a generalized Maxwell model (both on the volumetric and deviatoric components). Following the work of Benelfellah et al. (Benelfellah, 2013; Picart et al., 2014), a microplane model is introduced on the viscoelastic part. In this discrete model, each fixed direction of the solid angle is characterized by a plane of normal $\underline{n}$. The strain tensor is projected on each microplane, which enables working with scalar and vector quantities. Here, a volumetric-deviatoric (VD) formulation is chosen (Leukart and Ramm, 2002, 2003). Kinematic constraints define volumetric ε_{ve}^{V} and deviatoric $\underline{\varepsilon_{ve}^{D\ mic}}$ strains as the projections on the microplane of the viscoelastic strain tensor $\underline{\underline{\varepsilon_{ve}}}$ (Carol et al., 2001):

$$\begin{cases} \varepsilon_{ve}^{V} = \underline{\underline{V}} : \underline{\underline{\varepsilon_{ve}}} \\ \underline{\varepsilon_{ve}^{D\ mic}} = \underline{\underline{\underline{\underline{D}}}}^{mic} : \underline{\underline{\varepsilon_{ve}}} \end{cases} \quad with : \quad \begin{cases} \underline{\underline{V}} = \frac{1}{3}\,\underline{\underline{1}} \\ \underline{\underline{\underline{\underline{D}}}}^{mic} = \underline{n}.\underline{\underline{\underline{\underline{I}}}}^{D} \end{cases} \tag{1}$$

$\underline{\underline{V}}$ and $\underline{\underline{\underline{\underline{D}}}}^{mic}$ are the projection tensors. $\underline{\underline{1}}$ is the second order identity tensor. $\underline{\underline{\underline{\underline{I}}}}^{D}$ is the deviatoric part of the fourth order identity tensor. The deviatoric component is decomposed on the different microplanes while the volumetric one is not. The exponent *mic* indicates the dependence on the microplane of normal $\underline{n}$.

Two equivalent methods are possible to couple the Maxwell viscoelastic model to the microplane damage model (Chatti et al., 2019): (1) in the external approach, the microplane model is put in series with the Maxwell one; (2) in the internal approach, the Maxwell model is integrated within the microplanes. The latter, easier to implement, is chosen. The calculations are therefore reduced to scalar equations, while the external approach involves fourth order tensors to invert.

The fundamental assumption ensuring the thermodynamic stability of microplane models has been postulated by (Carol et al., 2001). It states that the total free energy corresponds to the integral over the solid angle of the energies defined on each microplane. After discretization of the solid angle, the deviatoric viscoelastic free energy ψ_{ve}^{D} is the sum of the viscoelastic deviatoric free energies of each microplane $\psi_{ve}^{D\ mic}$. An angular weighting coefficient ω^{mic} related to the number N_m of microplanes gives a balance to microplanes (Bažant and Oh, 1985) (Fig. 8, *projection on microplanes*).

The generalized Maxwell model involves a purely elastic branch (index ∞) and N_b viscoelastic ones featuring an elastic stiffness (index *elast*) and a viscous dashpot (index *visc*). The bulk and shear modules of the bth viscoelastic branch are respectively noted k_{Vb} and μ_{Db} ($k_{V\infty}$ and $\mu_{D\infty}$ for the elastic branch). The volumetric ψ_{ve}^{V} and the deviatoric free energies of the microplane $\psi_{ve}^{D\ mic}$ are the sum of the free energies of each branch. A damage term d_V (respectively d_D^{mic}) affects the elastic modulus k_{Vb} and $k_{V\infty}$ (respectively μ_{Db} and $\mu_{D\infty}$). A function α_{Vb} weights the volumetric damage effectivity on each viscoelastic branch ($\alpha_{V\infty}$ for the elastic branch). The postulated expression of the free energy of each branch is given Fig. 8.

The damage variables d_V and d_D^{mic} are respectively related to the volumetric and the deviatoric strain of the purely elastic branch from potentials noted $Y_{V\infty}$ and $Y_{D\infty}^{mic}$:

$$Y_{V\infty} = \frac{1}{2}\,k_{V\infty}\,\varepsilon_{ve}^{V^2}; \quad Y_{D\infty}^{mic} = \frac{1}{2}\,\mu_{D\infty}\underline{\varepsilon_{ve}^{D\ mic}}.\underline{\varepsilon_{ve}^{D\ mic}} \tag{2}$$

so, they are independent of the branch. They range between 0 and 1 and cannot decrease. Their evolution law is determined from the experimental degradation of the bulk and shear modules.

The definition of the damage effectivities must meet the thermodynamic consistency. The stress-strain response must be continuous. Benelfellah et al. (Benelfellah, 2013; Picart et al., 2014) have chosen the simplest formulation. Effectivity is defined as Heaviside function of its corresponding elastic strain. In VD formulation, the deviatoric component is vectorial. Only the volumetric component enables the definition of such a function. The α_{Vb} effectivity is related to the strain $\varepsilon_{ve^{V_{b,elast}}}$. For the purely elastic branch, $\alpha_{V\infty}$ is related to $\varepsilon_{ve^{V}}$.

The sum of the stresses of each branch defines a hydrostatic pressure σ^{V} independent of the microplane and a deviatoric stress on each microplane $\underline{\sigma^{D^{mic}}}$:

$$\begin{cases} \sigma^{V} = \sigma^{V_\infty} + \sum_{b=1}^{N_b} \sigma^{V_b} \\ \underline{\sigma^{D^{mic}}} = \underline{\sigma^{D_\infty\ mic}} + \sum_{b=1}^{N_b} \underline{\sigma^{D_b\ mic}} \end{cases} \tag{3}$$

The stresses σ^{V_∞} and $\underline{\sigma^{D_\infty\ mic}}$ are the hydrostatic pressure and the deviatoric stress of the purely elastic branch. The stresses σ^{V_b} and $\underline{\sigma^{D_b\ mic}}$ are the hydrostatic pressure and the deviatoric stress of the bth viscoelastic branch.

The behaviour of the elastic branch is linear when damage is constant:

$$\begin{cases} \sigma^{V_\infty} = (1 - \alpha_{V\infty} d_V)\,k_{V\infty}\,\varepsilon_{ve^{V}} \\ \underline{\sigma^{D_\infty\ mic}} = (1 - d_{D^{mic}})\,\mu_{D\infty}\,\underline{\varepsilon_{ve^{D}}^{mic}} \end{cases} \tag{4}$$

The volumetric and deviatoric differential equations ruling the

behaviour of each viscoelastic branch are:

$$\begin{cases} \dot{\sigma^V}_b + \left(\frac{1}{\tau_b} + \frac{\alpha_{Vb}\dot{d}_V}{1-\alpha_{Vb}d_V}\right)\sigma^{V_b} = (1-\alpha_{Vb}d_V)\, k_{Vb}\, \dot{\varepsilon}_{ve^V} \\ \dot{\underline{\sigma^D}}_b^{\,mic} + \left(\frac{1}{\tau_b} + \frac{\dot{d}_{D^{mic}}}{1-d_{D^{mic}}}\right)\underline{\sigma^{D_b}}^{mic} = (1-d_{D^{mic}})\, \mu_{Db}\, \dot{\underline{\varepsilon}}_{ve^D}^{\,mic} \end{cases} \tag{5}$$

the dot above a variable means that it is its time derivative. The principle of virtual work enables deducing the total stress $\underline{\sigma}$ (Carol et al., 2001):

$$\underline{\sigma} = \sigma_V \underline{V} + \sum_{mic=1}^{N_m} 3\omega^{mic}\, \underline{\sigma_D}^{mic} . \underline{\underline{D}}^{mic} = \sigma_V \underline{V} + \sum_{mic=1}^{N_m} 3\omega^{mic}\, \underline{\underline{D}}^{mic^T} . \underline{\sigma_D}^{mic} \tag{6}$$

with $\underline{\underline{D}}^{mic^T}$ the transposed tensor of $\underline{\underline{D}}^{mic}$. As the viscoelasticity and viscoplasticity are added in series, the stress tensor $\underline{\sigma}$ also applies to the viscoplastic part.

3.1.2. Viscoplastic part

A number N_s of yield surfaces are put in series in the sense of the plastic strain additivity to define a non-linear viscoplastic strain $\underline{\underline{\varepsilon_{vp}}}$. s is the index of the surface number. The viscoplastic free energy ψ_{vp} is therefore the sum of the free energies of each surface $\underline{\underline{\psi_{vp\,s}}}$. The latter depend only on the kinematic hardening variable $\underline{\underline{\xi_s}}$, homogeneous to a strain. Free energies are chosen to follow the linear strain hardening law of Prager (Fig. 8). The hardening modulus of the surface s is denoted C_s.

A surface s is defined by its yield stress σ_{Y_s} and its kinematic hardening tensor $\underline{\underline{X_s}}$. The von Mises yield criterion f_s is written in the effective stress space:

$$f_s = \left|\underline{\underline{\tilde{\sigma}}}^D - \underline{\underline{X_s}}\right| - \sigma_{Y_s} \tag{7}$$

The effective stress $\underline{\underline{\tilde{\sigma}}}$ is related to the stress $\underline{\underline{\sigma}}$ by an effectivity tensor $\underline{\underline{\underline{\underline{M}}}}$ depending on the state of damage:

$$\underline{\underline{\tilde{\sigma}}} = \underline{\underline{\underline{\underline{M}}}}^{-1} : \underline{\underline{\sigma}} \;\Rightarrow\; \begin{cases} \sigma^V = M^V \tilde{\sigma}^V \\ \underline{\underline{\sigma}}^D = \underline{\underline{\underline{\underline{M}}}}^D : \underline{\underline{\tilde{\sigma}}}^D \end{cases} \tag{8}$$

where $\tilde{\sigma}^V$ is the effective hydrostatic pressure and $\underline{\underline{\tilde{\sigma}}}^D$ is the effective deviatoric stress tensor. M^V and $\underline{\underline{\underline{\underline{M}}}}^D$ are the volumetric and deviatoric parts of $\underline{\underline{\underline{\underline{M}}}}$. The nature of the tensor $\underline{\underline{\underline{\underline{M}}}}$ is discussed below.

Without unilateral effect of damage, working in the effective stress space preserves the convexity of the yield surfaces. With a unilateral effect, a yield surface defined in effective stress is not convex and the yield criterion must be adapted (Liénard, 1989; Desmorat and Cantournet, 2008). Here, the effectiveness is carried by the volumetric component while the yield surfaces are only deviatoric. The convexity of the load surfaces is therefore preserved in effective stress space.

The plastic flow of the surfaces is not associated. The volumetric flow $\dot{\varepsilon}_{vp\,s^V}$ is related to the deviatoric one $\dot{\underline{\underline{\varepsilon_{vp\,s}}}}^D$ by the dilatancy function β. The deviatoric flow is normal to the load surface:

$$\begin{cases} \dot{\varepsilon}_{vp\,s^V} = \beta \left|\dot{\underline{\underline{\varepsilon_{vp\,s}}}}^D\right| \\ \dot{\underline{\underline{\varepsilon_{vp\,s}}}}^D = \dot{\lambda}_s \frac{\partial f_s}{\partial \underline{\underline{\sigma}}^D} = \frac{3}{2}\dot{\lambda}_s \frac{\underline{\underline{\tilde{\sigma}}}^D - \underline{\underline{X_s}}}{\left|\underline{\underline{\tilde{\sigma}}}^D - \underline{\underline{X_s}}\right|} : \underline{\underline{\underline{\underline{M}}}}^{D^{-1}} \end{cases} \tag{9}$$

In multilayer models (Mroz, 1967; Montáns, 2000, 2001; Yan and Oskay, 2017) the sliding direction of the surfaces is constrained such that they remain nested within each other (Fig. 7 right). They cannot overlap. The smallest surface moves first, until it becomes tangent to the second. The second surface becomes active from the contact. The two surfaces then remain tangent while moving. This pattern is repeated until the last surface is reached. The last surface defines an associated flow. To our knowledge, no thermodynamic justification is given to this last constraint.

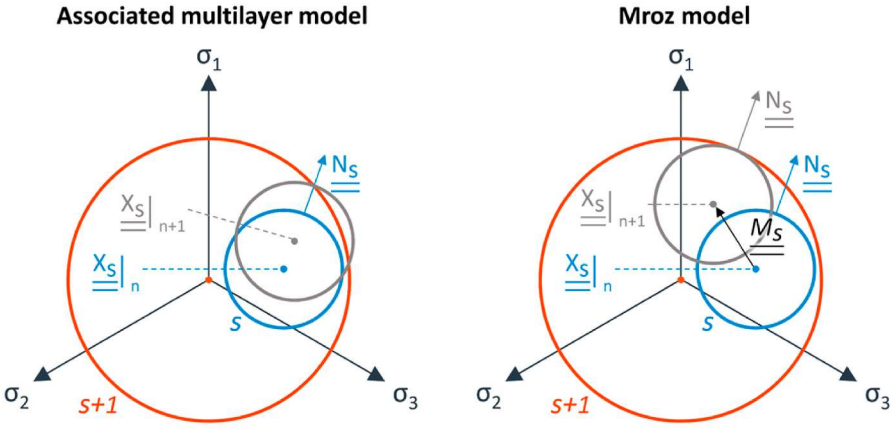

Fig. 7. Left, diagram representing the possible exit of surface s with respect to surface s+1 during non-proportional loading (negligible in the simulations below). Right, the solution provided by Mroz (1967) to ensure the nesting of the surfaces. The tensor $\underline{\underline{N_s}}$ is the flow direction. The tensor $\underline{\underline{M_s}}$ is the sliding direction of the surface s.

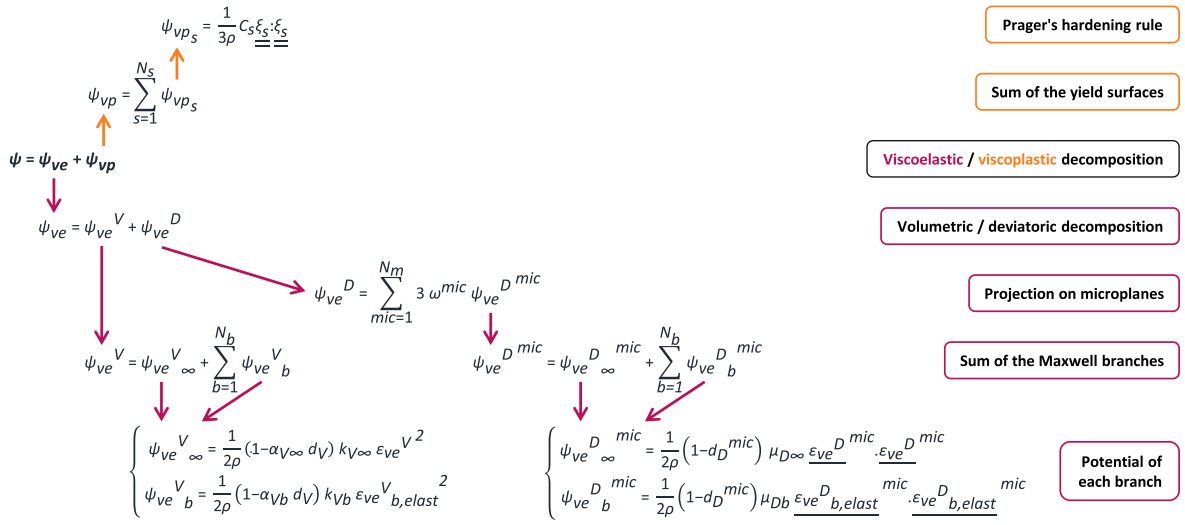

Fig. 8. Decomposition of the free energy. The variable ρ is the density of the material.

With viscoplastic flow, a surface could be activated when the previous one has not yet reached it. The classic Mroz surface displacement scheme is not applicable here. The sliding direction of a surface is along its normal and it is not constrained by other surfaces. So, surfaces can slightly overlap in non-proportional loadings (Fig. 7 left). This could be improved in future work. However, the simulations (presented below later in this paper) show a negligible overlap.

Dilatancy is a function of the effective pressure $\tilde{\sigma}^V$ and the norm of the total deviatoric viscoplastic strain $\left|\underline{\underline{\varepsilon_{vp}}}^D\right|$. Its expression is determined from the experimental data. We work here with the norm of the viscoplastic strain $\underline{\underline{\varepsilon_{vp}}}^D$. It is an instantaneous measurement. Using the cumulative plasticity as Chiarelli (2000) and Le et al. (2010) is not suitable here. Numerically, given the kinematic strain hardening, there is an accumulation of the viscoplastic strain when unloading and reloading. At a same stress level, the accumulated viscoplastic strain depends on the number of cycles performed. To match our curve of a monotonic simulation with the envelope of the corresponding cyclic simulation, the instantaneous viscoplastic strain must be considered in the expression of the dilatancy.

The model being viscoplastic, the criterion outputs (f_s>0) are allowed. As seen in section 2, the pressure slows down the plastic flow of polymers (Rinaldi, 2006; Dasriaux, 2013). The viscoplastic multiplier $\dot{\lambda}_s$ of each surface follows a classical exponential-power law (Lemaître et al., 2020), but with dependence on effective pressure $\tilde{\sigma}^V$:

$$\dot{\lambda}_s = \left(\frac{f_s}{a_1}\right)^n exp\left((a_2 + a_3\tilde{\sigma}^V) f_{s^{n+1}}\right) \tag{10}$$

The pressure is effective as for the whole viscoplastic model. The coefficients a_1, a_2, a_3 and n are material parameters (same set for each surface). The a_3 parameter being positive, the greater the confinement, the slower the flow. The Norton term (power function) is dominant for low values of f_s while the exponential one dominates for higher values of f_s.

Each surface has a linear kinematic hardening defined by the Prager's law (Fig. 8). The thermodynamic force associated with $\underline{\underline{\xi_s}}$ is the kinematic hardening tensor $\underline{\underline{X_s}}$, homogeneous to a stress:

$$\underline{\underline{X_s}} = \frac{2}{3} C_s \underline{\underline{\xi_s}} \tag{11}$$

Note that the norm $\left|\underline{\underline{\tilde{\sigma}}}^D - \underline{\underline{X_s}}\right|$ in equation (7) corresponds to the second deviatoric invariant J_2 of the tensor $\left(\underline{\underline{\tilde{\sigma}}}^D - \underline{\underline{X_s}}\right)$.

The Prager's linear hardening law is written:

$$\dot{\underline{\underline{\xi_s}}} = -\dot{\lambda}_s \frac{\partial f_s}{\partial \underline{\underline{X_s}}} = \dot{\underline{\underline{\varepsilon_{vp}}}}_s^D : \underline{\underline{\underline{\underline{M}}}}^D \tag{12}$$

hence:

$$\dot{\underline{\underline{X_s}}} = C_s \dot{\lambda}_s \frac{\underline{\underline{\tilde{\sigma}}}^D - \underline{\underline{X_s}}}{\left|\underline{\underline{\tilde{\sigma}}}^D - \underline{\underline{X_s}}\right|} \tag{13}$$

Finally, for the implementation of the law, the effectiveness tensor $\underline{\underline{\underline{\underline{M}}}}$ would only appear through the tensor $\underline{\underline{\underline{\underline{M}}}}^{D-1}$ in the expression of $\dot{\underline{\underline{\varepsilon_{vp}}}}_s^D$ (equation (9)). To simplify the implementation of the deviatoric flow $\dot{\underline{\underline{\varepsilon_{vp}}}}_s^D$, $\underline{\underline{\underline{\underline{M}}}}^{D-1}$ is unity in this equation. This approximation is acceptable due to the low level of damage of the material M2. This simplification will have to be reconsidered when identifying the model to the material M1 which suffers more damage. For this material, the tensor $\underline{\underline{\underline{\underline{M}}}}$ will probably have to be calculated.

3.1.3. Global rheological scheme

Finally, the model corresponds to the rheological diagram in Fig. 9.

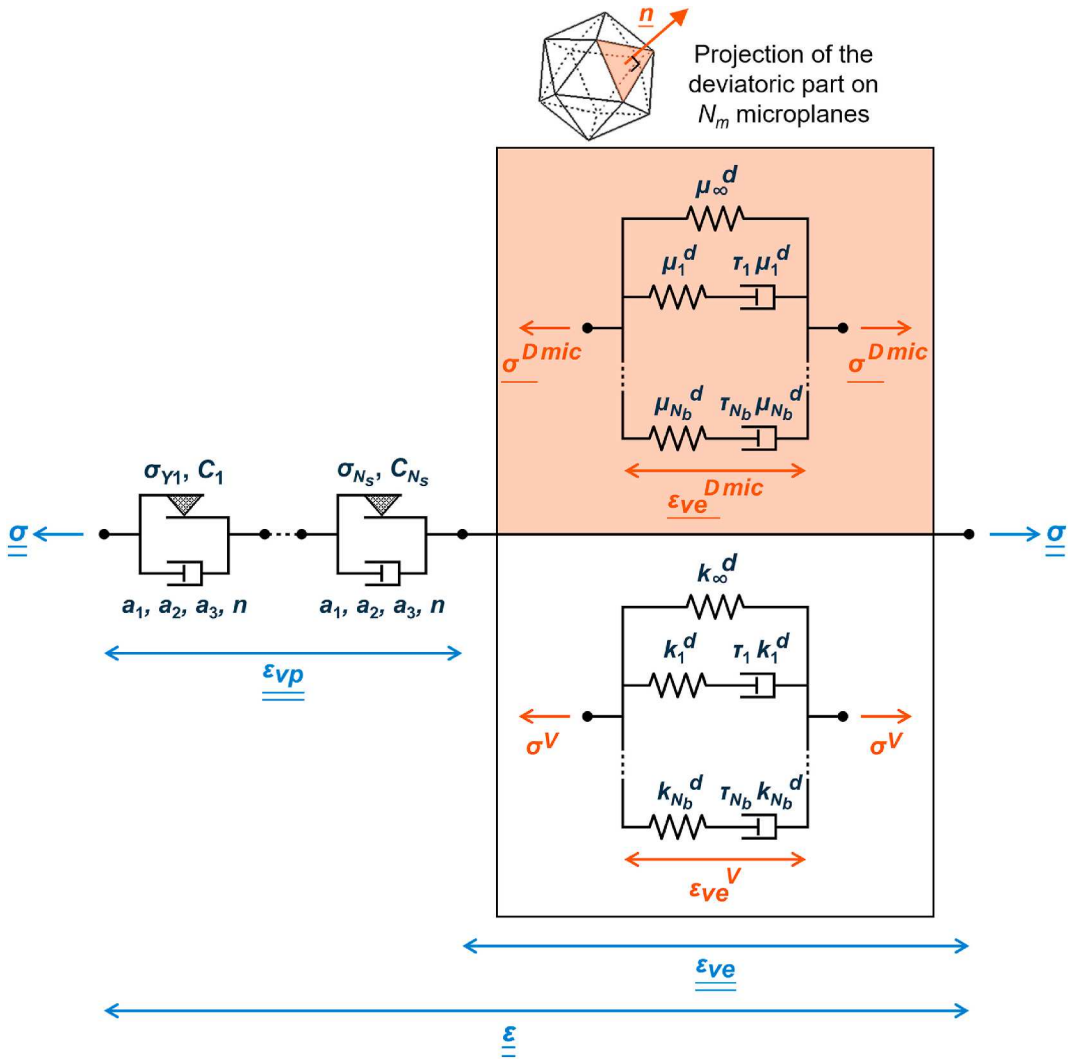

Fig. 9. Rheological diagram of the constitutive law. The elastic modules k_b^d and μ_b^d correspond to the damaged volumetric and deviatoric elastic modules: $k_b^d = (1-\alpha_{Vb} d_V)\, k_{Vb}$ and $\mu_b^d = (1 - d_{D^{mic}})\mu_{Db}$. The terms τ_b correspond to the characteristic viscoelastic times.

3.1.4. Failure criteria

In addition to the data from uniaxial compression and tensile tests, the results of multiaxial tests (Brazilian test, channel-die, equibiaxial compression, torsion) make it possible to identify an asymmetric failure criterion in tensile and compression. To do so, two independent failure criteria must be used. It turns out that the failure criterion developed for the material M1 (Caliez et al., 2014; Picart and Pompon, 2016) is perfectly suited to the material M2. The first criterion is based on the critical value of the maximum effective positive principal stress. Stress states as biaxial tensile conditions, tensile test, shear loading, and Brazilian experiments can be predicted by the first criterion. The second criterion relates the maximum positive principal strain to the pressure. It enables predicting loading conditions as uniaxial and triaxial compressions, channel-die tests and equibiaxial compressions. These thresholds are not discussed here. The reader must refer to Picart and Pompon (2016) for more details.

3.2. Implementation

The model is implemented in incremental form as an Abaqus UMAT subroutine as illustrated in Fig. 10 (Plassart, 2020). The principle of the resolution is as follows. As input to the UMAT, the variables at the time t and the strain increment $\Delta\underline{\underline{\varepsilon}}$ between t and $t+\Delta t$ are known. The UMAT calculates the evolution of the variables over the time increment and the constitutive Jacobian. Abaqus then computes the strain increment for the next step.

The UMAT code has two parts: the viscoelastic one and the viscoplastic one. At the beginning of a time increment (time $t+\Delta t$), a viscoelastic prediction is formulated. The predictor/corrector methodology is a standard approach for integrating ordinary differential equations. For example, see Doghri (1993). The viscoelastic differential equation (5) are integrated at times t and $t+\Delta t$ to express the stress increments $\Delta\sigma^{V_b}$ and $\Delta\underline{\sigma^{D_b}}^{mic}$ of each branch. To do so, the strain rates $\dot{\varepsilon}_{ve^V}$ and $\underline{\dot{\varepsilon}_{ve^D}}^{mic}$ are assumed to be constant over the time interval Δt. This provides an estimate of the total stresses (effective and not). The yield criteria f_s are then tested. If there is no active surface, the prediction is correct. Otherwise, a return mapping algorithm applied to viscoplasticity is run. A viscoplastic correction of the prediction is then made following a Newton-Raphson scheme solved by gaussian elimination. Residues are calculated on the stresses $\widetilde{\sigma}^V$ and $\underline{\widetilde{\sigma}}^D$, and on the viscoplastic multiplier $\dot{\lambda}_s$ ($\Delta\lambda_s/\Delta t$ in incremental form). Then comes a system of corrective equations for these three quantities. It is solved by a gaussian elimination method. From the corrected effective stresses and viscoplastic multiplier, strains and hardening are updated. A new viscoelastic computation leads to new values of stresses. If they correspond to the stresses calculated on the viscoplastic part (within a tolerance), the balance is found. Otherwise, a new correction calculation is started. This scheme is

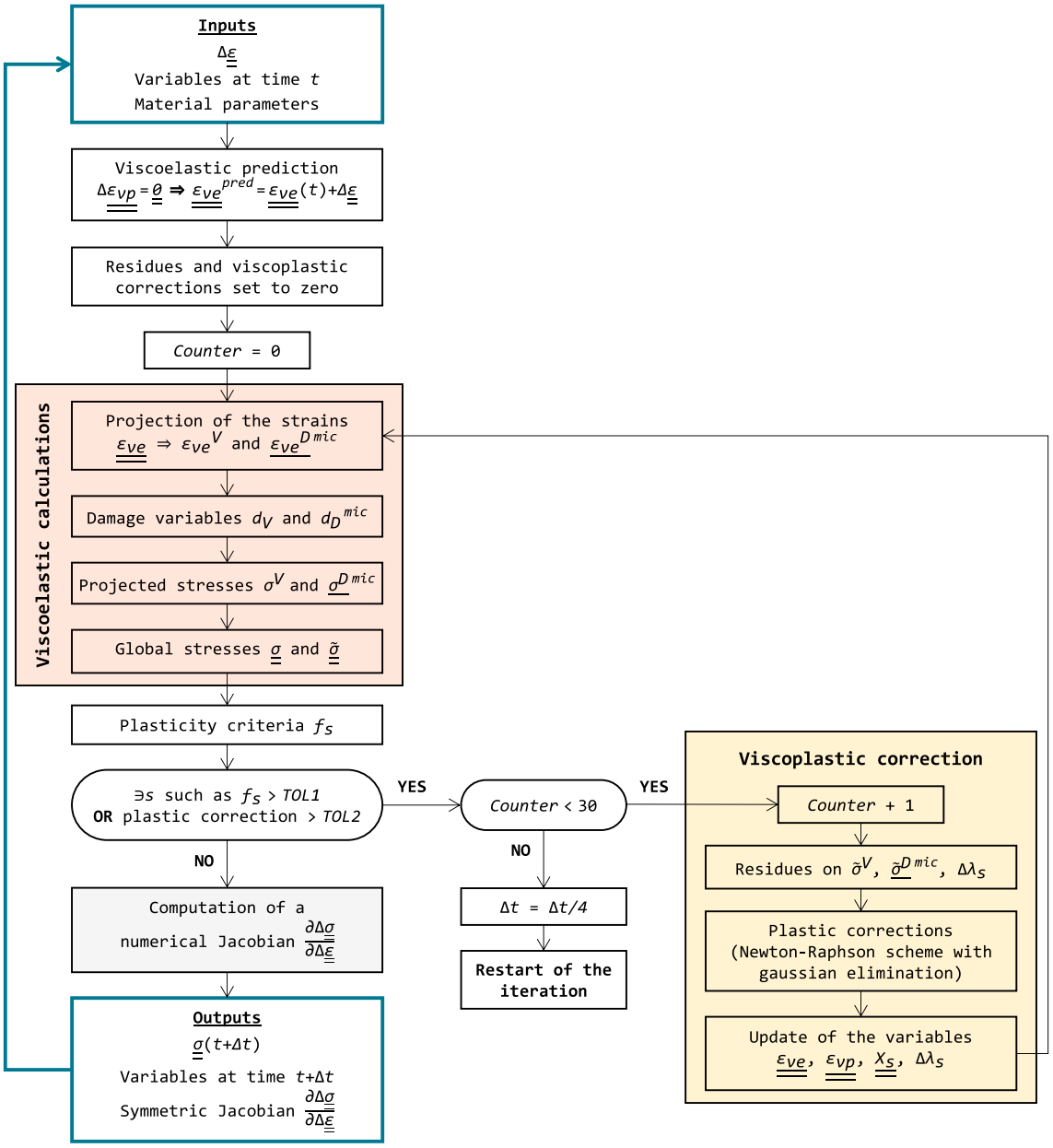

Fig. 10. Algorithm for the integration of the behaviour law in the Abaqus/Standard calculation code.

Table 3
Values of relaxation times and longitudinal elastic modules for a reference temperature of 0 °C.

Branch b	∞	1	2	3	4	5	6	7	8	9	10	11	12	13	14
$\tau_{ref\ b}$ (s)	/	10^{-2}	10^{-1}	1	10	10^{2}	10^{3}	10^{4}	10^{5}	10^{6}	10^{7}	10^{8}	10^{9}	10^{10}	10^{11}
E_b (MPa)	4480	140	100	110	110	120	130	140	150	220	380	550	840	710	1

repeated until the balance is found. If this is not the case after thirty iterations, the time interval Δt is divided by four and the calculation on the increment is reset.

Sometimes a surface initially detected as active is no longer active after the viscoplastic correction because the estimate effective stress decreases. In this case, the iteration is restarted without considering this surface in the viscoplastic correction.

To provide the constitutive Jacobian $\frac{\partial\Delta\underline{\underline{\sigma}}}{\partial\Delta\underline{\underline{\varepsilon}}}$, we have chosen a numerical computation rather than an analytical one. This Jacobian is determined by a perturbation method of the strain increment tensor. The principle is to determine the stress increment obtained for a perturbation one hundred times smaller than the strain increment $\Delta\underline{\underline{\varepsilon}}$ (a minimum amplitude of the perturbation is guaranteed). This Jacobian is automatically symmetrised by the software.

Table 4
Values of the parameters of the damage law.

y_{D0} (MPa)	ξ_{D1} (MPa^{-1})	ξ_{D2}
7×10^{-3}	12	1.4

Table 5
Values of the yield strength and kinematic strain hardening modulus.

Surface s	1	2	3	4	5	6	7	8	9
σ_{Ys} (MPa)	1	6	11	15	18	20	22	23	23.5
C_s (MPa)	15000	11000	8000	4500	3000	2000	500	100	1

Table 6
Values of the parameters of the viscoplastic law.

n	a_1 (s^{-1}.MPa)	a_2 (MPa^{-n-1})	a_3 (MPa^{-n-2})
2	3.0×10^4	1.3×10^{-2}	-5.3×10^{-2}

Table 7
Values of the parameters of the dilatancy function.

β_{t1}	β_{t2} (MPa^{-1})	β_{c1} (MPa^{-1})	β_{c2}	β_{c3} (MPa^{-1})	β_{c4}	β_{c5}	β_{c6}	β_{c7}
0.2	60×10^3	10^6	7.4	1.5×10^{-2}	7.25	2.4	0.5	960

3.3. Determining the parameters

The microplanes directions and the corresponding angular weighting coefficients has been calculated by Bažant and Oh (1985) for a discretization of the hemisphere in 21, 33, 37 and 61 directions. For modelling the material M2, 21 microplanes are used.

The parameters of the generalized Maxwell model have been determined by discretizing the master curves at 0 °C in fourteen characteristic times. These times and the corresponding longitudinal elastic modules are given in Table 3. To get the values of the relaxation times at 20 °C, the time-temperature equivalence is used. The bulk and shear modules are determined with a Poisson's ratio of 0.35 experimentally measured (Plassart et al., 2020).

The damage is determined from the degradation of the modules measured in cyclic loading. For M2, the bulk modulus does not decrease. So, there is no volumetric damage. The shear modulus slowly decreased after a given threshold. This modulus being global, it does not enable to highlight the damages for each microplane d_D^{mic}. Their evolution law is determined by an inverse method. The parameters of the law are fitted to reproduce the degradation of the global shear modulus in uniaxial tensile, uniaxial compression and triaxial compression. This module is not calculated at each stage of the simulation. It is evaluated from the final simulation curve.

A power law triggered by threshold is used:

$$\begin{cases} d_D^{mic}(t+\Delta t) = d_{D0} & if\ Y_{D\infty}^{mic} \le y_{D0} \\ d_D^{mic}(t+\Delta t) = max\left(d_D^{mic}(t), min\left(1, \xi_{D1}\left(Y_{D\infty}^{mic} - y_{D0}\right)^{\xi_{D2}}\right)\right) & if\ Y_{D\infty}^{mic} > y_{D0} \end{cases} \tag{14}$$

with ξ_{D1} and ξ_{D2} the parameters of the power law and y_{D0} the triggering threshold. Their values are given in Table 4.

To describe the non-linear viscoplastic flow, nine yield surfaces are chosen. It is the smallest number leading to smooth curves. The yield strength and the hardening modulus of each surface have been set to reproduce the experimental relaxed stress points in cyclic compression. The selected values are given in Table 5.

The objective of the viscoplastic calibration is double. The global stress level (envelope curve) must be reached, and the viscous flow (relaxation and recovery times) must be reproduced. In the viscoplastic flow law (equation (10)), the power function (parameter a_1) manages the small flows (low levels of f_s) and the time evolution of the stress relaxation. The exponential function (parameters a_2 and a_3) manages the larger levels of f_s and the pressure dependence. The parameter n appearing in both functions manages their weighting. The parameters are given in Table 6. They have been calibrated from a cyclic compression test. The monotonic compression at 10 MPa pressure has been used to identify the parameter a_3.

A single dilatancy function is chosen. It regulates the ratio between the volumetric and deviatoric flows of each yield surface (equation (9)) as follows:

$$\beta = \frac{\dot{\varepsilon}_{vp}^V}{\sum_s \left| \underline{\underline{\dot{\varepsilon}_{vp\ s}}}^D \right|} \tag{15}$$

To estimate the experimental viscoplastic strains developed during a test, a model without plasticity has been implemented. The viscoelastic parameters and the damage law are those described above. The test is simulated and compared to experimental data. Viscoelasticity and viscoplasticity additively acting in the model, the "experimental" viscoplastic strains are the difference between the total experimental strains and the viscoelastic simulated strains. However, the experimental data only enable accessing the norm of the total viscoplastic strains. In monotonic proportional loading, the loading surfaces all have the same direction and the rates $\underline{\underline{\dot{\varepsilon}_{vp\ s}}}^D$ have the same sign. The equality $\left| \sum_s \underline{\underline{\dot{\varepsilon}_{vp\ s}}}^D \right| = \sum_s \left| \underline{\underline{\dot{\varepsilon}_{vp\ s}}}^D \right|$ is then verified. The dilatancy function β has been determined on the monotonic proportional loading tests (uniaxial and triaxial compressions, uniaxial traction, torsion):

$$\beta = \beta_{t1}\langle \tilde{\sigma}^V \rangle_+ + \left(1 - \exp\left(-\beta_{t2}\left|\underline{\underline{\varepsilon_{vp}}}^D\right|\right)\right) + \tanh\left(\beta_{c1}\langle \tilde{\sigma}^V \rangle_-\right)\left(\beta_{c2} + \beta_{c3}\,\tilde{\sigma}^V - \beta_{c4}\exp\left(-\beta_{c5}\left|\underline{\underline{\varepsilon_{vp}}}^D\right|\right) - \beta_{c6}\exp\left(-\beta_{c7}\left|\underline{\underline{\varepsilon_{vp}}}^D\right|\right)\right) \tag{16}$$

The terms $\langle \tilde{\sigma}^V \rangle_+$ and $\tanh(\beta_{c1}\langle \tilde{\sigma}^V \rangle_-)$ describe a continuous function, null at zero pressure, with two different expressions in tensile and compression. The β_{ti} and β_{ci} are parameters. They are given in Table 7.

4. Results and discussion

The simulations have been performed using the Abaqus/Standard

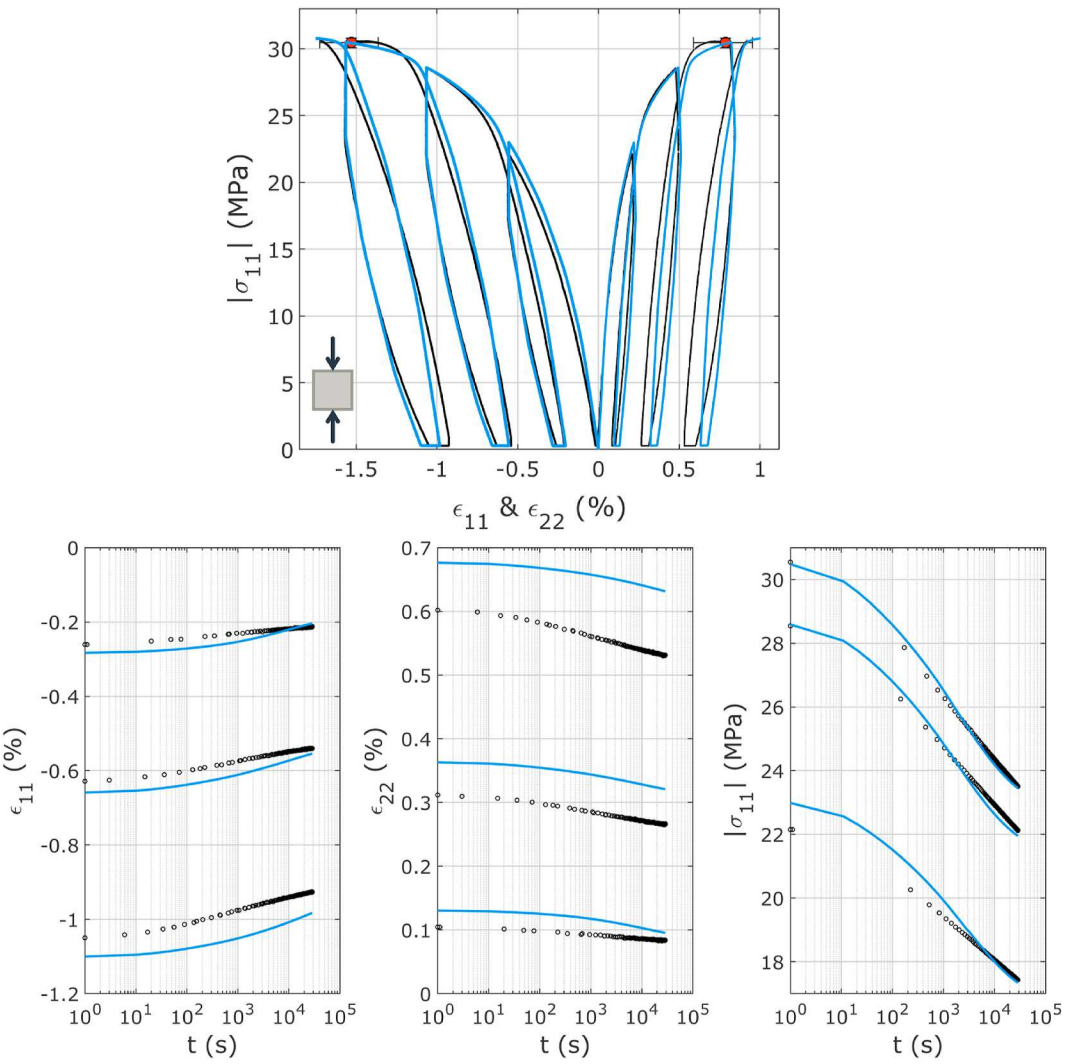

Fig. 11. Simulation of a cyclic uniaxial compression test performed at 1.7×10^{-5} s^{-1}. The bottom figures present the strain recoveries and the stress relaxations. The experimental data are in black. This simulation, used to calibrate the parameters, is in blue.

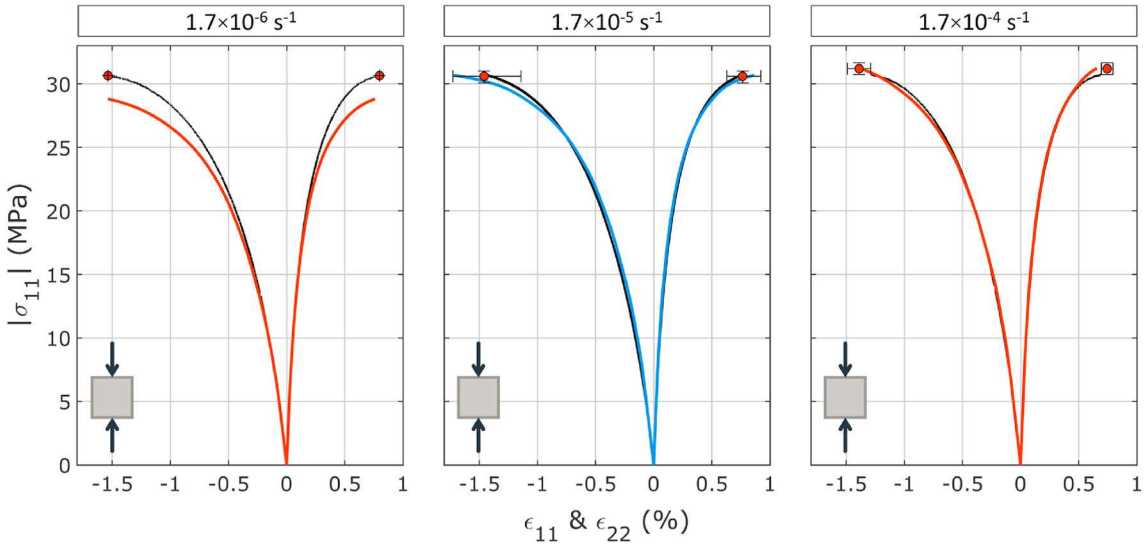

Fig. 12. Simulation of the monotonic uniaxial compression tests performed at the three strain rates. The experimental data are in black. The simulation at 1.7×10^{-5} s^{-1}, which has been used to calibrate the dilatancy, is in blue. The two others simulations are in red.

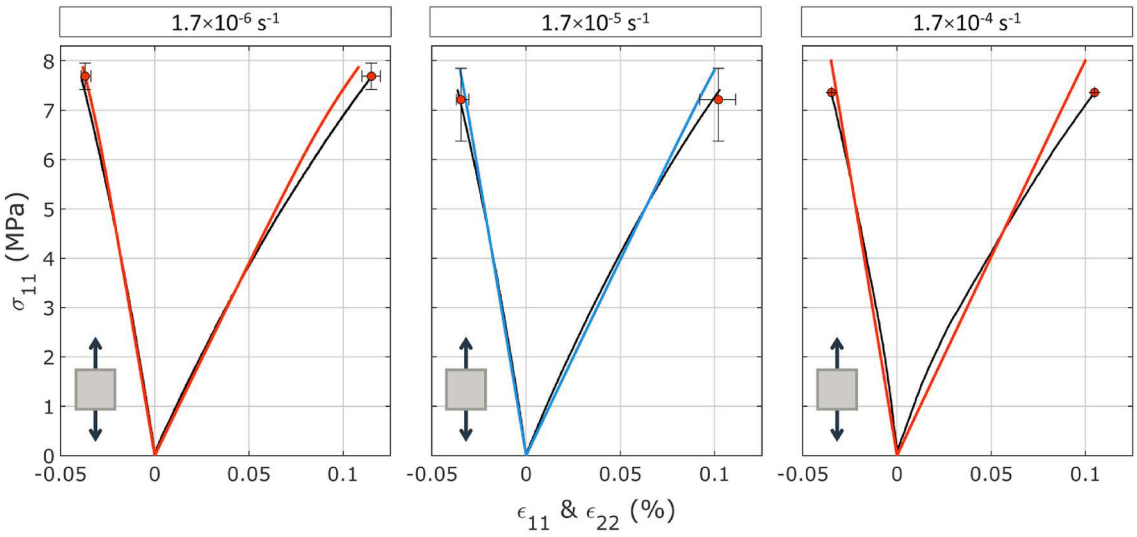

Fig. 13. Simulation of the monotonic uniaxial tensile tests performed at the three strain rates. The experimental data are in black. The simulation at $1.7 \times 10^{-5}\ s^{-1}$, which has been used to calibrate the dilatancy, is in blue. The two others simulations are in red.

finite element code on a C3D8 element (unless otherwise stated). Symmetry constraints were imposed on three faces of respective normal x, y, and z. Small time steps were used to describe the non-linearity (a monotonic compression curve has about 100 points). The step time independence of the results has been verified. In the following figures, the experimental data are in black. The simulations of tests used for the determination of the parameters are in blue. The simulations of the other tests are in red. This colour code does not apply to the simulation of 0°–0° and 0°–90° compressions.

First, the model is tested in cyclic uniaxial compression test at $1.7 \times 10^{-5}\ s^{-1}$ (the reference strain rate). The simulation (envelope curve and hysteresis) is close to the experimental data (Fig. 11). The longitudinal strains levels are excellent. The dilatancy is well reproduced, although it is a little too large when the unloadings end (upper graph Fig. 11). Remind that the dilatancy was parameterized on monotonic tests. All loading and unloading elastic modules are reproduced. The amplitude of the relaxation and recovery phases is good. The lower graphs (Fig. 11) show the time versus the strain recovery on the first two graphs and versus the stress relaxation on the last one. Flow is reproduced along time.

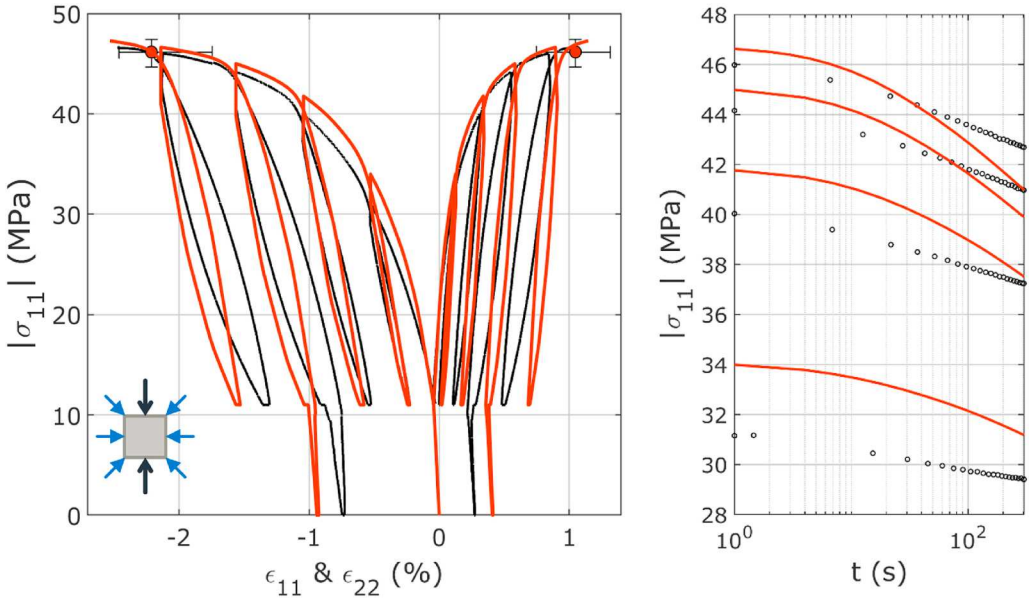

Fig. 14. Simulation of the cyclic triaxial compression test performed at $1.7 \times 10^{-5}\ s^{-1}$ at 10 MPa pressure. The right figure presents the stress relaxations. The experimental data are in black. The simulation is in red.

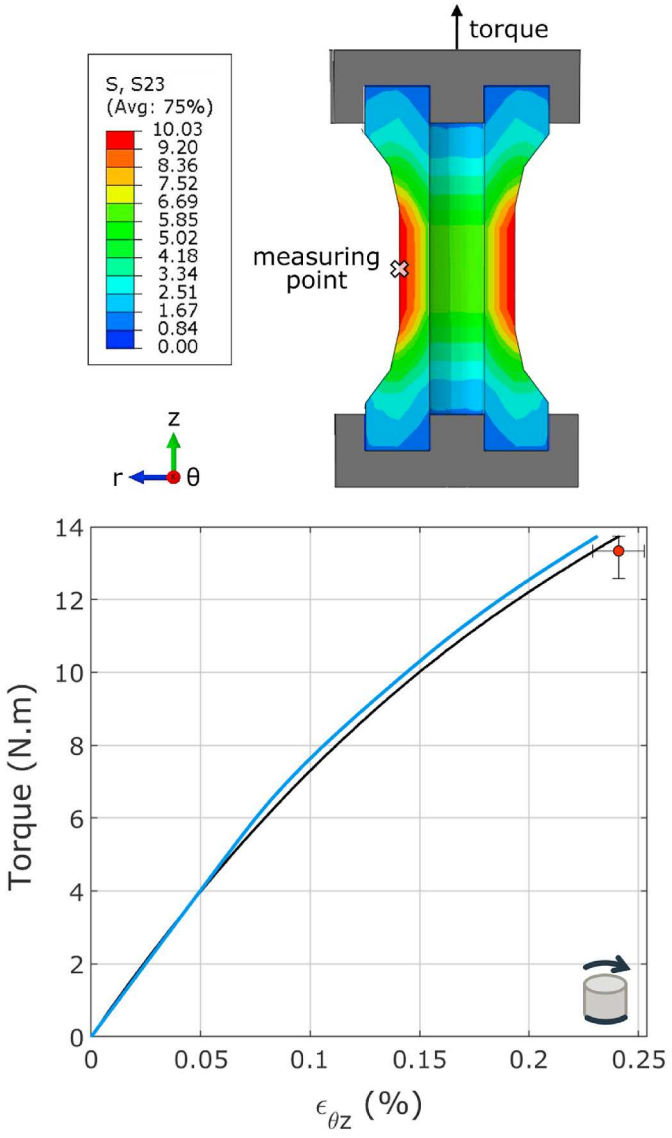

Fig. 15. Simulation of the monotonic torsion test performed at $0.015°s^{-1}$. The stress S23 (corresponding to rθ-plane) is expressed in MPa. The experimental data, which has been used to calibrate the dilatancy, are in black. The tests dispersion is shown by the error bar. The simulation is in blue.

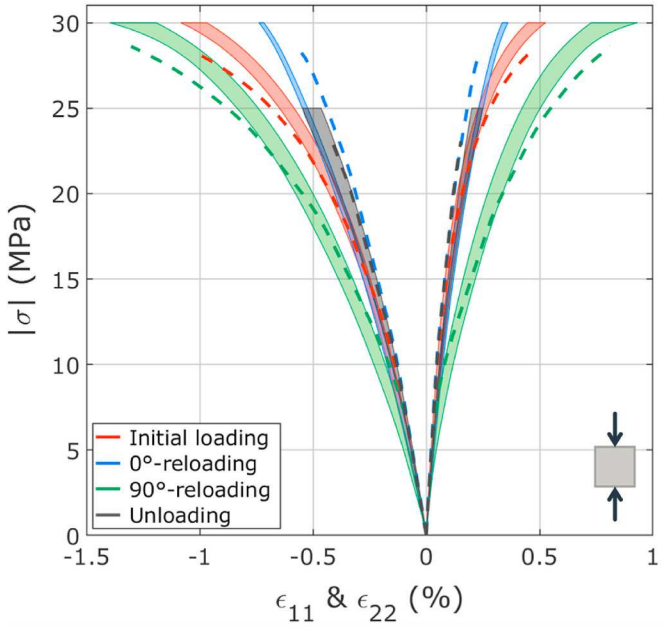

Fig. 16. Simulation of the 0°–0° and 0°–90° compression tests. The experimental data are the surfaces. The simulations are the dotted lines. These tests were not used to parameterize the model. The initial loadings are in red. The 0° reloading is in blue. The 90° reloading is in red. The unloadings are in grey.

The rate effect of the model was tested in uniaxial compression (Fig. 12) and tensile (Fig. 13). Fig. 12 shows that the maximum stress in compression at 1.7×10^{-6} s^{-1} is slightly underestimated and good at 1.7×10^{-4} s^{-1}. In tensile, Fig. 13, the overall behaviour lacks non-linearity, but the strain and stress levels are correct. The shape of the tensile curves is related to the parameter a_1 of the viscoplastic flow. a_1 controlling the flow in relaxations and recoveries as well as in tensile, a compromise was found here.

The dilatancy and the pressure effect have been calibrated on the monotonic triaxial tests, and the model correctly reproduces these tests. The Fig. 14 presents the simulation of a cycling compression under a confinement of 10 MPa. The envelope behaviour is well simulated. However, the relaxation amplitude is a little too high. Furthermore, the unloads are too stiff which leads to excessive residual strains. For reminder, the viscoplastic flow depends on pressure. In future work, a dependence of the strain hardening modules to the pressure could be add. At a given stress level, the hardening modules seems too low since there is too much flow during relaxation.

Since the torsion test is a heterogeneous one, a modelling of the experimental set-up has been made. The sample is embedded between two plates (Fig. 15 left). The bottom one is fixed, the top one applies the torque. The strains are those of a node at the centre of the sample on the outer radius ("measuring point" on the scheme). This corresponds to the place where the gauges were experimentally glued. The comparison between the simulation and the three tests performed shows a good fit of the model (Fig. 15 right). The alternating torsion test, twenty times cycled (Fig. 6), has also been simulated. As experimentally, the model is accommodated from the second cycle.

The 0°–0° and 0°–90° compression tests gave information to choose the kind of hardening. Their simulation highlights the behaviour of the material is well understood (Fig. 16). The model reproduces the experimental mechanisms: a compression stiffens the longitudinal direction of the load and softens the transversal one; the unloadings behave like a reloading at 0°.

At last, the subroutine has been evaluated under multiaxial loading. The channel-die test and the equibiaxial compression (described in Plassart et al., 2020) have been simulated. The results, shown Fig. 17, are positive. The experimental data are very noisy (poor quality of image correlation), but the model describes the trend.

Finally, the model calibrated on M2 can reproduce about ten experimental loading paths in the principal stress space. These loading paths are plotted Fig. 18. In this graph, the principal stresses are sorted

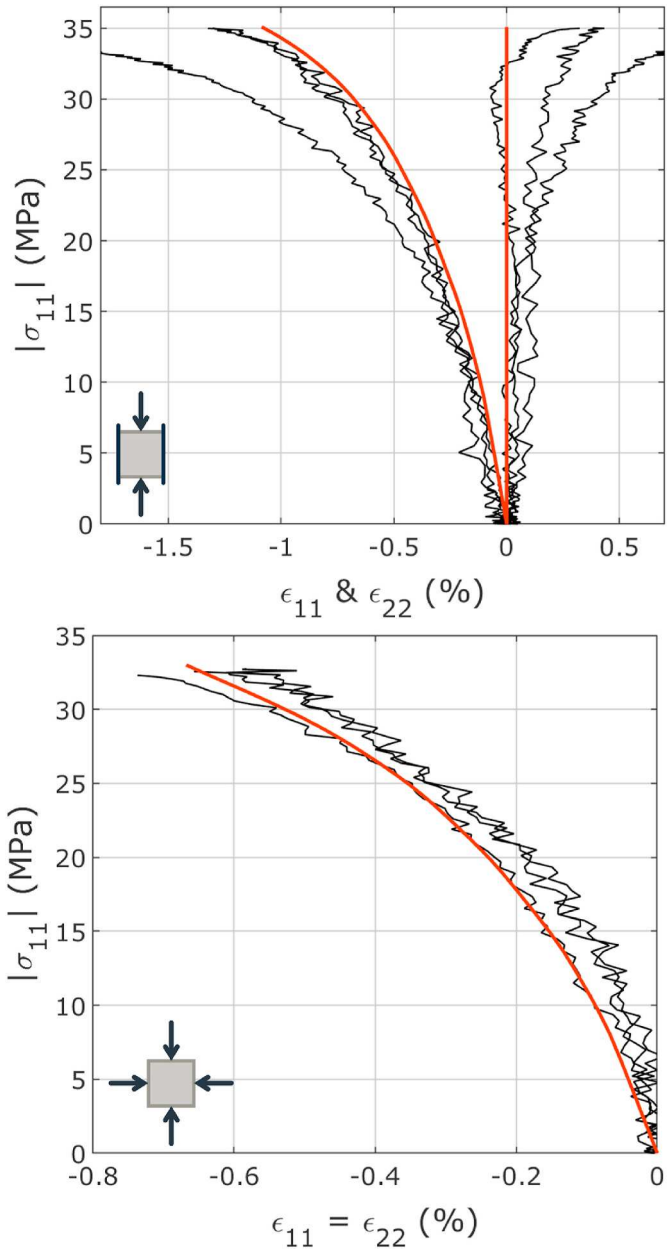

Fig. 17. Simulation of the channel-die test on the top, and of the equibiaxial compression on the bottom. The experimental data are in black (three tests of each). The simulations are in red.

in descending order ($\sigma_I > \sigma_{II} > \sigma_{III}$). A compression has a negative sign while a traction as a positive one. Torsions are in the $(\sigma_I; \sigma_{II})$ plane. Channel-die tests and equibiaxial compressions are in the $(\sigma_{II}; \sigma_{III})$ plane. The recompression at 90° (in light blue) follows a uniaxial compression (in dark blue).

In addition of these loading paths, the rate-dependence has been considering in the model: three strain rates in compression and tensile plus slowest rates in relaxation and recovery. About the integration of the temperature dependence, the reader is invited to read Plassart, 2020.

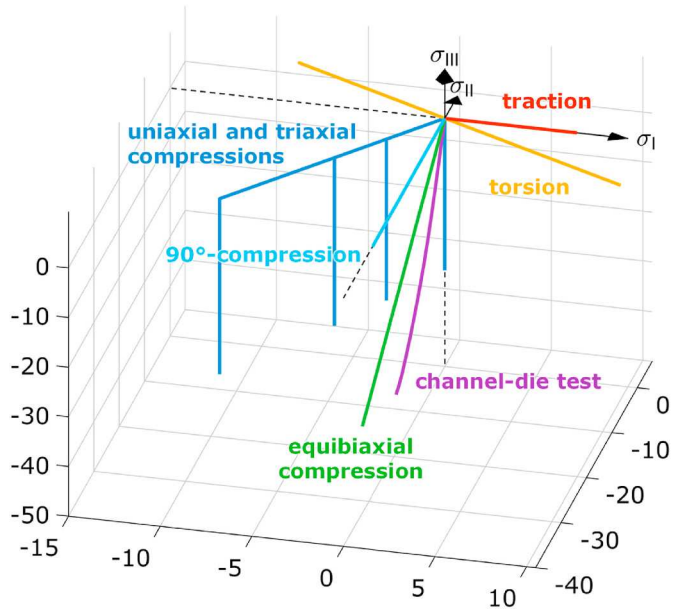

Fig. 18. Representation in the space of the three principal stresses of the loading paths performed experimentally on M2 and reproduced by the model. In this graph, $\sigma_I > \sigma_{II} > \sigma_{III}$. A compression has a negative sign while a traction as a positive one.

5. Conclusion

Nowadays, ensuring the safety and reliability of pyrotechnic structures is done by numerical simulations. The explosive composition must be accurately modelled. A recent exhaustive state of the art of quasistatic mechanical tests shown that few experimental campaigns have been carried out on energetic materials (except for an HMX-based material, the explosive composition M1), resulting in many assumptions about their behaviour. To fill the gap on TATB-based PBXs, an exhaustive characterization of M2 was provided by the authors. This database includes atypical tests (multiaxial, cyclic, alternated) with transversal strains measurements, which enables understanding the behaviour of M2. The key features of the behaviour of M2, close to that of M1, has been recall in this paper: strain rate-, temperature- and pressure-dependence, inelastic strain, and a load-induced anisotropy. The main deformation mechanism of M2 is the non-associated viscoplastic flow with kinematic strain hardening. This material develops few damages. In contrast, the load-induced anisotropy of M1 was attributed to damage. Since HMX- and TATB-based PBXs have similar macroscopic properties, a single constitutive law is attainable for this class of materials. The mechanisms implemented would be the same, each explosive composition having its own set of parameters.

Because of the lack of experimental study, the already proposed constitutive laws are based on many assumptions. None of these models describes all the deformations mechanisms of the PBXs. Therefore, a new constitutive law has been proposed in this paper. The proposed model has a damageable viscoelastic component in series with a non-associated viscoplastic component. There are two sources of load-induced anisotropy: anisotropic damage and kinematic strain hardening. The pressure-dependence has been integrated in the viscoplastic flow law. A calibration has been proposed for the explosive composition M2.

The law has been implemented as a UMAT subroutine for Abaqus/

Standard. The tests from the experimental database have been simulated for comparison. There is a good agreement between the experimental data and the simulations whatever the loading path and the strain rate. The simulation of non-proportional loadings (0°–90° compression and channel-die test) give satisfactory results.

Since this model incorporates damage-induced anisotropy, modelling the behaviour of other PBXs would be possible. Future work will focus on applying it to M1. This will require a new identification of the model parameters.

However, several improvements have been pointed out. To describe the non-associated flow, a dilatancy function has been defined. It has been determined in monotonic loadings, but its calibration is not optimal in unloading. In addition, this function has nine parameters. Furthermore, in the absence of experimental information, we have chosen to integrate the pressure effect only on the viscoplastic flow law. The simulation of the cyclic triaxial compression at 10 MPa pressure shows an excess of stress relaxation. A pressure-dependence to the strain hardening parameters could be incorporated to the model. The confinement would increase the yield stress or/and the hardening modules and so the relaxed stresses.

Declaration of competing interest

The authors declare the following financial interests/personal relationships which may be considered as potential competing interests: Gaetane Plassart reports financial support was provided by French Alternative Energies and Atomic Energy Commission Division of Military Applications Le Ripault.

Acknowledgements

This work has been carried out within the framework of the research program of the Corresponding Research Laboratory (CosMa), a joint laboratory combining CEA Le Ripault and the Gabriel LaMé Mechanical laboratory.

References

Ambos, A., Willot, F., Jeulin, D., Trumel, H., 2015. Numerical modeling of the thermal expansion of an energetic material. Int. J. Solid Struct. 60–61. https://doi.org/10.1051/mattech/2015019.

Armstrong, P.J., Frederick, C.O., 1966. A Mathematical Representation of the Multiaxial Bauschinger effect Central Electricity Generating Board [and] Berkeley Nuclear Laboratories. Research & Development Department.

Armstrong, P.J., Frederick, C.O., 2007. A mathematical representation of the multiaxial Bauschinger effect. Mater. A. T. High. Temp. 24 (1) https://doi.org/10.1179/096034007X207589.

Arora, H., Tarleton, E., Li-Mayer, J., Charalambides, M.N., Lewis, D., 2015. Modelling the damage and deformation process in a plastic bonded explosive microstructure under tensile using the finite element method. Comput. Mater. Sci. 110 https://doi.org/10.1016/j.commatsci.2015.08.004.

Bažant, Z.P., Oh, B.H., 1985. Microplane model for progressive fracture of concrete and rock. J. Eng. Mech. 111 (4) https://doi.org/10.1061/(ASCE)0733-9399(1985)111:4(559).

Benelfellah, A., 2013. Contribution à la modélisation de l'anisotropie induite par endommagement d'un matériau agrégataire énergétique. PhD thesis. https://hal.archives-ouvertes.fr/tel-02966078/.

Benelfellah, A., Frachon, A., Gratton, M., Caliez, M., Picart, D., 2014. Analytical and numerical comparison of discrete damage models with induced anisotropy. Eng. Fract. Mech. 121–122. https://doi.org/10.1016/j.engfracmech.2014.03.022.

Benelfellah, A., Frachon, A., Gratton, M., Caliez, M., Picart, D., 2017. VDT microplane model with anisotropic effectiveness and plasticity. Mech. Industry 18 (607). https://doi.org/10.1051/meca/2017032.

Bennett, J.G., Haberman, K.S., Johnson, J.N., Asay, B.W., Henson, B.F., 1998. A constitutive model of the non-shock ignition and mechanical response of high-explosives. J. Mech. Phys. Solid. 46 https://doi.org/10.1051/meca/2017032.

Benouniche, S., 1979. Modélisation de l'endommagement du béton par microfissuration en compression (PhD thesis).

Buechler, M.A., 2012a. Observed Physical Processes in Mechanical Tests of PBX 9501 and Recommendations for Experiments to Explore a Possible Plasticity/damage Threshold. Los Alamos National Laboratory rapport n° LA-UR-12-21072. https://www.osti.gov/servlets/purl/1039687.

Buechler, M.A., 2012b. Viscoelastic-viscoplastic Combined Hardening Constitutive Model Based on the Drucker-Prager Yield and Flow Potentials. Los Alamos National Laboratory rapport n° LA-UR-12-24895. https://www.osti.gov/servlets/purl/1052364.

Buechler, M.A., 2013. Viscoelastic-viscoplastic Damage Model Development, Parameters Estimation, and Comparison to PBX9501 Experimental Data. Los Alamos National Laboratory rapport n° LA-UR-13-DRAFT. https://www.osti.gov/servlets/purl/1095206.

Caliez, M., Gratton, M., Frachon, A., Benelfellah, A., Picart, D., 2014. Viscoelastic plastic model and experimental validation for a granular energetic material. Int. J. Energ. Mater. Chem. Propuls. 13 https://doi.org/10.1016/j.engfracmech.2014.09.009.

Cambou, B., Lanier, J., 1988. Induced anisotropy in cohesionless soil: experiments and modelling. Comput. Geotech. 6 https://doi.org/10.1016/0266-352X(88)90071-7.

Carol, I., Jirásek, M., Bažant, Z., 2001. A thermodynamically consistent approach to microplane theory. Part I: free energy and consistent microplane stresses. Int. J. Solid Struct. 38 (17) https://doi.org/10.1016/S0020-7683(00)00212-2.

Chaboche, J.L., Dang, Van K., Cordier, G., 1979. Modelization of the strain memory effect on the cyclic hardening of 316 stainless steel. In: Transactions of the 5th International Conference of SMiRT, Berlin.

Chatti, M., Frachon, A., Gratton, M., Caliez, M., Picart, D., Aït Hocine, N., 2019. Modelling of the viscoelastic behaviour with damage induced anisotropy of plastic-bonded explosive based on the microplane approach. Int. J. Solid Struct. 168 https://doi.org/10.1016/j.ijsolstr.2018.08.018.

Chiarelli, A.S., 2000. Étude expérimentale et modélisation du comportement mécanique de l'argilite de l'Est : influence de la profondeur et de la teneur en eau. PhD thesis. https://www.theses.fr/2000LIL10072.

Clements, B.E., Mas, E.M., 2004. A theory for plastic-bonded materials with a bimodal size distribution of filler particles. Model. Simulat. Mater. Sci. Eng. 12 https://doi.org/10.1088/0965-0393/12/3/004.

Dasriaux, M., 2013. Évolutions microstructurales du PEEK au-dessus de sa température de transition vitreuse lors de maintiens sous pression et température. PhD thesis. https://tel.archives-ouvertes.fr/tel-00786016.

Desmorat, R., Cantournet, S., 2008. Modeling microdefects closure effect with isotropic/anisotropic damage. Int. J. Damage Mech. 17 (1) https://doi.org/10.1177/1056789507069541.

Dienes, J.K., 1978. A statistical theory of fragmentation. In: Proceedings of 19th US Rock Mechanics Symposium. University of Nevada. https://permalink.lanl.gov/object/tr?what=info:lanl-repo/lareport/LA-UR-78-0616.

Dienes, J.K., 1996. A Unified Theory of Flow, Hot-Spots, and Fragmentation with an Application to Explosive Sensitivity. High Pressure Shock Compression of Solids II. Springer. https://doi.org/10.1007/978-1-4612-2320-7_14.

Dienes, J.K., Zuo, Q.H., Kershner, J.D., 2006. Impact initiation of explosives and propellants via statistical cracks mechanics. J. Mech. Phys. Solid. 54 https://doi.org/10.1016/j.jmps.2005.12.001.

Doghri, I., 1993. Fully implicit integration and consistent tangent modulus in elasto-plasticity. Int. J. Numer. Methods Eng. 36 (22) https://doi.org/10.1002/nme.1620362210.

Gasnier, J.B., Willot, F., Trumel, H., Jeulin, D., Biessy, M., 2018. Thermoelastic properties of microcracked polycrystals. Part II: the case of jointed polycrystalline TATB. Int. J. Solid Struct. 155 https://doi.org/10.1016/j.ijsolstr.2018.07.025.

Gotuwka, V., 1999. Étude expérimentale du comportement mécanique des bétons à très hautes performances sous sollicitations multiaxiales simples et complexes. PhD thesis. https://ori-nuxeo.univ-lille1.fr/nuxeo/site/esupversions/19bee463-ede4-40f3-91cd-f6a018ce16be.

Gratton, M., Gontier, C., Rja Fi Allah, S., Bouchou, A., Picart, D., 2009. Mechanical characterisation of a viscoplastic material sensitive to hydrostatic pressure. Eur. J. Mech. Solid. 28 (5) https://doi.org/10.1016/j.euromechsol.2009.03.002.

Green, S.J., Swanson, S.R., 1973. Static Constitutive Relations for Concrete. Air Force Weapons Laboratory rapport technique n°AFWL-TR-72-244. https://apps.dtic.mil/sti/pdfs/AD0761820.pdf.

Hackett, R.M., Bennett, J.G., 2000. An implicit finite element material model for energetic particulate composite materials. Int. J. Numer. Methods Eng. 49 (9) https://doi.org/10.1002/1097-0207(20001130)49:9<1191::AID-NME997>3.0.CO;2-V.

Homand-Etienne, F., Hoxha, D., Shao, J.F., 1998. A continuum damage constitutive law for brittle rocks. Comput. Geotech. 22 (2) https://doi.org/10.1016/S0266-352X(98)00003-2.

Hu, D.W., Zhou, H., Zhang, F., Shao, J.F., 2010. Evolution of poroelastic properties and permeability in damaged sandstone. Int. J. Rock Mech. Min. Sci. 47 https://doi.org/10.1016/j.ijrmms.2010.06.007.

Lanier, J., Di Prisco, C., Nova, R., 1991. Étude expérimentale et analyse théorique de l'anisotropie induite du sable d'Hostun. Rev. Fr. Geotech. 57 https://doi.org/10.1051/geotech/1991057059.

Le, V.D., 2007. Modélisation et identification du comportement plastique visco-élastique endommageable d'un matériau. PhD thesis. https://www.theses.fr/2007TOUR4044.

Le, V.D., Gratton, M., Caliez, M., Frachon, A., Picart, D., 2010. Experimental mechanical characterization of plastic-bonded explosives. J. Mater. Sci. 45 (21) https://doi.org/10.1007/s10853-010-4655-5.

Lemaître, J., Chaboche, J.L., Benallal, A., Desmorat, R., 2020. Mécanique des matériaux solides, 3e édition. Editions Dunod.

Leukart, M., Ramm, E., 2002. An alternative split within the microplane material model. In: Proceedings of the 5th World Congress on Computational Mechanics.

Leukart, M., Ramm, E., 2003. A comparison of damage models formulated on different material scales. Comput. Mater. Sci. 28 (3–4) https://doi.org/10.1016/j.commatsci.2003.08.029.

Liénard, C., 1989. Plasticité couplée à l'endommagement en conditions quasi-unilatérales pour la prévision de l'amorçage des fissures. PhD thesis. http://www.theses.fr/1989PA066317.

Liu, M., Huang, X.C., Wu, Y.Q., Chen, C.J., Huang, F.L., 2019. Numerical simulations of the damage evolution for plastic-bonded explosives subjected to complex stress states. Mech. Mater. 139 https://doi.org/10.1016/j.mechmat.2019.103179.
Mazars, J., Berthaud, Y., Ramtani, S., 1990. The unilateral behaviour of damaged concrete. Eng. Fract. Mech. 35 (4/5) https://doi.org/10.1016/0013-7944(90)90145-7.
Montáns, F.J., 2000. Implicit algorithms for multilayer J2-plasticity. Comput. Methods Appl. Mech. Eng. 189 (2) https://doi.org/10.1016/S0045-7825(99)00323-0.
Montáns, F.J., 2001. Implicit multilayer J2-plasticity using Prager's translation rule. Int. J. Numer. Methods Eng. 50 (2) https://doi.org/10.1002/1097-0207(20010120)50:2<347::AID-NME28>3.0.CO;2-Q.
Mroz, Z., 1967. On the description of anisotropic workhardening. J. Mech. Phys. Solid. 15 (3) https://doi.org/10.1016/0022-5096(67)90030-0.
Picart, D., 1993. Comportement et mise en forme d'un explosif agrégataire. PhD thesis. https://www.theses.fr/1993DENS0007.
Picart, D., Benelfellah, A., Brigolle, J.L., Frachon, A., Gratton, M., Caliez, M., 2014. Characterization and modeling of the anisotropic damage of a high-explosive composition. Eng. Fract. Mech. 131 https://doi.org/10.1016/j.engfracmech.2014.09.009.
Picart, D., Brigolle, J.-L., 2010. Characterization of the viscoelastic behaviour of a plastic-bonded explosive. Mater. Sci. Eng. A 527(29-30). https://doi.org/10.1016/j.msea.2010.08.057.
Picart, D., Pompon, C., 2016. Experimental characterization of the multiaxial failure of a plastic-bonbed explosive. Int. J. Energ. Mater. Chem. Propuls. 15 (2) https://doi.org/10.1615/IntJEnergeticMaterialsChemProp.2016013662.
Plassart, G., Picart, D., Gratton, M., Frachon, A., Caliez, M., 2020. Quasistatic mechanical behaviour of HMX- and TATB-based plastic-bonded explosives. Mech. Mater. 150 https://doi.org/10.1016/j.mechmat.2020.103561.
Plassart, G., 2020. Comportement mécanique anisotrope induit des explosifs comprimés. PhD thesis. https://hal.archives-ouvertes.fr/tel-03199577.
Rinaldi, R.G., 2006. Loi physique de comportement des polymères amorphes et intégration dans un code éléments finis. PhD thesis. https://tel.archives-ouvertes.fr/tel-00103408.
Tan, H., Huang, Y., Liu, C., Ravichandran, G., Inglis, H.M., Geubelle, P.H., 2007. The uniaxial tensile of particulate composite materials with non-linear interface debonding. Int. J. Solid Struct. 44 (6) https://doi.org/10.1016/j.ijsolstr.2006.09.004.
Tan, H., Liu, C., Huang, Y., Geubelle, P.H., 2005. The cohesive law for the particle/matrix interfaces in high explosives. J. Mech. Phys. Solid. 53 (8) https://doi.org/10.1016/j.jmps.2005.01.009.
Thompson, D.G., Wright, W.J., 2004. Mechanical Properties from PBX 9501 pressing study. AIP Conf. Proc. 706, 503. https://doi.org/10.1063/1.1780287.
Thompson, D.G., Brown, G.W., Olinger, B., Mang, J.T., Patterson, B., DeLuca, R., Hagelberg, S., 2010. The effects of TATB ratchet growth on PBX 9502. Propellants, Explosives. Pyrotechnics 35 (6). https://doi.org/10.1002/prep.200900067.
Trumel, H., Rabette, F., Willot, F., Brenner, R., Ongari, E., Biessy, M., Picart, D., 2019. Understanding the thermomechanical behaviour of a TATB-based explosive via microstructure-level simulations. Part I: microcracking and viscoelasticity. In: Europyro 44th International Pyrotechnics Seminar. https://hal.archives-ouvertes.fr/hal-02312483.
Van Mier, J.G.M., 1984. Strain-softening of Concrete under Multiaxial Loading Conditions. PhD thesis. https://citeseerx.ist.psu.edu/viewdoc/download?doi=10.1.1.980.2406&rep=rep1&type=pdf.
Van Mier, J.G.M., 1986. Multiaxial strain-softening of concrete. Part II: load-Histories. Mater. Struct. 19 (3) https://doi.org/10.1007/BF02472035.
Wiegand, D.A., Redingus, B., Leppard, C., 2011. Pressure and friction dependent mechanical strength-cracks and plastic flow. Int. J. Solid Struct. 48 (11–12) https://doi.org/10.1016/j.ijsolstr.2011.01.025.
Wu, Y.Q., Huang, F.L., 2009. A micromechanical model for predicting combined damage of particles and interface debonding in PBX explosives. Mech. Mater. 41 (1) https://doi.org/10.1016/j.mechmat.2008.07.005.
Yan, H., Oskay, C., 2017. Multi-yield surface modeling of viscoplastic materials. Int. J. Multiscale Comput. Eng. 15 (2) https://doi.org/10.1615/IntJMultCompEng.2017020087.
Zubelewicz, A., Thompson, D.G., Ostoja-Starzewski, M., Ionita, A., Shunk, D., Lewis, M. W., Lawson, J.C., Kale, S., Koric, S., 2013. Fracture model for cemented aggregates. AIP Adv. 3 (1) https://doi.org/10.1063/1.4789791.

3 PERSPECTIVES

Les différentes approches et pistes d'amélioration explorées durant les travaux présentés pourraient laisser à penser qu'un modèle de comportement « généralisé » pourrait être proposé pour M1 et M2. C'était un des objectifs des travaux menés au travers de la thèse de Gaëtane Plassart. Un travail conséquent a été effectué en ce sens, mais il est clair que des mécanismes distincts sont à l'œuvre dans ces deux matériaux, aboutissant à des différences de comportement dont les moteurs sont sûrement très différents d'un point de vue microscopique. De ce fait, le modèle proposé dans la thèse de G. Plassart ne peut être directement appliqué à M1. Le test effectué montre des résultats encourageants, mais des moyens importants doivent être mis en œuvre concernant notamment les fonctions d'effectivité d'endommagement, la stratégie d'identification des paramètres… afin de reproduire correctement le comportement de M1 et les tendances observées.

Toutes les approches mentionnées ont été menées dans le but d'obtenir un modèle macroscopique et phénoménologique. Assurément, une des voies à prospecter concerne au moins l'observation, si ce n'est la modélisation, des phénomènes mis en jeu à l'échelle microscopique. L'observation quantitative de l'endommagement à cette échelle, vue au travers de la fissuration et de son évolution mais peut-être aussi observée via la désorganisation de la matière, est nécessaire. Cela nécessite des moyens expérimentaux adaptés et conséquents mais la présence par exemple d'un microtomographe au laboratoire permet de faire de l'observation in situ. De plus, l'expérience des collègues tourangeaux concernant la nanoindentation devraient permettre d'accéder à certains traits de comportement à l'échelle fine. Enfin, le retour d'expériences montre que le comportement de M1 semble plus complexe à appréhender d'un point de vue macroscopique de celui de M2. La microstructure particulière de M1, avec de gros grains noyés dans une matrice constituée de petits grains et de liant, n'est sans doute pas étrangère à cela. Une approche prenant explicitement en compte cette particularité (modèle à champs de phase par exemple) pourrait peut-être donner des pistes à explorer.

La dégradation du module réel constaté après un aller-retour entre températures ambiante et froide lors d'essais DMA, ainsi que la déformation irréversible constatée lors des essais de dilatométrie sur M2 après ce même aller-retour, indiquent que la température pourrait jouer un rôle important dans l'évolution du comportement matériau. Une investigation est donc souhaitable, au travers d'un modèle avec couplage thermomécanique par exemple.

La problématique récurrente concernant le volume matériau disponible pour la caractérisation est toujours d'actualité. Une étude va être démarrée en septembre 2023 en vue de modifier la géométrie des éprouvettes de traction et de compression de confinement. Concernant la traction, l'objectif est de réaliser un essai avec éprouvette collée entre plateaux, et de converger vers une géométrie usinable dans un massif de hauteur 60mm. Une première étape d'optimisation sera effectuée numériquement avec la loi de comportement du matériau I2 identifiée au LaMé. Ces résultats serviront de base à une étude expérimentale, pour application ensuite sur M2. Concernant la compression sous confinement, le protocole de test mis en œuvre dans la thèse de M. Chatti ainsi que les plans de l'enceinte réalisée en interne vont être transférés au CEA, permettant le passage à des éprouvettes ∅10H20mm au lieu d'actuellement ∅50H100mm.

Enfin, une évolution du domaine d'étude vers les cas d'impacts basse vitesse (< à 100ms^{-1}) est en cours au travers des travaux de thèse menés par Emilien Hamon, démarrée en 2021. L'objectif général concerne la modélisation de la relation entre endommagement et vitesse de combustion dans le cas d'un impact moyenne vitesse. La vitesse de combustion joue en effet un rôle essentiel dans le phénomène de Transition Combustion-

Déflagration-Détonation (TCoDD) d'un matériau explosif. De même la densité de fissuration, traduite sous forme de surface offerte à la combustion, est un des paramètres influent. Un modèle décrivant l'évolution du taux de fissuration sous sollicitation dynamique dans un cadre anisotrope est actuellement à l'étude afin d'être adapté au matériau M1. Des essais en bombe manométrique vont être réalisés afin de relier la vitesse de propagation de combustion, la surface offerte à celle-ci et la pression des gaz de décomposition au voisinage de la flamme. Des essais sur barres d'Hopkinson sont aussi programmés.

4 ANNEXE A

Mechanics of Materials 150 (2020) 103561

Contents lists available at ScienceDirect

Mechanics of Materials

journal homepage: www.elsevier.com/locate/mechmat

Quasistatic mechanical behavior of HMX- and TATB-based plastic-bonded explosives

Gaëtane Plassart[a], Didier Picart[a,*], Michel Gratton[b], Arnaud Frachon[b], Michaël Caliez[b]

[a] CEA DAM Le Ripault, F-37260, Monts, France
[b] INSA CVL, Univ. Orléans, Univ. Tours, LaMé, EA 7494, F-41000, Blois, France

ARTICLE INFO

Keywords:
Plastic-bonded explosives
Constitutive law
Experimental characterization
Induced anisotropy

ABSTRACT

Data on the macroscopic quasistatic mechanical behavior of pressed HMX- and TATB-based plastic-bonded explosives (PBXs) are listed in this paper. This review shows that (1) few characterizations are available for TATB-based PBXs. This gap is filled in this paper. An extensive database is detailed for the CEA M2 explosive composition. The HMX and TATB database then enables selection of the deformation mechanisms to be considered: viscoelasticity, damage-induced anisotropy and its effectivity (i.e.: whether or not the damage is influenced by the loading direction), plasticity with kinematic and isotropic hardenings, pressure and temperature dependencies and asymmetric failure threshold. The review also shows that (2) HMX- and TATB-based materials share close elastic and ultimate properties when the compositions (binders, solid volume fractions) and the mechanical behavior of the two crystals differ. The constitutive laws proposed in the literature are reiterated. In our opinion, a universal law could be proposed in the near future, each material being considered by its own set of parameters. The objective of this paper is to draw up the guidelines for model improvement.

1. Introduction

When designing a pyrotechnic structure, simulations must be performed to assess mechanical strength. This step consists, in particular, in developing and implementing a constitutive law for the energetic material. In addition, the thermomechanical stresses that such a material undergoes during its life cycle can alter its microstructure and potentially modify its mechanical and/or reactive behavior. To guarantee the safety and reliability of pyrotechnic structures, understanding and modelling the thermomechanical behavior of these materials is essential.

Among the existing energetic materials, pressed explosives are granular materials with a small amount of polymeric binder. This paper focuses on the thermomechanical characterization of some pressed explosives, from experimental study to modelling, highlighting the state of the art in this field. Our objective is to determine if a unified model could be proposed in the near future for plastic-bonded explosives (PBXs). This study is limited to the quasistatic domain with strain rates of 10^{-6} to $10^{-3}\ s^{-1}$ and strains in the order of one percent, which justifies the small strains assumption. The temperature ranges between -30 °C and $+80$ °C and the confinement pressure between 0.1 and 10 MPa. The post-peak behavior is outside the field of this study, with safety margins requiring the stress path to remain below the maximum stress.

The plastic-bonded explosives of interest are made of HMX (octahydro-1,3,5,7-tetranitro-1,3,5,5,7-tetrazocine) or TATB crystals (1,3,5-triamino-2,4,6-trinitrobenzene). The CEA (Commissariat à l'Energie Atomique et aux Energies Alternatives - French Alternative Energies and Atomic Energy Commission) has developed several explosive compositions such as M1 and M2, composed respectively of more than 95 wt% HMX or TATB, mixed with polymeric binders and densified by hot isostatic compression. The residual porosity is less than 5%. Other TATB- and HMX-based PBXs frequently mentioned in the literature are PBX-9502 (95 wt% TATB, 5 wt% Kel-F 800 binder), LX-17-1 (92.5 wt% TATB, 5 wt% Kel-F 800 binder), PBX-9501 (95 wt% HMX, 2.5 wt% Estane binder and BDNPA/F), LX-14 (95.5 wt% HMX, 4.5 wt% Estane binder) and EDC-37 (91 wt% HMX, 1 wt% NC binder and DNEB/TNEB). These explosives are formed by isostatic compression at relatively high temperatures and pressures (Picart, 1993; Thompson and Wright, 2004). They are isotropic in their initial state with a low residual porosity. The literature reports that, until the 1980s, PBX-9502 could be densified by uniaxial compression (Blumenthal et al., 1999; Skidmore et al., 1998), leading to an initial anisotropic macroscopic behavior caused by the perpendicular alignment with the pressing direction of the TATB crystals (Schwarz et al., 2013).

The mechanical properties of PBXs have been studied since the 1980s and quasistatic constitutive laws have been developed. The

* Corresponding author.
E-mail address: didier.picart@cea.fr (D. Picart).

https://doi.org/10.1016/j.mechmat.2020.103561
Received 3 January 2020; Received in revised form 6 August 2020; Accepted 6 August 2020
Available online 03 September 2020

characterization of the material being the first step, phenomena must be isolated and identified from data. A review of the various tests carried out on these materials is proposed in section 2 of this paper. Published experimental data on PBXs are essentially limited to uniaxial compression or tension tests, at various temperatures, in which only longitudinal strains are measured (Blumenthal et al., 1999; Browning et al., 1984; Buechler, 2012a; 2012b; Buechler et al., 2013; Ellis et al., 2005; Funk et al., 1996; Gagliardi and Cunningham, 2007; Gray et al., 1998; Skidmore et al., 1998; Thompson, 2002; Thompson et al., 2010; Zubelewicz et al., 2013). Some compression tests on an HMX-based PBX under various confinement pressures can be mentioned (Wiegand et al., 2011) as well as a torsion test on PBX-9501 (Gagliardi and Cunningham, 2009). Dynamic Mechanical Analysis (DMA) has been performed on PBX-9501 and PBX-9502 (Thompson et al., 2012a, 2012b). The database on M1 is much more complete (see section 2 and Benelfellah, 2013; Benelfellah et al., 2017; Caliez et al., 2014; Le et al., 2010; Picart et al., 2014; Picart and Brigolle, 2010; Picart and Pompon, 2016).

The constitutive laws of PBXs can be divided into macroscopic and micromechanical models. To the authors' knowledge, the first macroscopic models appeared in the 1980s in France and in the United States. A first model of non-linear viscoelastic behavior, pressure- and temperature-dependent, was established by Belmas et al. (1982). This model is limited to monotonic loadings. Peeters and Hackett (1981) have reproduced the time-dependence of the behavior of pressed explosives. They developed two unidimensional models: a law for compression and creep for monotonic loadings, and a linear viscoelastic model able to simulate unloading and reloading (see also Browning et al., 1984). A famous macroscopic model is the SCRAM (Statistical CRAcks Mechanics) model (Dienes, 1978; 1996; Dienes et al., 2006). SCRAM is based on the strain rates additivity and contains an elasto-plastic part with kinematic hardening describing the behavior of the matrix, plus anisotropic damage describing the microcrack network (nucleation, growth and coalescence). IsoSCRAM (Addessio and Johnson, 1990) is a simplified version of SCRAM with isotropic damage and without microcracks coalescence. The reader will also find the ViscoSCRAM model (Bennett et al., 1998; Hackett and Bennett, 2000) based on IsoSCRAM with a viscoelastic part. Recently, Liu et al. (2019) have modified the ViscoSCRAM model adding a Bodner-Partom viscoplasticity and changing the microcracking kinetics. Most of the other models focus on the viscosity of these polymer-bonded materials, and all of them include damage. Le et al. (2010) have developed a Maxwell viscoelastic model coupled with isotropic damage and pressure-dependent plastic behavior with isotropic hardening and non-associated flow. Buechler (2012b, 2013) has added combined isotropic/kinematic hardening to the viscoplasticity. Zubelevicz et al. (2013) have introduced different damage rates in tension and compression coupled with viscoplasticity. Lastly, a microplane model with anisotropic damage added to non-associated plasticity with isotropic hardening was proposed by Benelfellah et al. (Benelfellah, 2013; Benelfellah et al., 2014; 2017; Picart et al., 2014).

The micromechanical models help us understand the influence of the different components on the macroscopic behavior since they capture the mechanisms at the grain scale (Ambos et al., 2015; Arora et al., 2015; Clements and Mas, 2004; Gasnier et al., 2018; Tan et al., 2005; 2007; Wu and Huang, 2009). However, at the engineering level, these models cannot yet be used to simulate the explosive behavior in a pyrotechnic structure due to a huge calculation cost. This paper focuses exclusively on macroscopic models of the quasistatic behavior of pressed explosives.

Firstly, the state of the art of experimental characterization of the quasistatic behavior of PBXs is presented in section 2 of this paper. This review provides an opportunity to consider all the data already available for the widely characterized M1 composition. In section 3, an extensive experimental campaign performed on the M2 TATB-based PBX is presented, and the data is exploited in section 4. A list of the deformation mechanisms to be considered in a constitutive law can be provided based on these three previous sections. Already published macroscopic thermomechanical models are detailed and compared in section 5. The discussion allows conclusions to be drawn on the relevance of these models for HMX- and TATB-based PBXs. Guidelines are proposed for future model improvements.

2. State of the art in experimental characterization of PBXs

2.1. HMX-based PBXs

Since 2000, the CEA and the Gabriel LaMé Laboratory have undertaken an extensive experimental campaign to characterize the various behavioral features of the material M1. This database includes monotonic and cyclic compressions at 20 °C and under atmospheric pressure, for four strain rates from 10^{-6} s^{-1} to 10^{-3} s^{-1}; monotonic and cyclic compressions at 20 °C under 5 and 10 MPa, at 10^{-5} s^{-1}; monotonic and cyclic tension tests at 0 °C, 20 °C, 35 °C and 50 °C under atmospheric pressure, at 10^{-5} s^{-1} (Benelfellah, 2013; Caliez et al., 2014; Gratton et al., 2009; Le, 2007; Le et al., 2010; Picart and Brigolle, 2010; RjaFiAllah, 2006); cyclic compressions at 0 °C, 35 °C and 50 °C under atmospheric pressure, at 10^{-5} s^{-1} (Le, 2007); heterogeneous tests such as the Brazilian test, biaxial tension (plate bending), channel-die test, Iosipescu test and three-point bending, at 20 °C under atmospheric pressure, at a strain rate of about 10^{-5} s^{-1} (Benelfellah, 2013; Le, 2007; Picart and Pompon, 2016); alternate tension-compression and compression-tension at 20 °C under atmospheric pressure, at 10^{-5} s^{-1} (Benelfellah, 2013; Picart and Brigolle, 2010); as well as a dynamic mechanical analysis (DMA) campaign (Picart and Brigolle, 2010). For each uniaxial or triaxial test of these papers, the longitudinal and transversal strains are given. Furthermore, each cycle of cyclic tests consists of four steps: a loading, a stress relaxation of at least 30 min, an unloading to zero stress and a strain recovery of at least 30 min. The authors studied the influence of temperature, pressure and loading rate. In particular, the elastic modulus increases with pressure up to 10 MPa and then remains constant (highly confined tests are presented in Vial, 2013). This highlights the influence of the initial porosity, completely closed under a 10 MPa pressure. Thus, the elastic modulus calculated under this confinement appears as the intrinsic Young's modulus of the material. The viscoelasticity of M1 has been characterized and the failure criterion has been obtained by multiaxial tests and conventional tension and compression tests. Cyclic compression tests revealed the inelastic strains and a load-induced anisotropy, resulting in a unilateral effect observed during the alternated tests.

For other HMX-based PBXs, such as the well-known PBX-9501, the literature shows monotonic uniaxial compression tests at room temperature and 60 °C for strain rates from 10^{-6} s^{-1} to 10^{-3} s^{-1} (Buechler, 2012a; Ellis et al., 2005; Funk et al., 1996; Gray et al., 1998) as well as tests with load-unload-recovery cycles at −15 °C, 23 °C and 50 °C with rates in the range of 10^{-5} s^{-1} and 10^{-4} s^{-1} during loading and 10^{-3} s^{-1} during unloading (Buechler, 2012b; Buechler et al., 2013). Monotonic tension tests are also mentioned at −18 °C and 10^{-4} s^{-1} (Thompson, 2002) and at room temperature at 2×10^{-5} s^{-1} (Ellis et al., 2005) as well as load-unload-recovery cyclic tests at 23 °C and about 10^{-4} s^{-1} (Buechler et al., 2013). For all these tests, only longitudinal strains are represented as a function of stress. A DMA campaign has been conducted on PBX-9501 (Thompson et al., 2012a). Torsion tests, with and without axial stress, have been performed at 25 °C and 0.08 deg. s^{-1} (Gagliargi and Cunningham, 2009). A three-point bending test at a displacement rate of 0.0212 mm s^{-1}, for a specimen measuring 75 × 15 × 10mm (Hackett and Bennett, 2000) and another at 0.2 mm s^{-1} for a specimen measuring 114 × 102 × 12mm (Ellis et al., 2005) are also mentioned. Furthermore, several publications are related to Brazilian tests and the failure mode of the material (intergranular or transgranular) (Chen et al., 2007; Liu and Thompson, 2010; Rae et al., 2002; Williamson et al., 2007).

From the DMA measurements (Thompson et al., 2012a), PBX-9501 is very viscous from −30 °C. The influence of the loading rate and the asymmetry between tension and compression were also highlighted. Tests at several temperatures were carried out by the various authors, but none of them presents a comparison of the behavior under various temperatures.

The influence of confinement pressure up to 140 MPa on EDC-37 has been studied by Wiegand et al. (2011) (monotonic compressions under confinement). The stress-strain curves show that the more the containment increases, the higher is the peak stress and the more the post-peak phase disappears. At high confinement (above 7 MPa), a long almost horizontal plateau appears. The authors calculate an elastic modulus at the beginning of the stress-strain curve (no details are given). The evolution of this module according to the confinement follows two regimes: it doubles between 0 and 7 MPa but varies very little beyond that. Tests with load-unload-reload were also carried out under various confinements. The authors say that at low confinement (up to 7 MPa) a decrease of the elastic modulus is observed when reloading. At high confinement, the modulus does not evolve. In addition, from a test conducted at a pressure above 30 MPa, the authors show that the yield strength (estimated for a 2% strain) has almost doubled. However, doubts can be expressed about calculating a plasticity threshold at 2% strain on a quasi-brittle material. According to the authors, over the pressure range of 0–7 MPa, a damage mechanism would be predominant, while beyond that a plastic flow would govern the behavior.

Lastly, acoustic emissions measurements have been made by Ellis et al. (2005) during compression, tension and three-point bending tests on EDC-37. In this method, the appearance of a crack generates an elastic wave which can be measured and analyzed. For EDC-37, the measured cracking remains very low or even zero as long as the stress/strain response is linear. The non-linearity that appears in compression is very progressive and cracking is observed. In tension/flexure, the response is practically linear (brittle fracture), so cracking only occurs during fracture.

Post-failure microscopies on a PBX-9501 sample subjected to a Brazilian test (Chen et al., 2007; Rae et al., 2002; Williamson et al., 2007) show that the predominant cracking mode is intergranular, by decohesion of grain interfaces. However, Williamson et al. (2007) note that for tests performed below the glass transition temperature of the binder (about −40 °C), the failure is transgranular.

The asymmetric nature of the behavior between tension and compression has been observed, but no alternating loading has been achieved. Measurements of transversal strains are never given, which means that no conclusions can be made about a possible induced anisotropy of these materials.

Recently, Buechler and coworkers (Buechler, 2012b; Buechler et al., 2013) applied the experimental procedure used on M1 to characterize PBX-9501, but only longitudinal strains are recorded. From load-unload-reload cycles, irreversible strains are detected. Assuming isotropic hardening due to lack of data, the longitudinal plastic strains are plotted as a function of the cycle maximum stress, and then these values are subtracted from the overall curves. The loading curves thus reconstructed can be considered elastic. Since they are not superimposed due to softening at each cycle, the authors assume the effect of the damage. Thus, this work on damage is more a matter of modelling than characterization.

2.2. TATB-based PBXs

Some data obtained on our TATB-based material M2 have already been published. The stress-strain curve of a cyclic uniaxial compression test, performed at 10^{-5} s^{-1} at room temperature, is presented in two papers (Ambos et al., 2015; Gasnier et al., 2018). Let us note that the ratchet growth phenomenon (cycles of temperature without mechanical loading yields irreversible strain) has never been observed for this material. For other TATB-based PBXs, the experimental database mainly includes monotonic uniaxial compression tests performed between 10^{-5} s^{-1} and 10^{-3} s^{-1} for temperatures from −52 °C to 74 °C (Blumenthal et al., 1999; Skidmore et al., 1998; Thompson et al., 2010; Zubelewicz et al., 2013), with creep phase (Gagliardi and Cunningham, 2007) or with load-unload cycles (Browning et al., 1984). There are also data on the tension behavior, in monotonic loading from 10^{-5} s^{-1} to 10^{-3} s^{-1} for temperatures from −52 °C to 74 °C (Thompson, 2002; Thompson et al., 2010; Zubelewicz et al., 2013) and two papers provide tension failure data for different temperatures and strain rates (Idar et al., 2000; Thompson et al., 2012a). In these papers, only longitudinal strains are given, as a function of stress or time. There are also in the literature some monotonic (Cunningham et al., 2013) and cyclic (Thompson et al., 2012b) thermal expansion tests, as well as a DMA campaign (Thompson et al., 2012a). The compression of a perforated plate in its center has been performed (Liu and Thompson, 2014) with measurement of the strain field by digital image correlation. Finally, it should be mentioned that an internal report from the Los Alamos laboratory written by Shunk in 2013 (Shunk, 2013) reviews the tests performed on the PBX-9502. Unfortunately, the majority of the references have not been published in the open literature.

The DMA test performed by Thompson et al. (Thompson et al., 2012a, 2012b) shows that the viscosity of the PBX-9502 increases significantly from +25 °C. For this material, temperature tends to make it more ductile while the strain rate 10^{-3} and 10^{-5} s^{-1} has very little influence on its behavior at −52 °C (Zubelewicz et al., 2013). Asymmetry of the behavior between tension and compression is also observed.

The experimental data on HMX- and TATB-based PBXs are summarized in Table 1.

3. Characterization of the TATB-based material M2

A substantial experimental database is necessary to characterize the complex behavior of the PBXs and to justify the modelling choices. While the HMX-based material M1 was extensively characterized (see section 2), data will now be provided for a TATB-based explosive composition. The tests performed on M2 are described in the current section, the analysis of the various curves being reported in the next section.

3.1. Material

M2 is composed of about 95% by weight of TATB grains bonded by a thermoplastic binder. The M2 fabrication has two successive steps. In the first, the explosive crystals are coated with a thin layer of polymeric binder. The mean diameter of TATB grains is about 50 μm and millimetric meta-grains are obtained by granulation. Next, the granules are vacuum-packed in a tight elastomer bag, before being submitted to several cycles of isostatic compression at a temperature of about 150 °C and a 200 MPa pressure cycle (Picart, 1993). The temperature is chosen to soften the binder. After cooling, a coherent material is obtained which enables machining samples to be taken. The compaction process eliminates most of the initial porosity, the residual porosity being of only a few percent. Fig. 1 shows a micrograph of the material M2. The color variations are due to the strong anisotropy of the TATB grains. However, the orientation of the grains and the binder being randomly distributed, the material is initially isotropic on a macroscopic scale. All the tests described in this paper have been performed on the same batch.

3.2. Experimental procedure

A list of the tests carried out on M2 in the quasistatic range is given in Table 1 (right column). Unless otherwise stated, the operating procedure of the tests is as follows. The test machine used was a Zwick

Table 1
Mechanical tests performed on HMX- and TATB-based PBXs in the literature. The last column CEA-M2 is a list of the data provided in this paper.

		PBX-9501 LX-14 EDC-37 (HMX-based)	PBX-9502 LX-17 (TATB-based)	CEA-M1 (HMX-based)	CEA-M2 (TATB-based)
Uniaxial compression	Long./transv. strains	√/no	√/no	√/√	√/√
	Temperature	−15 °C–60 °C	−52 °C–74 °C	0 °C–50 °C	−30 °C–80 °C
	Strain rate	10^{-6} s^{-1} to 10^{-3} s^{-1}	10^{-5} s^{-1} to 10^{-3} s^{-1}	10^{-6} s^{-1} to 10^{-4} s^{-1}	10^{-6} s^{-1} to 10^{-4} s^{-1}
	Creep/relaxation		✓	✓	✓
	Load – unload cycles	✓	✓	✓	✓
	References	Buechler (2012a, 2012b); Buechler (2013); Ellis et al. (2005); Funk et al. (1996); Gray et al. (1998)	Blumenthal et al. (1999); Browning et al. (1984); Funk et al. (1996); Skidmore et al. (1998); Thompson et al. (2010); Zubelewicz et al. (2013)	Benelfellah (2013); Caliez et al. (2014); Gratton et al. (2009); Le (2007); Le et al. (2010); RjaFiAllah (2006)	
Uniaxial tension	Long./transv. strains	√/no	√/no	√/√	√/√
	Temperature	−18 °C and 20 °C	−52 °C–74 °C	20 °C	−30 °C à 80 °C
	Strain rate	10^{-5} s^{-1} to 10^{-4} s^{-1}	10^{-5} s^{-1} to 10^{-3} s^{-1}	10^{-5} s^{-1}	10^{-6} s^{-1} to 10^{-4} s^{-1}
	Creep/relaxation			✓	✓
	Load – unload cycles	✓		✓	✓
	References	Buechler et al. (2013); Ellis et al. (2005); Thompson (2002)	Thompson (2002); Thompson and Wright (2004); Zubelewicz et al. (2013)	Benelfellah (2013); Caliez et al. (2014); Gratton et al. (2009); Le (2007); Le et al. (2010); Picart and Brigolle (2010); RjaFiAllah (2006)	
Torsion	Shear strains	✓			✓
	Temperature	25 °C			20 °C
	Strain rate	0.08 deg/s			0.01 deg/s
	Creep/relaxation				
	Load – unload cycles				✓
	References	Gagliardi and Cunningham (2009)			
Triaxial compression	Long./transv. strains	√/no		√/√	√/√
	Pressure	0.6–140 MPa		5 and 10 MPa	
	Temperature	20 °C		20 °C	20 °C
	Strain rate	5×10^{-4} s^{-1}		10^{-5} s^{-1}	10^{-5} s^{-1}
	Creep/relaxation			✓	✓
	Load – unload cycles			✓	✓
	References	Wiegand et al. (2011)		Benelfellah (2013); Caliez et al. (2014); Gratton et al. (2009); Le (2007); Le et al. (2010); RjaFiAllah (2006)	
Alternative loadings	Long./transv. strains			√/√	√/√
	Temperature			20 °C	20 °C
	Strain rate			10^{-5} s^{-1}	10^{-5} s^{-1}
	Creep/relaxation				✓
	Load – unload cycles				✓
	References			Benelfellah (2013); Picart and Brigolle (2010)	
Other tests	DMA	−30 °C to +70 °C Thompson et al. (2012a)	−25 °C to +116 °C Thompson et al. (2012a)	−100 °C to +100 °C Picart and Brigolle (2010)	0 °C to +90 °C
	Multiaxial tests	Brazilian test Chen et al. (2007); Liu and Thompson (2010); Rae et al. (2002); Williamson et al. (2007)	Compression of perforated plate Liu and Thompson (2014)	Brazilian test, channel-die, plate bending Benelfellah (2013); Le (2007); Picart and Pompon (2016)	Brazilian test, channel-die, equibiax. comp. bending test

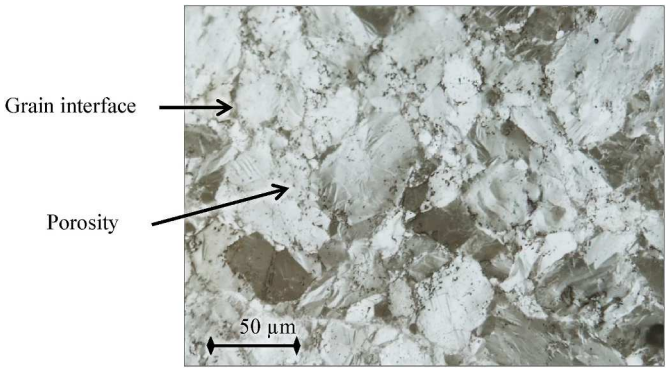

Fig. 1. Micrograph of material M2. The color variations are due to the strong anisotropy of the TATB crystals. Porosity is mainly located inside the grains (small black dots) and at the grain/grain interfaces.

Z100, a compression/traction machine with a 100 kN load cell. Two other machines were on occasion used: a Metravid DMA instrument, and an Instron compression/torsion machine ElectroPuls™ E10000 whose capacities are ± 100 Nm and ± 7 kN. The geometry of the specimens was in the centimeter range. Consequently, the applied force rarely exceeded ± 10 kN. Since the strains never reached 2%, the variation in cross-section during the test was negligible and the infinitesimal strain theory was available. Thus, the stress was calculated from the force and the initial effective area of the specimen. For compression and tension tests, two strain gauge rosettes were glued opposite each other in the center of the specimen (Vishay M-Bond 200 adhesive). Each rosette had two measuring grids arranged at an angle of 0°/90° (Kyowa KFGS-2-120-D16-11). For torsion tests, three rosettes were glued at 120° around the central diameter of the specimen. Each rosette had three measuring grids arranged at an angle of −45°/0°/+45° (Kyowa KFGS-2-120-D17-11). The grids of each gauge were 2 mm long, so the strain was measured on a large surface compared to the grain size and small enough compared to the specimen size. The strains correspond to the average of the two opposite gauges. The tests were strain-controlled from one gauge at the reference rate of 10^{-5} s^{-1}, at room pressure and temperature (unless otherwise stated). Each test was repeated three times to ensure a minimum repeatability of the results. Among the three curves, the test representing the mean response was selected and plotted on the graphs discussed in this paper. The results scatter is shown on the curves by the dispersion at the maximum stress. The mean of the maximum stress and the corresponding strains are represented by a point and the tests dispersion is represented by a line.

On the graphs, the stress is represented in absolute value, except for alternate loading tests for which the usual convention is used (negative stress in compression). The nomenclature used is as follows: σ_{11} is the tension/compressive stress calculated from the force cell and the initial dimensions of the specimen; σ_{12} is the shear stress calculated on the external radius of the specimen from the measured torque because that is where the gauges were glued but also where the stress was the greatest; ε_{11}, ε_{22} and ε_{12} are respectively the strains in the longitudinal (negative in compression), transversal (positive in compression) and shear directions; they correspond to the average of the gauge measurements.

3.3. Dynamic mechanical analysis (DMA)

Dynamic mechanical analysis (DMA) tests were carried out in the temperature range from 0 °C to 90 °C to characterize the material. The samples were 8 × 8× 8mm rods glued on the machine plates. A sinusoidal strain of 0.016% amplitude was imposed, to subject the specimen to tension/compressive cycles with a null average stress at a frequency of 2–60 Hz. Measurements had shown that over these frequency and temperature ranges the material behavior is reversible and linear.

The difference in the stress and strain signals amplitude leads to (1) the amplitude $|E^*|$ of the complex elastic modulus and (2) a phase shift (loss factor $\tan\delta$). The real and imaginary elastic moduli, E' and E'', are evaluated as follows: $E' = |E| * \cos\delta$ and $E'' = |E| * \sin\delta$. Considering the high stiffness of this material, measurements were corrected by removing the machine stiffness. The uncertainty on the measurement of E' is 4% while that of E'' rises to 40% due to the low viscosity of such material.

These moduli are plotted as a function of the logarithm of the inverse of the frequency f for each temperature. A reference temperature is defined (here 0 °C) and, from the time-temperature equivalence principle, the other temperature curves are shifted by a coefficient $a_{t\theta}$ in order to form the master curves. The shift function is a polynomial function determined automatically by minimization of the gap between two consecutive isotherms (T is the temperature in Celsius):

$$\log_{10}\left(\frac{1}{a_{t\theta}}\right) = 8.031x10^{-4}\,T^2 + 4.930x10^{-2}\,T + 4.631x10^{-2} \quad (1)$$

Thus, in Fig. 2, the lowest reduced times correspond to the lowest temperature (0 °C) and the longest times to the highest temperature (90 °C).

3.4. Uniaxial monotonic loadings

Monotonic uniaxial compression, tension and torsion tests were performed at ambient temperature and pressure. The stress-strain curves are given in Fig. 3. The compression samples (cylinders 20 mm high and 10 mm in diameter) were placed between two lubricated compression plates. The tension samples (150 mm high and dog-bone-shaped), with a 10 mm-sided square base, were held by two clamping jaws. For the torsion tests, the samples were hollow dog-bones, 60 mm high, 18 mm in outer diameter and 9 mm in inner diameter. These tests were controlled at $0.01°.s^{-1}$, which corresponds to a shear strain rate of around 10^{-5} s^{-1}. No axial force was applied. The maximum stress dispersion was around 1 MPa. The spread observed at the peak of the compressive test is due to the flat response (plateau) of the material.

3.5. Alternating tension and compression loadings

An experimental campaign of alternative tension/compressive tests was performed on M2. Two tests were conducted: (1) a compression up to 30 MPa (~0.95 σ_{max}, where σ_{max} is the maximum compressive stress) followed by a tension loading to failure, and (2) a traction up to 7 MPa (~0.95 σ_{max}, where σ_{max} is the maximum tension stress) followed by a compressive loading to failure. Dog-bone-shaped samples with a cylindrical base 10 mm in diameter and 20 mm in height were used.

The experimental data show that the failure stress is the same for alternative tests as it is for monotonic tests. The curve of the compression/tension test is given in Fig. 4. There is a defect on the curve linked to the machine software when the force sign changes. Concerning the tension/compression test (not presented here), the tension unloading curve was similar to the loading curve. The global curve of the test overlaps with the tension and compression monotonic curves.

3.6. Pressure-, temperature- and strain rate-dependence

Compression and tension tests at several temperatures and strain rates are presented in Fig. 5 and Fig. 6. The procedure was identical to the simple compression and simple tension tests at room temperature as already described. To guarantee the temperature setting, specimens were conditioned for at least 2 h before the test. In Fig. 6, the tension tests at 20 °C at 10^{-6} and 10^{-4} s^{-1} are not represented despite having been performed, because the rate effect is negligible at this temperature.

To study the influence of the confinement, monotonic triaxial compressive tests at various confinements (2.5 MPa, 5 MPa and

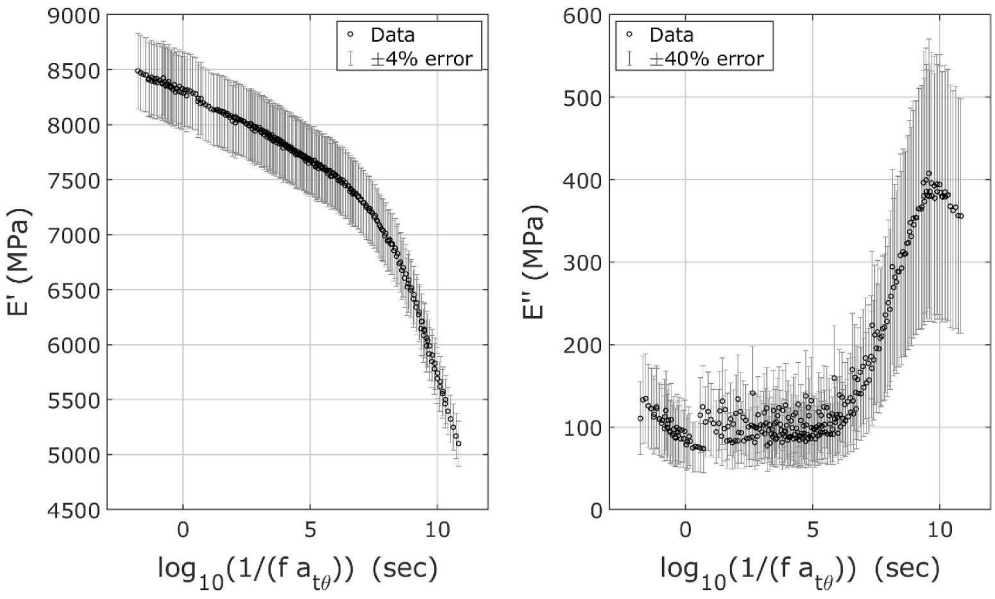

Fig. 2. Real (E′) and imaginary (E″) elastic moduli of M2 with respect to the reduced time where *f* is the frequency of the sinusoidal loading. Master curves (black dots) show a relative strain rate- and temperature-independence while the temperature does not exceed 50–60 °C.

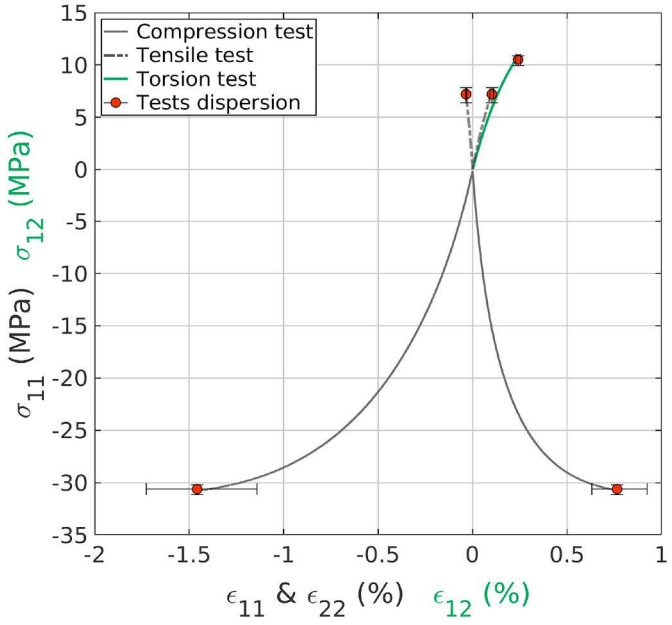

Fig. 3. Stress-strain curves of compression (black solid lines), tension (black dashed lines) and torsion (green solid lines) tests showing a nonlinear response and an asymmetric behavior. (For interpretation of the references to color in this figure legend, the reader is referred to the Web version of this article.)

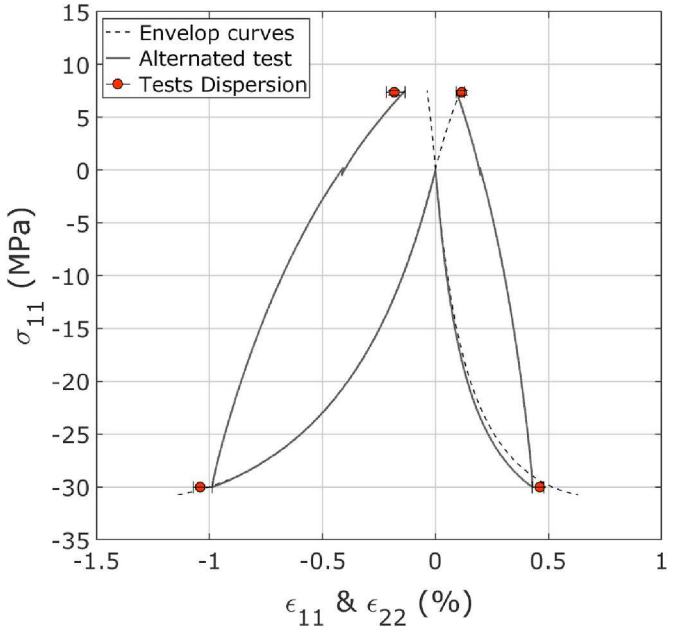

Fig. 4. Alternating compressive/tension test (solid lines) compared to monotonic compression and tension curves (dashed lines). The compression loading changes the tension response.

10 MPa) were carried out. Cylindrical specimens 50 mm in diameter and 100 mm in height were used, on which two strain gauge rosettes were glued at 0°/90°. The sample was placed in a confinement chamber installed inside a sealed elastomer bag. Then, the chamber was filled with water until the desired confinement pressure was reached. Afterwards, a uniaxial stress was applied at the reference strain rate of $10^{-5}\,s^{-1}$ until failure. The influence of the pressure is shown in Fig. 7.

3.7. Cyclic loadings

Cyclic compression and tension loadings were performed on M2 (for cyclic tension data, see supplementary materials). The loading cycles had four phases: 1) load at a controlled strain rate, 2) stress relaxation at fixed longitudinal strain, 3) unload at a controlled strain rate, 4) strain recovery at rest. These tests are inspired by those performed on the material M1 (Gratton et al., 2009; Le et al., 2010). The experimental set-up was the same as for the monotonic tests. The relaxation and strain recovery lasted 8 h, 1 h and 10 min respectively for the uniaxial compression, the tension and the triaxial compression (Fig. 7). Evolutions of stress and strain recorded during the relaxation and recovery parts of these experiments are plotted with respect to the time (see supplementary materials).

3.8. Double compression tests

An experimental campaign, inspired by Cambou and Lanier (Cambou and Lanier, 1988; Lanier et al., 1991) was carried out to

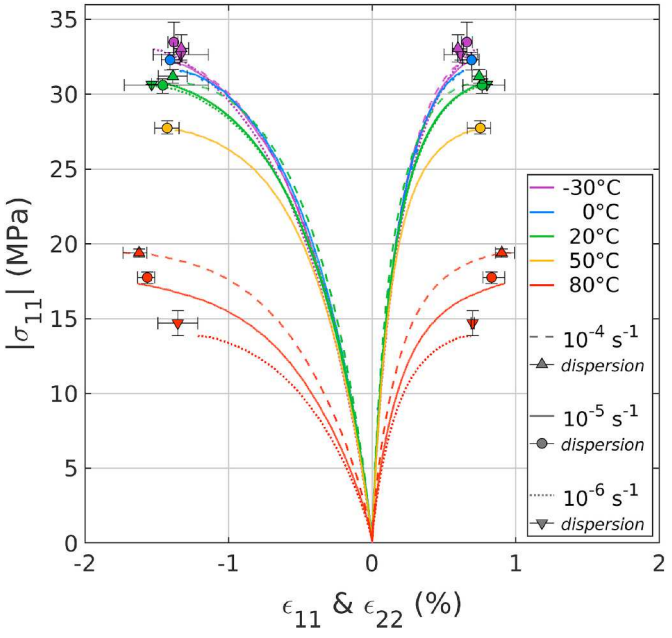

Fig. 5. Temperature- and strain rate-dependencies in compression. Only one strain rate has been experienced at 50°C. Decrease of the stress and increase of the strain rate influence as the temperature increases above 50°C.

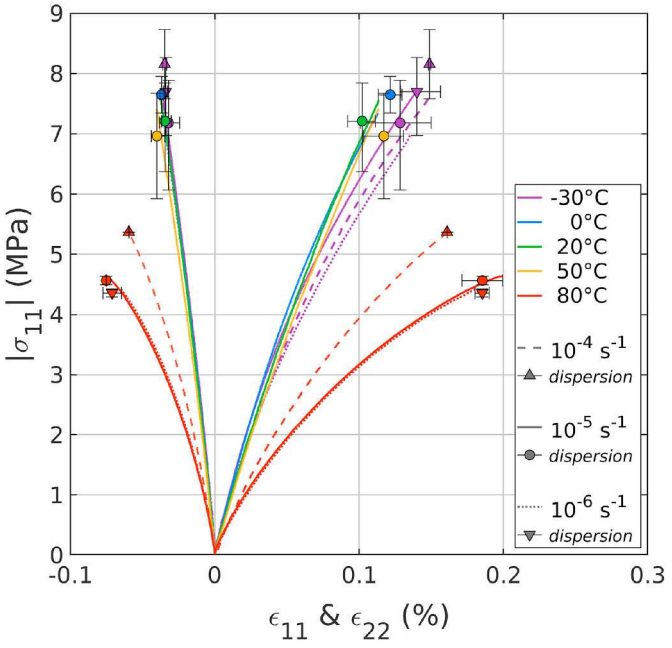

Fig. 6. Temperature- and strain rate-dependencies in tension. Only one strain rate has been experienced at 50°C. Decrease of the stress and increase of the strain rate influence as the temperature increases above 50°C.

highlight a possible loading-induced anisotropy, the latter being observed during a second loading in a different direction. Cubes with 20 mm sides were used. Here, only one bidirectional rosette was glued to the sample surface. The opposite side was covered with a pattern to perform a digital image correlation. The displacement rate was controlled by the mobile crosshead at 10^{-2} mm s^{-1} corresponding to the reference strain rate up to a given stress. During the stress relaxation, the crosshead deforms even if its position (imposed at its ends) is fixed. This leads to an additional small compression of the sample. To avoid friction at the interfaces, lubricated Teflon was used. The displacement homogeneity was checked by digital image correlation.

First, the sample was compressed up to 30 MPa (0.95 times the maximum stress). After a 1-h relaxation, unloading and a night of recovery, the sample was submitted to a second compression, either in the same direction (test called "0°–0° compression"), or in an orthogonal direction by turning the cube (test called "0°–90° compression"). During this second loading, the sample was again compressed up to 30 MPa. Two representative tests (out of three of each kind) are illustrated in Fig. 8 and Fig. 9. The dispersion at the peak-stress of each cycle is also plotted. In these graphs, σ is the stress in the loading direction, ε_{11} (respectively ε_{22}) is the strain which is longitudinal (respectively transversal) during the first load.

3.9. Fatigue test

The samples used were 20 mm high and 10 mm diameter cylinders. The loading rate was controlled by the crosshead at 0.025 mm min^{-1}, which is approximately the reference strain rate. Two linear variable differential transformers (LVDT) were used to record the longitudinal strains of the specimen. The test was carried out with cycles between 1 and 30 MPa and until failure. The stress-strain curve – not reported here – shows the same hysteresis loop progressing on the strain axis for each cycle. The evolution of the strain amplitude $\Delta\varepsilon_{11}$ between two consecutive cycles at the maximum stress (in red) and at the minimum stress (in blue) is given in Fig. 10.

A repeated torsional cyclic test was also performed, using the same procedure as the monotonic test. The torsion cycles were applied between +8 MPa and −8 MPa. This test shows an immediate accommodation of the material, the second and twentieth hysteresis cycles being the same.

3.10. Multiaxial failure tests

Three multiaxial tests were performed on M2: a Brazilian test, a channel-die test and an equibiaxial compression test.

For Brazilian tests, cylinders were compressed between two horizontal surfaces. The specimens were 15 mm diameter and 30 mm high cylinders. Latex 1.5 mm thick was placed on the interfaces to avoid a localized failure in the contact zone. A pattern was deposited on the circular surface of the cylinder to enable digital image correlation. The test was controlled by the displacement of the crosshead of the machine at a rate of 0.2 mm min^{-1}. The specimen failed by traction along the transversal direction (centered and vertical macro-crack). The tension stress σ_1 and compressive stress σ_2 (at the center of the face) are estimated from the measured force F and the specimen dimensions as follows: $\sigma_1 = 2F/\pi\varnothing h$ and $\sigma_2 = -3\sigma_1$(Picart and Pompon, 2016). The reader should be aware that the latter equations come from an elastic interpretation of the Brazilian test measurements, which could be discussed in light of the global behavior of M2.

A channel-die test is the compression of a cube for which one of the transversal directions is blocked. A picture of the set-up is given in Picart and Pompon (2016). The specimen used for these tests were a 20 mm-sided cubes whose faces were lubricated using 0.7 mm thick Teflon on the walls. The displacement field was measured by digital image correlation and a loading rate of 1.4×10^{-3} mm s^{-1} (equivalent to a strain rate of about 3×10^{-5} s^{-1}) was applied using the crosshead. The longitudinal stress σ_2 is determined from the axial force applied to the sample. Since the transversal stress σ_1 is not measured, an estimation is proposed here using (1) the relation $\sigma_1 = \nu\sigma_2$ and (2) a secant "Poisson's ratio" (here, the ratio of the transversal strain to the longitudinal) at failure of $\nu = 0.5$ as seen in Fig. 3.

Equibiaxial compression tests were carried out on 20 mm-sided cubes (Fig. 11). For the Brazilian and channel-die tests, the displacement field was measured by digital image correlation and the loading rate was controlled by the crosshead at 2.8×10^{-3} mm s^{-1}, which is equivalent to about 1.5×10^{-5} s^{-1} in strain. 0.7 mm-thick Teflon, previously lubricated, was placed at the interfaces to limit friction. The

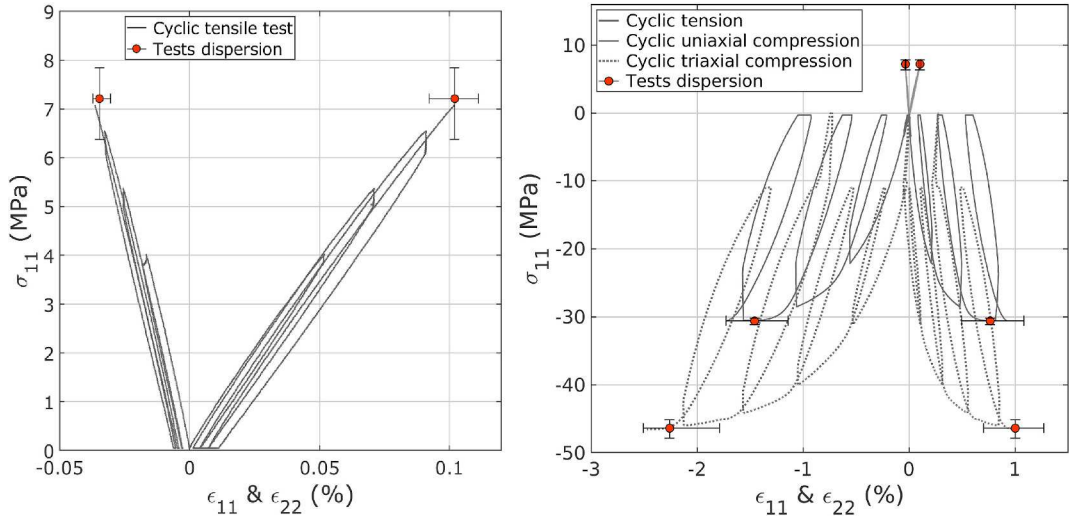

Fig. 7. Stress-strain curves for uniaxial tension (left), uniaxial compression (right, solid line; negative stress) and triaxial compression at 10 MPa pressure (right, dashed line; negative stress). This figure shows the pressure-dependence of the behavior.

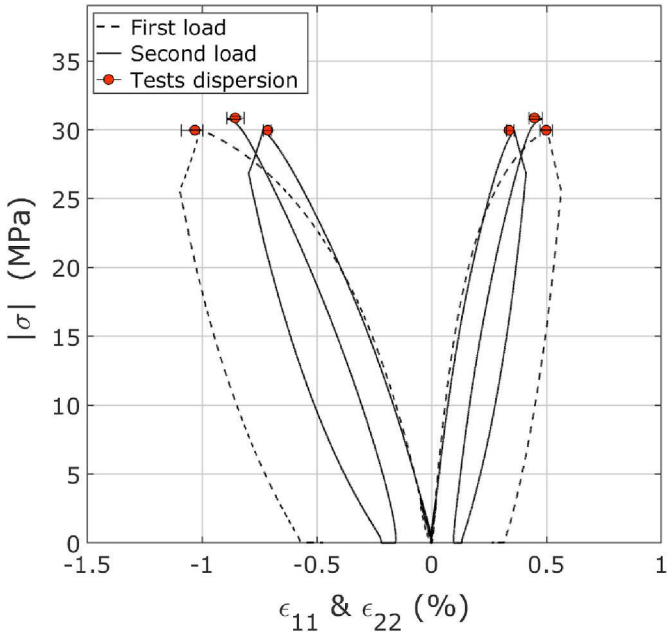

Fig. 8. Two compressions consecutively applied in the same direction (0°-0° compression). Strain set to zero at the beginning of the second load.

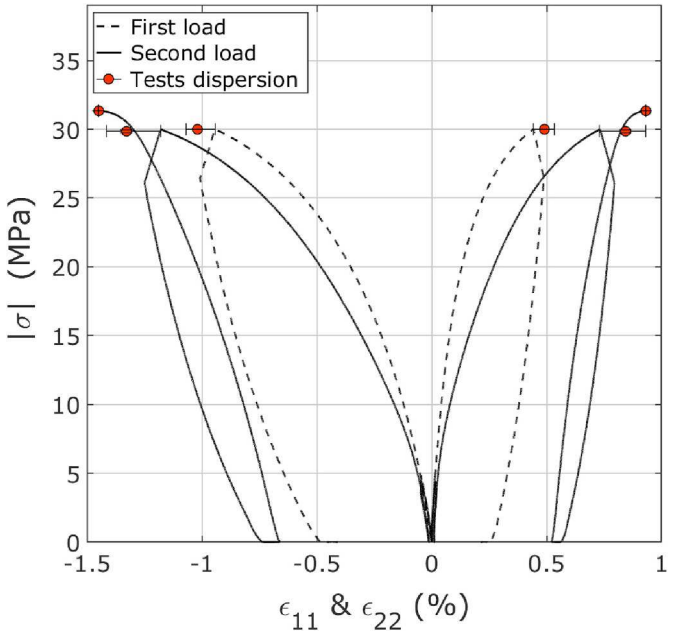

Fig. 9. Two compressions successively applied in two orthogonal directions (0°-90° compression). Strain set to zero at the beginning of the second load. Comparison with Fig. 8 shows the influence of the direction of the second loading.

main stresses are determined from the applied force F: $\sigma_1 = \sigma_2 = F/\sqrt{2}S$, with S the surface of a face of the cube.

The maximum principal stresses and strains recorded during these tests are given in Table 2.

4. Main features of M2 behavior

The DMA measurements highlight a linear viscoelastic behavior verified using a displacement sweep study. Between 0 °C and 60 °C (reduced time lower than 6), the real modulus E' shows a slight decrease with an average value of about 8000 MPa and the imaginary modulus E″ reveals that the material is slightly viscous. From about 60 °C, E' drops down to reach about 5000 MPa at 90 °C, while E'' reflects a significant material viscosity. However, this does not prove that viscoelasticity will remain linear at higher stress levels. Unfortunately, our Metravib apparatus does not allow us to investigate this question.

The comparison of the compression, tension and torsion curves (Fig. 3) reveals a non-linear behavior and dependence on the loading direction. The tension and torsion curves show a brittle fracture at around 7.1 ± 0.7 MPa in tension and 10.5 ± 0.6 MPa in torsion. The compression shows increasing softening as the stress increases, until failure at 30.6 ± 0.5 MPa. The compression failure is relatively more ductile but occurs at still low strains (1.50 ± 0.2%). The asymmetry of the material behavior is highlighted. M2 is thus defined as a quasi-brittle material.

Let us note that, in torsion, the same maximum stress at failure is expected as for the tension test (failure in tension mode). An overestimation of the failure stress in torsion may result from a size effect: the effective area of a torsion sample is smaller than during a tension experiment, which decreases the probability of finding a defect (see for example Bazant and Planas, 1997). This effect has already been recorded on M1 and M2 when comparing data from tension test and

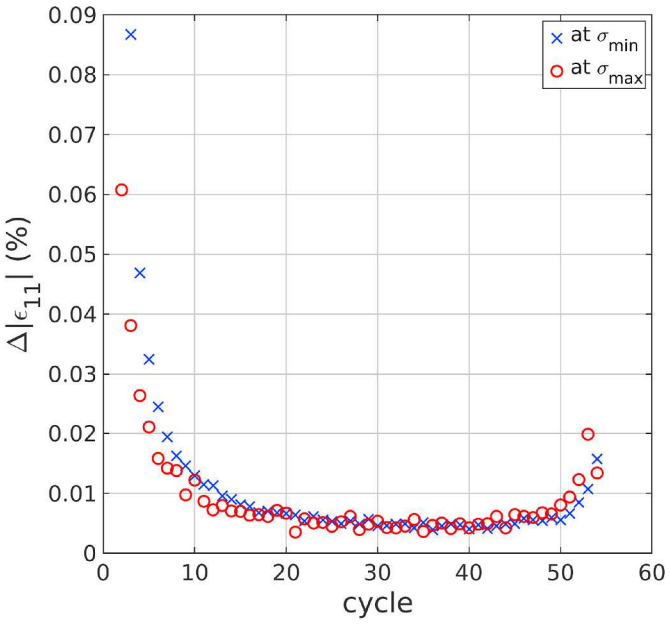

Fig. 10. Evolution of the strain amplitude $\Delta\varepsilon_{11}$, recorded between two consecutive σ_{min} (crosses) and σ_{max} (circles) of a compression fatigue test.

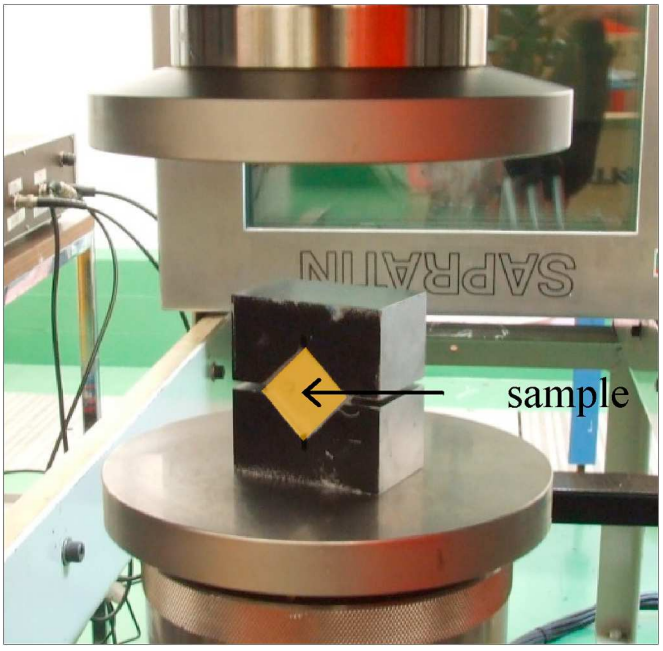

Fig. 11. Photograph of the equibiaxial compression test setup placed between the plates of the testing machine.

three-point bend experiments (Picart and Pompon, 2016).

Fig. 7 highlights a confinement-dependence of the material strength. Concerning the temperature-dependence, the material strength in compression (Fig. 5) increases as the temperature decreases but there is little variation between 20 °C and −30 °C. In tension

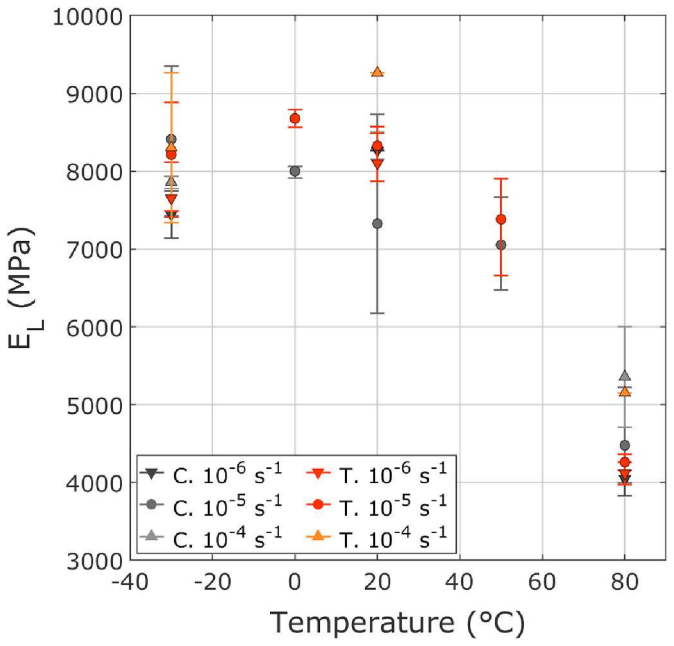

Fig. 12. Young's modulus in tension (in red) and compression (in grey) versus temperature for three strain rates at ambient pressure. A decrease is observed above 60°C. (For interpretation of the references to color in this figure legend, the reader is referred to the Web version of this article.)

(Fig. 6), a relative temperature-independence is noticed between −30 °C and 50 °C. At 80 °C, in compression as in tension, a more ductile behavior is observed, probably related to the glass transition of the explosive composition. Clear strain rate dependence is observed at 80 °C. In the near future, some other tests will be made for a better description of the response of the material in the +50 °C/+80 °C thermal range.

The influence of loading conditions such as pressure, temperature, strain rate and stress sign on the Young's modulus and the Poisson's ratio is studied in detail. Since the curves do not show a clear transition to plasticity, an elastic longitudinal modulus is calculated by linear regression over a window of 0.05% longitudinal strain, while the Poisson's ratio is determined by the ratio of longitudinal and transversal strains at 0.05% longitudinal strain. The variations of the Young's modulus (respectively the Poisson's ratio) are given in Fig. 12 and Fig. 13 (respectively Fig. 14 and Fig. 15).

The Young's modulus appears to be independent of stress sign, strain rate, and temperature in the ranges from 0 to 10 MPa and between 0 °C and 20 °C. There is a slight decrease of the modulus at 50 °C. At 80 °C, it is halved, and its value increases with rate. The Poisson's ratio is independent of temperature, strain rate and stress sign on the range from 0 °C to 80 °C.

Let us discuss the observations made between 0 °C and −30 °C. From 0 to −30 °C, DMA had shown a constant E' and a decrease of approximately 6–8% of E' after returning to 20 °C. This observation is correlated on Fig. 12 on the longitudinal modulus E_L. A linear extrapolation of data obtained between 0 °C and 50 °C yields E_L between 8500 and 9000 MPa (Figs. 2 and 12) at −30 °C when less than 8000 MPa was measured (Fig. 12). This phenomenon is observed in

Table 2
Maximum principal stresses and strains recorded from the three tests. Data obtained using a model (elastic behavior or a secant "Poisson's ratio") are given in italics.

	σ_1 (MPa)	σ_2 (MPa)	ε_1 (%)	ε_2 (%)
Brazilian test	*7.35 ± 0.13*	*−22.07 ± 0.23*	0.34 ± 0.07	−0.33 ± 0.11
Channel-die test	*−6.81 ± 3.49*	−34.45 ± 0.57	0.50 ± 0.17	−1.50 ± 0.38
Equibiaxial compression	−32.57 ± 0.15	−32.57 ± 0.20	−0.68 ± 0.06	−0.62 ± 0.24

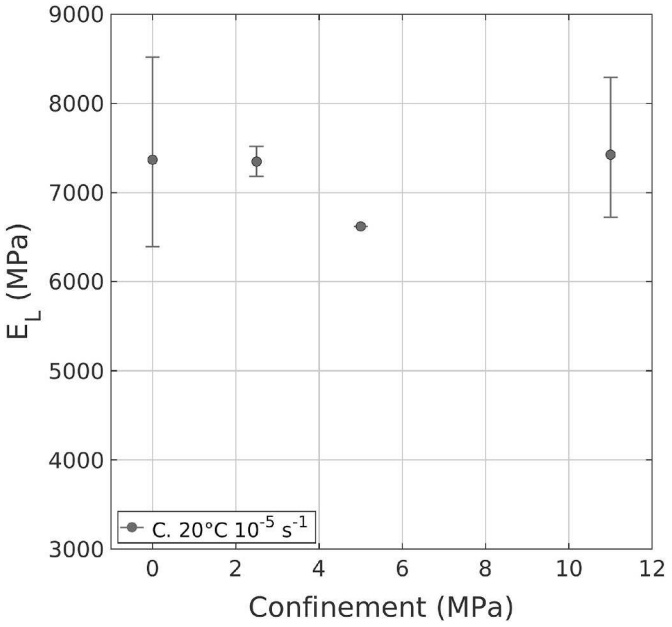

Fig. 13. Constant Young's modulus in compression versus confinement at a strain rate of $10^{-5}\,s^{-1}$ and ambient temperature.

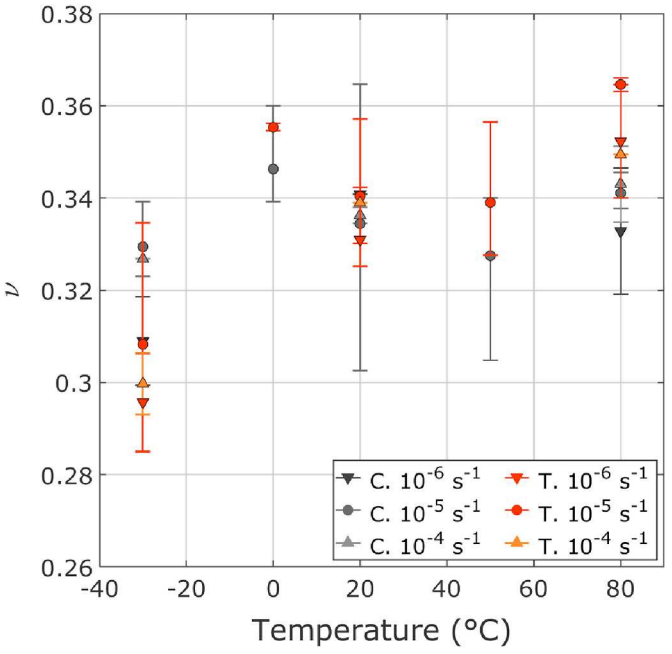

Fig. 14. Poisson's ratio in tension (in red) and compression (in grey) versus temperature for three strain rates at ambient pressure. Poisson's ratio is constant except a sudden decrease below 0°C. (For interpretation of the references to color in this figure legend, the reader is referred to the Web version of this article.)

both compression and tension modes. The Poisson's ratio also shows a curious evolution at the coldest temperature. Furthermore, a loss of linearity has been observed on M2 on its dilation coefficient under 0 °C (decrease of the coefficient). This phenomenon seems different than the known ratchet-growth observed for PBX-9502 (Thompson et al., 2010) when the glass transition temperature of the material is crossed during thermal cycles. It could be attributed to "thermally activated damage" and possibly linked to the traction applied to the binder at the binder/grain interfaces. This damage was also observed on M1, for which glass transition is far less than for M2 (Picart and Brigolle, 2010). Since an in-

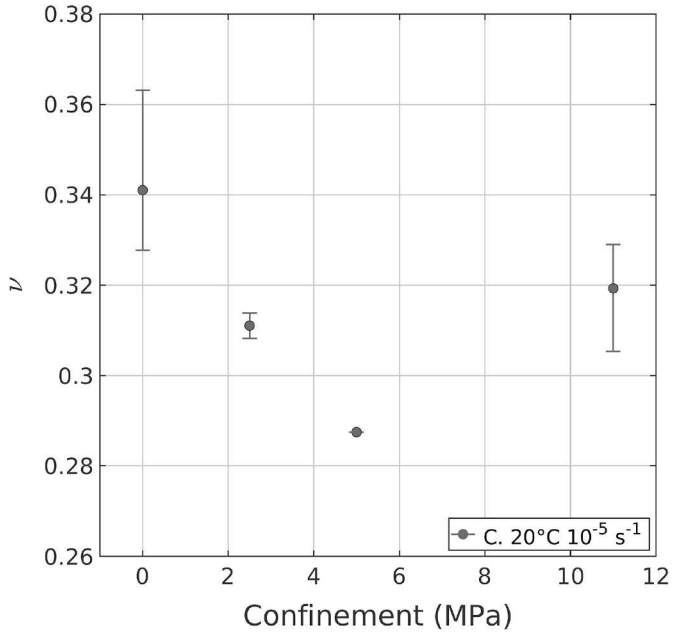

Fig. 15. Poisson's ratio in compression versus confinement at a strain rate of $10^{-5}\,s^{-1}$ and ambient temperature. A non-monotonic evolution (not explained) is observed as the pressure increases.

depth analysis is required to determine the reasons of such an inelastic behavior, this phenomenon is beyond the scope of this paper.

The pressure-dependence of the elastic modulus is negligible since the values at 2.5, 5 and 10 MPa are included in the dispersion of the point at 0 MPa. This behavior is different from what Wiegand et al. (2011) and Picart et al. (2014) observed on two pressed HMX-based explosives. The pressure effect on Poisson's ratio is quite strange, showing a decrease of between 0 and 5 MPa in pressure before an increase for a 10 MPa confinement. The authors would like to point out that the phenomena (low modulus at 5 MPa) has been observed on other materials using different solid phase and binder (for an HMX-based PBX, see Benelfellah, 2013; Benelfellah et al., 2014, 2017 and Chatti, 2018; Chatti et al., 2018 on a mock material) and for experiments made by two different teams and set-ups. Further study of this point will be provided in future work.

The influence of loading conditions on stresses and strains at the peak have also been studied. Graphs can be found in the supplementary materials. The maximum tension stress is constant between −30 °C and 50 °C and decreases at 80 °C. In compression, it regularly decreases between −30 °C and 50 °C and falls by half at 80 °C. As for the Young's modulus, the strain rate influence is only observed at 80 °C, for which the maximum stress increases with rate. Pressure increases the maximum stress, as is the case for granular materials. The maximum strains are constant while a slight increase is observed in compression in absolute values as the temperature rises. Furthermore, a small evolution of the maximum strains is recorded as the pressure rises. Temperature and pressure increase the peak-strain but not for the same reasons: the higher the temperature, the greater is the plastic flow of the material whereas the higher the pressure, the stronger is the material due to the internal friction.

An asymmetry between the tension and compressive responses is often observed for quasi-brittle granular materials (see Mazars et al., 1990 for concrete; Thomson et al., 2010 for PBX-9502; Buechler et al., 2012a for PBX-9501; and Picart et al., 2014 for M1). When these materials are submitted to alternating tension/compression loading, a stiffness recovery is observed at the beginning of compression (Mazars et al., 1990; Picart et al., 2014). This phenomenon is called unilateral effect and is classically related to damage. During the traction, cracks

are created, the damage inducing a loss of stiffness. Then, during compression, these cracks close and a stiffness recovery is obtained. This interpretation also justifies that the material is more brittle in tension than in compression. For M2, the alternating tension/compression and compression/tension tests do not reveal any stiffness recovery when the sign of stress changes. However, it is possible that the material viscosity smooths the curves and hides the phenomenon. The unilateral effect of M2 is in any case negligible compared to other strain mechanisms. Furthermore, it has been noticed that the failure point in tension and in compression is not influenced by the previous loading.

The cyclic tests carried out on M2 and shown in Fig. 7 provide a lot of information on the mechanical behavior of the material. The relaxation and recovery steps enable the viscous effects to be removed. The strains at the end of the recovery step highlight the irreversible strains suffered by the material. Moreover, the comparison between the cyclic and monotonic curves shows that the cyclic test envelope corresponds to a monotonic test, so the addition of the cycles does not influence the overall behavior of M2. Assuming the stress state remains elastic during unloading, an elastic tangent modulus can be calculated at the beginning of each load and unload. They are determined by linear regression over a strain window of 0.05%. In doing so, constant moduli are observed during tension, uniaxial compression and triaxial compression tests (blue and red lines in Fig. 16 for a uniaxial cyclic compression test). Consequently, damage is negligible on M2 up to 95% of the failure stress (peak-stress of the last cycle). Moreover, let us now suppose there is elastic unloading. Consequently, for each cycle, the secant modulus between the end of the relaxation and the end of the recovery is elastic (green lines in Fig. 16). This assumption, made in previous papers (Gratton et al., 2009; Le et al., 2010; Picart et al., 2014) on M1, is commonly used for estimating the damage evolution of concrete (Benouniche, 1979; Gotuwka, 1999). Tangent and secant moduli are compared in Fig. 16. The two methods give very different results: whereas tangent moduli (in blue and red) are constant, secant moduli (in green) decrease. Since the variations of the secant moduli cannot be imputed to damage, the observation demonstrates that some plasticity may develop during unloading. The same observations were made for cyclic compression under 10 MPa of confinement and cyclic

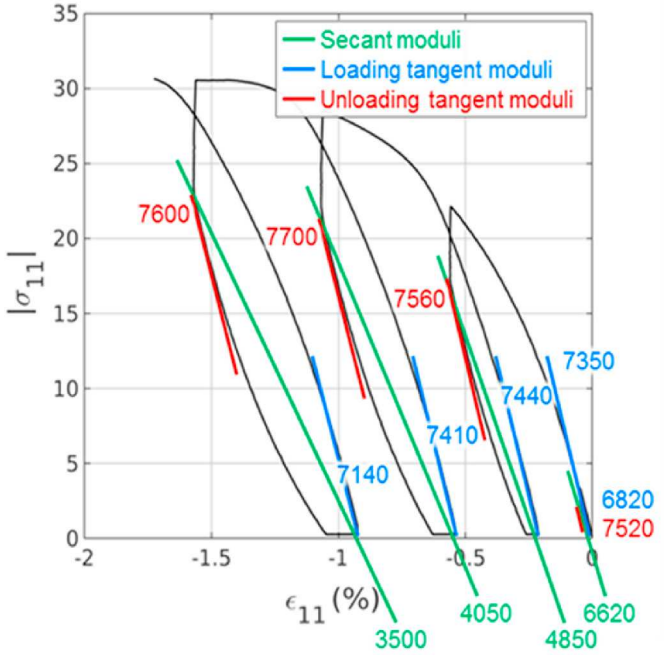

Fig. 16. Secant and tangent longitudinal moduli for a cyclic compression test. Secant moduli decrease is interpreted as a damage effect when the tangent moduli do not show any evolution.

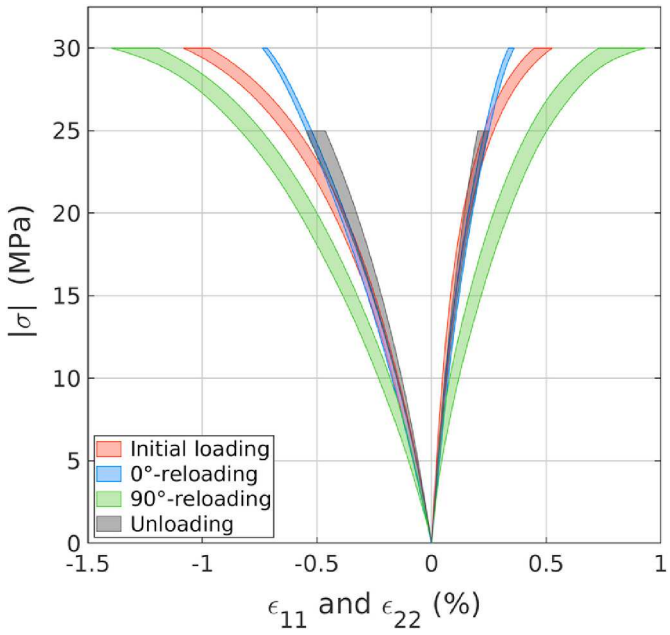

Fig. 17. Comparison of the loading and unloading curves of the 0°-0° and 0°-90° tests. The response depends on the reloading direction highlighting an induced-anisotropic during the first loading.

tension, on both the longitudinal and the transversal strains. So, no induced anisotropic damage has been detected. However, theses cyclic tests highlight that the transversal strains grow faster than the longitudinal ones. Therefore, M2 develops a load-induced anisotropy.

The 0°–0° and 0°–90° compression tests have been performed to test the load-induced anisotropy of M2. To do this, the curves of the three kinds of loading of this campaign are compared in Fig. 17, as conducted by Cambou and Lanier on Hostun sand (Cambou and Lanier, 1988). The strains are reinitialized at the beginning of each loading. The unloading curves are also shown in this graph. They have been inverted so that they read in the direction of their evolution and can be compared to the loadings curves. Fig. 17 shows the first compression in red, the 0° reloading in blue, the 90° reloading in green and all the unloadings in grey. Since the strains are measured by only one gauge in each direction, the measured curves are more scattered than for the other experimental campaigns, the discrepancy being highlighted using a colored area.

Fig. 17 shows different blue and green curves. One is stiffer than the initial compression (beyond 15 MPa), while the other is softer. The anisotropy induced by the first load is obvious. The direction of the sample which has undergone an expansion (the 90° direction, in green) is more ductile than initially. Conversely, the direction previously compressed (the 0° direction, in blue) is more rigid beyond a stress level of 15 MPa. This induced anisotropy cannot be attributed to damage since we have shown that this was negligible. This observation is confirmed by the fact that all the curves beginnings are superimposed: the elastic moduli have not been influenced by the first load. Furthermore, according to Fig. 17, the unloading curves (in grey) are the same and match with the 0° reloading. It should also be noted that the 0° reloading (in blue) and the initial loading (in red) have overlapping areas up to 15 MPa. The same observations were made by Cambou and Lanier on a Hostun sand (Cambou and Lanier, 1988). The behavior of our material can be interpreted using a kinematic strain-hardening plasticity model, as described by the schemes in Fig. 18. During a 0°–0° compression, the initial loading moves the plasticity surface up to 30 MPa. Then, the unloadings and the 0° reloading remain within this surface yielding an elastic response. During a 0°–90° compression, the initial loading moves the plasticity surface so that the yield strength

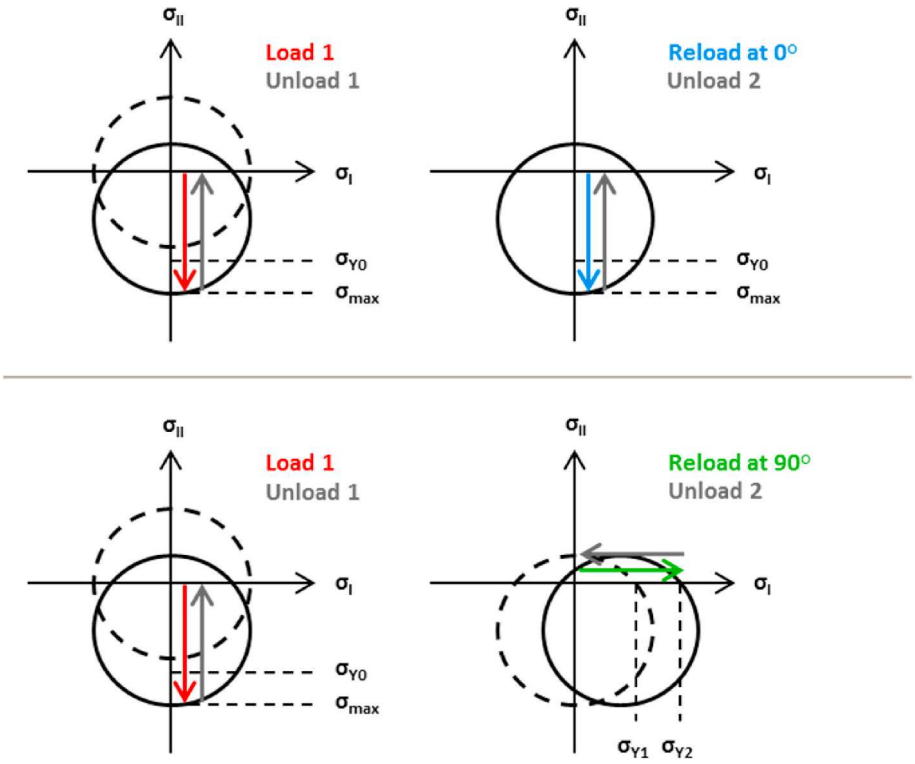

Fig. 18. Sketch illustrating the material response during the 0°-0° (top) and 0°-90° (bottom) compressions by a kinematic strain-hardening plasticity model. The displacement of the yield surface due to the first load induces a different response depending on the reloading direction.

decreases in the 90° direction. Thus, reloading at 90° yields more plasticity than during the first load. The plasticity surface is brought up to 30 MPa in the new direction, so the last unloading is then elastic.

To properly apply this interpretation to our case, the zero-stress point must stay within the plasticity surface, implying an initial yield stress higher than $\sigma_{max}/2 = 15$ MPa. If this condition is not satisfied, unloading at 90° would be different from the other unloading curves. However, the assumption of elastic unloading has been previously refuted. Nevertheless, if unloadings from cyclic compression of cylindrical samples get some plastic flow, it may be possible that for cubes an artificial confinement induced an artificial increase of the yield stress even if the interfaces were lubricated.

The analysis of the compression, tension and torsion curves (Fig. 3) shows that the behavior is non-linear starting from about 4 MPa. From the compression tests performed at 2.5, 5 and 10 MPa, the equivalent Von Mises yield stress is also about 4 MPa. These observations let us assume that the initial yield surface of M2 is a tube centered on the pressure axis, with a deviatoric 4 MPa radius. Furthermore, from the compression tests performed in temperature at various strain rates, non-linearity appears at about 4 MPa for tests at −30 °C–50 °C, independently of the strain rate. At 80 °C, the non-linearity appears from 2 MPa, whatever the strain rate. An in-depth study of the yield stress must be performed to complete these observations, but the initial plasticity criterion of M2 is independent of the pressure, the temperature up to the glass transition, and the strain rate.

For the fatigue test, the strain amplitude $\Delta\varepsilon_{11}$ between two cycles represented on Fig. 10 rapidly decreases during the first twenty cycles before becoming constant. A few cycles before failure, a rapid increase of $\Delta\varepsilon_{11}$ is observed. These observations can be interpreted by assuming that two mechanisms with opposite effects add up: a plastic accommodation yielding a decrease of the strain amplitude and late damage which will increase the strain amplitude. The plastic accommodation – also called ratchetting effect – can be modelled by a combined kinematic-isotropic hardening. Furthermore, let us recall that the torsion fatigue test with zero mean stress has shown an immediate accommodation of the material. This phenomenon should be taken into account for the hardening modelling.

From the longitudinal strain ε_{11} and transversal strain ε_{22} measured during uniaxial compression and tension tests, the volumetric strains ε_V and deviatoric strains ε_D can be plotted with respect to the mean stress P and the equivalent Von Mises stress Q:

$$\begin{cases} \varepsilon_V = \varepsilon_{11} + 2\,\varepsilon_{22} \\ \varepsilon_D = |\,\varepsilon_{11} - \varepsilon_{22}\,| \end{cases} \quad and \quad \begin{cases} P = \frac{1}{3} tr(\underline{\underline{\sigma}}) = \frac{\sigma_{11}}{3} + \sigma_{22} \\ Q = \sqrt{\frac{3}{2}\,\underline{\underline{\sigma_D}} : \underline{\underline{\sigma_D}}} = |\sigma_{11} - \sigma_{22}| \end{cases} \tag{2}$$

The volumetric curves of the compression tests at various strain rates, temperatures and pressures (Fig. 19 and Fig. 23) show an almost linear compacting behavior up to a stress level of about 70%–90% of the peak stress. Beyond that, the material develops a dilatant behavior, which reflects a rapid increase of the transversal strains compared to the longitudinal ones. This dilatancy is often attributed to anisotropic damage (see what is done in the concrete community for example), but this interpretation is not possible for M2 since the damage independence has been highlighted under these stress levels (no variation of elastic moduli). The simplest interpretation is to attribute this phenomenon to a volumetric plastic flow, as this is often the case for geomaterials, for example Gotuwka, 1999.

For tension tests, while the deviatoric behavior is temperature-independent between −30 °C and 50 °C (Fig. 22), the volumetric behavior reveals temperature dependence (Fig. 21). Given the measurement dispersion, the tests performed at 20 °C and 50 °C can be considered as identical, but the tests at 0 °C and −30 °C show some differences. The colder the temperature, the more the non-linearity of the stress - volumetric strain curve increases, leading to higher failure strains. This phenomenon correlates the observations in DMA, which suggest the existence of thermal isotropic damage. Moreover, according to the dispersion and the curves ordering, there is no strain rate effect at −30 °C in tension. The 20 °C curves at $10^{-6}\,s^{-1}$ and $10^{-4}\,s^{-1}$ are close to the curve recorded at $10^{-5}\,s^{-1}$, and thus not shown.

The deviatoric behavior (Fig. 20, Figs. 22 and 24) seems to be

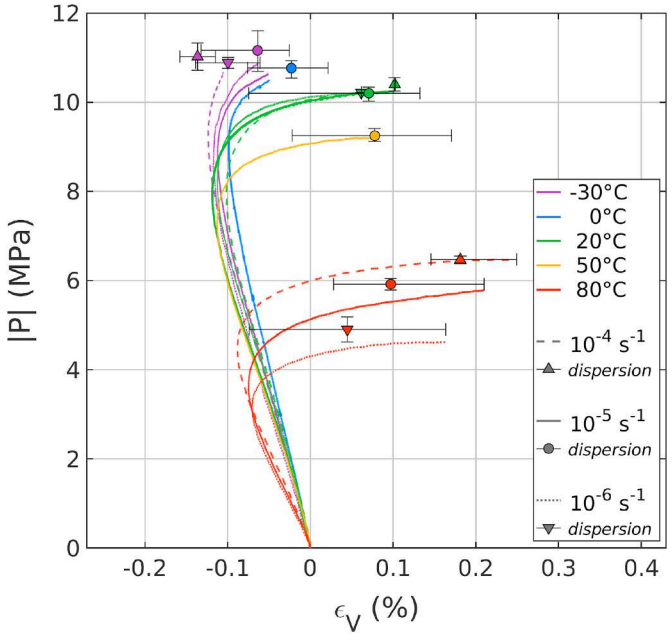

Fig. 19. Mean stress evolution with volumetric strain for simple compression tests performed between -30°C and 80°C for three strain rates. Whatever the loading conditions, a compaction is first followed by a positive volume change.

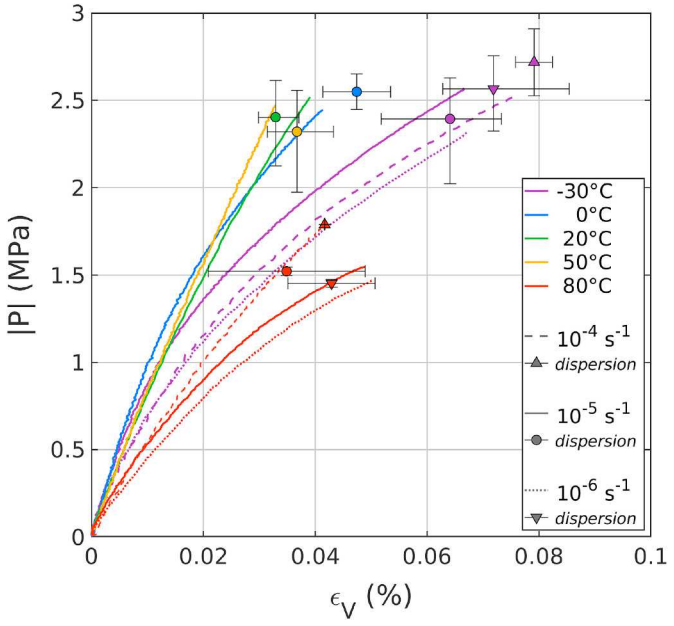

Fig. 21. Mean stress evolution with volumetric strain for simple tension tests performed between -30°C and 80°C for three strain rates. Whatever the loading conditions, the volume of the sample increases.

independent of strain rate, temperature between −30 °C and 50 °C, pressure and stress sign up to an equivalent stress of about 10–15 MPa. For compression tests (Figs. 20 and 24), a pronounced non-linearity appears beyond this, tending towards an asymptotic behavior. By imputing these volumetric and deviatoric behaviors to the plastic flow, this would point to a non-linear strain-hardening.

Fig. 21 shows more flexible behavior at −30 and + 80 °C than the mild temperature response. The measurement made at +80 °C could be related to the decrease of the viscosity of the material with the temperature as in Figs. 19, 20 and 22. At −30 °C, the DMA measurements point to “damage” thermally activated below 0 °C. This “damage” has a negligible influence during compressive loading when its influence is

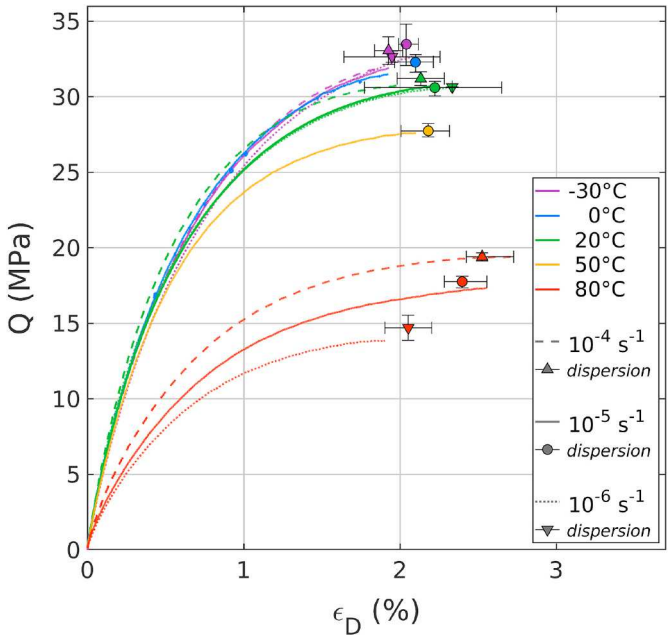

Fig. 20. Equivalent stress evolution with deviatoric strain for simple compression tests performed between -30°C and 80°C for three strain rates.

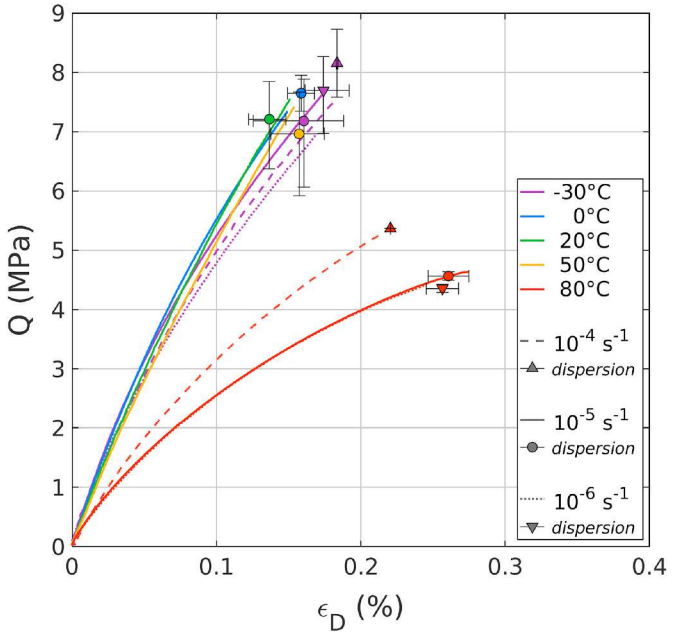

Fig. 22. Equivalent stress evolution with deviatoric strain for simple tension tests performed between -30°C and 80°C for three strain rates.

enhanced for tension loadings. More in-depth study is needed to identify its causes.

For the tests with the third principal stress as null, the M2 failure points can be represented in the principal stress plane (σ_1;σ_2), as Picart and Pompon (2016) have done for the material M1. This indicates that the failure criterion developed for M1 could potentially be adapted to M2 (see Table 2).

5. Guidelines for model improvement

The experimental data on HMX- and TATB-based PBXs have been summarized in Table 1 and in sections 3 and 4 of M2. HMX- and TATB-based PBXs are made of a very high solid fraction of organic crystals. If

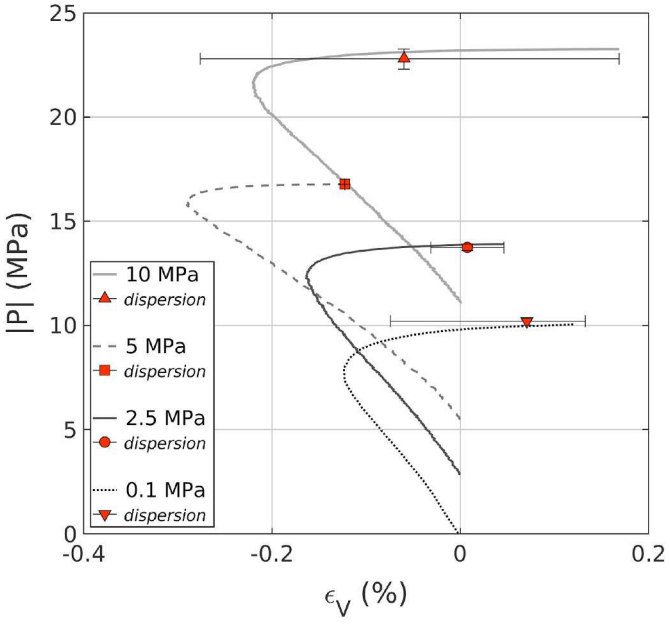

Fig. 23. Mean stress evolution with volumetric strain for triaxial compression tests performed between 0.1 and 10 MPa at a strain rate of 10^{-5} s^{-1}. Compaction is first observed followed by a positive volume change.

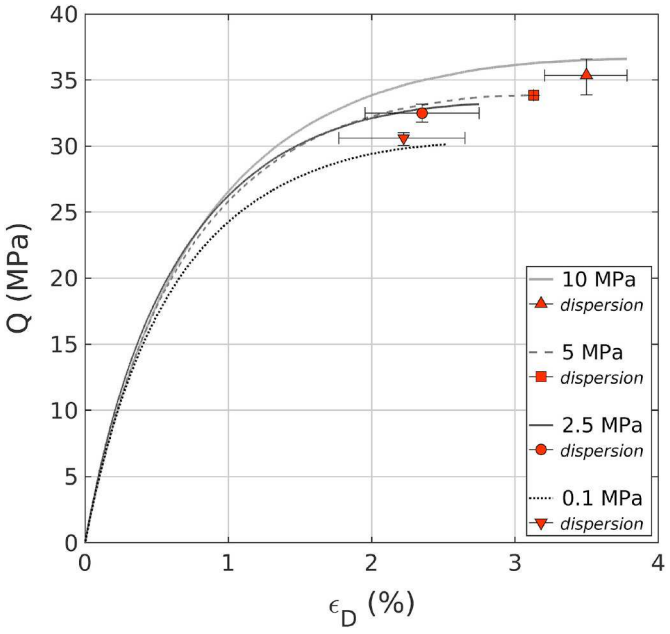

Fig. 24. Equivalent stress evolution with deviatoric strain for triaxial compression tests performed between 0.1 and *10 MPa* at a strain rate of 10^{-5} s^{-1}.

the behaviors of the TATB and HMX crystals differ (anisotropy, elastic constants, etc.), the stiffnesses of the latter remain of the same order of magnitude. Adding a few percentage of a polymeric binder gives different viscous responses for the explosive compositions. For pressed PBXs studied here, the residual porosity is of the same order (a few percent) and the Young's moduli, the Poisson's ratios and the maximum stresses (and associated strains) are comparable. As an example, in uniaxial compression or tension loadings, the peak stresses and the strain differ by a factor of 2 only. Therefore, in the authors' opinion, a "unified constitutive law" could be proposed for this class of materials, taking into account an in-depth characterization of the behavior. If mechanisms implemented in this future law could be the same, each explosive composition would have its own set of parameters, like the von Mises threshold for metals and the different initial yield stresses depending on the materials.

The aim of this section is to provide guidelines to model improvement. A constitutive law for the state of the art is first proposed, highlighting data used to calibrate or validate each model. There then follows a discussion, to determine what future work needs to be done.

The following nomenclature is adopted for splitting the stress $\underline{\underline{\sigma}}$ and strain $\underline{\underline{\varepsilon}}$ tensors into mean (denoted.^{V}) and deviatoric (denoted.^{D}) parts using the second order unit tensor $\underline{\underline{1}}$: $\sigma^V = tr(\underline{\underline{\sigma}})/3$ and $\underline{\underline{\sigma}}^D = \underline{\underline{\sigma}} - \sigma^V \underline{\underline{1}}$; $\varepsilon^V = tr(\underline{\underline{\varepsilon}})$ and $\underline{\underline{\varepsilon}}^D = \underline{\underline{\varepsilon}} - \frac{1}{3}\varepsilon^V \underline{\underline{1}}$.

5.1. SCRAM model

The SCRAM model, sketched by Dienes in 1978 (Dienes, 1978), is particularly well-detailed in a 2006 paper (Dienes et al., 2006). This model was developed in order to understand anomalous behavior of some energetic materials: low-speed impact can lead to violent reactions in a seemingly random and unpredictable way. The commonly accepted theory is that a low-speed impact can involve the formation and coalescence of hotspots, which can lead to a deflagration or a detonation. The SCRAM model links damage to the formation of hotspots and the initiation (thermal explosion) of the explosive. For the present study, we are interested in the quasistatic declination of this model. The theory is based on the strain rates additivity at the macroscopic scale. The deformation mechanisms are as follows: matrix elasticity; anisotropic crack nucleation, growth and coalescence; friction of shear-closed cracks; and plasticity. The model is written, in small strains, from the addition of the strain rates:

$$\dot{\underline{\underline{\varepsilon}}}_{tot} = \dot{\underline{\underline{\varepsilon}}}_{el} + \dot{\underline{\underline{\varepsilon}}}_{pl} + \dot{\underline{\underline{\varepsilon}}}_{c} + \dot{\underline{\underline{\varepsilon}}}_{g} \tag{3}$$

where $\dot{\underline{\underline{\varepsilon}}}_{tot}$ is the total strain rate, $\dot{\underline{\underline{\varepsilon}}}_{el}$ the matrix elasticity, $\dot{\underline{\underline{\varepsilon}}}_{pl}$ the matrix plastic flow, $\dot{\underline{\underline{\varepsilon}}}_{c}$ the microcracks opening and shearing, and $\dot{\underline{\underline{\varepsilon}}}_{g}$ the microcracks growth and coalescence. The elastic contribution is defined by Hooke's law. The plastic response of the material is described by a deviatoric linear kinematic hardening and an associated flow. The model takes the following general form:

$$\dot{\underline{\underline{\sigma}}} = \left(\underline{\underline{\underline{\underline{\mathbb{C}}}}}^{-1} + \underline{\underline{\underline{\underline{\mathscr{F}}}}}_c\right)^{-1} : \left(\dot{\underline{\underline{\varepsilon}}}_{tot} - \underline{\underline{\underline{\underline{\mathscr{F}}}}}_g : \underline{\underline{\sigma}} - \dot{\lambda}\frac{\underline{\underline{\sigma}}^D - \underline{\underline{X}}^D}{\sqrt{(\underline{\underline{\sigma}}^D - \underline{\underline{X}}^D) : (\underline{\underline{\sigma}}^D - \underline{\underline{X}}^D)}}\right) \tag{4}$$

where $\underline{\underline{\sigma}}$ is the global stress tensor and $\underline{\underline{\underline{\underline{\mathbb{C}}}}}$ is the elastic stiffness matrix. $\underline{\underline{X}}^D$ is the deviatoric kinematic hardening tensor and $\dot{\lambda}$ is the plastic multiplier. The plasticity criterion is written as follows (σ_Y is the initial yield stress):

$$f = (\underline{\underline{\sigma}}^D - \underline{\underline{X}}^D) : (\underline{\underline{\sigma}}^D - \underline{\underline{X}}^D) - \sigma_Y{}^2 \tag{5}$$

The 4th-order tensors $\underline{\underline{\underline{\underline{\mathscr{F}}}}}_c$ and $\underline{\underline{\underline{\underline{\mathscr{F}}}}}_g$ respectively refer to crack opening/shearing and to crack growth. The solid angle associated with the hemisphere is discretized into $\Delta\psi$. This corresponds to the sum of the contributions of each crack network defined by its normal (vector $\underline{n}$) orienting the solid angle portion $\Delta\psi$.

$$\underline{\underline{\underline{\underline{\mathscr{F}}}}}_c = \beta \sum_{\substack{hemi-\\sphere}} F(\underline{n})\left(H(\sigma_n)\ \underline{\underline{\underline{\underline{C}}}}^o(\underline{n}) + H(-\sigma_n)\,1 - \eta(\underline{n})\underline{\underline{\underline{\underline{C}}}}^s(\underline{n})\right)\Delta\psi \tag{6}$$

$$\underline{\underline{\underline{\underline{\mathscr{F}}}}}_g = \beta \sum_{\substack{hemi-\\sphere}} \dot{F}(\underline{n})\left(H(\sigma_n)\ \underline{\underline{\underline{\underline{C}}}}^o(\underline{n}) + H(-\sigma_n)\,1 - \eta(\underline{n})\ \underline{\underline{\underline{\underline{C}}}}^s(\underline{n})\right)\Delta\psi \tag{7}$$

where $H(\sigma_n)$ is the Heaviside function of the normal stress

$\sigma_n = \underline{n}\ \underline{\underline{\sigma}}\ \underline{n}$. $H(\sigma_n)$ is zero for opened microcracks and one for closed microcracks. The term $1-\eta(\underline{n})$, with $\cdot$ denoting the Macaulay brackets, corresponds to the microcrack sliding criterion: this term is equal to zero when the crack is blocked (no shear) and is one when it is sliding-free. The coefficient η is defined from the friction state of the family of cracks oriented by $\underline{n}$ and the friction coefficient μ: $\eta = \frac{\mu - \sigma_n}{s_n}$, with $s_n = \sqrt{\underline{n}\ \underline{\underline{\sigma}}\ \underline{\underline{\sigma}}\ \underline{n} - \sigma_n^2}$. Thus, whereas the pressure is not involved in the plasticity criterion, damage evolution and effectivity (defined as how the damage of a given network does or does not affect the behavior depending on the loading direction) as well as frictional sliding are pressure-dependent since they depend on the sign of σ_n. The tensors $\underline{\underline{\underline{\underline{C}}}}^o(\underline{n})$ and $\underline{\underline{\underline{\underline{C}}}}^s(\underline{n})$ of equation (4) describe the opening and shearing directions of the microcrack. β [MPa^{-1}] is a constant coming from analytic solutions for penny-shaped cracks. The function $F(\underline{n}) = \int_0^\infty n(c, \underline{n})\, c^3\, dc$ describes the crack distribution, with $n(c, \underline{n})$ representing the distribution of the microcracks of length c and normal vector $\underline{n}$. The crack growth rate $\dot{c}$ is controlled by the rate of dissipated energy $g(\underline{\underline{\sigma}}, \underline{n}, c)$:

$$\begin{cases} \dot{c}(\underline{\underline{\sigma}}, \underline{n}, c) = \dot{c}_{max} \frac{1}{1+m} \left(\frac{g(\underline{\underline{\sigma}}, \underline{n}, c)}{(1+\frac{1}{m}) g_c} \right)^m & \text{if } g(\underline{\underline{\sigma}}, \underline{n}, c) \le \left(1+\frac{1}{m}\right) g_c \\ \dot{c}(\underline{\underline{\sigma}}, \underline{n}, c) = \dot{c}_{max} \left(1 - \frac{g_c}{g(\underline{\underline{\sigma}}, \underline{n}, c)}\right) & \text{if } g(\underline{\underline{\sigma}}, \underline{n}, c) \ge \left(1+\frac{1}{m}\right) g_c \end{cases} \tag{8}$$

where m is an exponent greater than one. In this model, the maximum crack growth rate $\dot{c}_{max}$ is assumed to have the magnitude of the Rayleigh wave speed and g_c is the critical rate of dissipated energy. The function g is written as follows:

$$g(\underline{\underline{\sigma}}, \underline{n}, c) = \frac{4}{\pi} \frac{1-\nu}{1-\frac{\nu}{2}} \frac{c}{2G} \left(H(\sigma_n) \left(\left(1 - \frac{\nu}{2}\right) \sigma_n^2 + s_n^2 \right) + H(-\sigma_n)\ \mu \sigma_n + s_n \right) \tag{9}$$

where ν and G are respectively the Poisson's ratio and the shear modulus.

It can be seen that g – and so $\dot{c}$ – is greater in tension (σ_n positive) than in compression (σ_n negative). In addition, for a closed microcrack (σ_n negative) whose frictional sliding is blocked (factor $1-\eta$null): $\eta \le 1 \implies s_n \le \mu \sigma_n \implies g = 0 \implies \dot{c} = 0$; the microcrack cannot grow. Apart from this particular case, as soon as the stress state of a microcrack is not zero, it expands.

The mechanical parameters of this model are determined for PBX-9501 from only one monotonic uniaxial compression test performed at 10^{-2} s^{-1} without transversal strain measurements. The fit of the parameters is not detailed. The validation of SCRAM on the quasistatic domain is missing. Dienes compares the simulation, calibrated on a compression at 10^{-2} s^{-1}, to experimental compression performed at 2×10^{-2} s^{-1}, the rate effect between these two tests being negligible (both experimentally and numerically).

5.2. ViscoSCRAM model (VS)

The ViscoSCRAM model defined in (Bennett et al., 1998) puts the deviatoric component of the IsoSCRAM model proposed by Addessio and Johnson (1990) for quasi-brittle materials in series with a generalized Maxwell model with N branches. The volumetric component of the model is described by a linear elastic law. The total strain rate is split into volumetric and deviatoric components. From the additivity of the viscoelastic and the crack growth strain rates (plasticity of the matrix is ignored), the ViscoSCRAM model is written as follows:

$$\begin{cases} \dot{\sigma}^V = K\, \dot{\varepsilon}_{tot}{}^V \\ \underline{\underline{\dot{\sigma}}}^D = \dfrac{2G\, \underline{\underline{\dot{\varepsilon}}}_{tot}{}^D - \sum_{b=1}^N \frac{\underline{\underline{\sigma}}_b{}^D}{\tau_b} - 3\left(\frac{c}{a}\right)^2 \frac{\dot{c}}{a}\, \underline{\underline{\sigma}}^D}{1 + \left(\frac{c}{a}\right)^3} \end{cases} \tag{10}$$

$\underline{\underline{\sigma}}^D$is the total deviatoric stress, corresponding to the sum of the stress $\underline{\underline{\sigma}}_b{}^D$of each branch. K is the bulk elastic modulus. G is the sum of the shear moduli of the N branches. τ_b is the characteristic time of the bth branch. The constant a is the average initial porosity size. Compared to SCRAM, the crack growth rate $\dot{c}$ is largely simplified by the assumption of isotropic damage:

$$\begin{cases} \dot{c}(\underline{\underline{\sigma}}^D, c) = \dot{c}_{max} \frac{1}{1+\frac{m}{2}} \left(\frac{J(\underline{\underline{\sigma}}^D, c)}{\sqrt{1+\frac{2}{m}} J_0} \right)^m & \text{if } J(\underline{\underline{\sigma}}^D, c) \le J_0 \sqrt{1+\frac{2}{m}} \\ \dot{c}(\underline{\underline{\sigma}}^D, c) = \dot{c}_{max} \left(1 - \frac{J_0{}^2}{J(\underline{\underline{\sigma}}^D, c)^2}\right) & \text{if } J(\underline{\underline{\sigma}}^D, c) \ge J_0 \sqrt{1+\frac{2}{m}} \end{cases} \tag{11}$$

where J_0 is a parameter (in Pa$\sqrt{m}$). The function J is written according to Hackett and Bennett (Hackett and Bennett, 2000):

$$J(\underline{\underline{\sigma}}^D, c) = \sqrt{\frac{3}{2} \pi c\ \underline{\underline{\sigma}}^D : \underline{\underline{\sigma}}^D} \tag{12}$$

With this formulation, the crack growth rate $\dot{c}$ depends only on the deviatoric stress and therefore is pressure-independent, unlike in the SCRAM model (previous equations (6) and (7)).

The model calibration is performed for PBX-9501 (Bennett et al., 1998). The shear moduli of the five viscoelastic branches (to cover different strain rates) are determined from the Young's modulus from four compressions in the quasistatic range and two at high strain rates, and an assumed Poisson's ratio of 0.3. The determination of the parameters J_0, a and m is not detailed.

In the quasistatic range, Hackett and Bennett (Hackett and Bennett, 2000) have compared ViscoSCRAM to a three-point bending test on PBX-9501, the model predicting the experimental force-displacement curves. Later, Rangaswamy et al. (2010) have simulated a Brazilian test. The quasi-linear part of the experimental curves is reproduced but the simulated displacement deviates from the measurements before reaching the maximum stress. The horizontal strain field from the finite element simulation is compared with experimental digital image correlation. The strains at the macrocrack boundary are largely underestimated.

5.3. ViscoSCRAM viscoplastic model (VS-VP)

Liu and coworkers (Liu et al., 2019) recently proposed a modified version of ViscoSCRAM by adding a deviatoric viscoplasticity (Bodner, 1987) in series with the original model, resulting in the following expressions:

$$\begin{cases} \dot{\sigma}^V = K\, \dot{\varepsilon}_{tot}{}^V \\ \underline{\underline{\dot{\sigma}}}^D = \dfrac{2G\, \underline{\underline{\dot{\varepsilon}}}_{tot}{}^D - \sum_{b=1}^N \frac{\underline{\underline{\sigma}}_b{}^D}{\tau_b} - \left(3\left(\frac{c}{a}\right)^2 \frac{\dot{c}}{a} + \dot{\lambda} \frac{2G}{\sqrt{\frac{2}{3}\, \underline{\underline{\sigma}}^D : \underline{\underline{\sigma}}^D}} \right) \underline{\underline{\sigma}}^D}{1 + \left(\frac{c}{a}\right)^3} \end{cases} \tag{13}$$

An isotropic hardening is computed from an upper limit weighted by a function of the ratio of deviatoric stress and plastic work, and not from a stress yield criterion with hardening. A viscoplastic strain rate always exists in this model.

The crack growth $\dot{c}$ is taken from Buechler and Luscher (2014) to introduce pressure dependence and tension–compression asymmetry as follows:

$$\begin{cases} \dot{c}(\underline{\underline{\sigma}}, c) = \dot{c}_{res} \frac{1}{1+\frac{m}{2}} \left(\frac{J(\underline{\underline{\sigma}}, c)}{J_{0\mu}(\sigma^V, c)\sqrt{1+\frac{2}{m}}} \right)^m & \text{if } J(\underline{\underline{\sigma}}, c) \leq J_{0\mu}(\sigma^V, c)\sqrt{1+\frac{2}{m}} \\ \dot{c}(\underline{\underline{\sigma}}, c) = \dot{c}_{res} \left(1 - \frac{J_{0\mu}(\sigma^V, c)^2}{J(\underline{\underline{\sigma}}, c)^2} \right) & \text{if } J(\underline{\underline{\sigma}}, c) \geq J_{0\mu}(\sigma^V, c)\sqrt{1+\frac{2}{m}} \end{cases} \tag{14}$$

Compared to the original ViscoSCRAM model (equation (9)), the speed $\dot{c}_{max}$ is replaced by $\dot{c}_{res}$ which is a logarithmic function of the strain rate, bounded by the Rayleigh wave speed. The function J depends on the pressure σ^V, and the constant J_0 is multiplied by a factor depending on pressure, crack length and dynamic friction coefficient μ', resulting in $J_{0\mu}$.

$$J(\underline{\underline{\sigma}}, c) = \sqrt{\pi c} \left(H(\sigma^V) \sqrt{\frac{3}{2}(\underline{\underline{s}}^D : \underline{\underline{s}}^D + 3\sigma^{V\,2})} + H(-\sigma^V) \sqrt{\frac{3}{2}\underline{\underline{s}}^D : \underline{\underline{s}}^D} \right) \tag{15}$$

$$J_{0\mu}(\sigma^V, c) = J_0 \sqrt{1 - \pi \frac{\mu' \sqrt{c}\, \sigma^V}{J_0} \left(1 - \frac{\mu' \sqrt{c}\, \sigma^V}{J_0} \right)} \tag{16}$$

With this formulation, J is greater in tension (σ^V positive) than in compression (σ^V negative) while the function $J_{0\mu}$ is lower in tension than in compression. Thus, the ratio $J/J_{0\mu}$ and so the growth rate $\dot{c}$ is higher in tension than in compression. As in SCRAM, an opened crack grows faster than a closed one.

There are 19 parameters fitted on the longitudinal strains of monotonic tension and compression tests performed at 50 °C and 10^{-4} s^{-1} on a PBX-9502 sample (Thompson et al., 2010), and secondly another set of parameters calibrated on a cyclic compression test performed on M2 using the curves taken from Ambos et al. (2015) and Gasnier et al. (2018). From these calibrations, all this results in the maximum strains in tension being underestimated by half. Furthermore, the unloading and reloading steps do not get any hysteresis.

In order to validate the model, Liu et al. (2019) have simulated a compression of a perforated plate of PBX-9502 (Liu and Thompson, 2014), and they compare the experimental and simulated force-displacement curves. The two plots coincide up to the maximum stress. The experimental horizontal strain field from digital image correlation is also compared to a finite element simulation. Although the shape is accurately reproduced, the displacement calculated around the hole is less significant than the measurements. The authors did not provide a comparison for vertical strains, for which experimental data are however available (Liu and Thompson, 2014).

5.4. Viscoelastic plastic model (VE-P)

The research carried out on M1 and M2 has led to several constitutive laws being developed from a substantial experimental base (see section 2). For material M1, a model describing a non-linear viscoelasticity with pressure and temperature dependencies was established in the 1980s (Belmas et al., 1982). Since this approach only enables simulation of monotonic tests, we refer the reader to the original paper for its description. A second model was proposed by Gratton et al. (2009), including an elasto-viscoplastic law with isotropic damage and pressure-dependent viscoplastic behavior. This model was later completed to describe the viscoelasticity visible during load-unload loops. In 2010, Le and coworkers (Le et al., 2010) proposed a viscoelastic-plastic constitutive law for M1 including isotropic damage. This model is based on a generalized Maxwell model in which one of the branches – numbered 0 – is elastoplastic. The other branches are viscoelastic. All the elastic moduli are identically damaged. The parabolic plasticity criterion is defined from the mean and deviatoric stresses of the elastoplastic branch with an isotropic strain-hardening:

$$f = \sqrt{\frac{1}{3}\underline{\underline{\sigma_0}}^D : \underline{\underline{\sigma_0}}^D + \frac{k^2}{R(k)}\sigma_0{}^V} - k \tag{17}$$

The isotropic hardening variables k and R(k) are related to the cumulative plastic strain $\overline{\varepsilon_{pl}}$. A non-associated plastic flow is empirically determined, involving a dilatancy coefficient β^* which controls the volumetric to deviatoric plastic strain ratio:

$$\begin{cases} \dot{\varepsilon}_{pl}{}^V = \dot{\lambda} \frac{\beta^*}{\sqrt{3(1+\beta^{*2})}} \\ \underline{\underline{\dot{\varepsilon}_{pl}}}^D = \dot{\lambda} \frac{1}{\sqrt{1+\beta^{*2}}} \frac{\underline{\underline{\sigma_0}}^D}{\sqrt{\underline{\underline{\sigma_0}}^D : \underline{\underline{\sigma_0}}^D}} \end{cases} \tag{18}$$

The elastoplastic stress, $\underline{\underline{\sigma_0}}$, and the viscoelastic stresses, $\underline{\underline{\sigma_b}}$, add up to give the global stress, leading to the following form of the model:

$$\begin{cases} \dot{\sigma}^V = K(1-d)\,\dot{\varepsilon}_{tot}{}^V - \sum_{b=1}^N \frac{\sigma_b{}^V}{\tau_b} - \frac{\dot{d}}{1-d}\sigma^V - \\ \qquad K_0((1-d)\,\dot{\varepsilon}_{pl}{}^V - \dot{d}(\varepsilon_{tot}{}^V - \varepsilon_{pl}{}^V)) \\ \dot{\underline{\underline{s}}}^D = 2G(1-d)\,\underline{\underline{\dot{\varepsilon}_{tot}}}^D - \sum_{b=1}^N \frac{\underline{\underline{\sigma_b}}^D}{\tau_b} - \frac{\dot{d}}{1-d}\underline{\underline{\sigma}}^D - \\ \qquad 2G_0\left((1-d)\,\underline{\underline{\dot{\varepsilon}_{pl}}}^D - \dot{d}\left(\underline{\underline{\varepsilon_{tot}}}^D - \underline{\underline{\varepsilon_{pl}}}^D \right) \right) \end{cases} \tag{19}$$

As for the deviatoric part, σ^V is the total mean stress, corresponding to the sum of the stress $\sigma_b{}^V$ of each branch. K_0 and G_0 are the moduli of the elastoplastic branch, while K and G are the sum of the moduli of each branch from 0 to N. The damage variable d is related to the maximum positive principal strain ε_{I+} such that:

$$d = (d_1 sup_t(\varepsilon_{I+}) + d_2) \frac{d_3 sup_t(\varepsilon_{I+})}{1 - d_3 sup_t(\varepsilon_{I+})} \tag{20}$$

where d_1, d_2 and d_3 are material parameters without units. In the previous models, damage – described by the variable c – was related to the stress. Here, damage is due to the largest positive strain in the load history, denoted $sup_{(t)}(\varepsilon_{I+})$.

A temperature extension of the model is presented in Le's thesis manuscript (Le, 2007) and a multiaxial failure criterion (the reader should note that failure here means “maximum stress”) is detailed in (Caliez et al., 2014; Picart and Pompon, 2016). This criterion takes into account two mechanisms: one on the maximum positive principal strain and another on the maximum positive principal effective stress, both defined in relation to the stress of the elastoplastic branch (index 0). The first of the two criteria reached indicates the actual failure.

First, a DMA campaign was conducted to determine the longitudinal viscoelastic moduli for a Maxwell model with ten dashpots. The 3D extension is performed using a Poisson's ratio, experimentally measured. In the absence of experimental data highlighting the hardening mechanism, the authors assume an isotropic hardening. This assumption implies that the unloadings are purely elastic and so the secant modulus calculated between the end of the relaxation and the end of the recovery of cyclic tests is supposed to be elastic. The damage is calculated for each cycle as the elastic longitudinal modulus degradation with respect to the first cycle value: $d = (E_0 - E)/E_0$. Plotting the damage evolution as a function of the maximum positive strain (i.e.: transversal strain in compression, longitudinal strain in tension) enables estimation of the coefficients d_1, d_2 and d_3. From cyclic tests again, the inelastic strains at the end of the recoveries are considered as plastic strains. Plotting these plastic strains against the corresponding relaxed stress provides an estimate of the plastic parameters β^*, k and the function R(k). Lastly, the calibration of the failure criterion from multiaxial loadings on M1 is detailed by Picart and Pompon (2016).

The validation of the model is presented in (Caliez et al., 2014; Le, 2007). The model is confronted with a Brazilian test and three-point bending performed on M1. For the three-point bending test, the experimental force-displacement curve is very well reproduced by the model. For the Brazilian test, the force-displacement curve differs from the experimental curve. For the same displacement, the simulated force is slightly lower than the experimental force and the failure point is slightly underestimated. In addition, the horizontal and vertical strain

fields measured by digital image correlation are compared to the finite element simulation. These comparisons show quite a good match. However, since the plasticity is put in parallel with the viscoelasticity, the envelope curves of the cyclic tests are not well reproduced.

For models calibrated on massive specimens, the underestimation observed in the three-point bending test could also be explained by the well-known "size effect" observed on concretes and other brittle materials (Bazant and Planas, 1997). Since this phenomenon is not being investigated for M1, we cannot conclude on its influence.

5.5. Viscoelastic viscoplastic model (VE-VP)

Buechler has proposed a viscoelastic-viscoplastic model (Buechler, 2012b) to which he has later added isotropic damage (Buechler, 2013) in order to reproduce the PBX-9501 behavior. The viscoelasticity is described by a generalized Maxwell model, involving a purely elastic branch and N viscous ones. The viscoplasticity is put in series with the viscoelasticity. It is described by a Drucker-Prager model whose yield strength depends on the cumulative plastic strain and its rate. The non-associated plastic flow combines isotropic and kinematic hardenings. The model is defined in small strains, and the additivity of the strain rates is written as follows:

$$\underline{\underline{\dot{\varepsilon}_{tot}}} = \underline{\underline{\dot{\varepsilon}_{ve}}} + \underline{\underline{\dot{\varepsilon}_{pl}}} + \underline{\underline{\dot{\varepsilon}_{d}}} \tag{21}$$

where $\underline{\underline{\dot{\varepsilon}_{ve}}}$ is the viscoelastic strain rate, $\underline{\underline{\dot{\varepsilon}_{pl}}}$ the viscoplastic strain rate and $\underline{\underline{\dot{\varepsilon}_{d}}}$ the strain rate due to damage. The plasticity criterion takes the following form:

$$f = \sqrt{\frac{2}{3}(\underline{\sigma}^D - \underline{X}^D) : (\underline{\sigma}^D - \underline{X}^D)} - A(\sigma^V - X^V) - \sigma_Y(\overline{\varepsilon_{pl}}, \dot{\overline{\varepsilon_{pl}}}) \tag{22}$$

where $\underline{X} = \underline{X}^D + X^V \underline{1}$ is the kinematic hardening tensor, σ_Y the yield stress and $\overline{\varepsilon_{pl}}$ the cumulative plastic strain. A is an internal friction coefficient of the material defining the Drucker-Prager slope. The non-associated plastic flow is related to the following potential (B being a constant):

$$g = \sqrt{\frac{2}{3}(\underline{\sigma}^D - \underline{X}^D) : (\underline{\sigma}^D - \underline{X}^D)} - B(\sigma^V - X^V) - \sigma_Y(\overline{\varepsilon_{pl}}, \dot{\overline{\varepsilon_{pl}}}) \tag{23}$$

The model takes the following general form:

$$\begin{cases} \dot{\sigma}^V = \left(K + \frac{\hat{K}}{\varphi_1 d}\right)\dot{\varepsilon}_{tot}{}^V - \sum_{b=1}^{N} \frac{\sigma_b{}^V}{\tau_b} + \frac{K\dot{\lambda}}{\sqrt{\frac{3}{2} + \frac{B^2}{3}}}\frac{B}{3} - \frac{\dot{d}}{d}\sigma^V \\ \underline{\dot{\sigma}}^D = \left(2G + \frac{2\hat{G}}{\varphi_2 d}\right)\underline{\dot{\varepsilon}_{tot}}^D - \sum_{b=1}^{N} \frac{\underline{\sigma_b}^D}{\tau_b} - \frac{2G\dot{\lambda}}{\sqrt{\frac{3}{2} + \frac{B^2}{3}}} \frac{\sqrt{\frac{3}{2}}(\underline{\sigma}^D - \underline{X}^D)}{\sqrt{(\underline{\sigma}^D - \underline{X}^D) : (\underline{\sigma}^D - \underline{X}^D)}} - \frac{\dot{d}}{d}\underline{\sigma}^D \end{cases} \tag{24}$$

The damage-induced strain $\underline{\underline{\varepsilon_d}}$ is written in volumetric and deviatoric parts:

$$\begin{cases} \hat{K}\,\varepsilon_d{}^V = \varphi_1 d\,\sigma^V \\ 2\hat{G}\,\underline{\underline{\varepsilon_d}}^D = \varphi_2 d\,\underline{\dot{\sigma}}^D \end{cases} \tag{25}$$

The damage d depends exclusively on the cumulative plastic strain $\overline{\varepsilon_{pl}}$. φ_1 and φ_2 are parameters without units controlling the damage effectivity (i.e.: whether or not the influence of the damage depends on the loading direction) on the volumetric and deviatoric components. $\hat{K}$ and $\hat{G}$ are bulk and shear moduli connecting the stress to the damage and the strain. No more details are given by the author.

The model is parameterized from PBX-9501 experimental results in uniaxial compression (Buechler et al., 2013) but the author points out that the calibration of the slope A is of poor quality due to scattered post-processed experimental data. Moreover, without experimental measurements of transversal strains, the parameter B which controls the plastic volumetric flow cannot be calibrated. The inaccurate fit of the plastic part of the model implies that the damage evolution (related to the cumulative plastic strain) is poorly determined. A comparison of a monotonic compression simulation at 7.5×10^{-5} s^{-1} with two monotonic tests performed at 10^{-5} s^{-1} and 10^{-4} s^{-1} is given in (Buechler, 2012b; Buechler, 2013). According to the author, the result is encouraging because the simulated curve is bordered by the experimental curves, but the model is not validated.

5.6. Elastic viscoplastic model (E-VP)

In the approach proposed by Zubelevicz and coworkers (Zubelewicz et al., 2013) the total strain tensor has three components:

$$\underline{\underline{\dot{\varepsilon}_{tot}}} = \underline{\underline{\dot{\varepsilon}_{el}}} + \underline{\underline{\dot{\varepsilon}_{pl}}}^{ch} + \underline{\underline{\dot{\varepsilon}_{pl}}}^{b} \tag{26}$$

The plasticity is split into two parts. The first, $\underline{\underline{\dot{\varepsilon}_{pl}}}^{ch}$, describes the macroscopic effect of the grain chains dilatancy and shearing with a Drucker-Prager viscoplastic criterion. The second, $\underline{\underline{\dot{\varepsilon}_{pl}}}^{b}$, purely deviatoric, describes the equivalent binder shearing. There is no hardening. The plastic flow accounts for temperature dependence. The elastic strains are linked to the stress by a stiffness tensor affected by an anisotropic damage tensor $\underline{\underline{d}}$ affected by the loading direction. This tensor $\underline{\underline{d}}$ is represented in terms of symmetric tensors depending on the stress state, "turning" for non-monotonic loading.

$$\underline{\sigma} = \left(\left(K - \frac{2}{3}G\right)(\underline{\underline{1}} - \underline{\underline{d}}) \otimes (\underline{\underline{1}} - \underline{\underline{d}}) + 2G(\underline{\underline{1}} - \underline{\underline{d}})\bar{\otimes}(\underline{\underline{1}} - \underline{\underline{d}})\right) : \underline{\underline{\varepsilon_{el}}} \tag{27}$$

$$\underline{\underline{d}} = d_c(\alpha_{0c}\,\underline{\underline{1}} + \alpha_{1c}\,\underline{\sigma}^D + \alpha_{2c}\,\underline{\sigma}^D.\,\underline{\sigma}^D) + d_t(\alpha_{0t}\,\underline{\underline{1}} + \alpha_{1t}\,\underline{\sigma}^D + \alpha_{2t}\,\underline{\sigma}^D.\,\underline{\sigma}^D) \tag{28}$$

The operator $\otimes$ defines the tensor product: $(a \otimes b)_{ijkl} = a_{ij}b_{kl}$, while $\bar{\otimes}$ defines: $(a\bar{\otimes}b)_{ij} = \frac{1}{2}(a_{ik}b_{jl} + a_{il}b_{jk})$. The brittle damage d_t depends on the full history over time of the strain projection on the t part of the tensor $\underline{\underline{d}}$, and the ductile damage d_c depends on the full history over time of an equivalent plastic strain being then pressure-dependent. The parameters α_{0t}, α_{1t}, α_{2t} (resp. indexed c) are functions of the Lode's angle, and can be assimilated to the damage effectivity as a function of the loading direction.

The 23 parameters of the model are calibrated from stress versus longitudinal strain curves of seven monotonic compression tests and seven tension tests performed on PBX-9502 at five temperatures between -52 °C and 74 °C and at 10^{-3} to 10^{-5} s^{-1}. It should be noted that it is not specified how the Poisson's ratio is determined without transversal strain measurements. The authors only validate their model using one comparison of the simulated versus experimental failure pattern of a compression sample.

5.7. Microplane formulation applied to pressed explosives (VDT-P)

Taking up the cyclic tests on M1, Benelfellah and coworkers (Benelfellah, 2013; Benelfellah et al., 2014; 2017; Picart et al., 2014) were interested in the induced anisotropy of the material highlighted by these tests. The authors determined longitudinal and transversal elastic moduli for each loading cycle. By tracing these moduli evolutions as a function of the maximum positive strain, they highlight a faster degradation of the transversal modulus than for the longitudinal one, due to an induced anisotropy of the material. The authors also observed that during tests alternating tension and compression loadings, the material recovers its initial stiffness shortly after being compressed. This phenomenon, called unilateral effect, has been observed for granular materials such as concrete (Mazars et al., 1990). The microstructural interpretation given is that the microcracks opened in tension close when the loading direction is reversed; once closed and blocked under the effect of compression, these cracks no longer have an effect on the

macroscopic behavior of the material.

The model coupled a damage-induced anisotropy (Benelfellah, 2013; Benelfellah et al., 2014; 2017; Picart et al., 2014) with the plasticity model proposed by Le et al. (2010), denoting $\underline{\underline{\underline{\underline{\mathbb{C}}}}}_d$ the damaged stiffness:

$$\underline{\underline{\sigma}} = \underline{\underline{\underline{\underline{\mathbb{C}}}}}_d : \left(\underline{\underline{\varepsilon}}_{tot} - \underline{\underline{\varepsilon}}_{pl} \right) \tag{29}$$

To describe the anisotropy of the damaged stiffness tensor, Benelfellah et al. have chosen a microplane approach (Benelfellah et al., 2014, 2017). In this model, each microplane is defined by its normal $\underline{n}$ and the elastic strains tensor is split in three components (volumetric, deviatoric and tangential) as follows (Carol and Bazant, 1997):

$$\underline{\underline{\varepsilon}}_{el} = \varepsilon_{V\,el}\, \underline{\underline{V}} + \varepsilon_{D\,el}\, \underline{\underline{D}} + \underline{\varepsilon}_{T\,el} \cdot \underline{\underline{T}} \tag{30}$$

where $\underline{\underline{V}}$, $\underline{\underline{D}}$ and $\underline{\underline{T}}$ are the tensors of projections on the microplane, expressed as a function of the second and the fourth order unit tensors and the normal vector $\underline{n}$ to the microplane:

$$\underline{\underline{V}} = \frac{1}{3}\underline{\underline{1}} \qquad \underline{\underline{D}} = \underline{n} \otimes \underline{n} - \frac{1}{3}\underline{\underline{1}} \qquad \underline{\underline{\underline{T}}} = \underline{n}\, \underline{\underline{I}} - \underline{n} \otimes \underline{n} \otimes \underline{n} \tag{31}$$

Let us note that the volumetric projection $\underline{\underline{V}}$ is not dependent on the microplane. The damaged stiffness tensor is discretized as a sum on the hemisphere of the stiffness contributions depending on the normal $\underline{n}$ to the microplane:

$$\begin{aligned} \underline{\underline{\underline{\underline{\mathbb{C}}}}}_d &= 3\, k_V\, (1 - \alpha_V\, d_V)\, \underline{\underline{V}} \otimes \underline{\underline{V}} + \\ &\sum\nolimits_{sphere}^{hemi-} 6\, \omega(\underline{n}) (\mu_D (1 - \alpha_D(\underline{n})\, d_D(\underline{n})) \underline{\underline{D}}(\underline{n}) \otimes \underline{\underline{D}}(\underline{n}) + \\ &\mu_T\, (1 - d_T(\underline{n}))\, \underline{\underline{\underline{T}}}(\underline{n})^T\, \underline{\underline{\underline{T}}}(\underline{n})) \end{aligned} \tag{32}$$

where d_V, d_D and d_T are the damage variables, α_V and $\alpha_D$the effectivity of the damage (without unit) and k_V, μ_D and μ_T elastic constants defined from the bulk modulus K and the shear modulus G. The damage variables for each direction are defined with respect to the elastic volumetric strains as follows:

$$d_{i=V,D,T} = max\left(d_i^0,\ max_t(d_i),\ 1 - exp\left(-p\,(a_3 F_i)^{a_4}\right)\right) \tag{33}$$

$$p = 1 + (a_5\, H(-\varepsilon_{V\,el}) + \widetilde{a_5} H(\varepsilon_{V\,el}))\, k_V\, \varepsilon_{V\,el} - \varepsilon_{V\,el}^{0\,H10}{}_{+} \tag{34}$$

where a_3 (MPa^{-1}), a_4, a_5 (MPa^{-1}) and $\widetilde{a_5}$ (MPa^{-1}) are material parameters. The damage function never decreases thanks to the term $max_t(d_i)$ denoting the maximal value over time of d_i. d_i^0 is the value of the "damage" of the virgin material, called pre-damage. The variable p carries the pressure-dependence (here a volume change dependence) where $\varepsilon_{V\,el}^{0\,H10}$corresponds to the volumetric strain resulting from a hydrostatic compression of 10.8 MPa. The variable F_i is the dual of damage d_i. The volumetric damage d_V depends on the volumetric strain $\varepsilon_{V\,el}$ and effectivity α_V; the deviatoric damage d_D depends on the deviatoric strain $\varepsilon_{D\,el}(\underline{n})$and effectivity α_D; the tangential damage d_T depends on the tangential strain $\underline{\varepsilon}_{T\,el}(\underline{n})$. The damage is therefore controlled by strain and pressure. The effectivity functions are defined from the Heaviside function $H(.)$ so that the partial derivative of the free energy is continuous even at zero, in respect to a good thermodynamic framework:

$$\begin{cases} \alpha_V = H(\varepsilon_{V\,el}) \\ \alpha_D(\underline{n}) = H(\varepsilon_{D\,el}(\underline{n})) + a_6 H(-\varepsilon_{D\,el}(\underline{n})) \end{cases} \tag{35}$$

where a_6 is a material parameter without unit.

The total stress tensor from equation (26) can be split as previously into a volumetric and a deviatoric part:

$$\begin{cases} \dot{\sigma}^V = 3k_V((1 - \alpha_V d_V)\dot{\varepsilon}_{V\,el} - \alpha_V\, \dot{d}_V\, \varepsilon_{V\,el})\, \underline{\underline{V}} \\ \underline{\underline{\dot{\sigma}}}^D = \sum\nolimits_{sphere}^{hemi-} 6\, \omega(\underline{n}) (\mu_D (1 - \alpha_D(\underline{n})\, d_D(\underline{n}) \dot{\varepsilon}_{D\,el}(\underline{n}) - \alpha_D(\underline{n})\, \dot{d}_D(\underline{n}) \\ \qquad \varepsilon_{D\,el}(\underline{n})) \underline{\underline{D}}(\underline{n}) + \mu_T (1 - d_T(\underline{n})\, \underline{\dot{\varepsilon}}_{T\,el}(\underline{n}) - \dot{d}_T(\underline{n})\, \underline{\varepsilon}_{T\,el}(\underline{n})) \underline{\underline{\underline{T}}}(\underline{n})) \end{cases} \tag{36}$$

The elastic moduli of the material are estimated from triaxial test under a pressure (10 MPa) which induces a collapse of the initial porosity. The k_V modulus is expressed from the bulk modulus under this pressure. The same should be true for μ_D and μ_T, but because the deviatoric effectivity α_D depends only on the deviatoric strain ε_D, the deviatoric shear modulus μ_D cannot be pressure dependent. Finally, the moduli μ_D and μ_T are worth twice the shear moduli measured from uniaxial compression test. The volumetric pre-damage is estimated from the comparison of uniaxial compressions tests (denoted *H0*) and triaxial compression tests with a 10.8 MPa confinement (*H10*): $d_V^0 = (K^{H10} - K^{H0})/K^{H10}$. Due to lack of data, pre-damages d_D^0*and* $d_T^0$are neglected. The coefficients a_3 and a_4 are fitted on the triaxial test at 10.8 MPa; a_5 is fitted on the uniaxial compression test and $\widetilde{a_5}$ on the uniaxial tension test; lastly, a_6 is calibrated from three cyclic tests.

The microplane model of Benelfellah does not yet describe viscoelasticity, so the viscosity (relaxation and recovery steps from cyclic tests) is removed from experimental data to be compared with the simulation. The evolution of the strains is well reproduced, so the induced anisotropy seems to be well described. Further work is necessary on this model for a complete validation.

Recently, Chatti and coworkers (Chatti et al., 2018) have incorporated a viscoelastic component into this model. They add a generalized Maxwell model on the V, D, T directions of each microplane. This work is still ongoing.

5.8. Discussion

A lot of tests were conducted to characterize the thermomechanical behavior of these materials. A wide range of strain rate, temperature and confinement was investigated. Many efforts focused on the (1) viscoelastic response and the determination of time-to-temperature equivalencies. Experiments showed (2) the asymmetric responses (compression versus tension); (3) induced anisotropy due to damage (and then unilateral effect) and/or plasticity (kinematic hardening for M2); (4) pressure-dependent Young's modulus probably due to predamage; (5) pressure-, strain rate- and temperature-dependence of elastic modulus and peak stresses; (6) close strain at peak stresses whatever the temperature and the strain rate for a fixed confinement (Figs. 5 and 6). Recently, digital image correlation technics have enabled measurement of the heterogeneous macroscopic field of strain at the surface of the sample. These data can be used to validate models. Let us now compare data to constitutive laws to yield some routes for future development.

The phenomena taken into account by the previous models are listed in Table 3. It must be noted that all the models, excluding VE-P and VDT-P, are calibrated for stress versus longitudinal strain curves only, for the compression and tension tests. Measuring only the longitudinal strain prevents observation of the volumetric and the deviatoric responses and a possible induced anisotropy. Historically, the experimentally observed non-linear behavior was attributed mainly to sophisticated damage rules neglecting plasticity. The "brittle material" point of view has progressively been completed by viscoelasticity to deal with temperature and strain rate dependencies. Recently, several studies have integrated a plastic mechanism as experiments reveal irreversible strains.

The guidelines for a future macroscopic "unified constitutive law" for HMX- and TATB-based pressed PBXs are now discussed. The concordance of the monotonic tests and the envelope curves of cyclic tests, regardless of the temperature, the strain rate or the type of binder (M1,

Table 3
Summary of the content of the models and materials on which the parameters have been fitted.

				SCRAM	VS	VS-VP	VE-P	VE-VP	E-VP	VDT-P
Material	PBX-9501 (HMX-based)			✓	✓					
	PBX-9502 (TATB-based)					✓			✓	
	CEA-M1 (HMX-based)						✓			✓
	CEA-M2 (TATB-based)					✓				
Model contents	Elasticity	Hooke's law	Volumetric	✓	✓	✓			✓	✓
			Deviatoric	✓					✓	✓
		Viscoelasticity	Volumetric				✓	✓		
			Deviatoric		✓	✓	✓	✓		
	Irreversibility	Viscoplasticity				✓	✓	✓	✓	✓
	/plasticity	Volumetric					✓	✓	✓	✓
		Deviatoric		✓		✓	✓	✓	✓	✓
		Isotropic hardening				✓	✓	✓		✓
		Kinematic hardening		✓				✓		
		Non-associated flow				✓	✓	✓		✓
		Pressure-dependence					✓	✓	✓	✓
	Damage	Isotropic			✓	✓	✓	✓		
		Anisotropic		✓					✓	✓
		Pressure-dependence		✓		✓	✓		✓	✓
	Temperature-dependence						✓		✓	
	Independent failure criterion						✓			✓

M2, PBX-9501), encourages the use in a reference model of so-called "serial" laws, where an irreversible mechanism (plasticity, damage, etc.) ensures the non-linearity of the response. This is the assumption made in SCRAM and its evolutions (VS, VS-VP). In the first M1 constitutive law (VE-P), the plasticity is in parallel with the viscoelasticity, which prevents the envelope curve from being well reproduced. The second model (VDT-P) combines elasticity with damage and plasticity in series.

Most of the models take into account a linear viscoelastic behavior which is experimentally validated for M1, M2 and PBX-9501 and -9502, as long as the strains remain low. This first viscous mechanism enables strain rate and temperature dependencies to be accounted for. The literature review shows that time-temperature equivalence is generally experimentally validated for PBXs. Williamson et al. (2008) have successfully compared time-temperature equivalence to ultimate stresses in compression for EDC-37. Thompson et al. (Thompson et al., 2012a, 2012b) do the same for PBX-9501, comparing the ultimate strain and the secant modulus at 25% of the peak-stress too. However, there is no real demonstration where a viscoelastic model would be compared to long duration and high temperature creep or relaxation. Furthermore, the "damage" observed on M1 and M2 at low temperature, even if it is thermally activated, prevents the application of time-temperature equivalence below 0 °C. Moreover, crossing the glass transition temperature could alter the accuracy of usual equivalence. Thus, time-temperature must be part of a future model, but attention will be paid to accurately defining its field of use. As shown in Table 3, linear viscoelasticity is embedded in VS, VS-VP, VE-P and VE-VP.

Some models consider damage as inducing additional strain (SCRAM, VS, VS-VP, VE-VP) while for others (VE-P, E-VP, and VDT-P), damage affects the (visco)elastic stiffness. However, by comparing the final equations of these models (equations ((10), (13), (19) and (24)), it is clear that these two modelling choices are the same. The damage is purely deviatoric in VS and VS-VP while it is also volumetric in VE-P and VE-VP. The bulk modulus K is affected by the damage (1-d) in VE-P and by $1 + \hat{K}/K\varphi_1 d(\overline{\varepsilon_{pl}})$ in VE-VP. The shear modulus G is affected by the damage $(1 + c^3/a^3)^{-1}$ in VS and VS-VP; by (1-d) in VE-P; and by $1 + \hat{G}/G\varphi_2 d(\overline{\varepsilon_{pl}})$ in VE-VP. In VS and its derivative VS-VP, for a constant damage ($\dot{c} = 0$), the crack length c affects the shear modulus G but also the viscous characteristic times. To our knowledge, this effect has not been experimentally demonstrated. In the VE-P, VE-VP and VDT-P models, the damage d only affects the instantaneous elastic moduli. Since M1 shows a pressure-dependence for the initial elastic properties, the authors recommend implementing damage also for the isotropic part of the constitutive law. This will enable pre-damage evolution to be tracked, as it is in the VDT-P model.

The extensive experimental study of M1 and M2 have showed that damage develops (late for M2) and that its nature is strongly anisotropic for M1. It therefore seems inevitable to incorporate induced anisotropy into future models to reproduce complex stress states and especially the effectivity of the damage seen on M1. Only SCRAM, E-VP and VDT-P described induced anisotropic damage.

The question of the damage evolution law is still open. Two regimes are distinguished (one in extension, the other in compression) in SCRAM, VS-VP and VDT-P by the Heaviside functions of the normal stress, the mean stress and the elastic volumetric strain, respectively. The variable driving damage in the models with/without anisotropic damage is either the cumulative plastic strain (VE-VP), the equivalent stress (VS) or the largest positive strain (VE-P, VDT-P). The experimental study of M1 is favorable to damage controlled by positive strain and pressure. As regards the behavior of M2, it is not possible to draw conclusions without experimental measurement of damage close to the peak stress. It should be pointed out that since the strain of pressed explosives remains low (quasi-brittle materials), the difficult problem of the rotation of anisotropy axes does not have to be treated. The effectivity of the damage, observed on M1, is treated in SCRAM, VS-VP and VDT-P. In VDT-P, the effectivity functions are related to the strain to satisfy thermomechanical considerations, but no experimental evidence justifies this. SCRAM and VS-VP generate a unilateral effect by using Heaviside functions of normal and mean stress respectively. Unfortunately, dealing with anisotropic damage prevents the characterization of the contribution of each microcracks system (each system is orientated along a plane), the recorded macroscopic damage being the consequence of all of them. As long as the unified model is to be used below maximum stress, and for moderate localization of strain, research will have to follow micromechanical model conclusions.

Cyclic tests on M1, M2 and PBX-9501 revealed irreversible strains after unloading. For some materials, the plasticity threshold appears to depend on pressure (M1, EDC-37), temperature (M1, M2 only beyond the glass transition) and strain rate (M1). The initial yield stress of M1 is pressure- and strain rate-dependent, which is not the case for M2.

Comparison between constitutive equations ((10), (13), (19) and (24) highlights that the damage affects plasticity in VS-VP and VE-P models while plasticity drives damage in VE-VP. There is no experimental data to allow any conclusions to be made. Our opinion is that for moderate loadings (low confinement and quasistatic strain rates), macroscopic loss of stiffness and irreversible strains are the

consequence of microcracks nucleation, opening/closing, growth, and relative displacement and friction of the lips of cracks. However, Vial (2013) also demonstrated that plasticity occurs in the HMX crystals of the M1 composition when they are sheared under low confinement. Microstructural post-mortem characterizations are missing, which would enable separation of the contribution of microcracks and crystal plasticity to the irreversible strains. Several routes could be followed only involving damage (see, for example, the work of Bargellini et al. (2008) for concretes), plasticity, or both, as in all the models previously presented. In the latter, the loss of stiffness is related to damage and the irreversible strain to a "plasticity" mechanism. This is the case in VDT-P, friction of microcracks being incorporated through a plastic law and an effective stress tensor.

A dilating plastic behavior has been demonstrated for M1 and is strongly suspected for M2. Yet only the VE-P, VE-VP, E-VP and VDT-P models describe a volumetric plasticity. In addition, the tests on M1 highlighted the need for a non-associated flow law, implemented in all models except SCRAM and VS.

We have also shown that a combined isotropic and kinematic hardening, not present in any model, is necessary to model at least the behavior of M2.

For the modelling of M1 (VE-P and VDT-P), failure (i.e.: maximum stress) and damage are totally dissociated. It has been experimentally demonstrated that damage depends on the loading history while failure depends only on the instantaneous stress and strain. One of the two failure criteria adopted for M1 is a function of the largest positive strain while the second takes account of the positive effective stress to describe the failure in tension states. These two failure modes have been favorably compared to multiaxial data in Picart and Pompon (2016). No failure criteria are presented in the other models.

The preceding remarks do not enable a model to be selected for this class of energetic materials, particularly when they are subjected to complex loads. Our guidelines for the development of a unified model are therefore as follows:

- The use of an additive decomposition of the strain into mechanisms rather than incorporating, for example, the plasticity as a new branch in a parallel Maxwell model (additivity of the viscous stresses).
- Because it is probably the hardest task, a mechanism for loading-induced anisotropic damage must first be taken into account. The two models SCRAM and VDT-P can serve as a basis for future development. Damage evolution could be linked to penny-shaped microcrack nucleation, growth and friction using a mean field homogenization approach. Many rules have been reported above, the difficulty being their experimental verification at the microscale. The second route, as in VDT-P, is to use a macroscopic phenomenological description of the damage (and of its effectivity). We have observed a close relation between damage evolution and the total strain tensor (positive strain for example). An isotropic pre-damage and its evolution with at least the pressure is also required.
- A linear viscoelasticity part for pressed PBXs (using a Maxwell's-like approach for example), including a time-temperature equivalence which domain of validity must be accurately defined.
- Irreversible strains description requires a (visco)plastic mechanism. Using an effective stress will help to separate the damage effect from the plasticity effect. The plastic threshold could be, for example, of the Drucker-Prager's type (pressure-dependent) but a non-associated flow rule must absolutely be proposed.
- Isotropic hardening is usually stated, but data show that a kinematic hardening rule is required to model the plastic anisotropy which could develop during complex loadings. This mechanism is an evidence for M2, while an in-depth analysis of M1 data is required.
- Multiaxial failure criteria could be separately proposed and implemented in the model to predict the ultimate loadings. These criteria must be calibrated on multiaxial tests at least, such as the one stated in section 3.10. For a pyrotechnic structure, such failures relate to the peak stresses rather than the failure stress.

Since improving models is closely related to experiments, the investigation of the possible non-linear viscoelasticity of such material is required. DMA measurements are made at low pressure. The question is to observe how the viscoelasticity evolves when the confinement, and thus the strain, increases.

Monotonic curves being the consequence of many deformation mechanisms, these data give some guidelines but are unusable for improving models. Moreover, only a few non-uniaxial experiments were done. Loadings at constant deviatoric to mean stress ratios, torsion experiments, tension under confinement, or perfect triaxial experiments (principal stresses separately loaded) would help to a better understanding of these quasi-brittle materials. Also, different loading conditions must be mixed. Tension under confinement, uniaxial compression at different temperatures and strain rates or conventional triaxial experiments at different pressures and strain rates (see Vial, 2013 for a first investigation) or temperatures could help to understand how the deformation mechanisms interact.

Finally, the study of M1 and M2 showed several surprising effects: (1) thermal damage at low temperature, different from the ratchet growth phenomenon (based on the glass transition temperature) observed on PBX-9501 and PBX-9502; (2) a non-monotonic effect of pressure on the volumetric behavior and on the elastic moduli, notably between 5 and 10 MPa; (3) a possible size effect, already observed on concrete.

6. Conclusion

Ensuring the safety and reliability of pyrotechnic structures is obviously indispensable. Nowadays this is done by numerical simulations, and the various materials which make up the pyrotechnic structure must be accurately modelled. An exhaustive state of the art of quasi-static mechanical tests provided in the literature has been proposed for pressed HMX- and TATB-based PBXs. This analysis has shown that few experimental campaigns have been carried out on these materials (except for an HMX-based material, the explosive composition M1), resulting in many assumptions about their behavior. An exhaustive characterization of CEA M2 has been provided in this paper to fill the gap on TATB-based PBXs. This material shows strain rate-, temperature- and pressure-dependence, inelastic strain and a load-induced anisotropy.

Since HMX- and TATB-based PBXs have similar macroscopic properties, a universal constitutive law is attainable for this class of materials. Although the mechanisms (elasticity, viscosity, damage, plasticity, etc.) implemented in this future law could be the same, each explosive composition would have its own set of parameters. Thus, a critical review of already proposed constitutive laws has been made. It has been shown that most of the models are poorly based on experimental facts, explaining the variety of assumptions made by their authors. Conversely, the constitutive laws proposed for M1 enables the simulation of complex loading conditions. The additivity of deformation mechanisms is justified for PBXs, as is the use of a linear viscoelastic component. A rigorous confirmation of their time-to-temperature equivalence is still needed, as is an in-depth study of the viscoelasticity linearity at high stress levels. An anisotropic damage law is advised by the authors, mainly controlled by the positive strain and the pressure, with effectivity. But how effectivity is controlled remains an open question. SCRAM or VDT-P could serve as a basis for future developments. This paper shows that kinematic hardening must be introduced in the constitutive law, and the model proposed for M1 will therefore reconsider this observation. Lastly, the described experimental database has shown unusual phenomena at low temperature or intermediate pressures, and this requires future work to understand the causes.

The development of such a model will need a lot of internal

variables, such as - at least - the elastic viscous stresses, dozens of damage variables depending on the spatial discretization of the unit sphere, and five variables per kinematic hardening mechanism. Such is the cost of yielding accurate finite element predictions of the thermo-mechanical response of these explosive compositions when subjected to complex loading paths.

Declaration of competing interest

The authors declare that they have no known competing financial interests or personal relationships that could have appeared to influence the work reported in this paper.

Acknowledgements

This work has been carried out within the framework of the research program of the Corresponding Research Laboratory (CosMa), a joint laboratory combining CEA Le Ripault and the Gabriel Lamé Mechanical laboratory.

The authors would like to thank J.L. Brigolle, T. Peyre and C. Pompon for their involvement in the experimental part of this paper, and the reviewers for their comments and suggestions.

Appendix A. Supplementary data

Supplementary data to this article can be found online at https://doi.org/10.1016/j.mechmat.2020.103561.

References

Hackett, R.M., Bennett, J.G., 2000. – an implicit finite element material model for energetic particulate composite materials. Int. J. Numer. Methods Eng. 49 (9), 1191–1209. https://doi.org/10.1002/1097-0207(20001130)49:9<1191::AID-NME997>3.0.CO;2-V.

Addessio, F.L., Johnson, J.L., 1990. – A constitutive model for the dynamic response of brittle materials. J. Appl. Phys. 67 (7), 3275–3286. https://doi.org/10.1063/1.346090.

Ambos, A., Willot, F., Jeulin, D., Trumel, H., 2015. – Numerical modeling of the thermal expansion of an energetic material. Int. J. Solid Struct. 60–61, 125–139. https://doi.org/10.1051/mattech/2015019.

Arora, H., Tarleton, E., Li-Mayer, J., Charalambides, M.N., Lewis, D., 2015. – Modelling the damage and strain process in a plastic bonded explosive microstructure under tension using the finite element method. Comput. Mater. Sci. 110, 91–101. https://doi.org/10.1016/j.commatsci.2015.08.004.

Bargellini, R., Halm, D., Dragon, A., 2008. – Modelling quasi-brittle behaviour: discrete approach coupling anisotropic damage growth and frictional sliding. Eur. J. Mech. Solid. 27 (4), 564–581.

Bazant, Z.P., Planas, J., 1997. – Fracture and Size Effect in Concrete and Other Quasi-Brittle Materials. CRC Press, New-York (USA).

Belmas, R., Reynaud, J., Sorel, J., 1982. – Simulation numérique du comportement viscoélastique non-linéaire d'un matériau explosif. Propellants, Explos. Pyrotech. 7, 8–11. https://doi.org/10.1002/prep.19820070104.

Benelfellah, A., 2013. – Contribution à la modélisation de l'anisotropie induite par endommagement d'un matériau agrégataire énergétique. *PhD thesis*. Université François Rabelais de Tours.

Benelfellah, A., Frachon, A., Gratton, M., Caliez, M., Picart, D., 2014. – Analytical and numerical comparison of discrete damage models with induced anisotropy. Eng. Fract. Mech. 121 (122), 28–39. https://doi.org/10.1016/j.engfracmech.2014.03.022.

Benelfellah, A., Frachon, A., Gratton, M., Caliez, M., Picart, D., 2017. – VDT microplane model with anisotropic effectiveness and plasticity. Mechanics & Industry 18 (607). https://doi.org/10.1051/meca/2017032.

Bennett, J.G., Haberman, K.S., Johnson, J.N., Asay, B.W., Henson, B.F., 1998. – A constitutive model of the non-shock ignition and mechanical response of high-explosives. J. Mech. Phys. Solid. 46, 2303–2322. https://doi.org/10.1016/S0022-5096(98)00011-8.

Benouniche, S., 1979. – Modélisation de l'endommagement du béton par microfissuration en compression. PhD thesis. Université de Paris VI.

Blumenthal, W.R., Gray III, G.T., Idar, D.J., Holmes, M.D., Scott, P.D., Cady, C.M., Cannon, D.D., 1999. – Influence of temperature and strain rate on the mechanical behaviour of PBX 9502 and Kel-F 800™. AIP Conference Proceedings 505, 671–674. https://doi.org/10.1063/1.1303562.

Bodner, S.R., 1987. – Review of a Unified Elastic—Viscoplastic Theory. *Unified Constitutive Equations For Creep And Plasticity*. Springer Dorddrecht https://doi.org/10.1007/978-94-009-3439-9_6.

Browning, R.V., Gurtin, E.M., Williams, W.O., 1984. – A one-dimensional viscoplastic constitutive theory of filled polymers. Int. J. Solid Struct. 20 (11/12), 921–934. https://doi.org/10.1016/0020-7683(84)90081-7.

Buechler, M.A., 2012a. – Observed Physical Processes in Mechanical Tests of PBX 9501 and Recommendations for Experiments to Explore a Possible Plasticity/damage Threshold. Los Alamos National Laboratory report n° LA-UR-12-21072.

Buechler, M.A., 2012b. – Viscoelastic-Viscoplastic Combined Hardening Constitutive Model Based on the Drucker-Prager Yield and Flow Potentials. Los Alamos National Laboratory report n° LA-UR-12-24895.

Buechler, M.A., 2013. – Viscoelastic-Viscoplastic Damage Model Development, Parameters Estimation, and Comparison to PBX9501 Experimental Data. Los Alamos National Laboratory, report n° LA-UR-13-DRAFT.

Buechler, M.A., Luscher, D.J., 2014. – A semi-implicit integration scheme for a combined viscoelastic-damage model of plastic bonded explosives. Int. J. Numer. Methods Eng. 99, 54–78. https://doi.org/10.1002/nme.4672.

Buechler, M.A., DeLuca, R., Thompson, D.G., 2013. – Review of Cyclic Experiments Performed on PBX9501. Los Alamos National Laboratory report n° LA-UR-13-27212.

Caliez, M., Gratton, M., Frachon, A., Benelfellah, A., Picart, D., 2014. – Viscoelastic plastic model and experimental validation for a granular energetic material. Int. J. Energ. Mater. Chem. Propuls. 13, 525–537. https://doi.org/10.1016/j.engfracmech.2014.09.009.

Cambou, B., Lanier, J., 1988. – Induced anisotropy in cohesionless soil: experiments and modelling. Comput. Geotech. 6, 291–311. https://doi.org/10.1016/0266-352X(88)90071-7.

Carol, I., Bazant, Z.P., 1997. – Damaged and plasticity in microplane theory. Int. J. Solid Struct. 34 (29). https://doi.org/10.1016/S0020-7683(96)00238-7.

Chatti, M., 2018. – Etude expérimentale et modélisation du comportement mécanique d'un matériau agrégataire. PhD thesis. https://tel.archives-ouvertes.fr/tel-02415344.

Chatti, M., Frachon, A., Gratton, M., Caliez, M., Picart, D., Aït Hocine, N., 2018. – Modelling of the viscoelastic behaviour with damage induced anisotropy of plastic-bonded explosive based on the microplane approach. Int. J. Solid Struct. 168, 13–25. https://doi.org/10.1016/j.ijsolstr.2018.08.018.

Chen, P.W., Huang, F.L., Ding, Y.S., 2007. – Microstructure, strain and failure of polymer bonded explosives. J. Mater. Sci. 42, 5272–5280. https://doi.org/10.1007/s10853-006-0387-y.

Clements, B.E., Mas, E.M., 2004. – A theory for plastic-bonded materials with a bimodal size distribution of filler particles. Model. Simulat. Mater. Sci. Eng. 12, 407–421. https://doi.org/10.1088/0965-0393/12/3/004.

Cunningham, B.J., Gagliardi, F.J., Ferranti, L., 2013. – Low strain rate measurements on explosives using DIC. Application of Imaging Techniques to Mechanics of Materials and Structures, vol. 4. Springer, New York, NY, pp. 25–31. https://doi.org/10.1007/978-1-4419-9796-8_5.

Dienes, J.K., 1978. – A Statistical Theory of Fragmentation. 19th US Rock Mechanics Symposium. American Rock Mechanics Association.

Dienes, J.K., 1996. – A Unified Theory of Flow, Hot-Spots, and Fragmentation with an Application to Explosive Sensitivity. High Pressure Shock Compression of Solids II. Springer, New York, NY, pp. 366–398. https://doi.org/10.1007/978-1-4612-2320-7_14.

Dienes, J.K., Zuo, Q.H., Kershner, J.D., 2006. – Impact initiation of explosives and propellants via statistical cracks mechanics. J. Mech. Phys. Solid. 54, 1237–1275. https://doi.org/10.1016/j.jmps.2005.12.001.

Ellis, K., Leppard, C., Radesk, H., 2005. – Mechanical properties and damage evaluation of UK PBX. J. Mater. Sci. 40 (23), 6241–6248. https://doi.org/10.1007/s10853-005-3148-4.

Funk, D.J., Laabs, G.W., Peterson, P.D., Asay, B.W., 1996. – Measurements of the stress/strain response of energetic materials as a function of strain rate and temperature: PBX 9501 and Mock 9501. AIP Conference Proceedings 370, 145–148. https://doi.org/10.1063/1.50735.

Gagliardi, F.J., Cunningham, B.J., 2007. – Creep Testing Plastic-Bonded Explosives in Uni-Axial Compression. *Society for Experimental Mechanics 11th International Congress*, Orlando (USA) 02-05, 6, 2007.

Gagliardi, F.J., Cunningham, B.J., 2009. – Axial Torsion Testing of Plastic Bonded Explosives to Failure. Society for Experimental Mechanics Annual Conference, Albuquerque (USA) 01-04, 6, 2009.

Gasnier, J.B., Willot, F., Trumel, H., Jeulin, D., Biessy, M., 2018. – Thermoelastic properties of microcracked polycrystals. Part II: the case of jointed polycrystalline TATB. Int. J. Solid Struct. 155, 257–274. https://doi.org/10.1016/j.ijsolstr.2018.07.025.

Gotuwka, V., 1999. – Etude expérimentale du comportement mécanique des Bétons à Très Hautes Performances sous sollicitations multiaxiales simples et complexes. PhD thesis. Université de Lille I.

Gratton, M., Gontier, C., Rja Fi Allah, S., Bouchou, A., Picart, D., 2009. – Mechanical characterisation of a viscoplastic material sensitive to hydrostatic pressure. Eur. J. Mech. Solid. 28 (5), 935–947. https://doi.org/10.1016/j.euromechsol.2009.03.002.

Gray III, G.T., Idar, D.J., Blumenthal, W.R., Cady, C.M., Peterson, P.D., 1998. – High- and low-strain rate compression properties of several energetic material composites as a function of strain rate and temperature. *11th Detonation Symposium*, Snowmass (USA), August 31. , Accessed date: 4 September 1998.

Idar, D.J., Larson, S.A., Skidmore, C.B., Wendelnerger, J.R., 2000. – PBX 9502 Tension Analysis. 23rd Aging, Compatibility, and Stockpile Stewardship Conference, Livermore (USA). 14-16, 11, 2000.

Lanier, J., Di Prisco, C., Nova, R., 1991. – Etude expérimentale et analyse théorique de l'anisotropie induite du sable d'Hostun. Rev. Fr. Geotech. 57, 59–74. https://doi.org/10.1051/geotech/1991057059.

Le, V.D., 2007. – Modélisation et identification du comportement plastique visco-élastique endommageable d'un matériau. *PhD thesis*. Université François Rabelais de Tours.

Le, V.D., Gratton, M., Caliez, M., Frachon, A., Picart, D., 2010. – Experimental mechanical

characterization of plastic-bonded explosives. J. Mater. Sci. 45 (21), 5802–5813. https://doi.org/10.1007/s10853-010-4655-5.
Liu, C., Thompson, D.G., 2010. – Macroscopic Crack Formation and Extension in Pristine and Artificially Aged PBX 9501. *14th International Detonation Symposium.* Coeur d'Alene (USA) 11-16, 2010, 4.
Liu, C., Thompson, D.G., 2014. – Crack initiation and growth in PBX 9502 high explosive subject to compression. J. Appl. Mech. 81 (10), 101004. https://doi.org/10.1115/1.4028087.
Liu, M., Huang, X.C., Wu, Y.Q., Chen, C.J., Huang, F.L., 2019. – Numerical simulations of the damage evolution for plastic-bonded explosives submitted to complex stress states. Mech. Mater. 139, 103179. https://doi.org/10.1016/j.mechmat.2019.103179.
Mazars, J., Berthaud, Y., Ramtani, S., 1990. – the unilateral behaviour of damaged concrete. Eng. Fract. Mech. 35 (4–5), 629–635. https://doi.org/10.1016/0013-7944(90)90145-7.
Peeters, R.L., Hackett, R.M., 1981. – Constitutive modeling of plastic-bonded explosives. Exp. Mech. 21 (3), 111–116. https://doi.org/10.1007/BF02326367.
Picart, D., 1993. – Comportement et mise en forme d'un explosive agrégataire. PhD thesis. https://www.theses.fr/1993DENS0007.
Picart, D., Brigolle, J.L., 2010. – Characterization of the viscoelastic behaviour of a plastic-bonded explosive. Mater. Sci. Eng. 527 (29–30), 7826–7831. https://doi.org/10.1016/j.msea.2010.08.057.
Picart, D., Pompon, C., 2016. – Experimental characterization of the multiaxial failure of a plastic-bonbed explosive. Int. J. Energ. Mater. Chem. Propuls. 15 (2), 141–165. https://doi.org/10.1615/IntJEnergeticMaterialsChemProp.2016013662.
Picart, D., Benelfellah, A., Brigolle, J.L., Frachon, A., Gratton, M., Caliez, M., 2014. – Characterization and modeling of the anisotropic damage of a high-explosive composition. Eng. Fract. Mech. 131, 525–537. https://doi.org/10.1016/j.engfracmech.2014.09.009.
Rae, P.J., Goldrein, H.T., Palmer, S.J.P., Field, J.E., Lewis, A.L., 2002. – Quasi-static studies of the strain and failure of β-HMX based polymer bonded explosives. Proceedings of the Royal Society of London. Serie A: Mathematical, Physical and Engineering Sciences 458, 743–762. https://doi.org/10.1098/rspa.2001.0894. 2019.
Rangaswamy, P., Thompson, D.G., Liu, C., Lewis, M.W., 2010. – Modeling the Mechanical Response of PBX 9501. *14th International Detonation Symposium.* Coeur d'Alene (USA) 11-16, 4, 2010.
RjaFiAllah, S., 2006. – Modélisation du comportement mécanique d'un matériau agrégataire. *PhD thesis.* Université François Rabelais de Tours.
Schwarz, R.B., Brown, G.W., Thompson, D.G., Olinger, B.W., Furmanski, J., Cady, H.H., 2013. – the effect of shear strain on texture in pressed plastic bonded explosives. Propellants, Explos. Pyrotech. 38, 685–694. https://doi.org/10.1002/prep.201200204.
Shunk, D., 2013. – PBX 9502 Literature Review: an Engineering Perspective. Los Alamos National Laboratory report n° LA-UR-13-21673.
Skidmore, C.B., Idar, D.J., Son, S.F., Sander, R.K., 1998. – ageing and PBX 9502. Conference on life cycles of energetic material, fullerton (USA). March 29 – April 1, 1998.
Tan, H., Liu, C., Huang, Y., Geubelle, P.H., 2005. – the cohesive law for the particle/matrix interfaces in high explosives. J. Mech. Phys. Solid. 53 (8), 1892–1917. https://doi.org/10.1016/j.jmps.2005.01.009.
Tan, H., Huang, Y., Liu, C., Ravichandran, G., Inglis, H.M., Geubelle, P.H., 2007. – the uniaxial tension of particulate composite materials with nonlinear interface debonding. Int. J. Solid Struct. 44 (6), 1809–1822. https://doi.org/10.1016/j.ijsolstr.2006.09.004.
Thompson, D.G., 2002. – Results of PBX 9501 and PBX 9502 round-robin quasi-static tension tests from JOWOG-9/39 focused exchange. *24th Aging, Compatibility, and Stockpile Stewardship Conference And Proceedings, BWXT Pantex, Amarillo (USA).* April 30 – May 2, *2002*.
Thompson, D.G., Wright, W.J., 2004. – Mechanical Properties from PBX 9501 pressing study. AIP Conference Proceedings 706, 503 https://doi.org/10.1063/1.1780287.
Thompson, D.G., Brown, G.W., Olinger, B., Mang, J.T., Patterson, B., DeLuca, R., Hagelberg, S., 2010. – the effects of TATB ratchet growth on PBX 9502. Propellants, Explos. Pyrotech. 3 (6), 507–513. https://doi.org/10.1002/prep.200900067.
Thompson, D.G., DeLuca, R., Brown, G.W., 2012a. – Time-temperature analysis, tension and compression in PBXs. J. Energetic Mater. 30 (4), 299–323. https://doi.org/10.1080/07370652.2011.569831.
Thompson, D.G., DeLuca, R., Brown, G.W., Sandstrom, M.M., Hagelberg, S., Giambra, A.M., Hill, L.G., 2012b. – Ratchet growth experiments on TATB and PBX 9502. AIP Conference Proceedings 1426 (1), 745–748. https://doi.org/10.1063/1.3686386.
Vial, J., 2013. – Etude expérimentale et numérique des modes de déformation d'un explosif comprimé. *PhD thesis.* Université d'Orléans.
Wiegand, D.A., Redingus, B., Ellis, K., Leppard, C., 2011. – Pressure and friction dependent mechanical strength-cracks and plastic flow. Int. J. Solid Struct. 48 (11–12), 1617–1629. https://doi.org/10.1016/j.ijsolstr.2011.01.025.
Williamson, D.M., Palmer, S.J.P., Proud, W.G., Govier, R., 2007. – Brazilian disc testing of a UK PBX above and below the glass transition temperature. AIP Conference Proceedings 955 (1), 803–806. https://doi.org/10.1063/1.2833246.
Williamson, D.M., Siviour, C.R., Proud, W.G., Palmer, S.J., Govier, R., Ellis, K., Blackwell, P., Leppard, C., 2008. – Temperature-time response of a polymer bonded explosive in compression (EDC-37). J. Phys. Appl. Phys. 41 https://doi.org/10.1088/0022-3727/41/8/085404. 085404.
Wu, Y.Q., Huang, F.L., 2009. – A micromechanical model for predicting combined damage of particles and interface debonding in PBX explosives. Mech. Mater. 41 (1), 27–47. https://doi.org/10.1016/j.mechmat.2008.07.005.
Zubelewicz, A., Thompson, D.G., Ostoja-Starzewski, M., Ionita, A., Shunk, D., Lewis, M.W., Lawson, J.C., Kale, S., Koric, S., 2013. – Fracture model for cemented aggregates. AIP Adv. 3 (1). https://doi.org/10.1063/1.4789791. 012119.

5 ANNEXE B

International Journal of Energetic Materials and Chemical Propulsion, 20(2):87–108 (2021)

EXPERIMENTAL INVESTIGATION OF MULTIAXIAL FAILURE AND IDENTIFICATION OF FAILURE CRITERIA FOR A PBX SIMULANT MATERIAL

Marwen Chatti,[1,*] Arnaud Frachon,[1] Michel Gratton,[1] Michael Caliez,[1] Florian Lacroix,[2] Didier Picart,[3] & Nourredine Aït Hocine[1]

[1]*INSA CVL, LaMé, 3 rue de la Chocolaterie, 41000 Blois, France*
[2]*Université de Tours, LaMé, 7 avenue Marcel Dassault, 37200 Tours, France*
[3]*CEA DAM Le Ripault, F-37260 Monts, France*

*Address all correspondence to: Marwen Chatti, INSA CVL, LaMé, 3 rue de la Chocolaterie, 41000 Blois, France, E-mail: chatti.marwen@hotmail.fr

Original Manuscript Submitted: 1/17/2021; Final Draft Received: 3/23/2021

This paper presents an original experimental study and modeling of the failure under multiaxial loading of a simulant material for plastic-bonded explosives. Measurements were obtained using tension, compression, torsion, channel-die, and triaxial compression tests. The experimental results were plotted, and the failure characteristics of the studied material were analyzed and discussed. Also, microstructural observations were carried out to highlight the initial state of the material and the different damage and failure mechanisms of the material. Two failure criteria from the literature and initially developed for concrete were selected and identified using the obtained experimental data. These criteria show a significant potential to predict the multiaxial failure of energetic materials. A numerical study is conducted at the end to determine the sensitivity of the experimental parameters.

KEY WORDS: *simulant material, plastic-bonded explosives, experimental tests, damage, failure criteria, sensitivity study*

1. INTRODUCTION

Pyrotechnic structures made of plastic-bonded explosives (PBXs) are commonly subjected to quasi-static loading during storage and transportation, which can induce high stress levels that can affect the material behavior. The feared consequences are (1) the ignition of the explosive due to a local hot-spot released by friction, and (2) the reactive decomposition (combustion or deflagration) influenced by the permeation of hot gas into the damaged material and the microcrack network (Picart and Pompon, 2016). To accurately identify a failure envelope of such a material, a thorough experimental investigation is required. The failure envelope delimits the safe zone of the material and corresponds to the threshold load levels beyond which the failure occurs. The considered PBX is an HMX (octahydro-1,3,5,7-tetranitro-1,3,5,7-tetrazocine)-based energetic material. Its microstructure is composed of more than 95 wt% of HMX energetic crystals mixed with a low percentage of a polymer binder. The mixture is pressed using an isostatic compaction

2150–766X/21/$35.00

process, which reduces the porosity of the material but generates many inter- and intragranular microcracks due to the high volume fraction of the solid phase (Le et al., 2010; Picart et al., 2014). The energetic material presents a nonlinear behavior, regardless of the loading conditions, with an asymmetry between tension and compression. Tension tests show a quasi-brittle behavior, unlike compression and triaxial tests that exhibit more ductile behaviors. The strain rate, temperature, and hydrostatic pressure dependencies are also observed (Le et al., 2010; Caliez et al., 2014; Chatti et al., 2019). Moreover, the material shows damage-induced anisotropy with unilateral effects caused by the opening and closing of microcracks (Benelfellah et al., 2014). The behaviors described above are similar to those of concrete materials (Wong et al., 2007; Chambart, 2009; Burlion, 2010; Kupfer and Gerstle, 1973; Kupfer et al., 1969; Lee et al., 2004). Furthermore, similar to concrete, PBX materials have a quasi-compact granular microstructure (Burlion, 2010; Le et al., 2010). Many experimental works have been published about different types of PBX materials (PBX9501, PBX9502, EDC37, or LX-14) subjected to quasi-static loading (Liu et al., 2009; Yeom et al., 2012; Zhou et al., 2011; Park et al., 2013; Bailly et al., 2011; Belmas, 1994; Idar et al., 1998; Ellis et al., 2005; Williamson et al., 2008; Le et al., 2010; Picart et al., 2014; Peeters, 1982). In particular, a recent work by Picart and Pompon (2016) reported on an experimental characterization of the multiaxial failure of a PBX based on uniaxial tension, uniaxial compression, biaxial tension, three-point bend, shear, diametric compression, channel die, and triaxial compression tests. These experiments were carried out at a quasi-static strain rate of 3.5×10^{-5} s^{-1} and ambient temperature. Strains were measured using a digital image correlation method. This study led to the addition of new points to the failure surface of PBX, such as shear and three-point bend, but data is still missing, especially in the compression-compression quadrant. An interesting work published by Gagliardi and Cunningham (2009) presented combined torsion-compression tests on another HMX-based material, LX-14. A thick hollow cylinder was mounted between two platens, and different combinations of axial force and torque were applied to the samples at a constant angular velocity of $0.08° s^{-1}$ (shear strain rate of 10^{-3} s^{-1}). Unfortunately, these tests were not instrumented. Nevertheless, new interesting points were added to the tension-compression quadrant of the failure envelope.

Although some experimental studies have been published on PBX materials, data is still missing to obtain a complete failure surface allowing the identification of failure criteria. It should be noted that conducting tests on PBXs is quite difficult, expensive, and subjected to several restrictions. Therefore, in this study, an inert simulant material obtained and recommended from the French Atomic Energy and Alternative Energies Commission (CEA) is used for experimental investigation. This simulant material is representative of the studied energetic material in terms of crystals weight fraction and shapes and sizes, and it presents the same behavioral aspects as the PBX. It should be noted that other simulants exist and have been used for different compositions of PBXs (Yeager et al., 2018; Liu et al., 2020).

In this work, tension, compression, torsion, channel die, and triaxial compression tests were performed. The obtained experimental results were discussed, and the failure characteristics of the simulant were highlighted. Also, microstructural observations were carried out to highlight, first, the initial state of the material microstructure and then the different damage and failure mechanisms between tension and compression.

Regarding the failure criteria of PBXs, studies in the literature are scarce. Only a few models have been developed, and the existing ones lack accuracy.

A failure criterion that separately takes into account compressive and tensile behaviors of the material by two uncoupled equations was proposed by Caliez et al. (2014). This criterion lacks accuracy, especially in compression-compression stress states.

Stevens (2014) proposed a strength model and a service envelope for PBX9501 based on the Mohr-Coulomb criterion. The proposed model is still insufficient to predict the failure of the material because of its linear evolution in the biaxial stress state plane.

Several explosive materials have been studied under uniaxial compression, over wide ranges of temperature, strain rate, and hydrostatic pressure (Wiegand, 2003; Wiegand et al., 2011; Williamson et al., 2008). As an outcome, a constant strain-based criterion and an empirical relationship among strength, pressure, and strain rate were proposed.

Finally, Thompson et al. (2012) applied the time-temperature principle to a wide range of mechanical properties data for two highly filled polymer composites, PBX9501 and PBX9502. This study included the values of ultimate stress and ultimate strain from quasi-static data determined using time-temperature superposition.

Despite the behavioral analogy between PBXs and concrete materials, and the extensive literature on concrete failure criteria, no authors have studied its potential when applied to energetic materials, except recently for Picart and Pompon (2016) who used the Kupfer-Gerstle stress-based criterion (Kupfer and Gerstle, 1973) defined in a biaxial compression stress state.

Therefore, in the present study, two criteria, initially developed for concrete, were selected and used to predict the failure envelopes of the studied simulant material.

The experimental investigation is presented first, as well as the studied material and the experimental protocols and dispositives. Then, the selected criteria are detailed, and their parameters are identified using two methods. The results are analyzed and discussed.

Finally, a sensitivity study on the experimental parameters was performed in order to improve the accuracy of experimental investigations.

2. CONCRETE FAILURE CRITERIA

2.1 Literature Review

On the basis of experimental results published in the literature, the following characteristics should be considered with respect to concrete failure criteria (Chen, 1982; Muthukumar and Kumar, 2014): (1) the failure surface should be convex and should contain smooth edges, (2) the cross section in the deviatoric plane changes from triangular to circular, with the increase in confinement, and (3) compressive and tensile meridians should be parabolic. A minimum of three types of tests, namely uniaxial compression, uniaxial tension, and biaxial compression, are required to predict with accuracy the concrete failure envelopes. Many three-parameter models were proposed in the literature, such as the Brestler and Pister (1958), Li and Harmon (1990), and Menetrey and Willam (1995) models. To account for the hydrostatic pressure sensitivity under compression, extensive investigations led to the representation of a concrete failure surface with four-parameter models, such as the Ottosen (1977) and Hsieh-Ting-Chen (Hsieh et al., 1982) models. Adding the hydrostatic pressure sensitivity under tension, Willam and Warnke (1975) proposed a five-parameter model, providing a more accurate prediction of the concrete failure. According to the literature review (Chen, 1982; Burlion, 2010; Muthukumar and Kumar, 2014), the three-parameter Menetrey–Willam model (Menetrey and Willam, 1995), the four-parameter Ottosen model (Ottosen, 1977), and the five-parameter Willam-Warnke model (Willam and Warnke, 1975) seem to have all the credentials to be used as failure criteria for concrete.

Because energetic materials behave like concrete, we might expect that these three models would be able to predict the failure surface of PBXs. Since the Willam-Warnke model requires

a confined tension test to be identified, only the Ottosen and Menetrey–Willam models were selected to be applied for the simulant material studied in this work.

2.1.1 Menetrey–Willam Criterion

Menetrey and Willam (1995) presented a three-parameter failure criterion defined in terms of three independent stress invariants. The uniaxial compression, uniaxial tension, and equibiaxial compression lead to direct parameter identification. For a geometric interpretation, the Haigh–Westergard coordinates—that is, hydrostatic stress invariant ξ [Eq. (1)], deviatoric stress invariant ρ [Eq. (2)], and deviatoric polar angle θ [Eq. (3)]—are used:

$$\xi = \frac{I_1}{\sqrt{3}} \tag{1}$$

$$\rho = \sqrt{2J_2} \tag{2}$$

$$\cos(3\theta) = \frac{3\sqrt{3}}{2}\frac{J_3}{\sqrt{J_2^3}} \tag{3}$$

with the invariants $I_1 = \mathrm{Tr}\left(\underline{\underline{\sigma}}\right)$, $J_2 = 1/2\left(s_1^2 + s_2^2 + s_3^2\right)$, and $J_3 = 1/3\left(s_1^3 + s_2^3 + s_3^3\right)$, in terms of the stress $\underline{\underline{\sigma}}$ and the deviatoric stress $\underline{\underline{s}} = \underline{\underline{\sigma}} - I_1/3\underline{\underline{I}}$.

The Haigh–Westergard coordinates span a cylindrical coordinate system of the stress space, in which the circular trace of the deviatoric polar radius $\rho(\theta)$ is transformed into a triple-symmetric ellipse through the elliptic function $r(\theta, e)$ [Eq. (4)] (Chen, 1982):

$$r(\theta, e) = \frac{4(1-e^2)\cos(\theta)^2 + (2e-1)^2}{2(1-e^2)\cos(\theta) + (2e-1)\left[4(1-e^2)\cos(\theta)^2 + 5e^2 - 4e\right]^{1/2}} \tag{4}$$

The eccentricity e describes the deviation from circularity of the deviatoric trace. The convexity and smoothness of the elliptic function requires that $0.5 \leq e \leq 1$. The value of the parameter e strongly affects the failure surface in the biaxial compressive zone.

The Menetrey–Willam failure (Menetrey and Willam, 1995) criterion is expressed as follows:

$$F(\xi, \rho, \theta) = \left[A_f \rho\right]^2 + m\left[B_f \rho r(\theta, e) + C_f \xi\right] - c = 0 \tag{5}$$

where c and m are measures of the cohesive and frictional strengths, respectively. A_f, B_f, and C_f are criterion parameters.

2.1.2 Ottosen Criterion

Ottosen proposed one of the most used failure criterion, with four independent material parameters (Ottosen, 1977). The criterion is expressed in terms of stress invariants:

$$F(I_1, J_2, \theta) = A\frac{J_2}{\sigma_{uc}^2} + \lambda\frac{\sqrt{J_2}}{\sigma_{uc}} + B\frac{I_1}{\sigma_{uc}} - 1 = 0 \tag{6}$$

In terms of ρ and ξ, Eq. (6) is given in a dimensionless form:

$$F(\xi, \rho, \theta) = \left(\sqrt{\frac{A}{2\sigma_{uc}^2}}\rho\right)^2 + \lambda(\theta)\frac{1}{\sqrt{2}\,\sigma_{uc}}\rho + \frac{B\sqrt{2}}{\sigma_{uc}}\xi - 1 = 0 \tag{7}$$

where A and B are material parameters, σ_{uc} is the uniaxial compressive strength, and λ is a function of $\cos(3\theta)$. The function λ is represented in the following form:

$$\lambda(\theta) = k_1 \cos\left\{\frac{1}{3}\cos\left[k_2\cos(3\theta)\right]^{-1}\right\}, \quad \text{for } \cos(3\theta) \geq 0 \tag{8}$$

$$\lambda(\theta) = k_1 \cos\left\{\frac{\pi}{3} - \frac{1}{3}\cos\left[k_2\cos(3\theta)\right]^{-1}\right\}, \quad \text{for } \cos(3\theta) \leq 0 \tag{9}$$

In previous equations, k_1 is a size factor and k_2 is a shape factor ($0 \leq k_2 \leq 1$). $\lambda_c = \lambda\ (3\theta = \pi)$ and $\lambda_t = \lambda\ (3\theta = 0)$ correspond, respectively, to the compressive and tensile meridians.

2.2 Identification of Failure Criteria Parameters

The failure criteria parameters can be identified according to the formulas in the literature or by an optimization fitting using all the data of the simulant. Both methods are presented and discussed.

2.2.1 Direct Identification of Failure Criteria

2.2.1.1 Menetrey–Willam Criterion

The cohesion and friction parameters are expressed in the following equations in terms of the uniaxial strengths under compression σ_{uc} and tension σ_{ut} (Menetrey and Willam, 1995):

$$m(e) = 3\frac{\sigma_{uc}^2 - \sigma_{ut}^2}{\sigma_{uc}\sigma_{ut}}\frac{e}{e+1} \tag{10}$$

$$c = 1 \tag{11}$$

A_f, B_f, and C_f are criterion parameters. These parameters are determined using the uniaxial compressive strength σ_{uc} as follows (Menetrey and Willam, 1995):

$$A_f = \frac{\sqrt{3/2}}{\sigma_{uc}} \tag{12}$$

$$B_f = \frac{1}{\sqrt{6}\,\sigma_{uc}} \tag{13}$$

$$C_f = \frac{1}{\sqrt{3}\,\sigma_{uc}} \tag{14}$$

Using the Haigh–Westergard coordinates, the Menetrey–Willam criterion [Eq. (5)] can be written as follows:

$$F(\xi, \rho, \theta) = \left[\frac{\sqrt{3/2}}{\sigma_{uc}}\rho\right]^2 + \frac{\sigma_{uc}^2 - \sigma_{ut}^2}{\sigma_{uc}\sigma_{ut}}\frac{e}{e+1}\left[\frac{r(\theta, e)}{\sqrt{2}}\rho + \xi\right] - 1 = 0 \tag{15}$$

There are three input data (σ_{ut}, σ_{uc}, e) to calculate four parameters (A_f, B_f, C_f). In particular, A_f, B_f, and C_f are coupled.

The Menetrey–Willam criterion requires tensile strength, compressive strength, and equibiaxial compressive strength to be calibrated [Eqs. (4), (10–14)]. The eccentricity was adjusted using the biaxial compression test, with $\sigma_T = \sigma_L$.

2.2.1.2 Ottosen Criterion

To determine the four parameters A, B, k_1, and k_2, the following failure stress states are commonly used: uniaxial tensile strength σ_{ut}, uniaxial compressive strength σ_{uc}, biaxial compressive strength σ_{bc}, and an arbitrary failure state, $(x, y) = \left(I_1, \sqrt{J_2}\right)$, along the compressive meridian. The Ottosen criterion parameters are identified using the following equations (Ottosen and Ristinmaa, 2005):

$$\kappa = \frac{x + y\sqrt{3}}{y - \sigma_{uc}/\sqrt{3}} \tag{16}$$

$$B = \frac{(3\sigma_{uc}y)/(\sigma_{bc}\sigma_t) - \sqrt{3}}{\kappa + 9y/(\sigma_{bc} - \sigma_{ut})} \tag{17}$$

$$A = -\frac{\sigma_c}{y}\left(\kappa B + \sqrt{3}\right) \tag{18}$$

$$\begin{cases} \lambda_t = \sqrt{3}\left[\dfrac{\sigma_{uc}}{\sigma_{bc}} + 2B - \dfrac{\sigma_{bc}}{3\sigma_{uc}}A\right] \\ \lambda_c = \sqrt{3}\left[1 + B - \dfrac{A}{3}\right] \end{cases} \tag{19}$$

$$k_1 = \frac{2}{\sqrt{3}}\sqrt{\lambda_t^2 + \lambda_c^2 - \lambda_t\lambda_c} \tag{20}$$

$$k_2 = 4\left(\frac{\lambda_t}{k_1}\right)^3 - 3\frac{\lambda_t}{k_1} \tag{21}$$

Note that there are five input data (σ_{ut}, σ_{uc}, σ_{bc}, x, y) to calculate four parameters (A, B, k_1, and k_2).

In addition to the three tests used for the Menetrey–Willam criterion, the Ottosen criterion requires an arbitrary failure state along the compressive meridian to determine the four parameters [Eqs. (16)–(21)]. In this work, the triaxial compression point at 10 MPa is used.

2.2.2 Identification of Failure Criteria by Optimization Fitting

To determine the coefficients of the two criteria, we use all available experimental data: tension, compression, hydrostatic compression, biaxial compression, and torsion. To fit the parameters as well as possible, we take into account the similarities and differences between tests. We minimize the following function:

$$\mathcal{F}(X_i) = \sum_j \frac{\rho_{\max}}{\rho_j}\left[F_{Xi}(Y_j)\right]^2, \tag{22}$$

where X_i are the parameters to be identified, Y_j are the experimental failure stress states, and $\rho_{\max} = \max\left[\rho(Y_j)\right]$ is fitted with the triaxial compression at 10 MPa. The subscript j refers to the jth path loading. This coefficient $\rho_{\max}/\rho_j$ highlights the same stress level as the tensile and torsion tests. As it seems to be singular and we do not yet have explanations for it, the triaxial compression of 5 MPa is not taken into account in Eq. (22). Moreover, to increase the freedom of the Menetrey–Willam criterion, we unlink the C_f parameter from the others. The method used to minimize the function is a conjugated gradient.

3. EXPERIMENTAL INVESTIGATION

3.1 Material

The simulant material is an aggregate composite constituted by inert crystals and a small amount of plastic binder. The crystal fraction of the material is composed of 29.3 wt% of barium meal ($BaSO_4$) and 65.2 wt% of melamine. The binder accounts for 5.5 wt% of the simulant, and it is made of an epoxy resin and a blue pigment. The material is manufactured by hot hydrostatic press molding. The manufacturing process induces a predamage in the simulant, as seen in PBX materials. The resulting material has a residual porosity of 28%. The same simulant was used also by Bailly et al. (2011). The morphology and mechanical properties of this simulant are similar to those of PBX, and both materials exhibit the same behavior (Le et al., 2010; Picart and Brigolle, 2010; Bailly et al., 2011; Caliez et al., 2014; Liu et al., 2009; Yeom et al., 2012; Zhou et al., 2011; Park et al., 2013).

3.2 Experiments

In this section, tension, compression, biaxial, and triaxial compression experimental protocols are presented first. As the viscous behavior of the material is not investigated in this study, monotonic and cyclic tests are conducted, at an imposed strain rate of 2×10^{-5} s^{-1}, using a tension-compression electromechanical testing (MTS) machine. Specimens were machined with a 0.05 mm tolerance with special attention to the parallelism of the faces.

Strains are measured with general-purpose 90° tee rosettes, glued in the middle of the specimens, on opposite sides (two longitudinal gauges, L_1 and L_2, and two transversal gauges, T_1 and T_2). One longitudinal gauge is connected directly to the MTS machine to drive the test.

In the triaxial compression tests, three general-purpose 90° tee rosettes, glued in the middle of the specimen and spaced by 120°, are used.

In the cyclic tests, each cycle consists of four steps: loading, relaxation, unloading until zero force, and finally, recovery by maintaining the zero force. The first three steps are driven by the strain measured by the gauge L_1, whereas the final step is force-controlled by the load cell. Previous studies (Le et al., 2010; Caliez et al., 2014) showed that experimental stress–strain curves of cyclic tests are embedded below the corresponding $\sigma(\varepsilon)$ experimental curves of monotonic tests, and that both configurations present almost the same failure points, as observed in concrete materials (Burlion, 2010). The cyclic tests are developed and conducted mainly to study the mechanical behavior and the evolution of the material properties over the loading, but only failure characteristics are the focus in this work.

Microstructure observations were carried out on the pristine material and also on the failure surfaces for each test. A scanning electron microscope (SEM) was used. The SEM is equipped with a backscattered electron detector, sensitive to the number of atoms in the sample constituents, and a secondary electron detector, sensitive to variations in the surface of the sample.

3.2.1 Tension and Compression Experiments

Dog-bone-shaped specimens are used for the uniaxial tension tests, with a cross section of 9×10 mm^2 and a total length of 150 mm. A particular gripping fixture, on which the specimen is glued, is designed to ensure that the loading is homogeneous during the test. Tensile tests are particularly difficult to achieve on the studied material because of its quasi-brittle behavior. In the compression tests, cylindrical specimens with a diameter of 10 mm and a height of 20 mm

are used. The specimen is pressed between two compression platens with a head alignment and with the intermediate of cartons with a diameter of 10.4 mm and a thickness of 1 mm to prevent misalignment and geometric defaults.

Monotonic and cyclic tension and compression tests are conducted.

3.2.2 Biaxial Tests

Channel-die tests consist of a biaxial monotonic loading performed on cubic specimens of 15 $\times$ 15 $\times$ 15 mm^3. These experiments enable obtaining several biaxial compression points by varying the ratio between transversal and longitudinal loadings, using a specific experimental setup that we designed. Figure 1 presents the experimental dispositive and test details. The specimen is loaded in the longitudinal direction, using the MTS machine, and in the transversal direction T_1, using an additional load cell, while the transversal direction T_2 is left free. Two strain gauges were glued on the two opposite free sides of the cube to measure the longitudinal strain ε_L and the transversal strain ε_{T1}. The second transversal strain ε_{T2}, in the free direction T_2, was measured using two opposite linear variable differential transformers. All the specimen-setup interfaces were lubricated using a Teflon-grease-Teflon-hard-paper sandwich to avoid friction and conical fracture (Picart and Pompon, 2016) and to limit the geometric default effects.

Five monotonic channel-die tests were performed. One test consisted of applying an initial transversal load ($\sigma_{T\text{–initial}} = 1$ MPa), then left free during the test, and a longitudinal load until failure. In two other tests, the initial transversal load was kept constant during the test ($\sigma_T =$ 2 MPa and $\sigma_T = 10$ MPa), while applying the longitudinal load until failure. The last two tests consisted of simultaneously applying longitudinal and transversal loads, keeping respectively a ratio of 0.5 and 1 between σ_T and σ_L until failure.

3.2.3 Triaxial Compression

Cyclic triaxial compression tests are performed using compression specimens at hydrostatic pressure levels of 5 and 10 MPa (Fig. 2). The specimen is compressed between two small plates and a small head alignment, inside a pressure vessel filled with paraffin oil. A pressure system group and a sensor mounted on the vessel are used to control the hydrostatic pressure level. A rod compressing the specimen inside the vessel is mounted on the MTS machine to apply

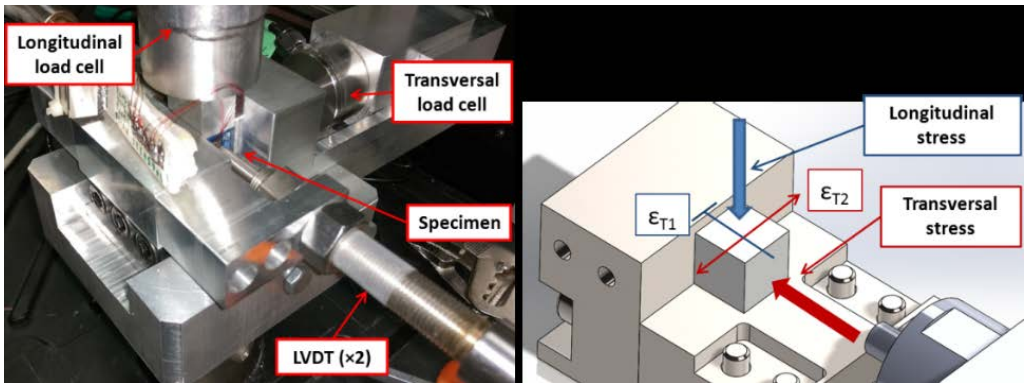

FIG. 1: Experimental dispositive of the channel-die tests

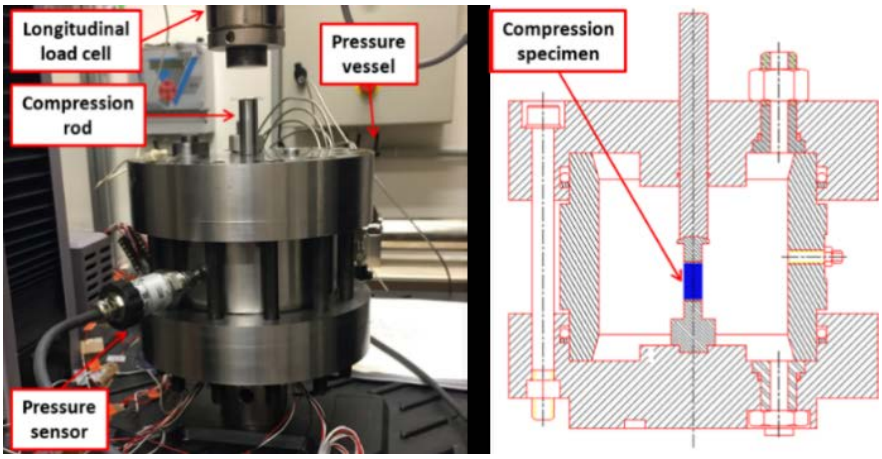

FIG. 2: Triaxial compression experimental dispositive

the longitudinal load. The specimen and the wires are coated by a silicone gel to ensure their impermeability.

3.2.4 Torsion

Cyclic alternated torsion tests are performed using an ElectroForce machine (Bose). A hollow cylindrical specimen with internal diameter of 17 mm, external diameter of 24 mm, and full length of 80 mm is glued to a fixing system on the machine. The tests are torque and axial load-controlled, with a torque rate of 0.04 $\mathrm{N\,m\,s^{-1}}$. The experiments involve the following steps: compression loading until the desired axial load, applying a torque load (T_n: torque value of the cycle n), maintaining a constant torque for a creep step, unloading the specimen until zero torque, and finally a recovery step at zero torque. The same steps are then repeated but in the opposite sequence by applying a negative torque $-T_n$. The next cycle, $n+1$, is performed at a higher torque value ($T_{n+1} = T_n +$ increment) until the failure of the specimen. Two torsion tests are conducted with axial forces of –50 and –2000 N, corresponding to compression stresses of –0.22 and –8.87 MPa, respectively. Local strains are measured with three rectangular rosettes (–45°, 0°, +45°) glued in the middle of the specimen and spaced by 120°. The thermal strain induced by room temperature fluctuation (± 2°C) is compensated using a half-bridge configuration with an unloaded specimen.

4. RESULTS AND DISCUSSIONS

4.1 Microstructural Observations of the Material Failure Surfaces

Figures 3 and 4 show the different constituents of the unloaded material. The initial microstructure reveals the presence of initial intergranular and granular microcracks generated by the manufacturing process.

Figures 5 and 6 show the microstructure of the material loaded in tension. The failure surfaces show long microcracks developed in the interface binder-crystals and sometimes inside the crystals. The microcrack orientations seem random and the damage propagates in all directions. Despite the presence of broken crystals, this failure mode doesn't seem widespread.

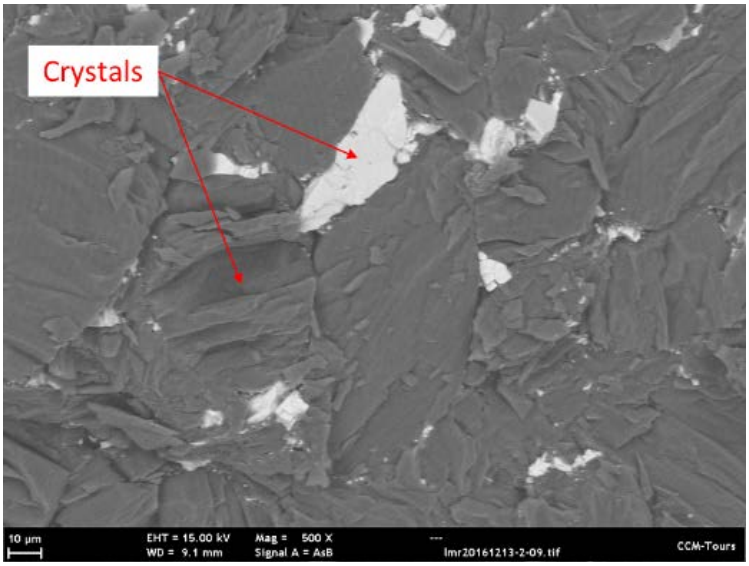

FIG. 3: Microstructure of the pristine material (backscattered electron detector)

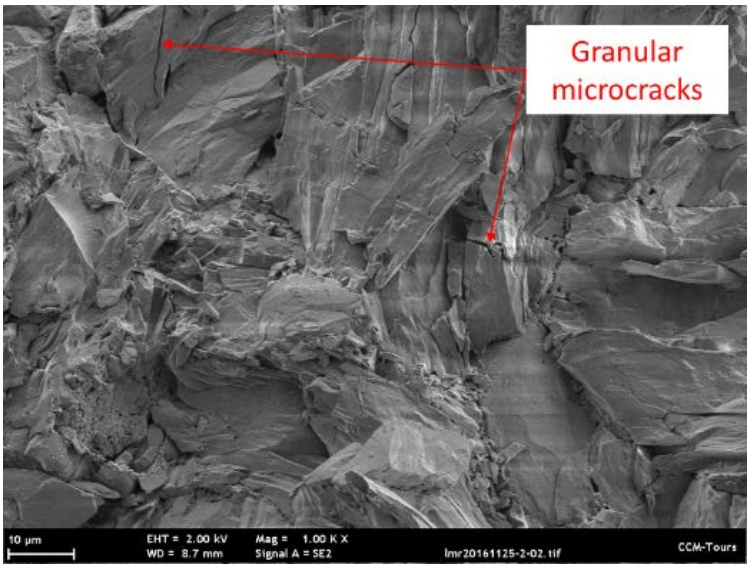

FIG. 4: Microstructure of the pristine material (secondary electron detector)

Failure surfaces observed in compression show higher levels of damage and a different failure mode than tension, as observed in Figs. 7 and 8. Many regions in the microstructure present a high concentration of small crystals due to a violent fracture of big crystals. Some shear bands are observed, also proving the presence of friction and irreversible strains. Same as tension, microcracks are randomly orientated and the damage propagates in all directions.

The microstructure of the material loaded under biaxial compression are presented in Figs. 9 and 10. It seems that those specimens present the same damage mechanisms as compression but

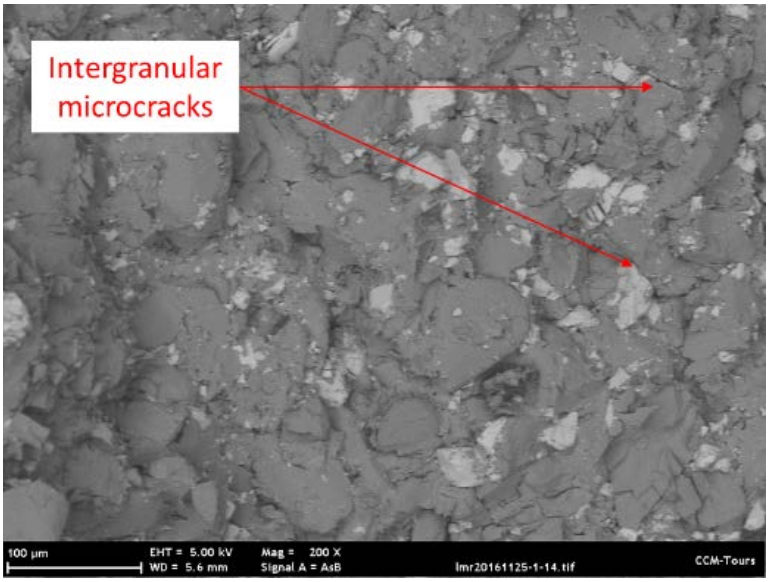

FIG. 5: Microstructure of the material loaded in tension (backscattered electron detector)

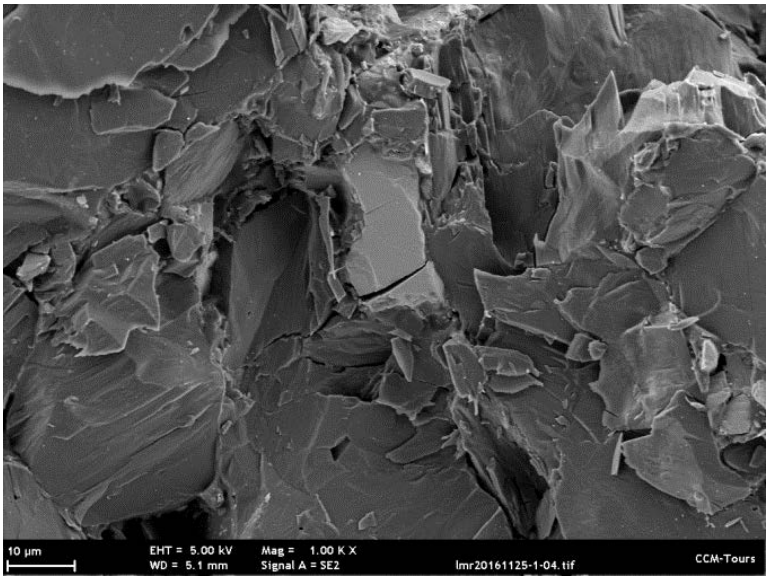

FIG. 6: Microstructure of the material loaded in tension (secondary electron detector)

in a more violent way. However, a new phenomenon consisting of the presence of voids in the microstructure is observed, probably due to the tearing of the crystals from the binder under the high stress levels in biaxial compression.

Observations of the failure surfaces from specimens loaded in torsion under –2000 N (not presented here) showed a mix of damage, and failure modes showed in uniaxial tension and uniaxial compression.

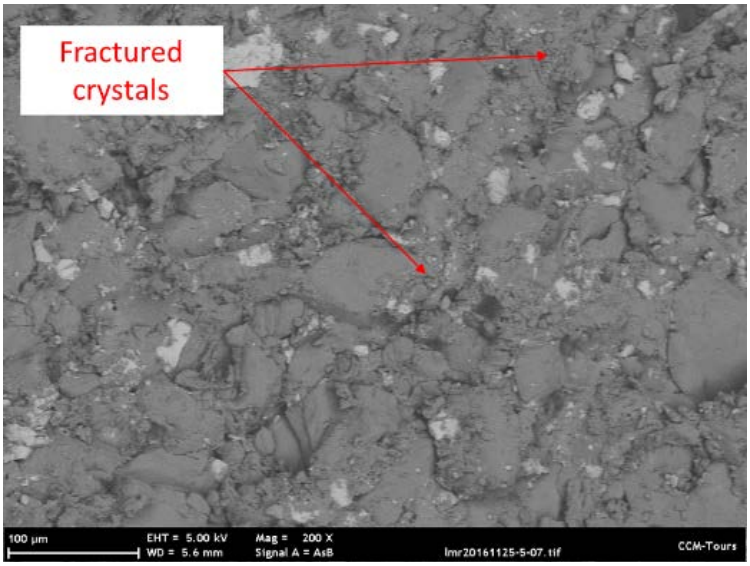

FIG. 7: Microstructure of the material loaded in compression (backscattered electron detector)

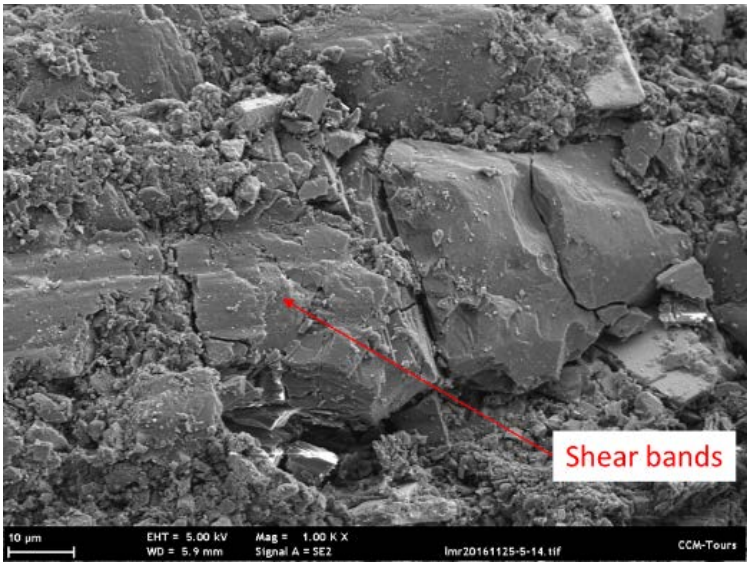

FIG. 8: Microstructure of the material loaded in compression (secondary electron detector)

4.2 Experimental Results

Figure 11 shows the $\sigma(\varepsilon)$ curve obtained from tension test. The low stress levels and thus the quasi-brittle nature of the material in tension can be noted.

Figure 12 compares the $\sigma(\varepsilon)$ curves of uniaxial compression and triaxial compression at 10 MPa. As with geo-materials, the maximum stress level increases with the confinement.

Figure 13 shows the results of the instrumented cyclic torsion test under –50 N.

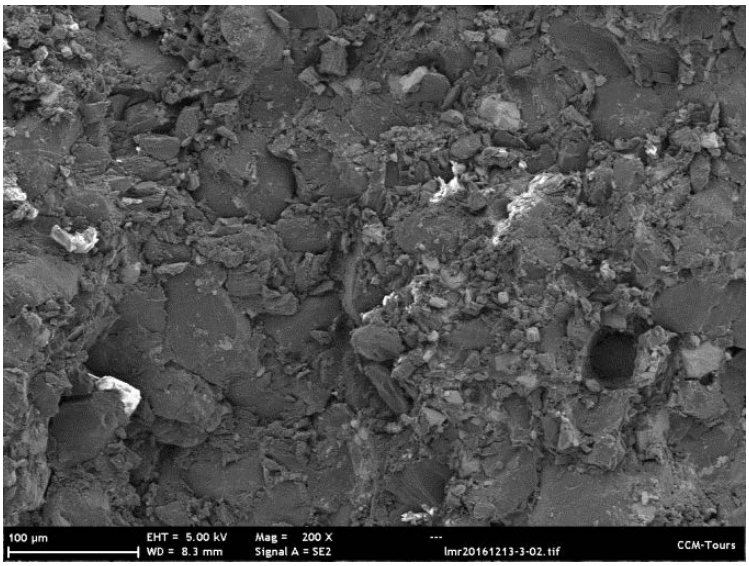

FIG. 9: Microstructure of the material loaded in channel die ($\sigma_{T-\text{initial}} = 1$ MPa)

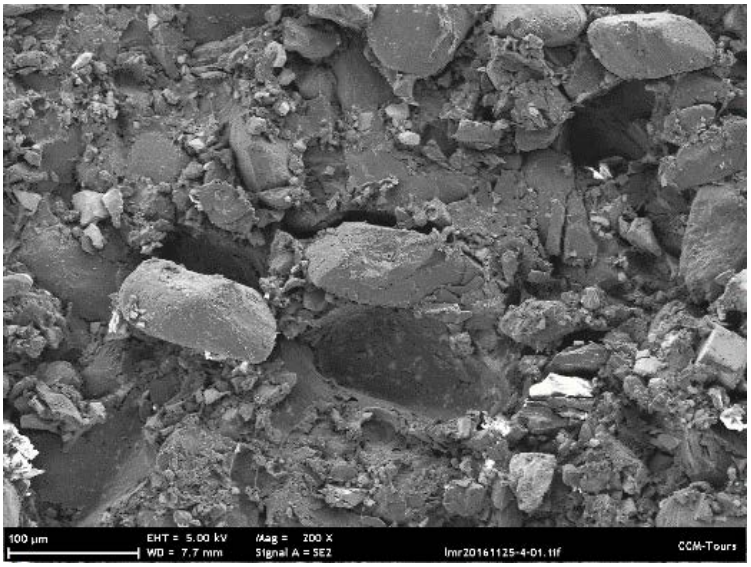

FIG. 10: Microstructure of the material loaded in channel die ($\sigma_L = \sigma_T$)

4.3 Experimental Failure Surface

Failure principal stresses are considered the maximum stress value. These failure stress values are reported in Tables 1–4, for all the conducted tests.

The experimental results (Tables 1–4) for the simulant material are plotted in the biaxial stress state in Fig. 14, in the normalized stress plane ($\sigma_1/|\sigma_{uc}|$, $\sigma_2/|\sigma_{uc}|$), with $\sigma_1 \geq \sigma_2$, $\sigma_3 = 0$, and σ_{uc} is the uniaxial compressive strength. This normalized representation allows the

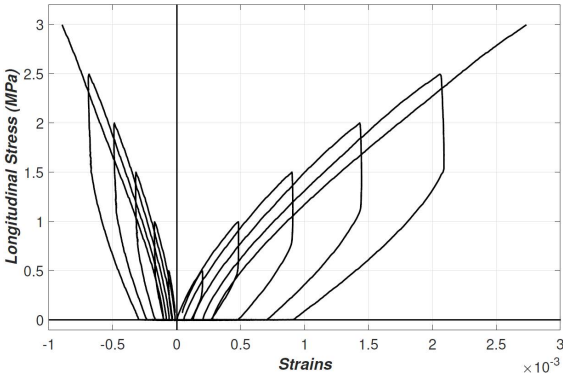

FIG. 11: Stress–strain curve of tension test until failure

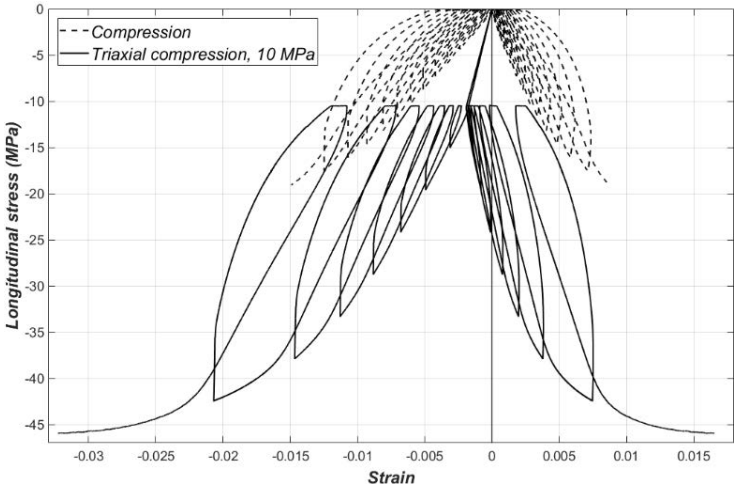

FIG. 12: Stress–strain curves of uniaxial compression and triaxial compression at 10 MPa cyclic tests until failure

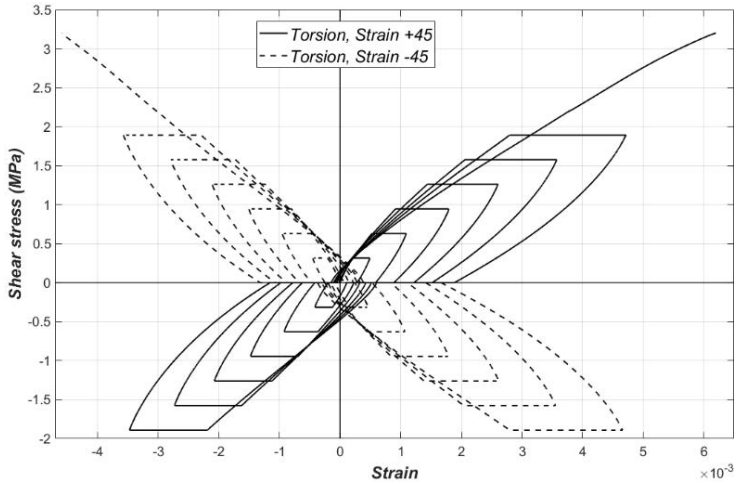

FIG. 13: Stress–strain curve of torsion cyclic test with axial load of –50 N

TABLE 1: Failure principal stresses of the simulant material in tension and uniaxial compression tests

Experiments	σ_1 (MPa)	σ_2 (MPa)	σ_3 (MPa)
Tension	2.77	0	0
Uniaxial compression	–19.55	0	0

TABLE 2: Failure principal stresses of the simulant material in modified channel-die tests

Experiments	σ_1 (MPa)	σ_2 (MPa)	σ_3 (MPa)
Channel-die, $\sigma_{T\text{–initial}} = 1$ MPa	–26.47	–4.42	0
Channel-die, $\sigma_T = 2$ MPa	–24.76	–2.05	0
Channel-die, $\sigma_T = 10$ MPa	–31.51	–10.8	0
Channel-die, $\sigma_T/\sigma_L = 0.5$	–32.88	–15.67	0
Channel-die, $\sigma_T = \sigma_L$	–34.98	–32.2	0

TABLE 3: Failure principal stresses of the simulant material in triaxial compression tests

Experiments	σ_1 (MPa)	σ_2 (MPa)	σ_3 (MPa)
Triaxial compression, 5 MPa	–30.5	–5	–5
Triaxial compression, 10 MPa	–45.96	–10	–10

TABLE 4: Failure principal stresses of the simulant material in compression-torsion tests

Experiments	σ_1 (MPa)	σ_2 (MPa)	σ_3 (MPa)
Torsion, $F_{\text{axial}} = -50$ N	3.09	–3.31	0
Torsion, $F_{\text{axial}} = -2000$ N	2.04	–11.83	0

comparison of failure envelopes of PBX material compositions at different strain rates (Picart and Pompon, 2016).

The failure stresses under tension are low, which confirms the brittle tensile behavior of the studied material. The biaxial tensile strength is missing for the simulant, but data from Picart and Pompon (2016) on PBX suggest that it is almost the same as the uniaxial tensile strength, as commonly seen for concrete materials.

The experimental failure surface presents a nonlinear evolution in the tension-compression quadrant. Moreover, it shows an asymmetry between compression and tension loading. In fact, the ratio between the compressive strength and tensile strength is approximately 7. The simulant material breaks earlier than PBX materials under tension (2.77 vs. 3.25 MPa), but under compression, it presents slightly higher strength (19.55 vs. 18.42 MPa) (Picart and Pompon, 2016). This could be explained first by normal experimental dispersion but also by the high porosity of the simulant material (28%) compared to that of PBX (5%): the opening of defects under tension increases, causing the brittleness, contrary to compression, under which the closure of

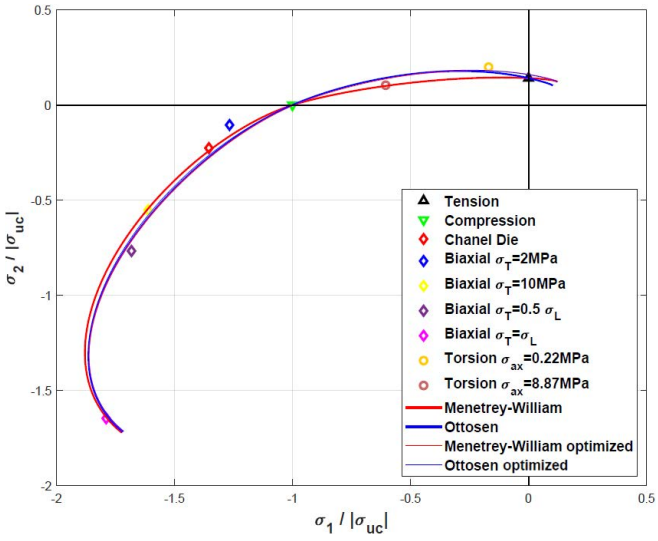

FIG. 14: Experimental and theoretical failure envelopes

cracks induces the recovery of the rigidity. Table 5 presents a comparison between the PBX and the simulant.

The compression-compression quadrant contains points corresponding to the σ_T/σ_L biaxial ratios of 0.083, 0.17, 0.34, 0.48, and 0.92, obtained from the modified channel-die tests. The strength of the material under biaxial compression loading is greater than its strength under uniaxial compression loading. The difference increases as the biaxial ratio increases, reaching 70% for equibiaxial loading ($\sigma_T/\sigma_L = 1$). This phenomenon, well known for concrete materials, can be explained by the increased contact area between crystals, inducing the increased friction under compression. Moreover, in the channel-die setup, the transversal strain L_{T1} is blocked or even negative, which increases the apparent strength of the material by a confinement effect. The characteristics of the simulant failure envelope presented above are similar to those of concrete materials (Chen, 1982; Kupfer and Gerstle, 1973). This supports the idea of testing concrete failure criteria on the studied material.

The results of the two identification methods are presented in Table 6. It appears that the parameters directly identified and the optimization fitting for the Ottosen criterion are very close. On the contrary, the parameters of the Menetrey–Willam criterion are relatively different.

TABLE 5: Comparison between PBX and simulant materials information

Parameters	Simulant	PBX
Particles	Inert crystals	HMX
Particles weight fraction	$\sim 94.5\%$	$\sim 95\%$
Porosity content	28%	5%
Tensile strength (MPa)	2.77	3.25
Compressive strength (MPa)	19.55	18.42
Triaxial compressive strength (at 10 MPa)	45.96	44

TABLE 6: Calibrated parameters of Menetrey–Willam and Ottosen failure criteria

Failure criteria	**Experimental data**					
Menetrey–Willam	$\sigma_{ut} =$ 2.77 MPa	$\sigma_{uc} =$ 19.55 MPa	$e =$ 0.635 MPa	—	—	—
Ottosen	$\sigma_{ut} =$ 2.77 MPa	$\sigma_{uc} =$ 19.55 MPa	$\sigma_{bc} =$ $1.72 \times \sigma_{uc}$	$x = -1.95 \times \sqrt{3} \times \lvert\sigma_{uc}\rvert$ $y = 1.502 \times \lvert\sigma_{uc}\rvert / \sqrt{2}$	—	—
Failure criteria	**Direct identification**					
Menetrey–Willam	$A_f =$ 0.0626	$B_f =$ 0.0209	$C_f =$ 0.0295	$m = 4.649$	$c = 1$	$e =$ 0.635
Ottosen	$A = 10.05$	$B = 3.918$	$k_1 = 4.639$	$k_2 = 0.953$	—	—
Failure criteria	**Identification by optimization fitting**					
Menetrey–Willam	$A_f =$ 0.094	$B_f =$ 0.0313	$C_f =$ 0.0745	$m = 3.61$	$c = 1$	$e =$ 0.646
Ottosen	$A = 7.059$	$B = 3.117$	$k_1 = 4.867$	$k_2 = 0.894$	—	—

To highlight the differences between these parameters, both criteria are first presented in a classical ($\sigma_1/\lvert\sigma_{uc}\rvert$, $\sigma_2/\lvert\sigma_{uc}\rvert$) plan (Fig. 14). This figure shows that both criteria fit well with the tension, compression, and equibiaxial compression points, and present a nonlinear evolution in the tension-compression quadrant. In the compression-compression quadrant, the two criteria pass through all biaxial compression points. It seems that the two applied concrete criteria are in good agreement with the experimental failure points of the simulant material, with satisfactory accuracy. Moreover, the theoretical failure envelopes are in close proximity.

To further investigate the accuracy of the Menetrey–Willam and Ottosen criteria, compressive and tensile meridians are plotted in Fig. 15, in the normalized plane ($\xi/\lvert\sigma_{uc}\rvert$, $\rho/\lvert\sigma_{uc}\rvert$). The evolution of ρ with respect to ξ increases with increasing hydrostatic pressure, following a parabolic trend, as obtained for concrete materials (Chen, 1982; Muthukumar and Kumar, 2014). For the Menetrey–Willam criterion directly identified from literature formulas, the compressive meridian fits reasonably to the experimental points. However, the theoretical compressive meridian is less accurate and passes far from the consolidated (10 MPa) experimental points. For the Ottosen criterion directly identified from literature formulas (Fig. 7), both meridians fit well to the experimental points. This ability of the Ottosen criterion to have a better fit than the Menetrey–Willam criterion is owed to the number of independent parameters used to describe the Ottosen criterion. As already noted, the Menetrey–Willam criterion uses three input data to calculate four parameters, three of which are proportional. Therefore, there are only two independent parameters. For the Ottosen criterion, five input data are used to calculate four independent parameters. Therefore, the latter criterion can best fit the experimental data.

To highlight the effect of the eccentricity parameter, Fig. 16 presents the evolution of both criteria with respect to the experimental data in a deviatoric plan. It can be seen that the Ottosen

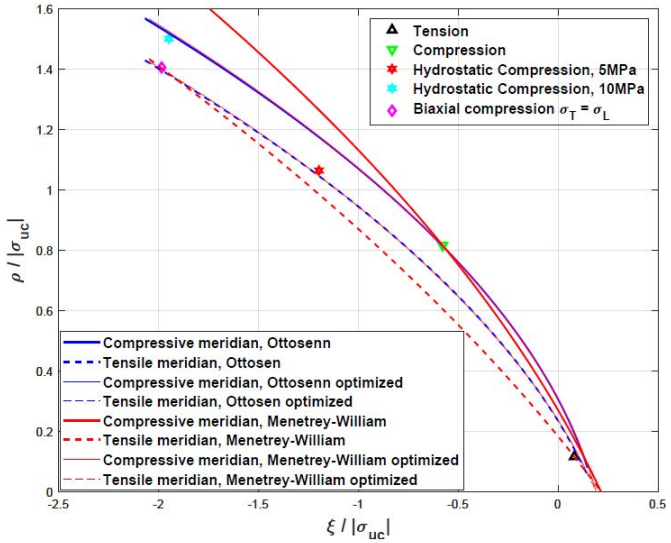

FIG. 15: Compressive and tensile meridians for the simulant material: experimental data, Menetrey–Willam and Ottosen criteria

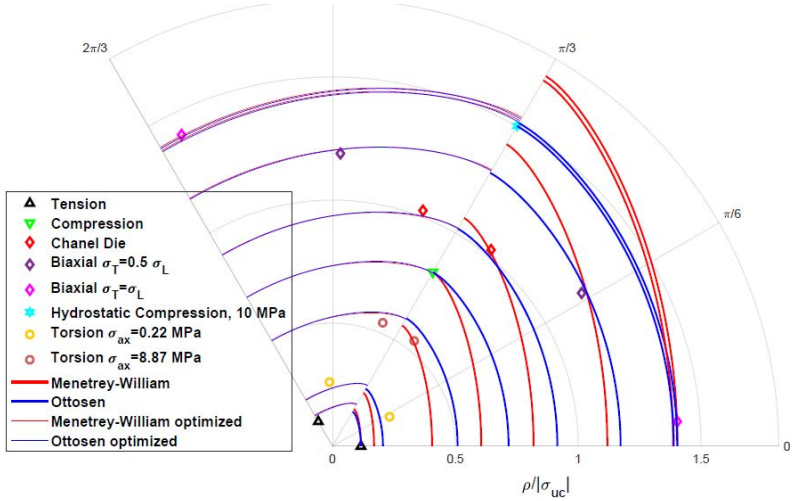

FIG. 16: Experimental data and failure criterion in deviatoric plan with initial $(0; \pi/3)$ and optimized $(\pi/3; 2\pi/3)$ parameters

criterion identified from literature formulas is particularly close to the experimental data in this plan. The Menetrey–Willam criterion is relatively far from the consolidated compression data points. This is at least partially related to the fact that, contrary to the Ottosen criterion, the Menetrey–Willam model does not use the experimental triaxial compression data for identification.

The optimization-based identification method is presented above. These figures show the similarity of the two criteria with this identification method. Therefore, it appears from this comparison that there is no obvious discriminator with which to choose one of the two models.

Figures 14–16 compare the identification results of the two criteria with both methods. This comparison shows that simple tension, simple compression, consolidated compression, and equibiaxial compression are sufficient to obtain a set of parameters for the Ottosen criterion that fits well to all the experimental data. In other words, this limited number of tests can accurately represent the failure criterion for these types of materials.

5. SENSITIVITY STUDY OF FAILURE CRITERIA PARAMETERS

During the identification of the criterion parameters, it is necessary to determine the measurement accuracy required to obtain the smallest possible error in failure prediction. In this section, we study the sensitivity of Eq. (22). We first define the sensitivity and then present the results and discussion.

5.1 Sensitivity Definition

This first-order sensitivity is determined by the ratio of the relative variation of the function to that of the variables. It corresponds to the first-order derivative of the function expressed in Eq. (22), normalized to the reference value of the function.

$$S(1) = \frac{X_i}{\mathcal{F}(X_i)} \frac{d\mathcal{F}}{dX_i}(X_i) \tag{23}$$

The argument 1 of S means the first order of the sensitivity. Discretizing Eq. (23) yields

$$S(1) = \frac{X_i}{\Delta X_i} \frac{\mathcal{F}(X_i + \Delta X_i) - \mathcal{F}(X_i)}{\mathcal{F}(X_i)} \tag{24}$$

5.2 Results and Discussion

Figure 17 presents the first-order sensitivity results. It highlights the predominant sensitivity of the complementary stress state (x, y), and in particular, the deviatoric part. The sensitivity of the equibiaxial compression and isotropic part of the complementary stress state are very close. As their isotropic and deviatoric stress levels are similar, the difference in sensitivity between the

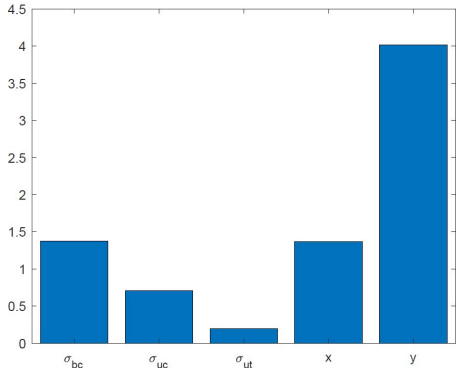

FIG. 17: Results of the sensitivity study on identification function

equibiaxial compression and triaxial compression at 10 MPa can be attributed to the third stress invariant.

This conclusion is confirmed by a similar analysis of the tensile and compression tests. In the case of triaxial compression, the deviatoric part is proportional to the difference between the axial and consolidation stress. This implies that the choice of this complementary stress state must be as accurate as possible to achieve the smallest relative error.

On the contrary, the low level of sensitivity to the tensile stress indicates that for this test, a low accuracy can be accepted.

6. CONCLUSIONS

A simulant material with a composition and behavior similar to those of PBXs was studied using a set of tests to characterize its multiaxial response and obtain a complete failure surface. Uniaxial tension and uniaxial compression tests were used to define the tensile and compressive strengths, respectively. In the tension-compression quadrant, torsion points were obtained from tests conducted at different levels of axial loading. In the compression-compression quadrant, biaxial compression experiments were achieved with a biaxial compression setup. Triaxial compression was performed at hydrostatic pressures of 5 and 10 MPa. The studied material presents similar failure characteristics as concrete materials. The failure envelope is elliptical, showing an increase in the strength with increasing confinement. Tensile and compressive meridians show a parabolic dependency between the hydrostatic stress invariant and deviatoric stress invariant. These observations motivated the use of concrete failure criteria for the studied material.

The Menetrey–Willam and Ottosen criteria were selected and identified for biaxial stress states and for compressive and tensile meridians. The obtained theoretical predictions of the two selected models identified using formulas from the literature show good agreement with the experimental results, especially for Ottosen's criterion. The use of another identification method based on an optimization function led to good agreement for both criteria. The method of identifying Ottosen criterion using the formulas from the literature yields the best fit for this type of criterion. Thus we can conclude that the selected experimental data are sufficient to characterize the yield failure surface for such materials. Finally, sensitivity studies highlighted the necessity of accurate measurements of the complementary failure stress state in the Ottosen criterion (here, the triaxial compression at 10 MPa), and therefore, experimental effort must be focused on such measurements. The importance of the triaxial compression as a complementary stress state comes from the necessity to fit the eccentricity at a high isotropic stress level. The failure stresses of PBX are slightly different from those of the simulant.

In particular, the biaxial compression failure stress state of PBX is lower than that of the simulant and the biaxial tensile is greater than the Ottosen criterion. Taking into account the flexibility of the Ottosen criterion, it would certainly fit the PBX data.

ACKNOWLEDGMENTS

The authors thank Region Centre Val de Loire, France and INSA Centre Val de Loire for funding this project. Additionally, the authors are grateful to CERMEL (Tours, France), and especially Mathieu Venin, for the assistance provided in performing the torsion experiments.

This work was carried out within the framework of the research program of the Corresponding Research Laboratory (CosMa), a joint laboratory combining the CEA Le Ripault and the Gabriel Lamé mechanical laboratory.

REFERENCES

Bailly, P., Delvare, F., Vial, J., Hanus, J.L., Biessy, M., and Picart, D., Dynamic Behavior of an Aggregate Material at Simultaneous High Pressure and Strain Rate: SHPB Triaxial Tests, *Int. J. Impact Eng.*, vol. **38**, pp. 73–84, 2011.

Belmas, R., Mechanical Behaviour of Passed Explosives, *Proc. of Int. Symp. Eng. Mater. Technol.*, Orlando, FL, 1994.

Benelfellah, A., Frachon, A., Gratton, M., Caliez, M., and Picart, D., Analytical and Numerical Comparison of Discrete Damage Models with Induced Anisotropy, *Eng. Fracture Mechan.*, vols. **121–122**, pp. 28–39, 2014.

Brestler, B. and Pister, K.S., Strength of Concrete under Combined Stresses, *Proc. ACI J.*, vol. **55**, no. 3, pp. 321–346, 1958.

Burlion, N., Test Techniques and Experimental Characterization, in J. Torrenti, G. Pijaudier-Cabot, and J. Reynouard, Eds., *Mechanical Behavior of Concrete*, Wiley, 2010.

Caliez, M., Gratton, M., Frachon, A., Benelfellah, A., and Picart, D., Viscoelastic Plastic Model and Experimental Validation for a Granular Energetic Material, *Int. J. Energetic Mater. Chem. Propuls.*, vol. **13**, no. 4, pp. 339–371, 2014.

Chambart, M., Endommagement Anisotrope et Comportement Dynamique des Structures en Béton Armé Jusqu'à la Ruine, PhD, Cachan – Paris: Ecole Normale Supérieure de Cachan – ENS Cachan, 2009.

Chatti, M., Frachon, A., Gratton, M., Caliez, M., Picart, D., and Hocine, N.A., Modelling of the Viscoelastic Behaviour with Damage Induced Anisotropy of a Plastic-Bonded Explosive Based on the Microplane Approach, *Int. J. Solids Struct.*, vol. **168**, pp. 13–25, 2019.

Chen, W.F., *Platicity in Reinforced Concrete*, New York: McGraw-Hill, 1982.

Ellis, K., Leppard, C., and Radesk, H., Mechanical Properties and Damage Evolution of a UK PBX, *J. Mater. Sci.*, vol. **23**, pp. 6241–6248, 2005.

Gagliardi, F.J. and Cunningham, B.J., Axial-Torsion Testing Plastic-Bonded Explosives to Failure, *Proc. of SEM Annual Conf.*, Albuquerque, New Mexico, USA, 2009.

Hsieh, S.S., Ting, E.C., and Chen, W.F., A Plastic-Fracture Model for Concrete, *Int. J. Solids Struct.*, vol. **18**, no. 3, pp. 181–197, 1982.

Idar, D.J., Peterson, P.D., Scott, P.D., and Funk, D.J., Low Strain Rate Compression Measurements of PBXN-9, PBX9501 and Mock9501, *Shock Compression of Condensed Matter*, 1998.

Kupfer, H. and Gerstle, K.H., Behaviour of Concrete under Biaxial Stresses, *J. Eng. Mech. Division*, pp. 853–866, 1973.

Kupfer, H., Hilsdorf, H.K., and Rusch, H., Behavior of Concrete under Biaxial Stresses, *ACI J.*, vol. **66**, pp. 656–666, 1969.

Lee, S.K., Song, Y.C., and Han, S.H., Biaxial Behavior of Plain Concrete of Nuclear Containment Building, *Nucl. Eng. Design*, vol. **227**, no. 2, pp. 143–153, 2004.

Le, V.D., Gratton, M., Caliez, M., Frachon, A., and Picart, D., Experimental Mechanical Characterization of Plastic-Bonded Explosives, *J. Mater. Sci.*, vol. **45**, pp. 5802–5813, 2010.

Li, L.Y. and Harmon, T.G., Three-Parameter Failure Criterion for Concrete, *J. Mater. Civil Eng.*, vol. **2**, no. 4, pp. 215–222, 1990.

Liu, C., Thompson, D.G., Woznick, C.S., Yeager, J.D., and Duque, A.L., PBX 9501 versus a New Thermomechanical Density Mock: Brazilian Disk Compression Test Comparison, *Proc. of AIP Conf.*, 2020.

Liu, Z.W., Xie, H.M., Li, K.X., Chen, P.W., and De Luca, R., Fracture Behavior of PBX Simulant Subject to Combined Thermal and Mechanical Loads, *Polymer Testing*, vol. **28**, no. 6, pp. 627–635, 2009.

Menetrey, P. and Willam, K.J., Triaxial Failure Criterion for Concrete and Its Generalization, *Proc. ACI J.*, vol. **92**, no. 3, pp. 311–318, 1995.

Muthukumar, G. and Kumar, M., Failure Criteria of Concrete – A Review, *Comput. Conrete*, vol. **14**, no. 5, pp. 503–526, 2014.

Ottosen, N.S., A Failure Criterion for Concrete, *J. Eng. Mech. Division*, vol. **103**, no. 4, pp. 527–535, 1977.

Ottosen, N.S. and Ristinmaa, M., *The Mechanics of Constitutive Modeling*, Elsevier, 2005.

Park, C., Jeong, S., Huh, H., and Park, J., Material Behaviors of PBX Simulant with Various Strain Rates, *Key Eng. Mater.*, pp. 117–120, 2013.

Peeters, R.L., Characterization of Plastic-Bonded Explosives, *J. Reinforced Plastics Compos.*, vol. **1**, no. 2, pp. 131–140, 1982.

Picart, D., Benelfellah, A., Brigolle, J.L., Frachon, M., and Caliez, M., Characterization and Modeling of the Anisotropic Damage of a High-Explosive Composition, *Eng. Fracture Mech.*, vol. **131**, pp. 525–537, 2014.

Picart, D. and Brigolle, J.L., Characterization of the Viscoelastic Behaviour of a Plastic Bonded Explosives, *Mater. Sci. Eng.: A*, vol. **527**, pp. 7826–7831, 2010.

Picart, D. and Pompon, C., Experimental Characterization of the Multiaxial Failure of Plastic Bonded Explosive, *Int. J. Energetic Mater. Chem. Propuls.*, vol. **15**, no. 2, pp. 141–165, 2016.

Stevens, R., A Strength Model and Service Envelope for PBX 9501, Los Alamos National Laboratory, 2014.

Thompson, D.G., Deluca, R., and Brown, G.W., Time-Temperature Analysis, Tension and Compression in PBXs, *J. Energetic Mater.*, vol. **30**, pp. 299–323, 2012.

Wiegand, D.A., Constant Strain Criteria for Mechanical Failure of Energetic Materials, *J. Energetic Mater.*, vol. **21**, pp. 109–124, 2003.

Wiegand, D.A., Redingius, B., Ellis, K., and Leppard, C., Pressure and Friction Dependent Mechanical Strength – Cracks and Plastic Flow, *Int. J. Solids Struct.*, vol. **48**, pp. 1617–1629, 2011.

Willam, K.J. and Warnke, E.P., Constitutive Model for Triaxial Behaviour of Concrete, *Proc. of International Association for Bridge and Structural Engineering*, Zurich, Switzerland, vol. **19**, pp. 1–30, 1975.

Williamson, D.M., Siviour, C.R., Proud, W.G., Palmer, S.J.P., Govier, R., Ellis, K., Blachwell, P., and Leppard, C., Temperature-Time Response of a Polymer Bonded Explosive in Compression (EDC37), *J. Phys. D: Appl. Phys.*, pp. 85404–85414, 2008.

Wong, R.C.K., Ma, S.K.Y., Wong, R.H.C., and Chau, K.T., Shear Strength Components of Concrete under Direct Shearing, *Cement Concrete Res.*, vol. **37**, pp. 1248–1256, 2007.

Yeager, J.D., Duque, A.L., Shorty, M., Bowden, P.R., and Stull, J.A., Development of Inert Density Mock Materials for HMX, *J. Energetic Mater.*, vol. **36**, no. 3, pp. 253–265, 2018.

Yeom, K.S., Jeong, S., Huh, H., and Park, J., New Pseudo-Elastic Model for Polymer-Bonded Explosive Simulants Considering the Mullins Effect, *J. Compos. Mater.*, vol. **47**, no. 27, pp. 3401–3411, 2012.

Zhou, Z., Chen, P., Huang, F., and Liu, S., Experimental Study on the Micromechanical Behavior of a PBX Simulant Using SEM and Digital Image Correlation Method, *Optics Lasers Eng.*, vol. **49**, pp. 366–370, 2011.